frontiers | Research Topics

Numerical and experimental studies on small/micro nuclear reactors

Edited by
Yugao Ma, Shanfang Huang, Shichang Liu, Peng Zhang and Jiankai Yu

Published in
Frontiers in Energy Research

ISSN 1664-8714
ISBN 978-2-8325-4703-8
DOI 10.3389/978-2-8325-4703-8

About Frontiers

Frontiers is more than just an open access publisher of scholarly articles: it is a pioneering approach to the world of academia, radically improving the way scholarly research is managed. The grand vision of Frontiers is a world where all people have an equal opportunity to seek, share and generate knowledge. Frontiers provides immediate and permanent online open access to all its publications, but this alone is not enough to realize our grand goals.

Frontiers journal series

The Frontiers journal series is a multi-tier and interdisciplinary set of open-access, online journals, promising a paradigm shift from the current review, selection and dissemination processes in academic publishing. All Frontiers journals are driven by researchers for researchers; therefore, they constitute a service to the scholarly community. At the same time, the *Frontiers journal series* operates on a revolutionary invention, the tiered publishing system, initially addressing specific communities of scholars, and gradually climbing up to broader public understanding, thus serving the interests of the lay society, too.

Dedication to quality

Each Frontiers article is a landmark of the highest quality, thanks to genuinely collaborative interactions between authors and review editors, who include some of the world's best academicians. Research must be certified by peers before entering a stream of knowledge that may eventually reach the public - and shape society; therefore, Frontiers only applies the most rigorous and unbiased reviews. Frontiers revolutionizes research publishing by freely delivering the most outstanding research, evaluated with no bias from both the academic and social point of view. By applying the most advanced information technologies, Frontiers is catapulting scholarly publishing into a new generation.

What are Frontiers Research Topics?

Frontiers Research Topics are very popular trademarks of the *Frontiers journals series*: they are collections of at least ten articles, all centered on a particular subject. With their unique mix of varied contributions from Original Research to Review Articles, Frontiers Research Topics unify the most influential researchers, the latest key findings and historical advances in a hot research area.

Find out more on how to host your own Frontiers Research Topic or contribute to one as an author by contacting the Frontiers editorial office: frontiersin.org/about/contact

Numerical and experimental studies on small/micro nuclear reactors

Topic editors

Yugao Ma — Nuclear Power Institute of China (NPIC), China
Shanfang Huang — Tsinghua University, China
Shichang Liu — North China Electric Power University, China
Peng Zhang — China Nuclear Power Engineering Co Ltd, China
Jiankai Yu — Massachusetts Institute of Technology, United States

Citation

Ma, Y., Huang, S., Liu, S., Zhang, P., Yu, J., eds. (2024). *Numerical and experimental studies on small/micro nuclear reactors*. Lausanne: Frontiers Media SA.
doi: 10.3389/978-2-8325-4703-8

Table of contents

04 Editorial: Numerical and experimental studies on small/micro nuclear reactors
Yugao Ma, Shanfang Huang, Jiankai Yu, Shichang Liu and Peng Zhang

06 Inherent Safety Characteristics of Lead Bismuth Eutectic-Cooled Accelerator Driven Subcritical Systems
Run Luo, Shripad T. Revankar, De Zhang and Fuyu Zhao

24 Peak power prediction method of heat pipe cooled reactor start-up and power-up processes based on ANN
Yu Liu, Mengqi Huang, Zhengyu Du, Changhong Peng and Zhe Wang

38 Analysis of heat transfer mechanism in supercritical fluids from the aspect of pool heating
Minyun Liu, Shenghui Liu, Dapeng Xi, Shanfang Huang and Yanping Huang

53 Analysis of the Brayton cycle coupled with a small fluoride salt-cooled high-temperature reactor
Xiuting Liu, Yanping Huang, Minyun Liu, Luyue Min, Ting Zhang, Xinyu Li and Wenbin Zhuo

67 Analysis of Th and U breeding in a heat pipe cooled traveling wave reactor
Kunfeng Ma and Po Hu

77 POD-based reduced-order modeling study for thermal analysis of gas-cooled microreactor core
Erhui Chen, Huimin Zhang and Yidan Yuan

90 Multiphysics analysis of heat pipe cooled microreactor core with adjusted heat sink temperature for thermal stress reduction using OpenFOAM coupled with neutronics and heat pipe code
Myung Jin Jeong, Jaeuk Im, San Lee and Hyoung Kyu Cho

103 An adaptive time stepping stiffness confinement method for solving reactor dynamics equations
Dan Wang, Wei Xiao, Zhaohui Du and Tengfei Zhang

114 Review of reactor conceptual design and thermal hydraulic characteristics for heat pipe in nuclear systems
Enpei Wang, Tingwei Ren and Lei Li

frontiers | Frontiers in Energy Research

TYPE Editorial
PUBLISHED 21 March 2024
DOI 10.3389/fenrg.2024.1394770

OPEN ACCESS

EDITED AND REVIEWED BY
Shripad T. Revankar,
Purdue University, United States

*CORRESPONDENCE
Yugao Ma,
yugao_ma@163.com

RECEIVED 02 March 2024
ACCEPTED 12 March 2024
PUBLISHED 21 March 2024

CITATION
Ma Y, Huang S, Yu J, Liu S and Zhang P (2024), Editorial: Numerical and experimental studies on small/micro nuclear reactors.
Front. Energy Res. 12:1394770.
doi: 10.3389/fenrg.2024.1394770

Editorial: Numerical and experimental studies on small/micro nuclear reactors

Yugao Ma[1]*, Shanfang Huang[2], Jiankai Yu[3], Shichang Liu[4] and Peng Zhang[5]

[1]Science and Technology on Reactor System Design Technology Laboratory, Nuclear Power Institute of China, Chengdu, China, [2]Department of Engineering Physics, Tsinghua University, Beijing, China, [3]Department of Nuclear Science and Engineering, Massachusetts Institute of Technology, Cambridge, MA, United States, [4]North China Electric Power University, Beijing, China, [5]China Nuclear Power Engineering Co Ltd, Beijing, China

KEYWORDS

numerical, experimental, small nuclear reactor, micro nuclear reactor, editorial

Editorial on the Research Topic
Numerical and experimental studies on small/micro nuclear reactors

Future space missions and deep-sea explorations are expected to rely on small/micro nuclear reactors, ranging from kilowatt-electric (kWe) to megawatt-electric (MWe) power output, for their power generation needs. These reactors offer numerous advantages over conventional energy systems, such as storage batteries and fossil fuels. They provide higher energy density, increased reliability, and longer operational lifetimes. Small/micro nuclear reactors can be classified into various categories based on the coolant they use, including heat pipe cooled reactors, liquid metal cooled reactors, and gas-cooled reactors. Currently, most of these reactors are still in the conceptual design stage, undergoing numerical studies and experimental research.

The unique core structure and operating principles of these emerging reactors differ significantly from existing light water reactors. Consequently, there is a need for the development of updated simulation methods and experimental studies to accurately understand their behavior. Researchers are actively working on improving simulation capabilities and validating them through experiments. They are also making efforts to develop multi-physics coupled analysis programs that consider various physical processes. These advancements provide researchers with a powerful tool to gain in-depth insights into the behavior and performance of small/micro nuclear reactors.

This Research Topic serves as a crucial platform for researchers to share and publish their latest findings and advancements in the field of small/micro nuclear reactors. The Research Topic covers various topics, including thermal-hydraulic and safety analysis, multiphysics coupling, computational code development, and validation, which is divided into three parts: reviews, experiments and simulation.

To comprehensively and systematically summarize and synthesize the field of small/micro nuclear reactors, reviews are provided. In this part, Wang et al. (Wang et al.) provide a comprehensive review of heat pipe cooled reactor (HPCR) conceptual designed by various countries in recent years. The research progress of high temperature heat pipes on flow and heat transfer performance is reviewed, with an emphasis on both transient and steady-state characteristics.

The current research on small/micro nuclear reactors primarily revolves around specific numerical simulations, which are instrumental in analyzing their behavior and performance. These simulations enable researchers to explore different operational scenarios and optimize various parameters for efficient and reliable reactor designs. In this part, Liu et al. (Liu et al.) focus on the impact of rapid power fluctuations in the core during the start-up and power-up processes of HPCR on the safe operation of the reactor. The peak power dataset of HPCR start-up and power-up processes is established and analyzed, using Monte Carlo sampling method. A fast prediction model of peak power was developed based on the artificial neural network. Ma and Hu focused on heat pipe cooled traveling wave reactor (HPTWR) and utilized the Monte Carlo program RMC (Reactor Monte Carlo) to obtain the reactivity swing, propagation of axial power peak, burnup, and productions of bred fissile nuclides for the HPTWR with Thu and U fuels. Liu et al. analyzed the design scheme of coupling a small fluoride-salt-cooled high-temperature reactor (FHR) with the Brayton cycle. A comparison was made among four different configurations of S-CO2 Brayton cycles coupled with FHR in terms of efficiency, exergy energy efficiency, and exergy loss. Meanwhile, the effects of the cooling conditions on the thermal efficiency and exergy efficiency of different cycle configurations are discussed. Jeong et al. developed a multi-physics coupled analysis program based on Open FOAM and the heat pipe thermal analysis code ANLHTP for accurate analysis of heat-pipe-cooled microreactors (HPRs) core. They validated the multi-physics analysis capabilities of this coupled program through analysis and verification of MegaPower. Chen et al. proposed a non-inclusive Proper Orthogonal Decomposition (POD) method based on a neural network. They validated the accuracy of this method using a transient heat conduction model for a two-dimensional plate and applied it to a rapid thermal analysis of the gas-cooled micro-reactor core. Wang et al. analyzed the errors of the stiffness confinement method and proposed a more achievable adaptive time-stepping (ATS) algorithm based on the error analysis by controlling the neutron flux amplitude error. The ATS algorithm yields a higher accuracy at a commensurate computational cost than calculations with fixed time-steps.

Luo et al. presents an inherent safety analysis of an ADS using the ARTAP code, investigating various accident scenarios, including proton beam interruption, transient overpower, reactivity insertion, loss of flow, and loss of heat sink. The results highlight the remarkable advantage of the ADS in mitigating severe accidents and underscore its inherent safety characteristics, demonstrating the ability to ensure reactor shutdown by cutting off the proton beam following accidents.

While numerical simulations dominate the research, complementary experimental studies and validation efforts are also underway to ensure the accuracy and reliability of the findings. In this part, Liu et al. addressed the phenomena of heat transfer deterioration or enhancement in supercritical fluid heat transfer. They proposed a new understanding for pseudo-boiling theory, emphasizing the essential difference between subcritical boiling and supercritical pseudo-boiling, and discussed the physical mechanisms of pseudo-boiling.

In conclusion, ongoing research and development in small/micro nuclear reactors for future space missions and deep-sea explorations are of great significance. Advanced simulation methods and rigorous experimental studies are essential for optimizing the design, operation, and application of these reactors, given their unique core structures and operational principles. Through these efforts, researchers aim to advance the integration of small/micro nuclear reactors into future missions, enabling their utilization in challenging environments for long-duration and high-energy applications. This Research Topic provides a valuable platform for researchers to share their latest findings, contributing to the broader understanding and continued progress in the field of small/micro nuclear reactors.

Author contributions

YM: Supervision, Writing–original draft, Writing–review and editing. SH: Conceptualization, Supervision, Writing–review and editing. JY: Conceptualization, Supervision, Writing–review and editing. SL: Conceptualization, Supervision, Writing–review and editing. PZ: Conceptualization, Supervision, Writing–review and editing.

Conflict of interest

Author PZ was employed by China Nuclear Power Engineering Co Ltd.

The remaining authors declare that the research was conducted in the absence of any commercial or financial relationships that could be construed as a potential conflict of interest.

Publisher's note

frontiers in Energy Research

ORIGINAL RESEARCH
published: 09 March 2022
doi: 10.3389/fenrg.2022.699599

Inherent Safety Characteristics of Lead Bismuth Eutectic-Cooled Accelerator Driven Subcritical Systems

Run Luo[1]*, *Shripad T. Revankar*[2], *De Zhang*[1] and *Fuyu Zhao*[3]

[1]School of Resource & Environment and Safety Engineering, Cooperative Innovation Center for Nuclear Fuel Cycle Technology and Equipment, University of South China, Hengyang, China, [2]School of Nuclear Engineering, Purdue University, West Lafayette, IN, United States, [3]School of Nuclear Science and Technology, Xi'an Jiaotong University, Xi'an, China

An accelerator driven subcritical system (ADS) is a new nuclear energy system which could not only produce clean energy but also incinerate nuclear waste. In this paper, inherent safety analysis of an ADS is performed with neutronics and thermal-hydraulics coupled code named ARTAP. Five typical accidents are carried out, including the cases of proton beam interruption, transient overpower, reactivity insertion, loss of flow, and loss of heat sink. The transient simulations are performed in the average channel and the hottest channel of the fuel pin in the ADS core. The simulation results for beam interruption show that the highest temperature of the pellet is in the middle of the fuel element in the average channel, while the peak temperature of the cladding is in the top of the fuel element. After the beam is interrupted for 20s, the maximum temperature drops at the fuel center, the cladding inner surface, and the outlet coolant in the hottest channel are 644.46K, 162.27K, and 136.42K respectively. For transient overpower accidents with the increase of beam intensity, the maximum temperature of the fuel and the cladding are below the safety limit. Concerning the reactivity insertion accident, it is found that the ADS has good inherent safety and its margin of criticality safety is large. The calculation results for loss of flow show that the power drop is small due to low sensitivity of the subcritical core to negative reactivity feedback, and the maximum temperature of the cladding reaches 1726K, which means the fuel element would rupture. However, the power and the temperatures of fuel, cladding, and coolant could decrease quickly to the safety level after the proton accelerator is cut off under a loss of flow accident. The results also show that the peak temperature of the cladding is lower than the safety limit under a loss of heat sink accident. The present simulation results reveal that the ADS has a remarkable advantage against severe accidents. It also implies that its inherent safety characteristics could ensure reactor shutdown by cutting off the proton beam after accidents occur.

Keywords: accelerator driven system, neutronics, thermal-hydraulics, safety analysis, accident

OPEN ACCESS

Edited by:
Ivan Vrbanic,
APOSS d.o.o., Croatia

Reviewed by:
Muhammad Saeed,
East China University of Technology, China
Zhu Rongsheng,
Jiangsu University, China

***Correspondence:**
Run Luo
luorun@usc.edu.cn
runluozh@163.com

Specialty section:
This article was submitted to Nuclear Energy, a section of the journal Frontiers in Energy Research

Received: *23 April 2021*
Accepted: *07 February 2022*
Published: *09 March 2022*

Citation:
Luo R, Revankar ST, Zhang D and Zhao F (2022) Inherent Safety Characteristics of Lead Bismuth Eutectic-Cooled Accelerator Driven Subcritical Systems. Front. Energy Res. 10:699599. doi: 10.3389/fenrg.2022.699599

1 INTRODUCTION

Nuclear energy is the hope of sustainable energy growth all over the world. An accelerator driven subcritical system (ADS) is a new nuclear energy system which could not only produce clean energy but also incinerate actinide nuclides and long-lived radioactive fission products (Maschek et al., 2008). The ADS device consists of a subcritical core, a high-energy proton accelerator, and a neutron spallation target, in which the fission process is sustained by a spallation neutron source. Compared with critical fast reactors, ADS have a better performance of nuclear waste transmutation due to a harder neutron spectrum. In recent years, ADS has been attracting more and more attention because of its superior neutronics and safety characteristics (Kumar and Katovsky, 2020). Conceptual designs of three types of eXperimental Accelerator Driven Systems (XADS) have been studied by the European Atomic Energy Community within its fifth framework program (Cinotti et al., 2004), which include a zero-power subcritical facility YALINA, a 80 MW Lead Bismuth Eutectic (LBE) cooled XADS, and a 50 MW multi-purpose hybrid research reactor MYRRHA for high-tech applications. A roadmap for developing an Accelerator Transmutation of Waste (ATW) technology was presented by the United States Department of Energy (DOE) (Van Tuyle et al., 2001), several researchers studied the physics design for using sodium or LBE as coolant of the ATW systems (Hill and Khalil, 2001; Yang and Khalil, 2001). The Japan Atomic Energy Agency (JAEA) has investigated an 800 MW LBE-cooled subcritical reactor with a 1.5 GeV proton accelerator to transmute minor actinides (Sugawara et al., 2018). The research of a HYbrid Power Extraction Reactor (HYPER) has been performed by Korea Atomic Energy Research Institute (KAERI) to produce energy and transmute nuclear waste (Park et al., 2000). The China Lead-based Reactor (CLEAR) and the Chinese initiative Accelerator Driven Subcritical System (CiADS) were proposed by the Chinese Academy of Sciences for the transmutation of nuclear waste and sustainability of nuclear energy development (Wu, 2016; Huang et al., 2021). The conceptual design of a 10 MW LBE-cooled CLEAR has been completed, and a proton accelerator with 650 MHz multicell superconducting radio frequency (SRF) was proposed in the CiADS device.

The components of the ADS system and its operation principle are significantly different from those of traditional nuclear reactor systems. To ensure safe operation of the ADS system, it is necessary to investigate the transient characteristics under accident conditions. Several codes have been developed for the safety analysis of ADS based on a point-kinetics model coupled with thermal and hydraulic feedback effects (Schikorr, 2001; D'Angelo et al., 2003), in which the dynamic behaviors of beam interruptions, loss of flow, and overpower accidents were performed. However, the point-kinetics method may be inaccurate in the case of severe source perturbations involving strong reactivity feedback that produce great flux distortion, which may happen during a serious accident (Eriksson et al., 2005; Rineiski and Maschek, 2005). Therefore, the variation of the spatial shape function with time should be considered in the ADS model. Chen et al. (2003) analyzed some safety characteristics for an LBE-cooled ADS using the extended SIMMER-III code, which is a two-dimensional fluid-dynamics system program coupled with a space-time dependent neutron kinetics model. In addition, Suzuki et al. (2005) investigated the unprotected blockage in a single fuel assembly and severe core-melt accidents with the updated SIMMER-III. The neutronics and thermal-hydraulics coupled simulation program was developed by the FDS team for the design and research of lead or LBE cooled ADS reactors (Wang G. et al., 2015), and three typical transient accidents were simulated with NTC code, such as beam trip and transient overpower condition (Wang Z. et al., 2015). Lu et al. (2016) used the RELAP5 program for the safety analysis on loss of flow accidents and external source transients of a 800 MW ADS with the code modifications of the point-kinetics model and the thermal property package. However, those calculations of safety characteristics mainly investigate the average fuel channel of the ADS assembly under accident conditions, very few studies have taken into account the case of the hottest fuel channel. The assessment of the hot channel factor (HCF) in the ADS core is very important for the quantification of safety margins.

The objective of this research is to analyze the inherent safety characteristics of the LBE-cooled ADS by using a neutronics and thermal-hydraulics coupled simulation code named ARTAP. The developed code consists of a space-time neutron diffusion equation with a spallation neutron source model and a thermal-hydraulics model with a package of thermophysical properties. Five typical accidents are calculated by ARTAP code, which include proton beam interruption, transient overpower, reactivity insertion, loss of flow, and loss of heat sink. In addition, the transient simulations are not only carried out in an average fuel pin of the ADS assembly, but also in the hottest fuel pin. The transient behaviors of the reactor power and the temperatures of the fuel, cladding, and coolant are investigated during the accident sequences.

2 COMPUTATIONAL MODEL AND METHOD

The primary system of the ADS device consists of a subcritical core, a high-energy proton accelerator, and a heavy metal spallation target. The configuration of a typical LBE-cooled ADS is shown in **Figure 1**. An accelerator proton beam is introduced into the target and then hits the metal target to initiate spallation reaction. As the result of spallation reaction process, neutrons will be supplied to the subcritical reactor core, which serve as an external neutron source to maintain fission chain reactions. The heat produced in the core will be carried out by the coolant of lead bismuth eutectic (LBE). The secondary coolant system is composed of three independent loops which contain three intermediate heat exchangers (IHX). The coolant of the primary loop is high temperature LBE in the IHX and the secondary coolant is an organic diathermic fluid for the Italian ADS system (Cammi et al., 2006).

In this paper, a developed computational code named ARTAP is applied in analysis of the inherent safety characteristics for the LBE-cooled ADS, which comprises of a steady-state analysis module and a transient analysis module. The steady-state

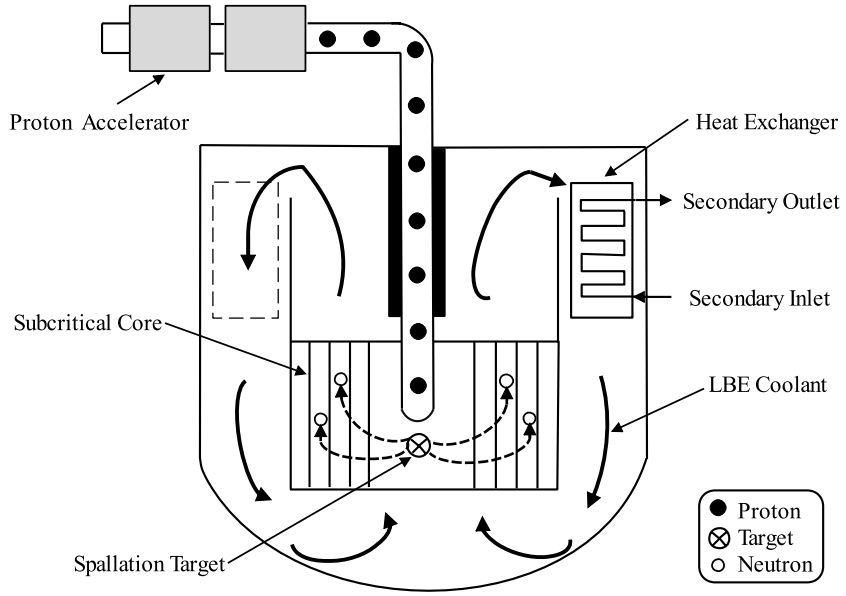

FIGURE 1 | Configuration of a typical LBE-cooled ADS.

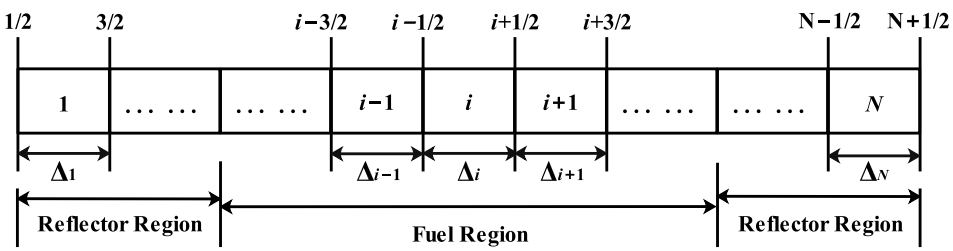

FIGURE 2 | Spatial discretization in the axial direction.

analysis module couples a one-dimensional neutron diffusion equation and a thermal-hydraulics single-channel model (Luo et al., 2018). The modeling process of steady-state neutronics is performed in two stages, a low-energy deterministic calculation for the subcritical core and a high-energy Monte Carlo simulation for the spallation neutron source. The single channel model is chosen for the ADS thermal-hydraulics calculation, which includes the heat conduction in the fuel element and the heat transfer from cladding to coolant. According to the power distribution obtained by the neutron diffusion calculation, the thermal-hydraulics analysis is performed, and the obtained temperature distributions of coolant and fuel are selected as the feedback parameters to update the nuclear cross sections. Then the neutron diffusion calculation is carried out to update the power distribution. This coupling iterative process continues until the convergence of power distribution is met. The transient analysis module consists of space-time neutron kinetic equations and thermal-hydraulics dynamic equations. The calculation of transient models is divided into two steps, i.e., the spatial discretization with the finite difference method and the numerical solution of nonlinear time-dependent differential equations with a backward differentiation formulas (BDFs) method (Shampine et al., 1999).

2.1 Space-Time Neutron Diffusion Model

Although the three-dimensional full core multi-physics modeling of a nuclear reactor is an effective way to obtain the key information of the reactor core with high precision, the required data storage space is huge and the running time is quite long. In a few special calculations like performing the reactor control system design, transient safety analysis, or load following study, the detailed radial information of the reactor core is not necessarily needed due to the radially symmetrical layout of fuel assemblies and control rod banks (Song et al., 2016). Thus, a one-dimensional neutron diffusion model in the axial direction will be more preferable when the calculation precision is not reduced.

2.1.1 Space-Time Neutron Kinetics Model

The space and time dependent neutron kinetics model of the ADS reactor is as follows (Duderstadt and Hamilton, 1976):

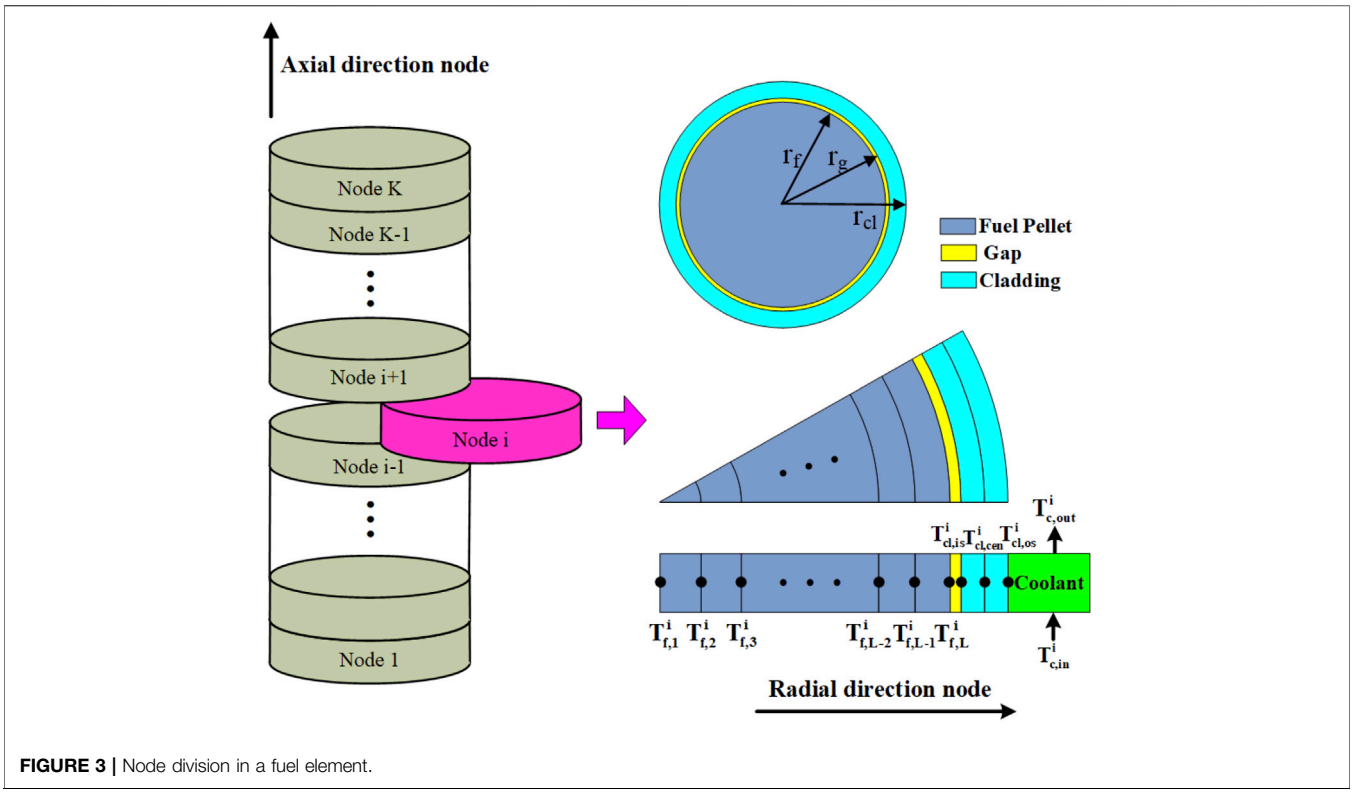

FIGURE 3 | Node division in a fuel element.

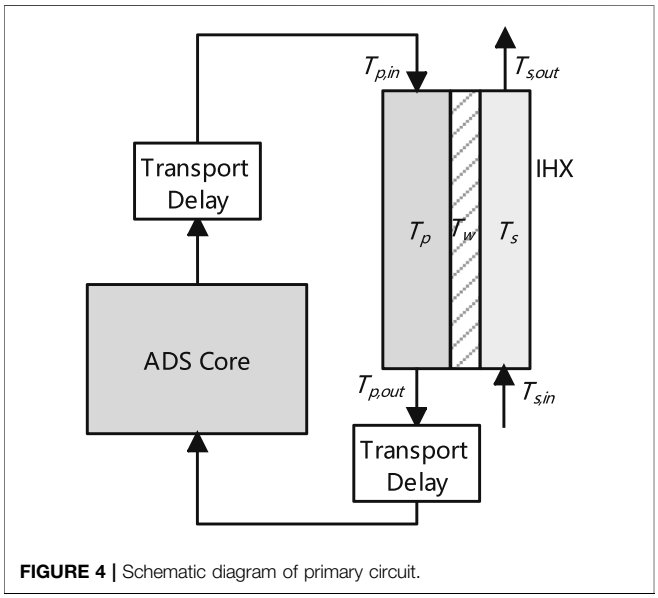

FIGURE 4 | Schematic diagram of primary circuit.

$$\frac{1}{v_a}\frac{\partial\phi(z,t)}{\partial t} = D\nabla^2\phi(z,t) - \Sigma_a\phi(z,t) + (1-\beta)\nu\Sigma_f\phi(z,t) + \sum_{j=1}^{6}\lambda_j C_j(z,t) + S(z,t) \quad (1)$$

$$\frac{\partial C_j(z,t)}{\partial t} = \beta_j\nu\Sigma_f\phi(z,t) - \lambda_j C_j(z,t); \quad j = 1,2,\ldots,6 \quad (2)$$

where v_a is the average speed of neutron, ϕ is the neutron flux, z is the axial position, t is the time, D is the diffusion coefficient, Σ_a and Σ_f are the macroscopic cross section of absorption and fission respectively, ν is neutrons yield per fission, S is the spallation neutron source, β is the total delayed neutron fraction, β_j is the delayed neutron fraction of group j, C_j and λ_j are the delayed neutron precursor concentration and decay constant, respectively.

In the process of the neutron flux calculation, the finite difference method will be used for the discretization in space. This discretization is shown in **Figure 2**, and the size of each node is Δ_i. The power iteration method is used to calculate steady-state diffusion equation (Duderstadt and Hamilton, 1976), and the corresponding distribution of neutron flux could be determined by this iterative scheme. After the spatial discretization, neutron kinetics models could be transformed into the normal forms of time-dependent differential Equations which could solved by a backward differentiation formulas (BDFs) method with a scheme of implicit time discretization.

2.1.2 Spallation Neutron Source Calculation

The space and energy distributions of the spallation neutrons $S(z, t)$ in the target for the ADS reactor are calculated by a Monte Carlo transport code, which could simulate the interaction between an accelerator proton beam and a metal target (Pelowitz et al., 2005). A model of the spallation target was built by using this code and the neutrons tracked in the spallation target are tallied into an output file, then the

TABLE 1 | Thermophysical properties of fuel, cladding and coolant.

Thermophysical parameters	Correlation
Fuel density (kg · m–3)	11 080[1 + 2.04 × 10^{-5} (T – 273) + 8.7 × 10^{-9} (T – 273)^2]$^{-1}$
Fuel thermal conductivity (W · m–1 · K–1)	(0.042 + 2.71 × 10^{-4} T)$^{-1}$ + 6.9, ×, 10^{-11} T^3
UO2 specific heat (J · kg–1 · K–1)	81.825 + 0.78 695T – 1.155 2 × 10–3T2 + 9.903 7 × 10–7T3–5.198 2 × 10–10T4 + 1.524 1 × 10–13T5–1.790 6 × 10–17T6
PuO2 specific heat (J · kg–1 · K–1)	–4.923 6 × 106T–2 + 240.89, +,0.32 556T – 3.539 8 × 10–4T2 + 1.512×10–7T3–1.970 7 × 10–11T4
Fuel specific heat (J · kg–1 · K–1)	0.7 944C_{UO_2} + 0.2 056C_{PuO_2}
Cladding density (kg · m–3)	7,785 [1–3 (–3.094 2 × 10–3 + 1.192 8 × 10–5T – 6.797 9, ×, 10–9T2 + 7.960 6 × 10–12T3–2.546 × 10–15T4)]
Cladding thermal conductivity (W · m–1 · K–1)	21.712 + 0.011T – 9.548 3 × 10–6T2 + 3.627 × 10–9T3
Cladding specific heat (J · kg–1 · K–1)	432.8 + 0.7 038T – 2.211 3 × 10–3T2 + 5.316 × 10–6T3–3.105 × 10–9T4
Coolant density (kg · m–3)	11,112–1.375T
Coolant thermal conductivity (W · m–1 · K–1)	3.35 + 1.59, ×, 10–2T – 1.95 × 10–6T2
Coolant specific heat (J · kg–1 · K–1)	164–4.06 × 10–2T + 1.33 × 10–5T2
Coolant dynamic viscosity (Pa · s)	4.94 × 10–4e (754.1/T)

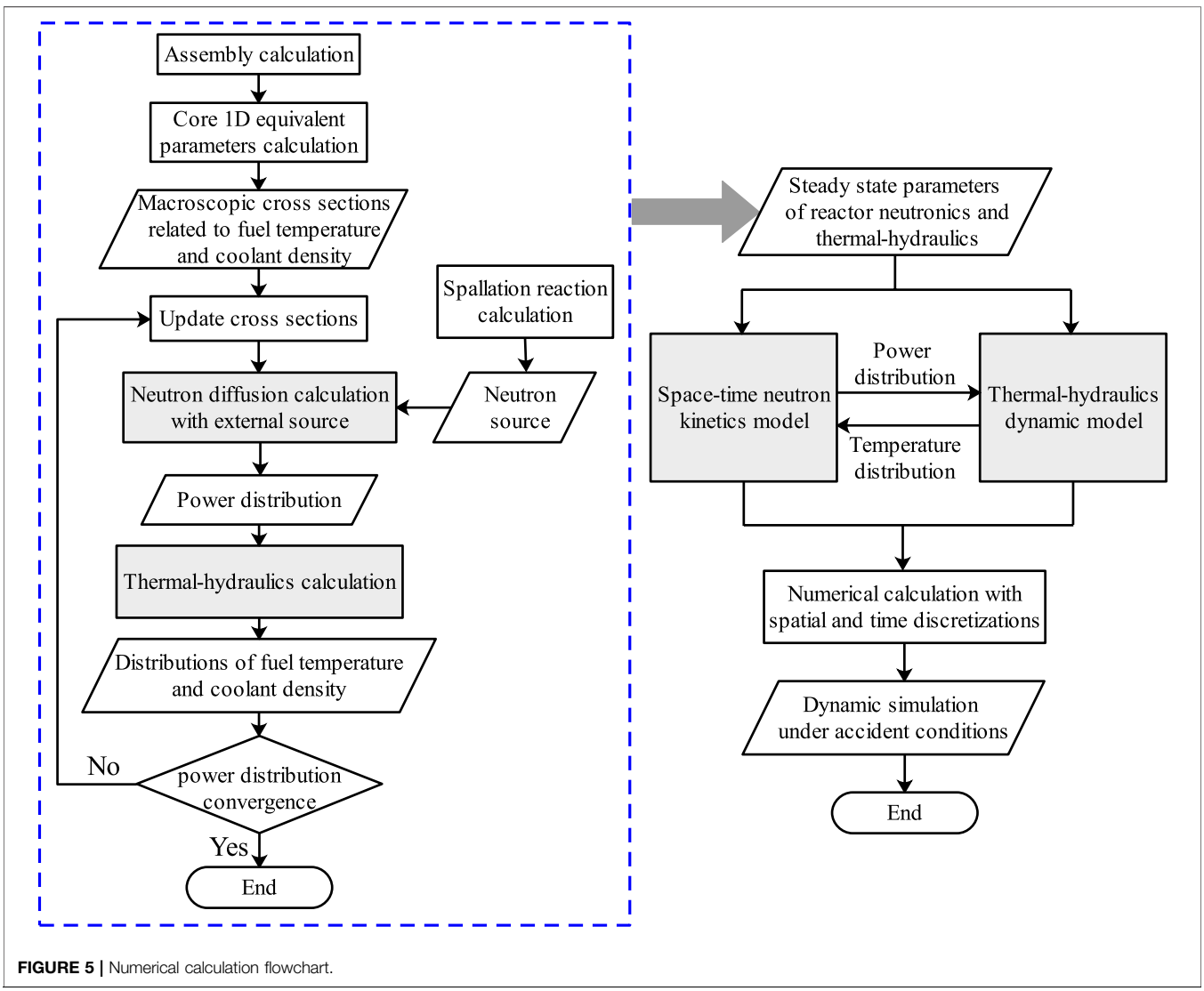

FIGURE 5 | Numerical calculation flowchart.

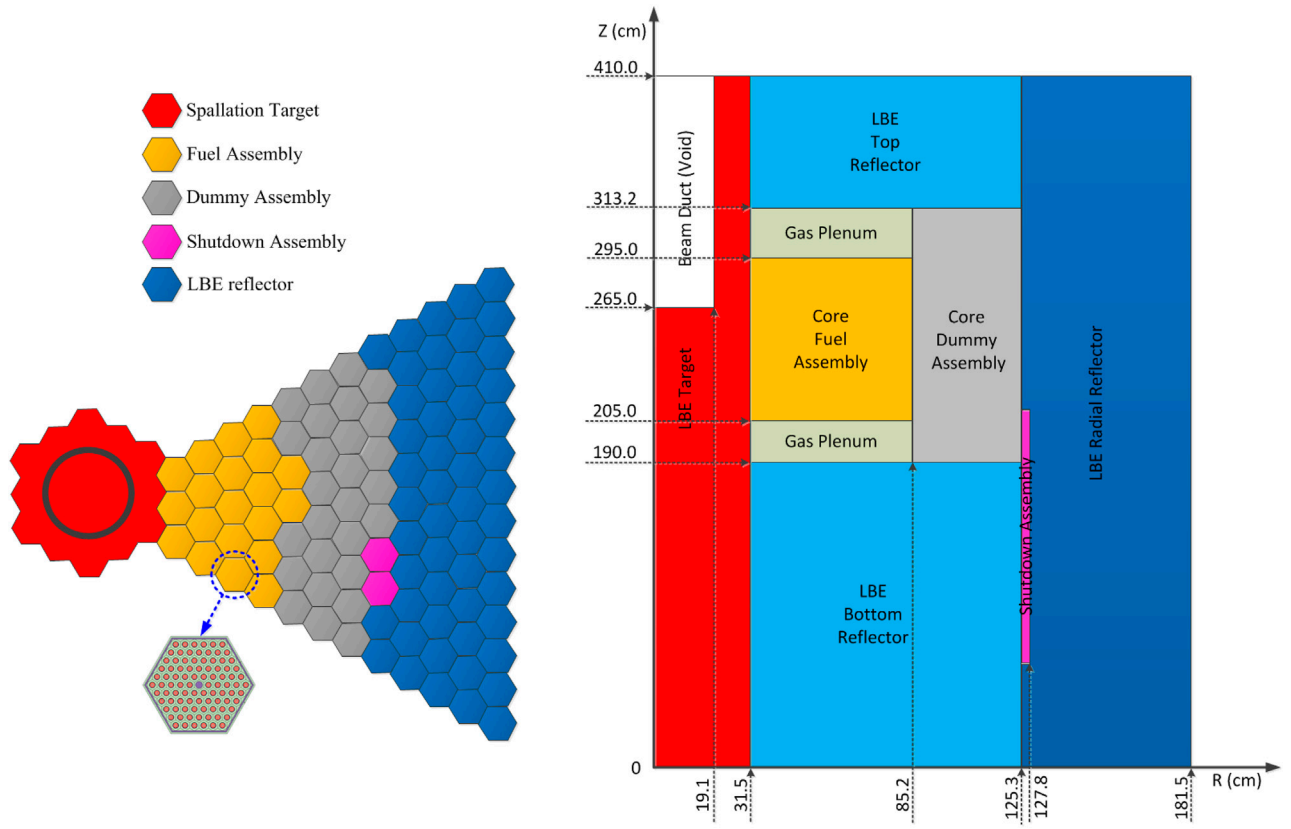

FIGURE 6 | Arrangement of assemblies and R–Z view of reactor model.

TABLE 2 | Main design parameters of the ADS system.

Parameters	Values
Total thermal power (MW)	80
Proton energy (MeV)	600
Intensity of proton beam (mA)	2.5
Effective multiplication factor	0.97
Fuel element height(m)	0.9
Fuel pellet outer diameter(m)	7.14 × 10–3
Cladding inner diameter(m)	7.37 × 10–3
Cladding outer diameter(m)	8.5 × 10–3
Coolant flow area (m2)	9.89, ×, 10–5
Pin pitch(m)	1.341 × 10–2
Core inlet temperature(K)	573
Core outlet temperature(K)	673

distribution of spallation neutrons could be obtained, which are used as the external source for the ADS neutron diffusion calculation. The intensity of the neutron source could be calculated using **Equation 3** (Zhou et al., 2014):

$$S = \frac{\eta_p}{e} I_p \tag{3}$$

where η_p is the number of spallation neutrons released per proton, e is the electric charge on an electron, I_p is the intensity of the proton beam that can be derived by the following formula (Zhou et al., 2014):

$$I_p = \frac{P_f \nu}{E_f} \frac{e}{\eta_p} \frac{1 - k_{eff}}{k_{eff}} \tag{4}$$

where P_f is the total thermal power of the subcritical core, E_f is the averaged energy released per fission, k_{eff} is the effective multiplication factor, which is an important concept in reactor physics. When neutron disappearance does not equal neutron regeneration, the k_{eff} is introduced to the steady state diffusion equation for the criticality calculation, and the subcriticality $1 - k_{eff}$ could be obtained, which means the distance from a criticality. After external source is added into the subcritical core, the neutron population is perfectly balanced, thus the k_{eff} should be eliminated in the ADS steady state calculation.

2.1.3 Macroscopic Cross Section Generation

Taking into account the Doppler effect and the coolant feedback effect, the parameters of macroscopic cross sections (D, Σ_a and $\nu\Sigma_f$) are mainly related to fuel temperature T_f and coolant density ρ_c in **Equation 1**. The calculation of macroscopic cross sections is performed using a lattice physics code at different temperature points (Luo et al., 2018). Then the values of these parameters D (T_f, ρ_c), Σ_a (T_f, ρ_c) and $\nu\Sigma_f$ (T_f, ρ_c) could be obtained by a linear

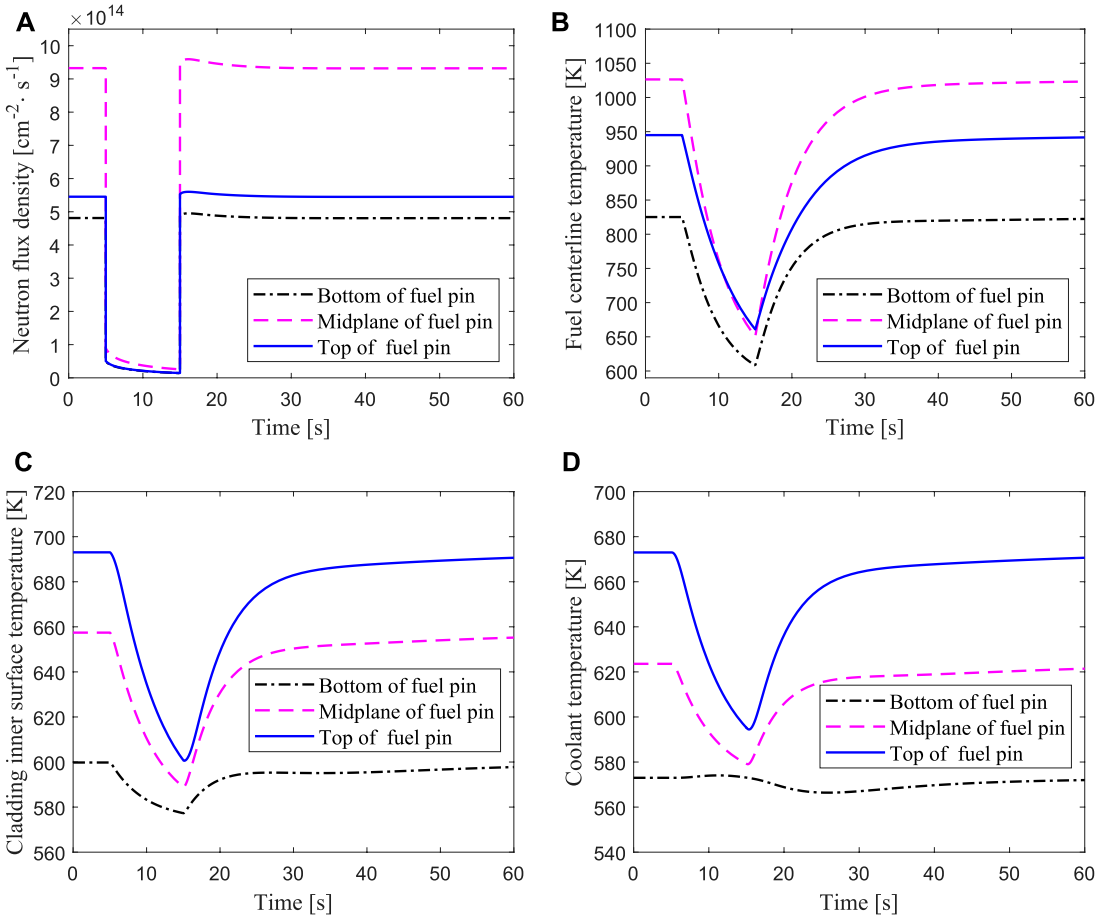

FIGURE 7 | Transient responses of the average channel under beam interruption accident for 10 s.

interpolation method. Finally, the one-dimensional equivalent parameters are obtained from flux volume weighting in three-dimensional space (Song et al., 2016):

$$M_i = \frac{\int_{V_i} M(\boldsymbol{r})\phi(\boldsymbol{r})dV}{\int_{V_i} \phi(\boldsymbol{r})dV} \tag{5}$$

where M_i is the average value of macroscopic cross-section (D, Σ_a and $\nu\Sigma_f$) in axial node i, $\boldsymbol{r}$ is the position vector in three-dimensional space, $\boldsymbol{r}$ is the volume of axial node i.

2.2 Thermal-Hydraulics Model

The energy released in the fission reaction in the ADS core and the quantity of heat must be removed from the fuel to the coolant immediately for the safety of the system operation. In this work, a single channel model is performed for the thermal-hydraulics calculation, which includes the heat conduction in fuel element and the heat transfer from cladding to coolant. As we all know, one of the main goals of the thermal-hydraulics core design is to ensure that the core temperatures remain below the damage limit of core components, especially for the fuel pellet and the cladding materials. Therefore, it is significant to obtain the maximum fuel temperature from the analysis of transient behavior of the average and hottest channels in the ADS core.

2.2.1 Heat Conduction in Fuel Elements

In order to obtain the spatial distribution of temperatures of fuel and cladding, the fuel element is divided into K nodes in the axial direction and L nodes in the radial direction, as shown in **Figure 3**.

Since the thickness and thermal resistance of cladding are much smaller than those of fuel pellet, the cladding is only divided into three nodes in the radial direction to obtain its inner surface and outer surface temperatures. Axial heat conduction is ignored because of prevailing radius to length ratios and axisymmetry (Wulff et al., 1985). Therefore, the heat conduction equation for the fuel pellet in the axial node i could be written as:

$$\rho_f^i C_f^i \frac{\partial T_f^i(r,t)}{\partial t} = \frac{1}{r}\frac{\partial}{\partial r}\left(rk_f^i \frac{\partial T_f^i(r,t)}{\partial r}\right) + q_v^i \tag{6}$$

The boundary conditions of the heat conduction equation for the fuel pellet can be described as:

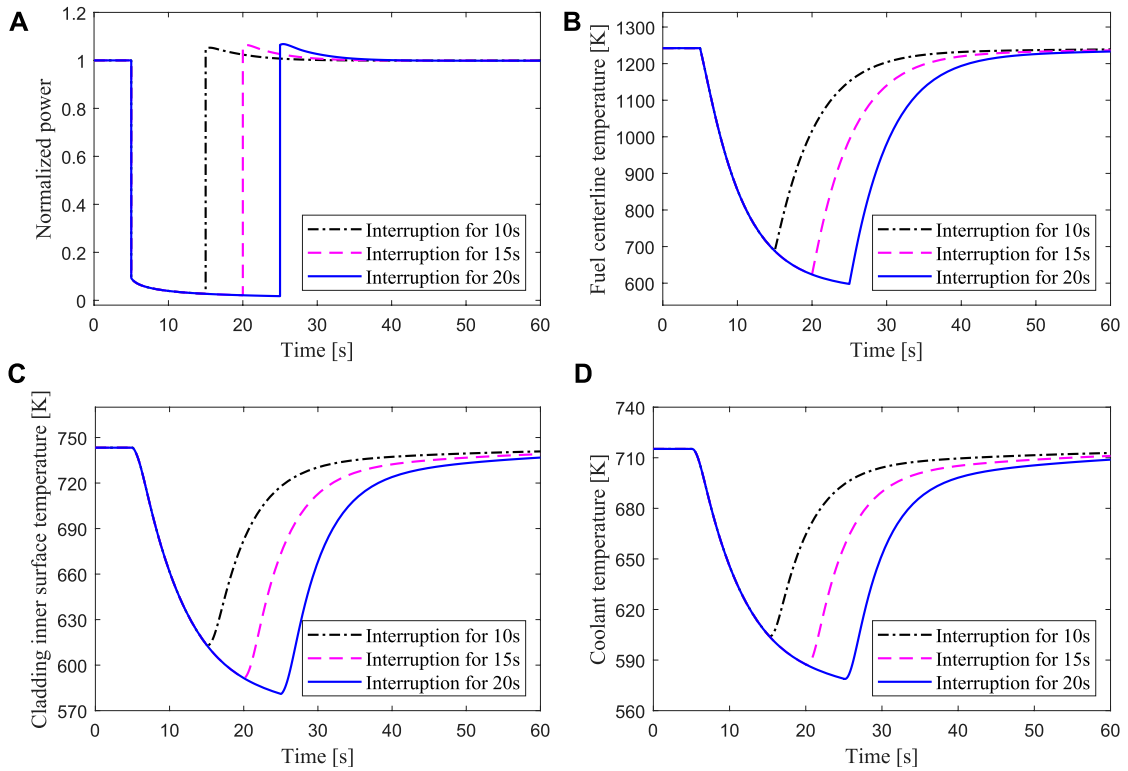

FIGURE 8 | Transient responses of the hottest channel under beam interruptions for 10 s, 15 s, 20 s respectively.

TABLE 3 | Temperature variations of the fuel center, cladding surface and outlet coolant in the hottest channel under beam interruptions for 10 s, 15 s, 20 s respectively.

Accident conditions	Maximum temperature drops (K)		
	Fuel center	Cladding surface	Outlet coolant
Interruption for 10 s	554.18	130.30	111.05
Interruption for 15 s	618.59	151.88	128.10
Interruption for 20 s	644.46	162.27	136.42

$$\left.\frac{\partial T_f^i}{\partial r}\right|_{r=0} = 0 \tag{7}$$

$$-k_f^i \left.\frac{\partial T_f^i}{\partial r}\right|_{r=r_f} = h_g^i \left(T_f^i \left|_{r=r_f} - T_{cl}^i \right|_{r=r_g}\right) \tag{8}$$

where ρ_f^i and C_f^i denote the density and specific heat of the fuel pellet in the axial node i respectively, k_f^i denote the heat conductivity of the fuel pellet, T_f^i and T_{cl}^i denote the fuel pellet and cladding temperatures respectively, q_v^i is the volumetric heat rate, $h_g^i$is the gap heat transfer coefficient, and r_f and r_g denote the fuel pellet outer radius and cladding inner radius respectively.

Ignoring the heat generated in the cladding (Schikorr, 2001), we obtain the heat conduction equation for the cladding in the axial node i as:

$$\rho_{cl}^i C_{cl}^i \frac{\partial T_{cl}^i(r,t)}{\partial t} = \frac{1}{r}\frac{\partial}{\partial r}\left(r k_{cl}^i \frac{\partial T_{cl}^i(r,t)}{\partial r}\right) \tag{9}$$

The boundary conditions of the heat conduction equation for the cladding can be described as:

$$-k_{cl}^i \left.\frac{\partial T_{cl}^i}{\partial r}\right|_{r=r_g} = h_g^i \left(T_f^i \left|_{r=r_f} - T_{cl}^i \right|_{r=r_g}\right) \tag{10}$$

$$-k_{cl}^i \left.\frac{\partial T_{cl}^i}{\partial r}\right|_{r=r_{cl}} = h_{cl,c}^i \left(T_{cl}^i \left|_{r=r_{cl}} - T_c^i\right.\right) \tag{11}$$

where ρ_{cl}^i and C_{cl}^i denote the density and specific heat of the cladding in the axial node i respectively, k_{cl}^i denotes the heat conductivity of the cladding, $h_{cl,c}^i$ denotes the heat transfer coefficient between cladding and coolant, T_c^i is the coolant temperature, r_{cl} is the cladding outer radius.

2.2.2 Heat Transfer to Coolant

The heat transfer from cladding to coolant in the ith node along the reactor axis direction can be described by the basic mass and energy conservation equations as (Schikorr, 2001):

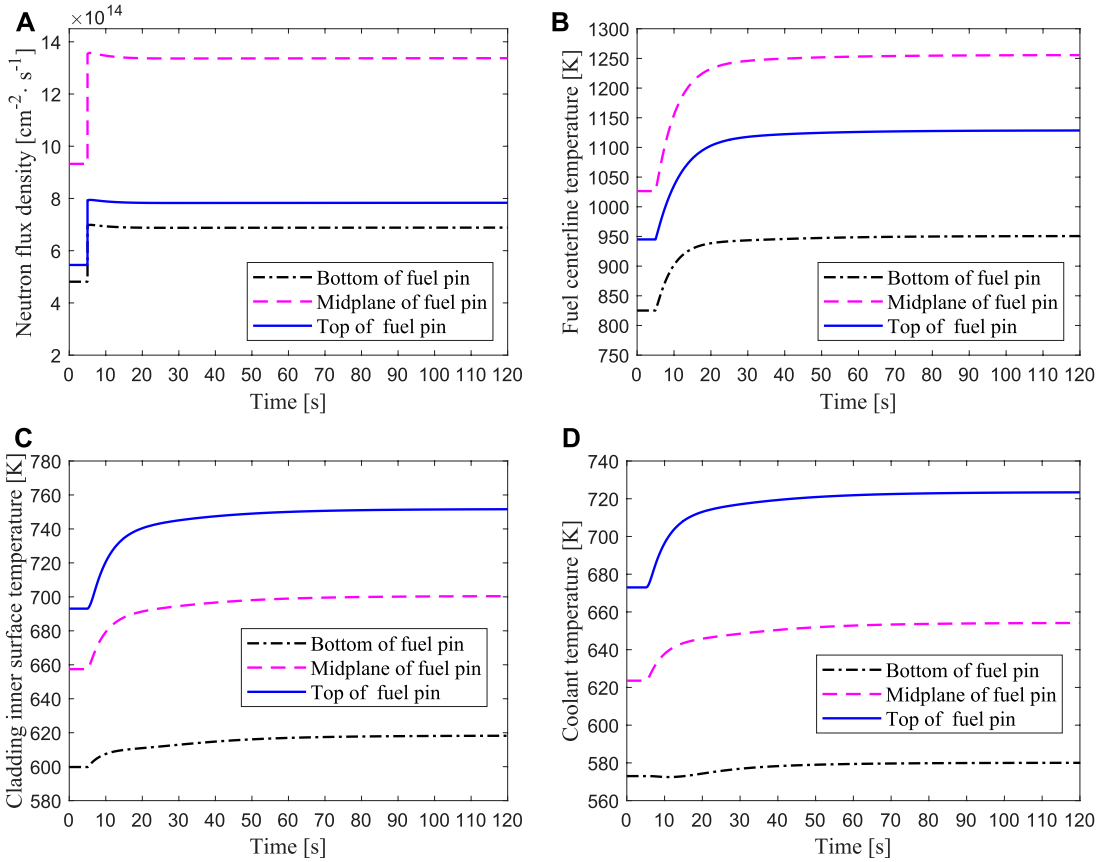

FIGURE 9 | Transient responses of the average channel when the intensity of proton beam increased by 50%.

$$\rho_c^i V_c^i C_c^i \frac{dT_c^i}{dt} = h_{cl,c}^i A_{cl,c}^i \left(T_{cl}^i \big|_{r=r_{cl}} - T_c^i\right) - G_c^i C_c^i \left(T_{c,out}^i - T_{c,in}^i\right) \quad (12)$$

where ρ_c^i, V_c^i and C_c^i denote the density, volume, and specific heat of the coolant in the axial node i respectively, $A_{cl,c}^i$ is the heat transfer area between cladding and coolant, G_c^i denote the mass flow rate of coolant, $T_{c,in}^i$ and $T_{c,out}^i$ denote coolant inlet and outlet temperatures respectively.

In fast spectrum ADS designs, heavy liquid metals such as lead (Pb) or lead bismuth eutectic (LBE) are usually adopted as the coolant materials for high heat transfer coefficient and large heat capacity. The fuel assembly of ADS is usually composed of triangular rod bundles, and thus the Ushakov correlation is used to analyze the heat transfer correlation between the heavy liquid metal coolant and the cladding (Pfrang and Struwe, 2007). The heat transfer coefficient between cladding and coolant is calculated by:

$$h_{cl,c} = \frac{k_c}{D_c} N_u \quad (13)$$

where k_c is the heat conductivity of the coolant, D_c is the hydraulic equivalent diameter, the Nusselt number N_u in the rod bundles is as follows (Pfrang and Struwe, 2007):

$$N_u = 7.55\frac{p}{d} - 20\left(\frac{p}{d}\right)^{-13} + \frac{3.67}{90\left(p/d\right)^2} Pe^{\left(0.56+0.19p/d\right)} \quad (14)$$

where p/d is the ratio of the pitch of fuel pins to its diameter, Pe is the Peclet number. It is valid for $1.2 < p/d < 2.0$, and $1 < Pe < 4{,}000$.

2.2.3 Heat Exchanger Model

The primary coolant flows out of the core and enters the heat exchanger through the ascending channel. The primary coolant then flows down to the lower plenum after its heat is transferred to the organic diathermic fluid on the secondary side. The schematic diagram of primary circuit is shown in **Figure 4**. The heat transfer models of primary coolant, tube wall, and secondary coolant are as follows (Cammi et al., 2006):

$$V_p \rho_p C_p \frac{dT_p}{dt} = G_p C_p \left(T_{p,in} - T_{p,out}\right) - h_{p,w} A_p \left(T_p - T_w\right) \quad (15)$$

$$V_w \rho_w C_w \frac{dT_w}{dt} = h_{p,w} A_p \left(T_p - T_w\right) - h_{s,w} A_s \left(T_w - T_s\right) \quad (16)$$

$$V_s \rho_s C_s \frac{dT_s}{dt} = h_{s,w} A_s \left(T_w - T_s\right) - G_s C_s \left(T_{s,out} - T_{s,in}\right) \quad (17)$$

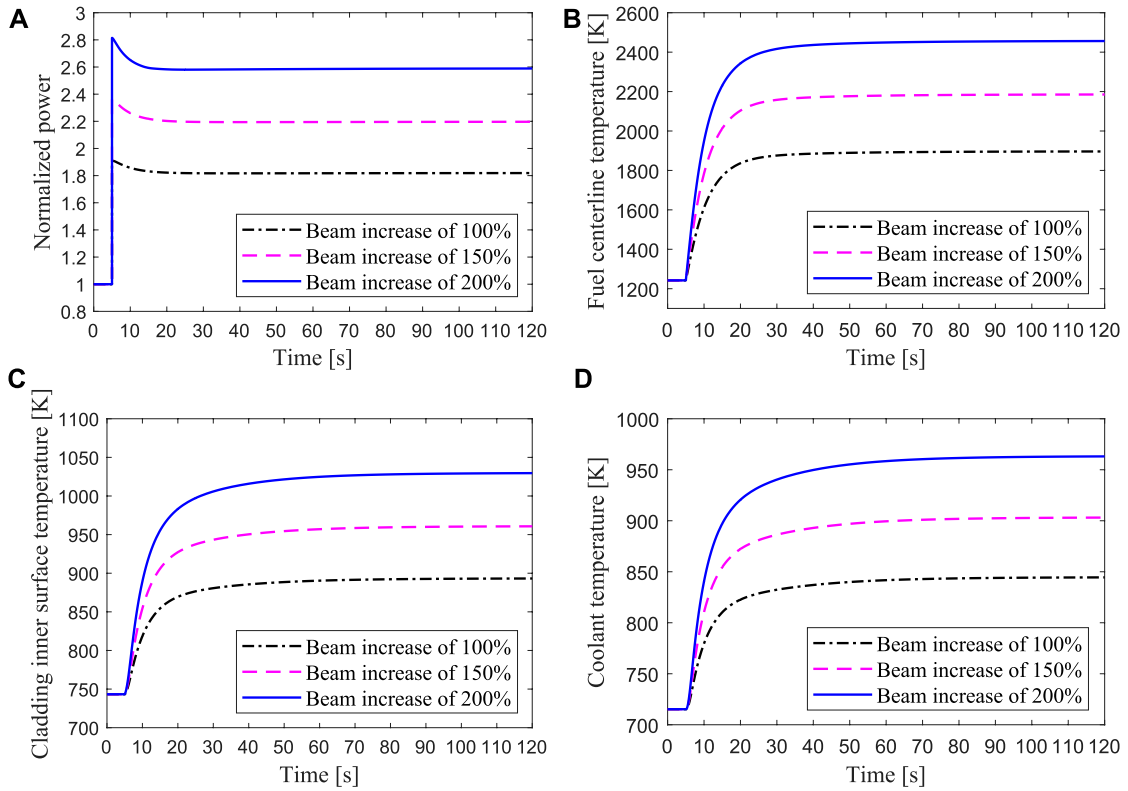

FIGURE 10 | Transient responses of the hottest channel when the intensity of proton beam increased by 100, 150, 200% respectively.

where $h_{p,w}$ is the heat transfer coefficient between the primary coolant and tube wall, $h_{s,w}$ denotes the heat transfer coefficient between the tube wall and secondary coolant.

2.2.4 Thermophysical Properties of Materials

The package of thermophysical properties of materials were developed to insert into the thermal hydraulic model based on the experimental data and empirical correlation (D'Angelo et al., 2004; Sobolev, 2011). The correlations of the thermophysical properties of coolant, cladding, and fuel are presented in **Table 1**.

2.3 Process of Coupling Calculation

The developed ARTAP code comprises of a steady-state analysis module and a transient analysis module. A flowchart of the neutronics and thermal-hydraulics coupled calculation is shown in **Figure 5**. After macroscopic cross sections and spallation neutron source are obtained, neutron diffusion equations are solved by the power iteration method. According to the power distribution by the neutronics calculation, the thermal-hydraulics analysis is performed, and the obtained distributions of fuel temperature and coolant density are selected as the feedback parameters to update the nuclear cross sections. Then the neutron diffusion calculation is carried out to update the power distribution again. This coupling iterative process continues until some criterion for convergence is met. The steady-state parameters of reactor neutronics and thermal-hydraulics are provided as initial parameters for dynamic simulation.

The ARTAP code was verified by comparing its predictions for both steady-state and transient cases of the OECD/NEA benchmark (D'Angelo et al., 2003). The benchmark summarizes a comparative analysis of ten different codes. Three cited codes for the comparison are: TRAC-MOD, SAS4ADS and EXCURS-M, as they represent the range of data scatter in the published results of benchmark report. The results indicate that ARTAP is accurate and efficient to be applied for the ADS safety analysis (Luo et al., 2018).

3 RESULTS AND DISCUSSIONS

The Italian 80 MW XADS reactor was chosen as a typical LBE-cooled ADS to investigate its inherent safety characteristics in this work. The arrangement of assemblies and R–Z view of this reactor are shown in **Figure 6** (Luo et al., 2015). The LBE-cooled core is divided into several regions. The inner region consists of 120 hexagonal MOX fuel assemblies with equal dimensions, and the top and bottom of the fuel assemblies are gas plenum, each assembly includes 90 triangle-distributed fuel rods. Dummy assemblies in the outer region mainly contain LBE which is taken as the reflector. The Central channel is designed to

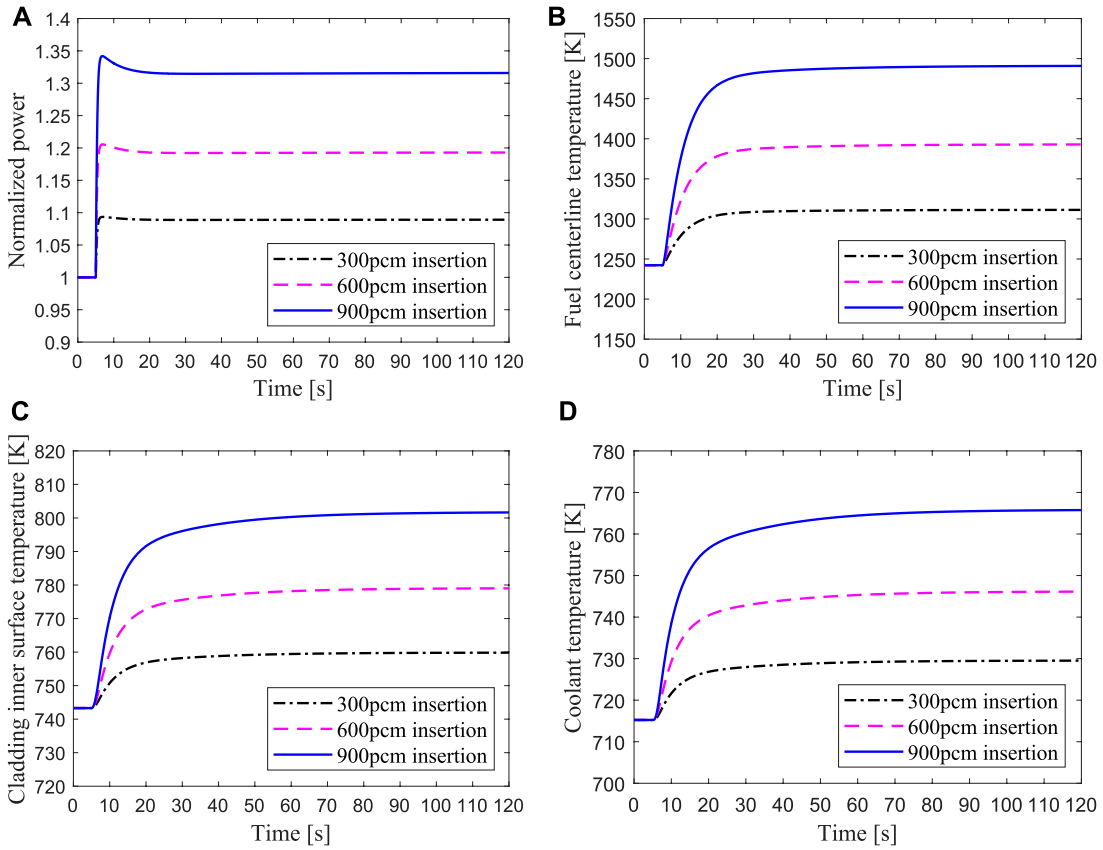

FIGURE 11 | Transient responses of the hottest channel for unprotected reactivity insertions of 300, 600, and 900 pcm respectively.

introduce proton beam into the spallation neutron target. The outside of core region is filled with LBE coolant, which serve as axial reflector and radial reflector. The main technical design parameters of the reactor are listed in **Table 2**. In order to study the transient behaviors and their uncertainties under different fuel power density conditions, the transient simulations are performed in the average fuel pin and the hottest fuel pin of the ADS assembly. The linear power density of the hottest fuel pin is 1.4375 times that of the average fuel pin (D'Angelo et al., 2004). Five typical accidents are carried out which include proton beam interruption, transient overpower, reactivity insertion, loss of flow, and loss of heat sink.

3.1 Beam Interruption Accident

The proton beam in the accelerator plays a very important role in the ADS core. On the one hand, in normal steady-state operation of the ADS system, the high-energy proton beam interacts with the spallation target to generate an external neutron source to maintain the sustainable fission reaction of the subcritical core. On the other hand, the power level could be changed by adjusting the beam intensity during the transient operating conditions, and the external neutron source in the core could be interrupted by quickly cutting off the accelerator beam so as to achieve the emergency shutdown protection under accident conditions. However, the reliability and stability of the accelerator device itself will also affect the safety operation of the ADS system, especially a sudden short-term interruption of accelerator beam would cause transient temperature changes of key materials in the fuel element, and even lead to thermal fatigue damage of the materials. Therefore, it is necessary to analyze the impact of beam trips on the temperature changes of the fuel, cladding, and coolant.

In this work, a beam interruption accident is simulated with ARTAP, in which the accelerator beam suddenly interrupted from the fifth second, and then restored to the initial value at the 15th second. The results of transient responses of the average channel are presented in **Figure 7**. It can be seen from **Figure 7A** that the neutron flux density drops sharply at the fifth second because the external neutron source generated by the proton beam and the spallation target disappears instantly, and the value of neutron flux in the middle of the core is greater than those at the top and bottom of the core. The neutron flux quickly declines to a very low value and then slowly decreases due to the production of delayed neutrons in the core and the negative feedback effect of reactivity. After the beam recovers to normal at the 15th second, the external neutron source returns to the initial value, so the neutron flux also rises rapidly and gradually restores to the steady state value. In the process of the proton beam being interrupted for a short time and then recovering, the thermal power firstly drops and then rises rapidly and gradually returns to

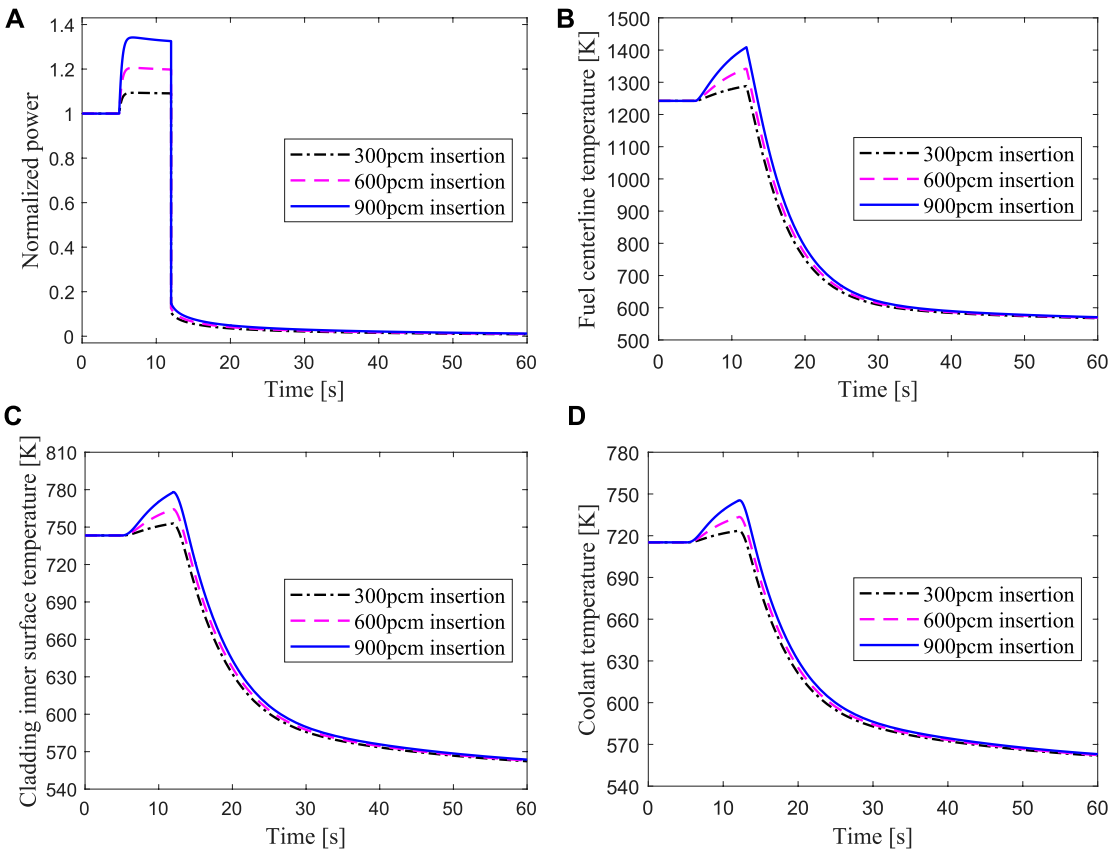

FIGURE 12 | Transient responses of the hottest channel for protected reactivity insertions of 300, 600, 900 pcm respectively.

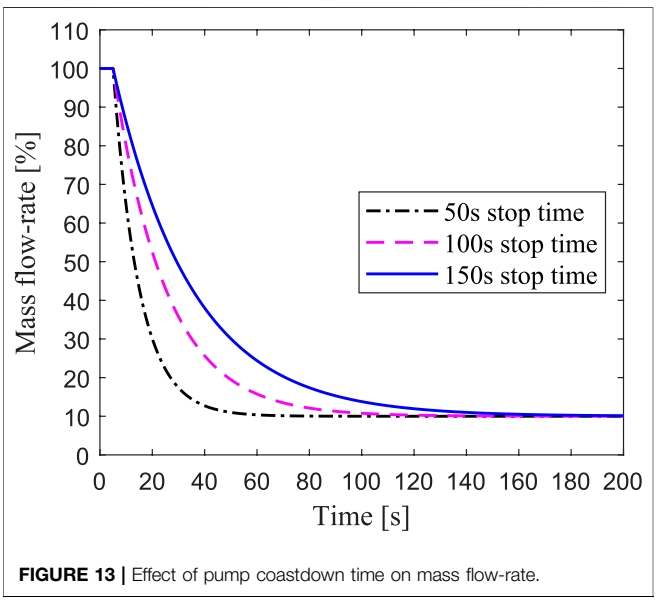

FIGURE 13 | Effect of pump coastdown time on mass flow-rate.

a steady-state level, the temperatures of the fuel, cladding and coolant also change sharply. The temperature variations at different positions of the fuel centerline is shown in **Figure 7B**, where the highest fuel temperature is in the midplane. **Figure 7C** reveals that the temperature of the cladding inner surface declines at a low value and then increases at a steady-state level, and the cladding temperature at the top of the core is the largest. The temperature variation of the coolant is shown in **Figure 7D**. The outlet coolant temperature (top of the core) changes the most, while the inlet coolant temperature (bottom of the core) changes the least, because there is a certain time lag of the coolant temperature from the heat exchanger outlet to the core inlet. Therefore, the coolant temperature change of the bottom position is slower than those of the middle and top positions.

Compared with the average fuel channel, there is also a fuel element with the highest linear power density in the core, which is usually called the hottest fuel channel. In the neutronics and thermal-hydraulics designs of the nuclear reactor, the local peak analysis of the neutron flux and material temperatures in the core should be carried out to ensure the safety operation of the reactor. From the foregoing, it can be seen that the highest fuel temperature is in the middle of the core, while the highest cladding and coolant temperature is in the top of the core. Therefore, it is very important to analyze whether these parameters of the hottest channel exceed the safety limits under accident conditions. In case of the beam interruptions for 10s, 15s, and 20s, the response results of the hottest channel

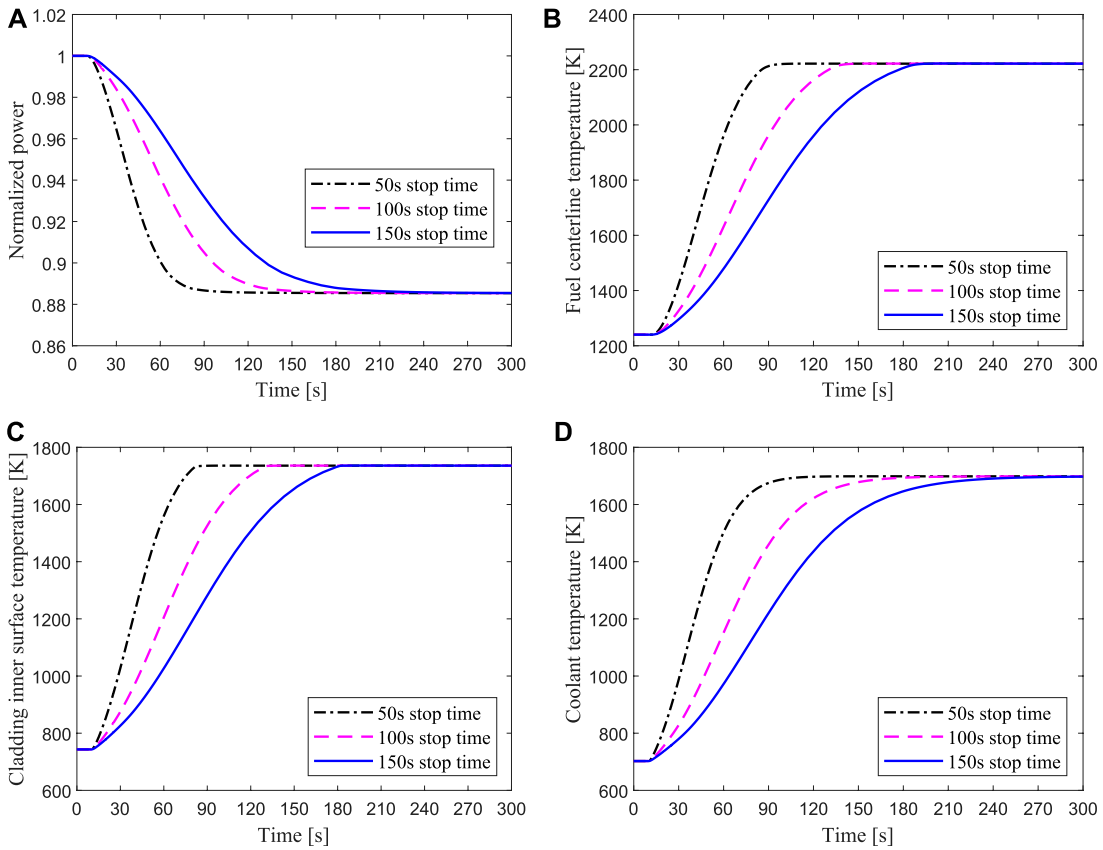

FIGURE 14 | Transient responses of the hottest channel for unprotected loss of flow due to 50, 100, 150 s pump coastdown respectively.

for the normalized thermal power, the fuel temperature in the middle of the fuel element, the cladding surface temperature and coolant temperature in the top of the fuel element are shown in **Figure 8**. It can be seen that the longer the beam interruption lasts, the lower the value that the power decreases by. Similarly, the longer the beam interruption lasts, the greater the temperatures of the fuel, cladding, and coolant change, and the variations of these parameters are shown in **Table 3**. When the beam is interrupted for 20s, the maximum temperature drops of the fuel center, the cladding inner surface and the outlet coolant are 644.46K, 162.27K, and 136.42K respectively. The fuel pellet and cladding will not be damaged for a short-term beam interruption accident, but if the proton accelerator could not maintain stable operation, the frequent interruptions may cause thermal fatigue damage of the cladding material, which will affect the life of the ADS core.

3.2 Transient Overpower Accident

With the operation of the reactor, the consumption of fission materials in the fuel element, and the accumulation of fission products, the effective multiplication factor would gradually decrease. The intensity of the proton beam would be increased by two or three times in order to compensate for the core-reactivity reduction during a refueling cycle. The reliability problem of the accelerator device and the error of the operator could cause the beam intensity to rise instantaneously and lead to overpower accidents. In the present study, transient responses of the average channel with 50% increase of beam intensity are simulated. As shown in **Figure 9**, the neutron flux density rises with the increase of the beam intensity at 5s. As a result of the increase of the neutron flux, the power and material temperatures of the core rise rapidly. Because of the negative feedback effect of the reactivity, the neutron flux gradually decreases after rising to the peak, and finally reaches a new equilibrium state. For the ADS core studied in this work, the melting point of the fuel is 3023K, the limit temperature of the cladding is 1043K, and the boiling point of the LBE coolant is 1927K (Mansani, 2002; Bobkov et al., 2008). The maximum temperature of the fuel center and the cladding surface are 1255 and 751K respectively under an overpower accident with 50% increase of beam intensity, both of which are far below the limit temperature of fuel damage.

For the hottest channel, three cases of beam step increase by 100, 150, and 200% are carried out. **Figure 10** shows that the core power rises rapidly after a sudden increase of the beam intensity, and the increase in power is almost proportional to the increase in beam current. With the rapid increase of the power, the temperatures of the fuel, cladding, and coolant also rise rapidly. Due to the negative reactivity introduced by the

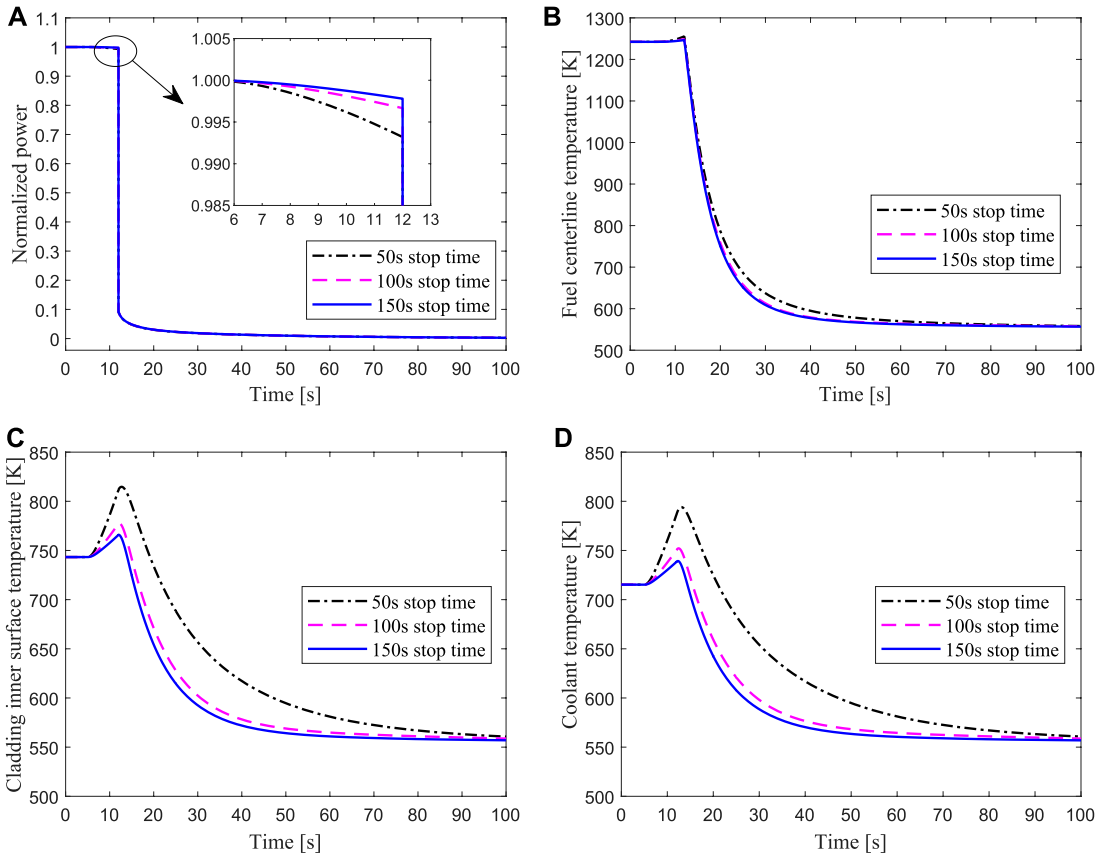

FIGURE 15 | Transient responses of the hottest channel for protected loss of flow due to 50, 100, 150 s pump coastdown respectively.

Doppler feedback effect and the coolant temperature feedback effect, the power rises to the highest value and then gradually drops to a new stable value. In these three overpower accidents, the maximum fuel temperature is 2456 K, which is lower than the melting point. However, the maximum temperature of the cladding inner surface reaches 1030K when the beam current increases by 200%, as shown in **Figure 10C**, which is close to the temperature limit of the cladding breakage. After the beam intensity suddenly increases by more than twice the steady-state value, the high temperature of the cladding may endanger the fuel elements in the core hot channel.

3.3 Reactivity Insertion Accident

The reactivity insertion accidents may be caused by the unanticipated control rod ejection. From the previous analysis results, as long as the maximum temperatures of the materials in the hot channel do not exceed the limit, it can be determined that the fuel elements in other channels of the core are also safe. Therefore, the transient process of the power and the maximum temperature of the fuel element in the hottest channel is mainly simulated and analyzed. Three positive reactivity insertions of 300, 600, and 900pcm are investigated in the present study. Two cases are taken into account, i.e., the unprotected case without beam trip and the protected case with reactor shutdown by cutting off the proton beam.

3.3.1 Unprotected Reactivity Insertion

In the case of positive reactivity insertions of 300, 600, and 900pcm in the ADS core during operation, the inherent safety characteristics of the ADS are analyzed by assuming that the emergency protection system has completely failed. The Transient responses of the hottest channel for unprotected reactivity insertions are shown in **Figure 11**. When different positive reactivity is introduced into the ADS core, the core power rises instantaneously, and then decreases slightly due to the negative feedback effect of the reactivity, and finally reaches a new equilibrium value. Meanwhile, the temperatures of the fuel center, cladding inner surface and coolant outlet also ascend sharply with the power increase and then gradually stabilize to a new equilibrium point. For the 900pcm insertion accident, the maximum temperatures of the fuel center and the cladding inner surface are far below the safety margin. This is principally because the ADS is a subcritical reactor driven by an external neutron source, in which the k_{eff} is far from the critical point and the neutron multiplication capacity is weak after the core is inserted 900pcm reactivity. Therefore, the power only rises to 1.32 times the steady-state value, and the peak temperature

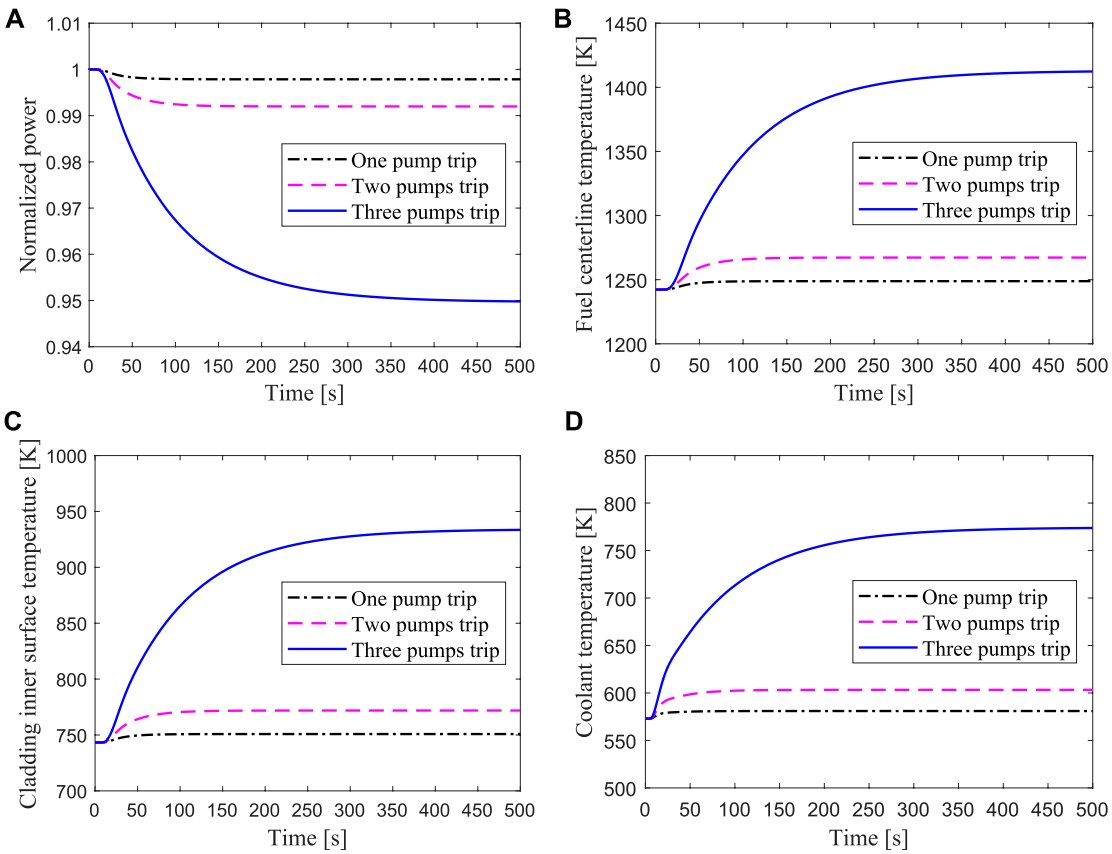

FIGURE 16 | Transient responses of the hottest channel for unprotected loss of heat sink due to one, two or three secondary pumps trip respectively.

of fuel and cladding are far below the safety limit under the unprotected reactivity insertion accident. The results show that the ADS has good inherent safety in the event of reactivity insertion accidents, and its margin of criticality safety is large.

3.3.2 Protected Reactivity Insertion

The results for the protected reactivity insertion at 5s are shown in **Figure 12**, where the beam shutdown signal occurs at 12s. It can be seen that the power and the temperatures of fuel, cladding, and coolant sharply decrease to the shutdown level after the proton accelerator is closed. It implies that ADS has the inherent safety characteristics to ensure reactor shutdown by cutting off the proton beam.

3.4 Loss of Flow Accident

The loss of flow accident is simulated with ARTAP, in which the coolant mass flow step changes from 100 to 10%. Both unprotected and protected cases are considered. The primary coolant pump of the reactor is always equipped with a flywheel with a large inertia to maintain the inertial flow rate of the core after a loss of flow accident and to reduce the consequences of the accident. The influence of the pump stop-time on the reactor flow rate was studied for loss of flow accident in the EBR-II fast reactor (Messick et al., 1987). As shown in **Figure 13**, three cases of the pump coastdown after the loss of flow accident are simulated respectively, and the flow finally dropped to 10% of the initial value.

3.4.1 Unprotected Loss of Flow

Figure 14 shows that the transient responses of the hottest channel for unprotected loss of flow due to 50, 100, and 150s pump coastdown respectively. The mass flow rate of the hottest channel dropped rapidly after the primary coolant pump stopped, which caused the heat produced by fission reaction in the fuel could not be taken out, and the cladding temperature rose rapidly. The maximum temperature of the cladding inner surface reached 1726K, which means it exceeded the damage limit. The results reveal that protective measures are not taken after the loss of flow accident, the fuel element would rupture, thereby endangering the safety of the ADS core. For one thing, the power drop is small due to the deep subcriticality of the core and low sensitivity to negative reactivity feedback, which is from 100% full power to 88% level. For another, the loss of flow rate prevents the heat transferring from the pellet to the

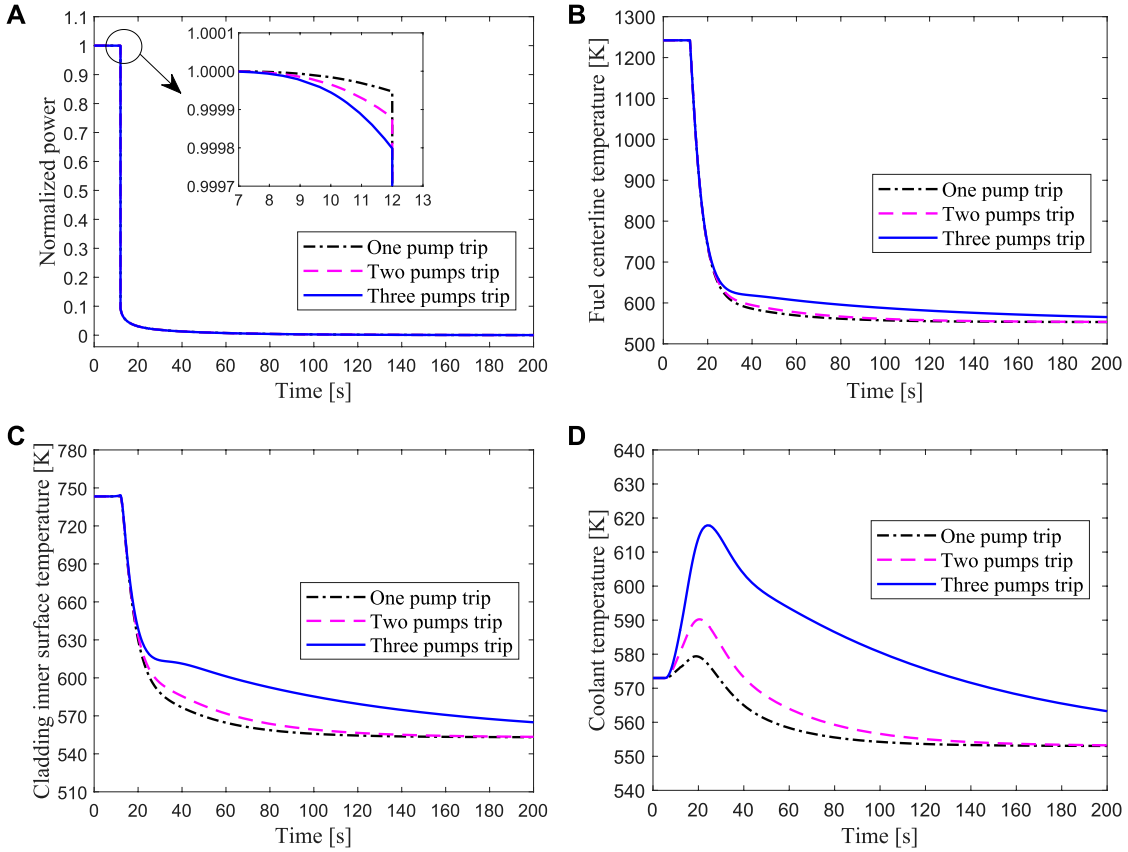

FIGURE 17 | Transient responses of the hottest channel for protected loss of heat sink due to one, two or three secondary pumps trip respectively.

coolant in time, so the temperature of the cladding rises to a very high value. As shown in **Figure 14C**, for the cases of the pump coastdown time for 50, 100, and 150s, the corresponding time for the cladding temperature reaching the maximum value are 26, 41, and 58s, respectively. Therefore, the protection system should be quickly activated to achieve an emergency shutdown after the loss of flow accident occurs, and the primary pump with a longer coastdown time should be used to ensure the safety of the ADS.

3.4.2 Protected Loss of Flow

The results of the protected loss of flow due to 50, 100, and 150s pump coastdown are presented in **Figure 15**, where the beam shutdown signal occurs at 12s. It can be seen that the power and fuel temperature dropped rapidly and then reached the shutdown level after the proton beam was quickly cut off, in which the core is subcritical without an external neutron source. During this process, the maximum temperature of the fuel center and the cladding surface is lower than the security limit. These simulation results indicate that the ADS core could quickly restore to safety by shutting off the beam under loss of flow accident, and the longer the coastdown time of the primary pump is, the lower the peak temperature of the cladding is.

3.5 Loss of Heat Sink Accident

Corresponding to the primary circuit system, the secondary circuit system is a heat sink of the core during the normal operation of ADS. When the cooling system of the secondary circuit fails, such as one or more secondary circuit pumps trip or the air cooler fan stops, insufficient cooling capacity of the core results in a heat sink accident. The ADS system studied in this paper has three secondary loops, in which each loop contains a secondary circuit pump and an air cooler. During the process of heat sink accident, a single or two or all of the circuit pumps in the secondary loop fails, which causes the mass flow of the entire secondary circuit to drop from 100 to 69, 37, and 8% within 20s, respectively.

3.5.1 Unprotected Loss of Heat Sink

Transient responses of the hottest channel for unprotected loss of heat sink due to one, two, or three secondary pump trips are shown in **Figure 16**. Because the mass flow rate of the secondary side in the heat exchanger drops rapidly after the loss of heat sink accident, the heat of the primary circuit loop could not be removed in time. It can be seen from **Figure 16** that the temperatures of the fuel center and the cladding inner surface rise rapidly, and the power drops slightly due to the negative feedback effect of reactivity. The higher the number of failed pumps in the secondary circuit is, the larger the temperature rise of fuel and cladding is. In the case of all the

secondary pumps failure, the peak temperature of the cladding surface reaches 934 K, which is lower than the safety limit.

3.5.2 Protected Loss of Heat Sink

The results of the protected loss of heat sink due to one, two, or three secondary pump trips are shown in **Figure 17**, where the beam shutdown signal occurs at 12s. The fission energy produced in the core decreases rapidly after the proton beam was quickly cut off, in which the core is subcritical without an external neutron source. Due to the rapid decrease of the power, the temperatures of the fuel center and cladding surface also drop rapidly. The outlet coolant of the core temperature drops quickly with the power decrease after the shutdown protection system is activated, hence the heat transferring from the core to the heat exchanger is correspondingly reduced. These simulation results indicate the safety potential of the LBE-cooled ADS design against loss of heat sink accident.

4 CONCLUSION

In the present study, a developed computational code named ARTAP is used to analyze the inherent safety characteristics of the ADS, which comprises of a steady-state analysis module and a transient analysis module. The steady-state analysis module couples a one-dimensional neutron diffusion equation and a thermal-hydraulics single-channel model. According to the initial power distribution obtained by the neutron diffusion calculation, temperature distributions of coolant and fuel could be calculated by the thermal-hydraulics model, which are selected as the feedback parameters to update the macroscopic cross-sections of the neutron diffusion equation, and then a new power distribution is obtained. This coupling iterative process continues until some criterion for convergence is met. The transient analysis module consists of space-time neutron kinetic equations and thermal-hydraulics dynamic equations, which was verified by comparing its results with the those of the OECD/NEA benchmark. In order to investigate the safety characteristics, five typical accidents in an 80 MW LBE-cooled ADS are carried out which include proton beam interruption, transient overpower, reactivity insertion, loss of flow, and loss of heat sink. The transient simulations are performed in the average fuel pin and the hottest fuel pin of the ADS assembly by using the ARTAP code.

The simulation for a beam interruption accident shows that the highest fuel temperature is in the middle of the average channel, while the highest cladding and coolant temperatures are in the top of the average channel. When the beam is interrupted for 20s, the maximum temperature drops of the fuel center, the cladding inner surface and the outlet coolant are 644.46K, 162.27K, and 136.42K respectively. The frequent interruptions may cause thermal fatigue damage of the cladding material in the hottest channel, which will affect the life of the ADS core. For transient overpower accident with 50% increase of beam intensity, the maximum temperature of the fuel center and the cladding surface are 1255 and 751K respectively, both of which are far below the safety limit. After the beam intensity suddenly increases by more than twice the steady-state value, the maximum temperature of the cladding inner surface reaches 1030K, which may damage the fuel element of the hot channel in the core. Concerning the reactivity insertion accident, it was found that the power only rises to 1.32 times the steady-state value, and the peak temperature of fuel and cladding are far below the safety limit after the core is inserted 900 pcm reactivity. The results show that the ADS has good inherent safety in the event of reactivity insertion accidents, and its margin of criticality safety is large. In the simulation of loss of flow accident, the power drop is small due to the deep subcriticality of the core and low sensitivity to negative reactivity feedback, which ranges from 100% full power to 88% level. The maximum temperature of the cladding inner surface reaches 1726K, that means the fuel element would rupture. After the protection system is activated, the power and the temperatures of fuel, cladding and coolant sharply decrease to the shutdown level after the proton accelerator is closed. It implies that ADS have the inherent safety characeristics to ensure reactor shutdown by cutting off the proton beam. The simulation results of Loss of heat sink accident show that the higher the number of failed pumps in the secondary circuit is, the larger the temperature rise of fuel and cladding is. In the case of all the secondary pumps failure, the peak temperature of the cladding surface reaches 934 K, which is lower than the safety limit. The present simulation results reveal that the ADS system has a remarkable advantage against severe accidents. It also implies that ADS has the inherent safety characteristics to ensure reactor shutdown by cutting off the proton beam.

DATA AVAILABILITY STATEMENT

The original contributions presented in the study are included in the article/Supplementary Material, further inquiries can be directed to the corresponding author.

AUTHOR CONTRIBUTIONS

RL: Conceptualization, Methodology, Software, Validation, Data curation, Writing - original draft. SR: Methodology, Writing - review and editing. DZ: Visualization, Data curation. FZ: Supervision, Writing - review and editing.

FUNDING

This research is supported by the Scientific Research Foundation of the Education Department of Hunan Province, China (Grant No. 18B265); High-tech Program of the Science and Technology Bureau of Hengyang City, China (Grant No. S2018G9031015321); Fundamental Research Fund for Young Teachers of the University of South China (Grant No. 190XQD064).

REFERENCES

Bobkov, V., Fokin, L., Petrov, E., Popov, V., Rumiantsev, V., and Savvatimsky, A. (2008). *Thermophysical Properties of Materials for Nuclear Engineering: A Tutorial and Collection of Data*. Vienna: IAEA.

Cammi, A., Luzzi, L., Porta, A. A., and Ricotti, M. E. (2006). Modelling and Control Strategy of the Italian Lbe-Xads. *Prog. Nucl. Energ.* 48, 578–589. doi:10.1016/j.pnucene.2006.03.006

Chen, X., Suzuki, T., Rineiski, A., Wiegner, E., Maschek, W., and Flad, M. (2003). "Unprotected Transients in a Small Scale Accelerator Driven System," in Proc. International Topical Meeting on Nuclear Applications of Accelerator Technology (AccApp'03), 1–5.

Cinotti, L., Giraud, B., and Abderrahim, H. A. (2004). The Experimental Accelerator Driven System (Xads) Designs in the Euratom 5th Framework Programme. *J. Nucl. Mater.* 335, 148–155. doi:10.1016/j.jnucmat.2004.07.006

D'Angelo, A., Arien, B., Sobolev, V., Van den Eynde, G., and Gabrielli, F. (2003). Benchmark on Beam Interruptions in an Accelerator-Driven System, Final Report on Phase I Calculations. *Nucl. Sci. NEA/NSC/DOC 17*.

D'Angelo, A., Arien, B., Sobolev, V., Van den Eynde, G., and Gabrielli, F. (2004). Benchmark on Beam Interruptions in an Accelerator-Driven System, Final Report on Phase Ii Calculations. *Nucl. Sci. NEA/NSC/DOC 79*.

Duderstadt, J. J., and Hamilton, L. J. (1976). *Nuclear Reactor Analysis*. New York: John Wiley & Sons.

Eriksson, M., Cahalan, J. E., and Yang, W. S. (2005). On the Performance of point Kinetics for the Analysis of Accelerator-Driven Systems. *Nucl. Sci. Eng.* 149, 298–311. doi:10.13182/nse03-103

Hill, R., and Khalil, H. (2001). *Physics Studies for Sodium Cooled ATW Blanket*. Lemont, IL, US: Tech. rep., Argonne National Lab.

Huang, Y.-L., Liu, L.-B., Jiang, T.-C., Wang, R.-X., Zhang, S.-X., Guo, H., et al. (2021). 650 Mhz Elliptical Superconducting Rf Cavities for Ciads Project. *Nucl. Instr. Methods Phys. Res. Section A: Acc. Spectrometers, Detectors Associated Equipment* 988, 164906. doi:10.1016/j.nima.2020.164906

Kumar, V. V., and Katovsky, K. (2020). "A Comprehensive Review of Developments of Accelerator Driven Subcritical Systems and Future Requirements," in 2020 21st International Scientific Conference on Electric Power Engineering (EPE) (Prague, Czech Republic: IEEE), 1–6. doi:10.1109/epe51172.2020.9269179

Lu, T., Shan, J., Gou, J., Zhang, B., Zhang, B., Ge, L., et al. (2016). Preliminary Safety Analysis on Loss of Flow Accidents and External Source Transients for Lbe Cooled Adsr Core. *Prog. Nucl. Energ.* 88, 134–146. doi:10.1016/j.pnucene.2016.01.001

Luo, R., Song, H., Zhang, L., and Zhao, F. (2015). Study of Minor Actinides Effect on Kinetic Parameters and Reactivity Coefficients in an Accelerator Driven System. *Prog. Nucl. Energ.* 83, 419–426. doi:10.1016/j.pnucene.2015.05.001

Luo, R., Wang, P., Wei, X., Revankar, S. T., and Zhao, F. (2018). "Development of Neutronics and thermal-hydraulics Coupled Code for Accelerator Driven Subcritical Systems," in 2018 26th International Conference on Nuclear Engineering (American Society of Mechanical Engineers Digital Collection). doi:10.1115/icone26-81276

Mansani, L. (2002). Specification for Core and Fuel Element Design for the Lbe-Cooled Xads. *PDS-XADS Deliverable D2*.

Maschek, W., Chen, X., Delage, F., Fernandez-Carretero, A., Haas, D., Matzerath Boccaccini, C., et al. (2008). Accelerator Driven Systems for Transmutation: Fuel Development, Design and Safety. *Prog. Nucl. Energ.* 50, 333–340. doi:10.1016/j.pnucene.2007.11.066

Messick, N. C., Betten, P. R., Booty, W. F., Christensen, L. J., Fryer, R. M., Mohr, D., et al. (1987). Modification of Ebr-Ii Plant to Conduct Loss-Of-Flow-Without-Scram Tests. *Nucl. Eng. Des.* 101, 13–23. doi:10.1016/0029-5493(87)90146-4

Park, W. S., Shin, U., Han, S.-J., Song, T. Y., Choi, B. H., and Park, C. K. (2000). Hyper (Hybrid Power Extraction Reactor): A System for Clean Nuclear Energy. *Nucl. Eng. Des.* 199, 155–165. doi:10.1016/s0029-5493(99)00066-7

Pelowitz, D. B., et al. (2005). *Mcnpxtm User's Manual*. Los Alamos: Los Alamos National Laboratory.

Pfrang, W., and Struwe, D. (2007). *Assessment of Correlations for Heat Transfer to the Coolant for Heavy Liquid Metal Cooled Core Designs, Vol. 7352*. Karlsruhe, BW: FZKA.

Rineiski, A., and Maschek, W. (2005). Kinetics Models for Safety Studies of Accelerator Driven Systems. *Ann. Nucl. Energ.* 32, 1348–1365. doi:10.1016/j.anucene.2005.03.007

Schikorr, W. M. (2001). Assessments of the Kinetic and Dynamic Transient Behavior of Sub-critical Systems (Ads) in Comparison to Critical Reactor Systems. *Nucl. Eng. Des.* 210, 95–123. doi:10.1016/s0029-5493(01)00431-9

Shampine, L. F., Reichelt, M. W., and Kierzenka, J. A. (1999). Solving index-1 Daes in Matlab and Simulink. *SIAM Rev.* 41, 538–552. doi:10.1137/s003614459933425x

Sobolev, V. (2011). *Database of Thermophysical Properties of Liquid Metal Coolants for Gen-Iv*. Mol, Belgium: Scientific Rep. the Belgian Nuclear Research Centre.

Song, H., Luo, R., Wan, J., Li, S., and Zhao, F. (2016). Development of a Novel 1d Coupled neutronics/thermal-hydraulics Code and its Verification on Pwr Rod Ejection Accident Benchmark. *Prog. Nucl. Energ.* 92, 197–210. doi:10.1016/j.pnucene.2016.07.008

Sugawara, T., Takei, H., Iwamoto, H., Oizumi, A., Nishihara, K., and Tsujimoto, K. (2018). Research and Development Activities for Accelerator-Driven System in Jaea. *Prog. Nucl. Energ.* 106, 27–33. doi:10.1016/j.pnucene.2018.02.007

Suzuki, T., Chen, X.-N., Rineiski, A., and Maschek, W. (2005). Transient Analyses for Accelerator Driven System Pds-Xads Using the Extended Simmer-Iii Code. *Nucl. Eng. Des.* 235, 2594–2611. doi:10.1016/j.nucengdes.2005.06.012

Van Tuyle, G., Hill, D., Beller, D., Bishop, W., Cotton, T., Finck, P., et al. (2001). A Roadmap for Developing ATW Technology: System Scenarios & Integration. *Prog. Nucl. Energ.* 38, 3–23. doi:10.1016/s0149-1970(00)00094-9

Wang, G., Gu, Z., Wang, Z., and Jin, M. (2015a). Verification of Neutronics and thermal-hydraulics Coupled Simulation Program Ntc by the Pds-Xads Transient Simulation. *Prog. Nucl. Energ.* 85, 659–667. doi:10.1016/j.pnucene.2015.08.013

Wang, Z., Wang, G., Gu, Z., Jin, M., and Wu, Y. (2015b). Benchmark of Neutronics and thermal-hydraulics Coupled Simulation Program Ntc on Beam Interruptions in Xads. *Ann. Nucl. Energ.* 77, 172–175. doi:10.1016/j.anucene.2014.11.017

Wu, Y. (2016). Design and R&D Progress of China Lead-Based Reactor for ADS Research Facility. *Engineering* 2, 124–131. doi:10.1016/j.eng.2016.01.023

Wulff, W., Cheng, H., and Mallen, A. (1985). Analytical Modeling Techniques for Efficient Heat Transfer Simulation in Nuclear Power Plant Transients. *Tech. rep., Brookhaven Natl. Lab.*

Yang, W. S., and Khalil, H. S. (2001). Blanket Design Studies of a lead bismuth Eutectic-Cooled Accelerator Transmutation of Waste System. *Nucl. Technol.* 135, 162–182. doi:10.13182/nt135-162

Zhou, S., Wu, H., Cao, L., Zheng, Y., Huang, K., He, M., et al. (2014). Lavender: a Steady-State Core Analysis Code for Design Studies of Accelerator Driven Subcritical Reactors. *Nucl. Eng. Des.* 278, 434–444. doi:10.1016/j.nucengdes.2014.07.027

Conflict of Interest: The authors declare that the research was conducted in the absence of any commercial or financial relationships that could be construed as a potential conflict of interest.

frontiers | Frontiers in Energy Research

TYPE Original Research
PUBLISHED 10 January 2023
DOI 10.3389/fenrg.2022.1075945

OPEN ACCESS

EDITED BY
Shanfang Huang,
Tsinghua University, China

REVIEWED BY
Hui He,
Shanghai Jiao Tong University, China
Jinbiao Xiong,
Shanghai Jiao Tong University, China

*CORRESPONDENCE
Zhengyu Du,
duzhy931004@163.com
Changhong Peng,
pengch@ustc.edu.cn

SPECIALTY SECTION
This article was submitted to Nuclear Energy,
a section of the journal
Frontiers in Energy Research

RECEIVED 21 October 2022
ACCEPTED 28 December 2022
PUBLISHED 10 January 2023

CITATION
Liu Y, Huang M, Du Z, Peng C and Wang Z (2023), Peak power prediction method of heat pipe cooled reactor start-up and power-up processes based on ANN. *Front. Energy Res.* 10:1075945. doi: 10.3389/fenrg.2022.1075945

Peak power prediction method of heat pipe cooled reactor start-up and power-up processes based on ANN

Yu Liu[1], Mengqi Huang[2], Zhengyu Du[1,2]*, Changhong Peng[2]* and Zhe Wang[3]

[1]Science and Technology on Reactor System Design Technology Laboratory, Nuclear Power Institute of China, Chengdu, Sichuan, China, [2]School of Nuclear Science and Technology, University of Science and Technology of China, Hefei, Anhui, China, [3]Nuclear and Radiation Safety Center of the Ministry of Ecology and Environment, Beijing, China

The start-up and power-up processes of the heat pipe cooled reactor are essential parts of the autonomous operations. The rapid power fluctuation in the processes can affect the safety of the heat pipe reactor. The fast and accurate prediction of the peak power is significant for the safe operation of the heat pipe cooled reactor. This paper generates the peak power datasets of heat pipe cooled reactor start-up and power-up processes by coupling Monte Carlo sampling, and system analysis program with heat pipe cooled reactor MegaPoweras the research object. A fast prediction model of peak power was developed based on the artificial neural network and evaluated in terms of cost, accuracy, and interpretability. The results show that the artificial neural network model has high prediction accuracy and is suitable for large datasets with complex non-linear relations. However, the training cost is high, and the interpretability is weak. The above characteristics are explained by theoretical analysis, and the ability of ensemble algorithms to improve the accuracy of the artificial neural networks is discussed.

KEYWORDS

start-up, power-up, neural network, heat pipe cooled reactor, peak power

1 Introduction

The heat pipe cooled reactor is an advanced solid-state reactor whose core consists of a hexagonal stainless-steel monolith structure containing uranium-oxide (UO_2) fuel pins and heat pipes. As the core heat transfer component, the heat pipes carry away the core heat to the second loop or the thermoelectric conversion device in a non-energetic manner, eliminating pumps, valves, and auxiliary support systems. Hence, unlike traditional light water reactors, heat pipe cooled reactors are characterized by high inherent safety, compact structure, low operation pressure, long core life, and sound economy, and can be applied to particular scenarios such as deep-sea, space, and star surface. However, due to the small delayed neutron fraction, low matrix heat capacity, weak fuel, and matrix Doppler effects in heat pipe cooled

Abbreviations: ANN, artificial neural network; BP, back propagation; CANDU, CANada Deuterium Uranium; CFX, Computational Fluid X; HPRTRAN, Heat Pipe cooled Reactor TRANsient analysis code; MCNP, Monte Carlo N Particle; M-P, McCulloch and Pitts; MSE, Mean Square Error; NBDT, Neural Backed Decision Tree; RMSE, Root Mean Square Error; SCWR FA, Super Critical Water Reactor Fuel Assembly; STD, standard deviation.

reactor, it faces rapid variation in power with reactivity perturbations and temperature fluctuations.

The peak power is an essential factor affecting reactor safety, and reactors are generally designed with over-power protection devices to protect the reactor from over-power. Once the over-power protection signal is triggered, the reactor will shut down urgently. In most application scenarios, heat pipe cooled reactors must operate unattended for an extended period. In the face of load changes, the operating system needs to startup or mediate power to match the reactor power to the load while keeping the peak power in a reasonable range. Considering the rapid power variation of heat pipe cooled reactor, the implementation of this function relies on the accurate and fast prediction of the core power.

The reactor core power is generally obtained by the physical model based on the nuclear reaction mechanism or the analytical method of the experimental model. Dias and Silva (2016) used the neutron flux density method to infer the reactor power. However, the neutron flux density is not only related to the power level but also affected by the degree of fuel consumption. Song (2002) sensors outside the core to measure the power, but it is challenging to arrange sensors in some scenarios. The sensitivities of the sensors will also affect the accuracy of power estimation. Simple mathematical or physical models cannot accurately describe or estimate the nuclear reaction process due to a large number of non-linearities and uncertainties involved.

Numerical simulation of the phenomena in the reactor by coupling the thermohydraulic and neutronics models is another means. Xi et al. (2013) analyzed the axial power distribution of the European supercritical water-cooled reactor SCWR FA by coupling the thermohydraulic code CFX and the neutronics code MCNP. Although the best estimation procedure provides accurate results, it does not meet the requirements for autonomous operation in remote due to a large amount of computation time.

With the development of machine learning techniques, the use of data-driven models to predict the trends of critical parameters in real-time based on the feature parameters plays an increasingly active role in the safe operation of nuclear power plants. Bae et al. (2021) proposed a data-driven model consisting of a multi-step prediction strategy and an artificial neural network, which can help the operators estimate the trend of parameters under emergencies to respond quickly to the current situation.

Given the data-driven model's excellent performance, this study try to apply it to the field of power prediction. This paper takes MegaPower, a heat pipe cooled reactor designed by Los Alamos National Lab for strategic power supply in remote as the subject (Sterbentz et al., 2017). Firstly, a model based on an artificial neural network to predict the peak power of heat pipe cooled reactor start-up and power-up processes is built. Then ensemble approaches are used to optimize the prediction performance further. After that, the applicability of this model is analyzed. Figure 1 shows the entire analysis flowchart of this article.

2 Problem introduction and dataset

2.1 Problem introduction

MegaPower is a heat pipe cooled reactor designed by Los Alamos National Lab for strategic power supply in remote (Mcclure et al., 2015; Sterbentz et al., 2017). Figure 2 shows some of the major reactor structures.

The core consists of a hexagonal stainless-steel monolith structure containing 5.22 Mt of uranium-oxide (UO_2) fuel pins and liquid metal potassium (K) heat pipes operating at 675°C. By vaporizing the potassium liquid in the heat pipes, the heat pipes remove heat from the monolith; no pumps or valves are needed. Heat is then

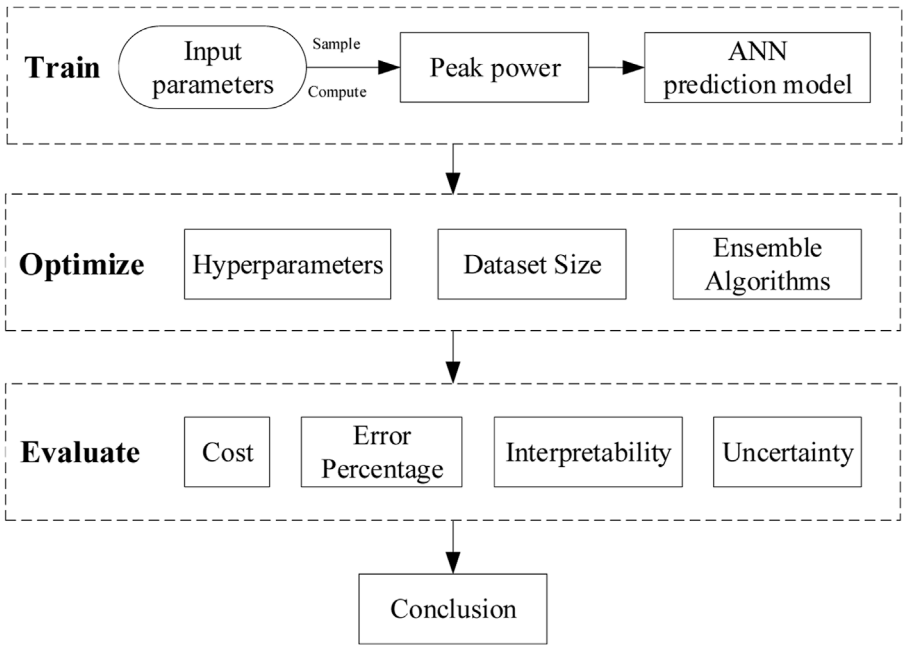

FIGURE 1
The flowchart of the whole analysis process of the neural network prediction model.

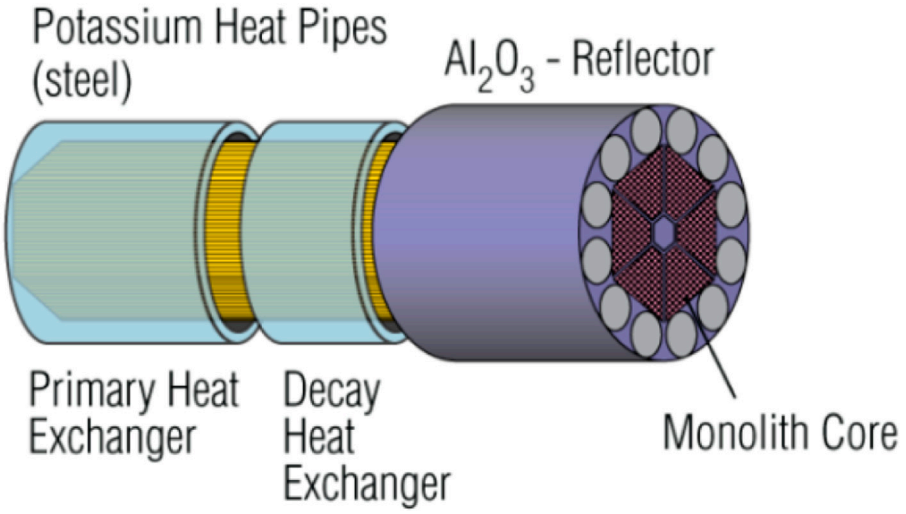

FIGURE 2
Concept schematicof heat pipe cooled reactor MegaPower (Sterbentz et al., 2017).

deposited in the condenser region of the heat pipe. Condenser regions can accommodate multiple heat exchangers. Reaction control is achieved using alumina (Al_2O_3) neutron side reflectors with 12 embedded control drums containing boron-carbide (B_4C) poison arcs.

The heat pipe cooled reactor increases reactivity by rotating the control drum. Zhong et al. (2021) have proposed a "frog-hopping" power control strategy to improve the safety of the heat pipe cooled reactor in the power mediation process. As shown in Figure 3, the system is as follows.

During the start-up process, when the reactor is critical, after each rotation of the control drum, if the change of the reactor power and the average fuel temperature is within limits during the subsequent observation time, the reactor is considered to be in a controllable state, and the control drum is continued to be rotated. Otherwise, the control drum is stopped until the conditions are satisfied again. In the power-up process, it is necessary to wait some time to perform the following operation after reaching the current power.

Therefore, the main operation parameters affecting the target parameters and their value ranges and distributions were identified, as shown in Table 1. During the process of reaching the target value of the core power, there is an urgent need to know the effect of the parameters on the power, as the different rotation patterns of the control drum may lead to a huge variation of the transient power. Model-based, knowledge-based, and data-driven methods are commonly used for prediction. However, the model-based method has a longer calculation time, the knowledge-based method has little empirical knowledge, and only the data-driven method can overcome the problems in peak power prediction.

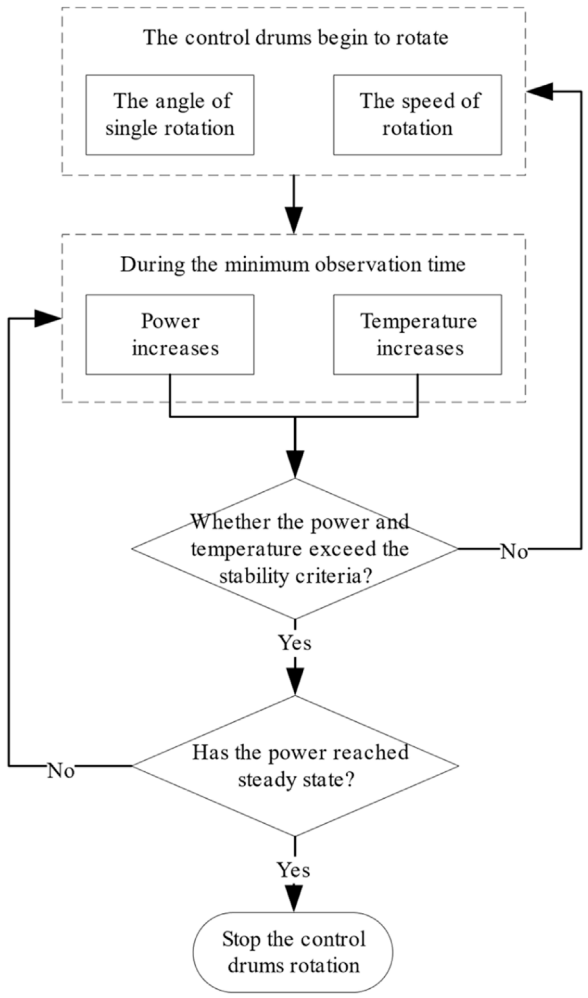

FIGURE 3
Control logic of the control drum.

2.2 Dataset

Although the data-driven method has shown promising applications, its performance is influenced by the quality of the

TABLE 1 The range and distribution of the input parameters in start-up and power-up processes.

Parameter	Acronym	Range	PDF	Process applied to
The angle of a single rotation	ASR	[0.5,5.5]°/0.5	Discrete	Start-up and power-up
The speed of rotation	SR	(10,60)°/min	Uniform	Start-up and power-up
The minimum observation time	MOT	(1,20)s	Uniform	Start-up and power-up
The power stability criteria	PSC	(1,30)K	Uniform	Start-up and power-up
The temperature stability criteria	TSC	(0.003,0.1)	Uniform	Start-up and power-up
Initial power factor	IPF	(0.0,1.0)	Uniform	Power-up
Target power factor	TPF	(0.0,1.0)	Uniform	Power-up
Delay time	DT	(11,000)s	Uniform	Power-up

Note: "Initial power factor" donates the relative power before the power-up process, "Target power factor" donates the relative power after the power-up process, "the relative power" donates the ratio of power to full power.

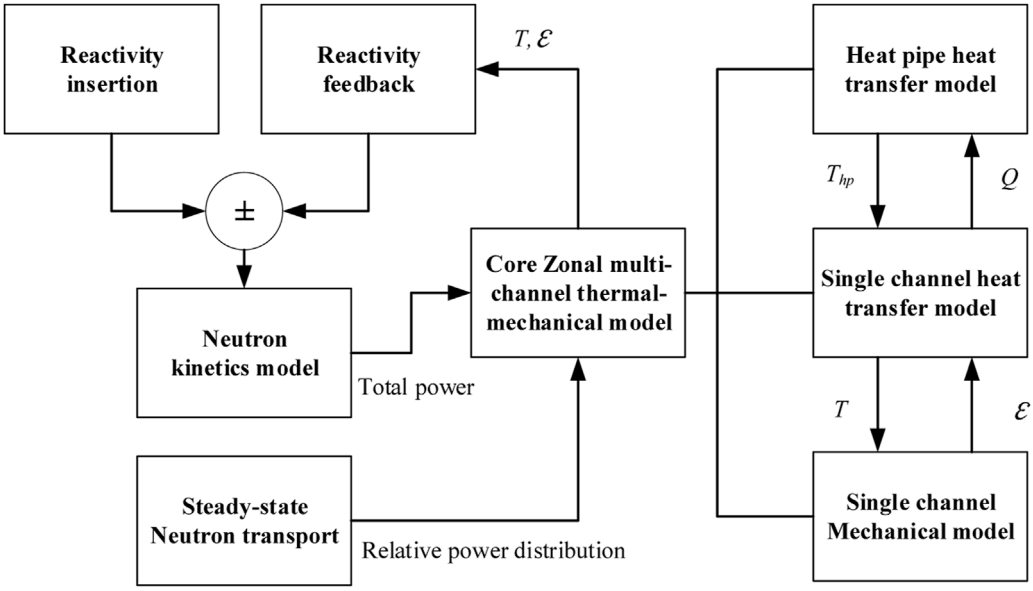

FIGURE 4
Flowchart of the models developed for the transient core analysis in the heat pipe cooled reactor (Ma et al., 2021b).

data. In practice, obtaining reliable training data is difficult, which relies on effective procedures. The HPRTRAN is a heat pipe cooled reactor system analysis code developed by the Nuclear Power Institute of China, consisting of a point reactor kinetics model, a reactivity feedback model, a core heat transfer and mechanical model, and a heat pipe model (Ma et al., 2021a).

Figure 4 shows the flowchart of the models in the HPRTRAN code. The neutronic kinetics model determines the total power with the neutron transport simulation to obtain the relative power distribution. Thermal-mechanical calculations are carried out with the transferred power. There are three components to the core multi-channel thermal-mechanical model: a heat pipe model, a single channel coupled thermal-mechanical model, and a radial heat transfer model. Using the heat pipe model, the evaporator outwall temperature and the monolith's inner wall temperature are determined. By transferring the thermal expansion and temperature distribution from the core thermal-mechanical model to the neutron kinetics model, the reactivity feedback can be considered.

The reasonability and feasibility of the models were verified by comparing the computational results of the HPRTRAN code with the ANSYS code and experimental results (Ma et al., 2021b; Ma et al., 2022).

HPRTRAN can well simulate the heat pipe reactor in the start-up and power-up processes. Taking the start-up process as an example, the system parameters, including core geometry parameters, power distribution, reactivity feedback, etc., are initialized, followed by transient calculations, where the point kinetic equations, core multi-channel heat transfer model, and heat pipe model are solved explicitly; The core internal reactivity is determined from the fuel, monolith, heat pipe, and reflector operating temperatures, and summed with the external reactivity introduced by the control drum as the total reactivity. Update the temperature field and the

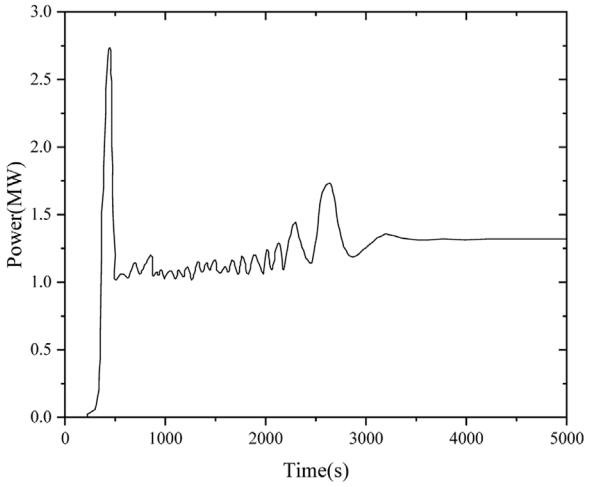

FIGURE 5
The power variation during the start-up process.

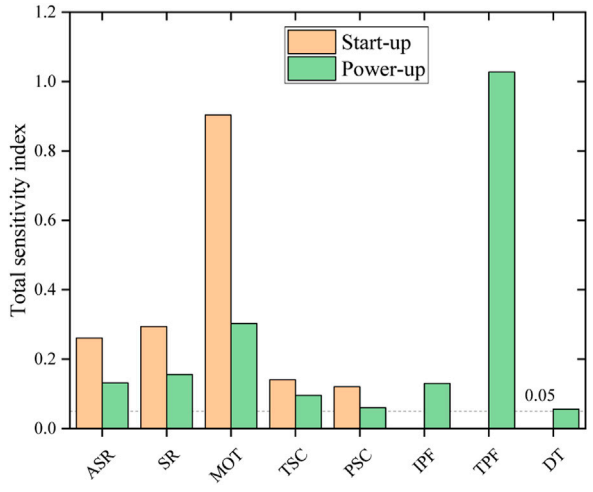

FIGURE 7
Total sensitivity indices between input features and targets of the dataset in the start-up process and power-up process.

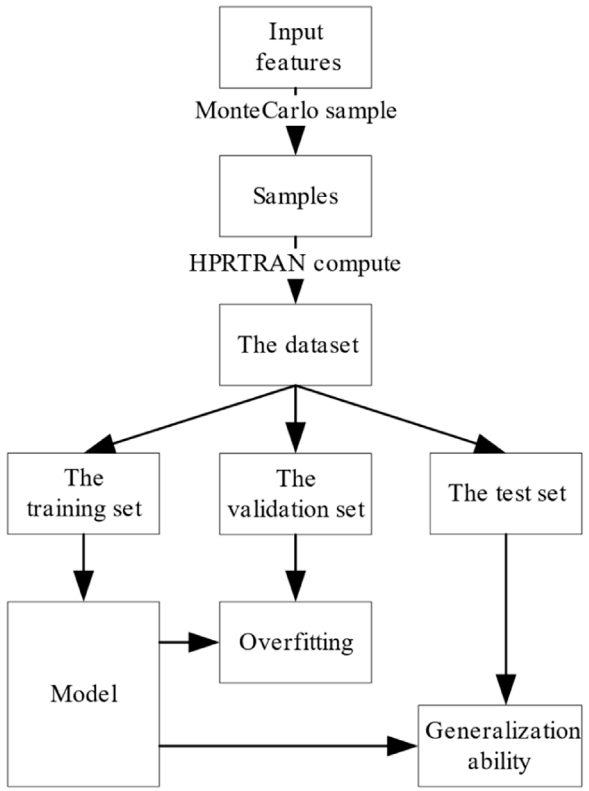

FIGURE 6
Flowchart of the data set calculation in the start-up process and power-up process.

heat transfer between channels. Multiple iterations are performed until the preset calculation time is reached. Figure 5 shows the power variation during the start-up process (Ma et al., 2021a).

As shown in Figure 6, a Monte Carlo simulation is performed for the input parameters of the process of start-up and power-up, respectively. The influence of the input parameters on the target parameters is calculated using HPRTRAN to obtain the dataset containing the input features and the target values. The dataset size for both the start-up and power-up processes is 2000.

The dataset is divided into a training set, validation set, and test set according to the ratio of 3:1:1. The training set is used to train the prediction model and calculate the model's parameters. The validation set determines whether the model is underfitting or overfitting. The test set is used to check the model generalization performance.

The model uses the root mean square error (RMSE) between the predicted and actual values of the target parameters as the evaluation metric, as shown in the following equation.

$$RMSE = \sqrt{\frac{1}{N}\sum_{i=1}^{N}\left[\left(f_i^{predict} - f_i^{true}\right)^2\right]} \quad (1)$$

Sobol sensitivity analysis is based on the variance decomposition technique. It is suitable for measuring the non-linear relationship between multiple input parameters and outputs (Ikonen, 2016), selecting a total sensitivity index value of 0.05 as a distinction between important and unimportant parameters (Zhang et al., 2015). Figure 7 shows the Sobol sensitivity index between the input parameters and the target values in the dataset. The results show that although there are differences in the sensitivity indices of each input feature, they satisfy the requirements of the critical parameters, and there are no redundant features.

3 Regression model

This section introduces the neural network algorithm and three ensemble algorithms.

3.1 Neural network

The neuronal action potential will change when a stimulus is delivered to a neuron in the human brain. If the potential exceeds a

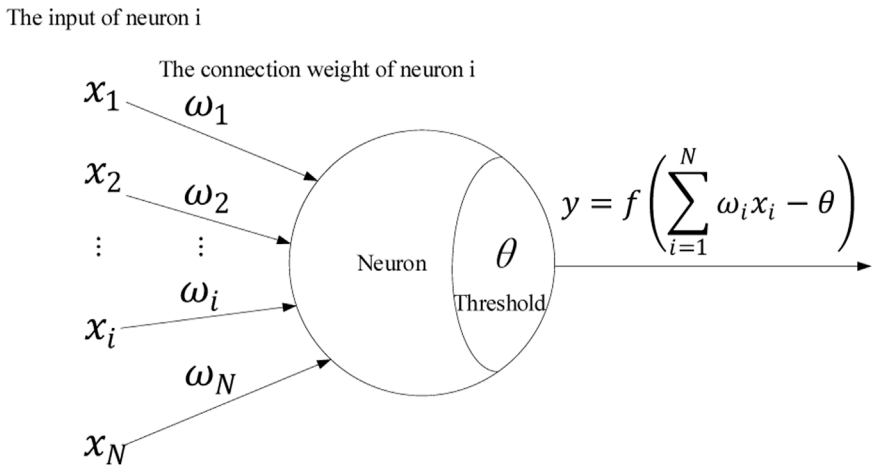

FIGURE 8
Concept schematicof the M-P neuron model.

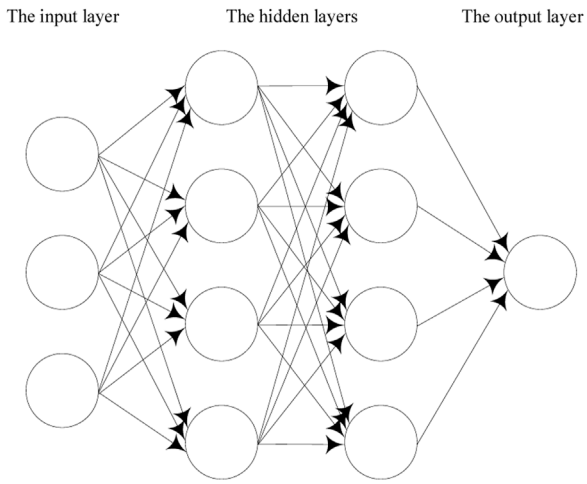

FIGURE 9
Concept schematic of the fully connected artificial neural network model.

threshold, the neuron is activated and sends neurotransmitters to other neurons. The artificial neural network (ANN) is built concerning the structure of the human brain nervous system. The M-P neuron shown in Figure 8 simulates the neuron in the human brain. The M-P neuron receives the input x_i from other neurons, multiplies it by the connection weight ω_i, and then subtracts the activation threshold θ to obtain the output value $\sum \omega_i x_i - \theta$. The non-linear activation function f transforms the original output value to consider the non-linear factor.

As shown in Figure 9, the artificial neural network consists of an input layer, several hidden layers, and an output layer. Each layer includes several M-P neurons. The data are propagated backward and forward, but no co-layer and cross-layer propagation occur.

The neural network optimizes the parameters ω and θ of the neurons using the error back propagation algorithm (BP). The BP algorithm updates the parameters through stochastic gradient descent and can step out of the local optimum values and find the optimum global value.

TABLE 2 Training and prediction time of the neural network model.

The dataset	Training time s)	Prediction time(s)
S (E)tart-up	120.1635	5.8364-3
Power-up	139.3435	6.0854-3

TABLE 3 Partial hyperparameters of the neural network.

Type of hyperparameters	Hyperparameter
Network structure	n_dense
	n_hidden
Model training	epochs
	batch_size
	earlystopping
	loss
	activation
	optimizer
	initialization
	regularization
	standardization
	learningrate

4.2 Model evaluation

This section provides a comprehensive evaluation of the neural network prediction model in terms of cost, accuracy, interpretability, and uncertainty.

4.2.1 Cost

The artificial neural network has many parameters. There are corresponding connection weights between neurons of adjacent two

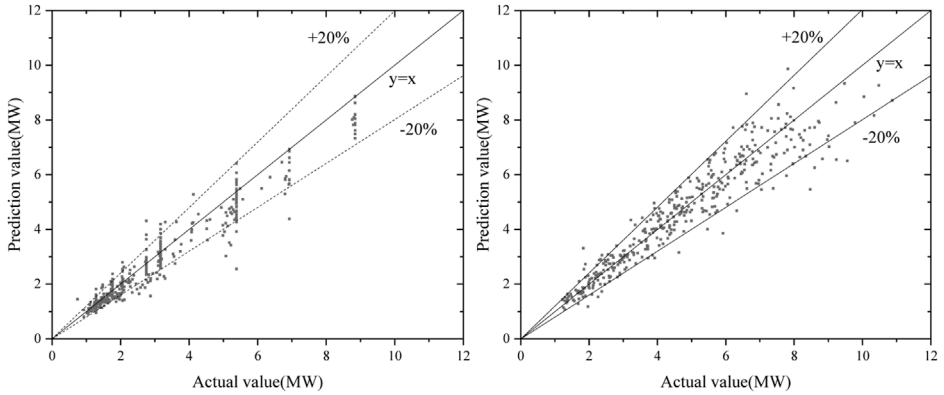

FIGURE 10
Error percentage distribution of test set prediction by the neural network during the start-up process and power-up process.

layers and thresholds on each. The artificial neural network adopts the BP algorithm to update parameters, which requires the input to be propagated layer by layer from front to back. Then the error is propagated step by step from back to front. Ittakes a long time to train the artificial neural network model. Table. 2 shows the time required to prepare and predict the neural network model on the two datasets.

The complexity of the neural network model is also reflected in the size of the model hyperparameters. Table. 3 shows part of the hyperparameters of the neural network.

The model's generalization performance can be driven to the best state by adjusting the values of hyperparameters. Due to a large number of hyperparameters, it usually takes time to adjust the parameters of the neural network. Thus, it is more sensible to select the random sampling method in tuning the neural network model.

4.2.2 Error percentage

The peak powers of the test set were predicted using the optimized neural network model, and the error percentage distributions are shown in Figure 10.

The error percentages of the neural network are within 20% in both the start-up and the power-up processes, showing the high accuracy of artificial neural networks. There are two reasons. One is that the neural network has lots of parameters that can fit complex functional relations. Hornik (1991) has proved that, under certain conditions, the artificial neural network is capable of arbitrarily accurate approximation to a function. Secondly, in updating the model parameters, the neural network uses the stochastic gradient descent algorithm; it can jump out of the local extremes and find the global minimum.

4.2.3 Interpretability

Talking about the interpretability of models, an eural network is more of a black box in that it delivers results without an explanation. It is only possible to observe what caused the neuron's activation on the first hidden layer and what the neuron's activation did on the last hidden layer. It is difficult to understand more neurons in the hidden layers in the middle. Therefore, the neural network is unsuitable for some scenarios requiring high interpretability.

The interpretability of neural networks is currently a research hotspot, which can be divided into active and passive interpretability studies according to whether interpretability interventions are made in the design and training processes of the model. Active interpretation drives neural network models in the direction of interpretability by adding physical information to the structure of the model, using physical constraints in the model's training process, or combining the neural network with other models with high interpretability. Wan et al. (2020) constructed the neural-backed decision tree NBDT by replacing each node in the decision tree with a neural network, claiming it preserves the high precision of a neural network and high-level interpretability of a decision tree and successfully applied in the field of image recognition. However, due to the specific modification of the internal structure of the neural network by active interpretation, it is less intuitive in interpretation and has a narrow scope of application. Therefore, more work is currently focused on passive interpretation.

In this section, the neural network prediction models are interpreted using the attribution interpretation and the distance interpretation, respectively, according to the decreasing interpretability completeness.

4.2.3.1 Attribution interpretation

The concept of attribution interpretation refers to the attribution of responsibility or blame based on the effects of the input features on the output. The rapid rotation of the control drum brings about a rapid rise in core temperature and the following negative temperature feedback, so the total reactivity fluctuates violently near the criticality, generating power fluctuations and the maximum peak power.

Figure 7 shows the contribution of the input features to the peak power, during the start-up process, with the minimum observation time having the most significant effect on the peak power, followed by the control drum's angle of a single rotation and speed of rotation. At the microscopic level, the single rotation angle and rotation speed of the control drum directly affect the speed of each control drum rotation. Thus, the contribution to the peak power is enormous. At the macroscopic level, the minimum observation time determines the length of the single rotation interval of the control drum during the "frog-hopping" start-up. Actually, it controls the overall speed of the control drum during the whole rotation.

TABLE 4 Attribution interpretation of the peak power prediction model in the power-up process.

Number	ASR	SR	MOT	TSC	PSC	Predict peak power
1	0.90	0.50	0.16	0.43	0.07	1,535,104
2	0.90	0.28	0.95	0.81	0.22	1,581,559
3	0.80	0.84	0.68	0.19	0.14	1,697,292
4	0.90	0.82	0.74	0.25	0.21	1,847,500
5	1.00	0.22	0.26	0.50	0.30	1,989,466
6	0.50	0.98	0.32	0.18	0.53	3,193,530
7	0.30	0.06	0.32	0.30	0.59	3,565,175
8	0.90	0.20	0.21	0.72	0.47	4,817,171
9	0.20	0.46	0.05	0.24	0.52	5,491,084
10	0.60	0.18	0.53	0.94	0.85	5,848,254

In the power-up process, the target power factor becomes the most influential factor on the peak power, which is well understood as it determines the steady-state power level and, naturally, the peak power range above the steady-state power.

The above analysis illustrates the usefulness of analyzing the effect of input features on the peak power according to Figure 7. This section takes the power-up process as an example to perform the attribution interpretation by sampling ten samples from the test set. All the samples are normalized and sorted by the output value. As shown in Table. 4, it is easy to identify the features that contribute most on the peak power when it is small or large. For instance, the small PSC value in sample No. 1 limits the speed of power increase. And the large MOT values in samples No. 2–4 extend therotation interval of control drum. All the above factors reduce the reactivity introduction speed. The large peak powers of samples No.8–10 come from the opposite reason.

The attribution interpretation explains the results from the mechanism, which can deepen the understanding of the peak power formation process, but it requires human confirmation in practice, which is inconvenient. Therefore, this section adopts the distance interpretation method based on Euclidean distance to prove the reliability of the model prediction results.

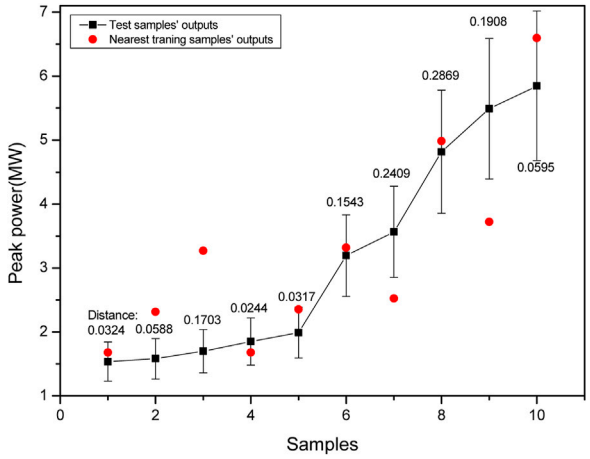

FIGURE 11
Distance interpretation of the peak power prediction model in the power-up process.

4.2.3.2 Distance interpretation

The distance interpretation finds the nearest training sample from the training set to explain the output for a particular test sample. A reasonable assumption is that the peak power is considered a function of the input features and that the "derivatives" are present and bounded over most of the domain so that the outputs of the test sample and the nearest training sample should not be too different from each other.

Therefore, this section still selects the above 10 test samples, searches for the nearest training samples and compares their outputs. The results are shown in Figure 11. It is found that the output values of five nearest training samples are within the 20% error range of test samples, indicating that the output of the neural network can be quickly verified by distance interpretation.

4.2.4 Uncertainty

The uncertainty of the model contains epistemic uncertainty and aleatory uncertainty, where the epistemic uncertainty comes from the lack of understanding of the physical system, and aleatory uncertainty comes from the uncertainty of the physical system itself, which is difficult to distinguish in practice. This section analyzes the uncertainty of neural network models by identifying the sources of uncertainty, performing uncertainty propagation, and finally analyzing the output uncertainty.

The uncertainty of neural network comes from the model hyperparameters, training data, and model parameters. The model hyperparameters and training data are controllable uncertainties and can be specified artificially before training. The model parameters are uncontrollable uncertainties, which are updated by the gradient descent method during the training process and cannot be interfered with artificially, so the uncertainty of the model parameters can be considered by adding a Dropout layer to abandon the model parameters randomly (Gurgen, 2021). The process of model uncertainty quantification is shown in the Figure 12.

The uncertainty of the model is propagated through the framework shown in Figure 12. And it is then quantified by

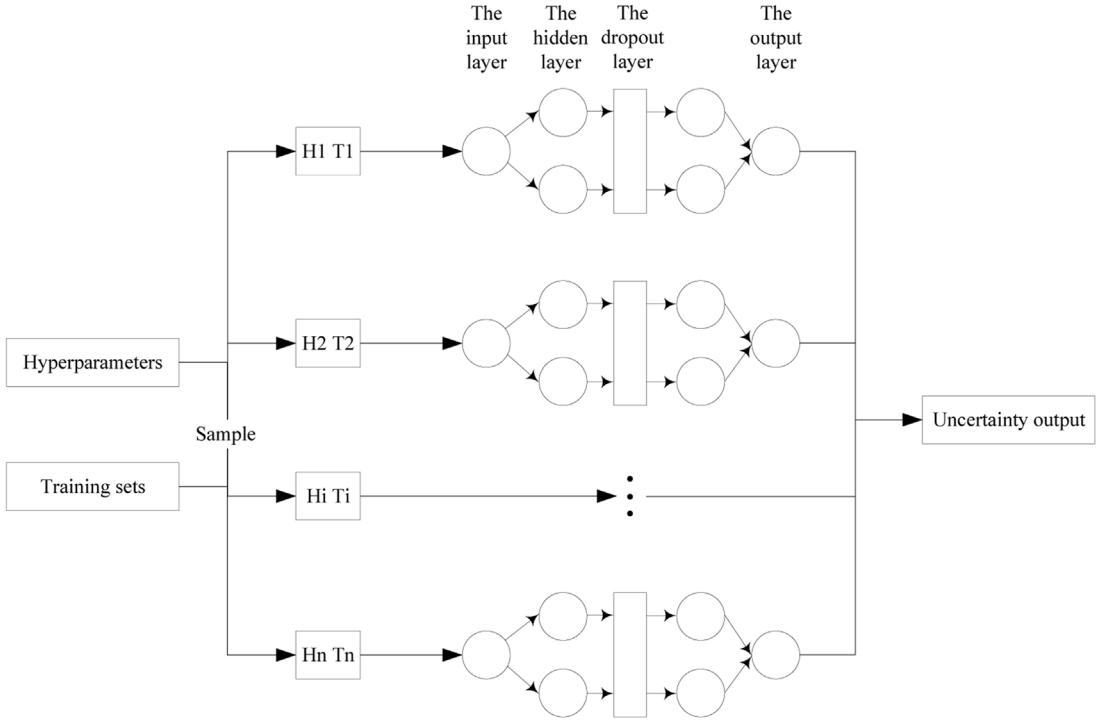

FIGURE 12
The process of uncertainty quantification.

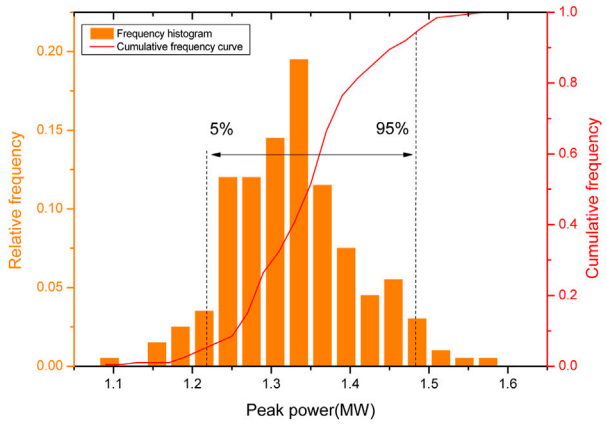

FIGURE 13
Uncertainty quantification of the peak power prediction model in the start-up process.

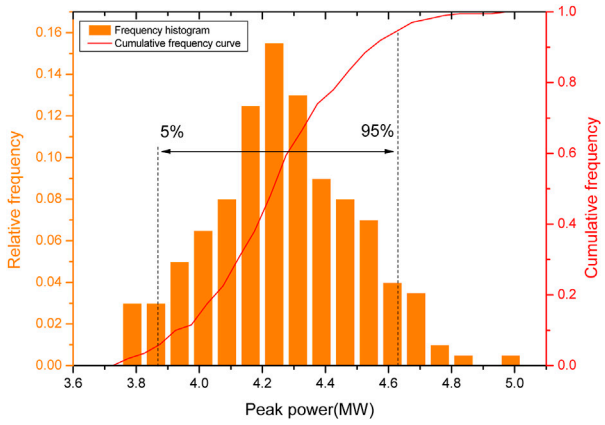

FIGURE 14
Uncertainty quantification of the peak power prediction model in the power-up process.

analyzing the uncertainty output. Taking a sample of the start-up process and the power-up process as an example respectively, the uncertainty outputs of the modelsare shown in Figures 13, 14.

3.2 Ensemble algorithms

The predictive ability of a regression model for unknown samples is defined as the generalization error, expressed as the mean square error (MSE) of the predicted and actual values of the target parameter. The mean square error (MSE) can be broken into two components: bias and variance.

$$MSE = Bias^2 + Variance \tag{2}$$

The bias indicates the accuracy of the model prediction, and the variance measures the stability of the prediction. The general relationship between bias and variance is shown in Figure 15 (Geman and Bienenstock, 1992).

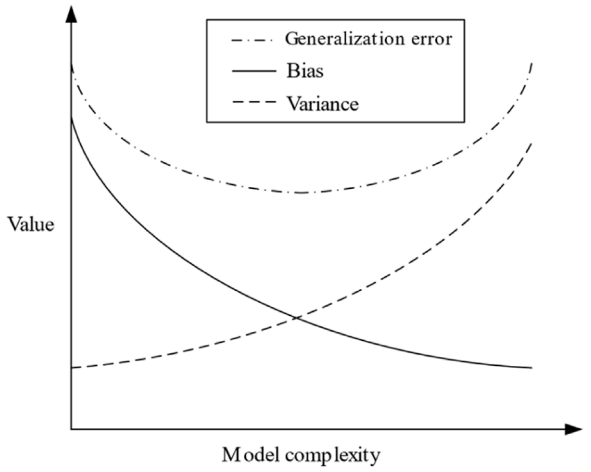

FIGURE 15
Bias and variance dilemma: the general relationship between bias and variance.

Zhou (2016) offers theoretical justification for ensemble algorithms that can improve the accuracy and stability of models and reduce generalization errors by enhancing the diversity of models. The conventional ensemble algorithms include bagging, boosting, and stacking based methods.

Bagging can reduce the variance of the ensemble model by sampling the dataset, training multiple regression models of the same type separately, and weighting the prediction results of the models to obtain the final output. Boosting uses the next model to predict the residuals of the previous model. Finally, it combines the prediction results of multiple weak regression models with an additive model, which can reduce the bias of the ensemble model.

Stacking has a two-layer structure, using different regression models to predict the dataset in the first layer and the prediction results as the dataset to train the meta-model in the second layer. Relearning the prediction results may obtain higher generalization performance.

This paper uses three ensemble algorithms to optimize the neural network, with the structure shown in Figure 16.

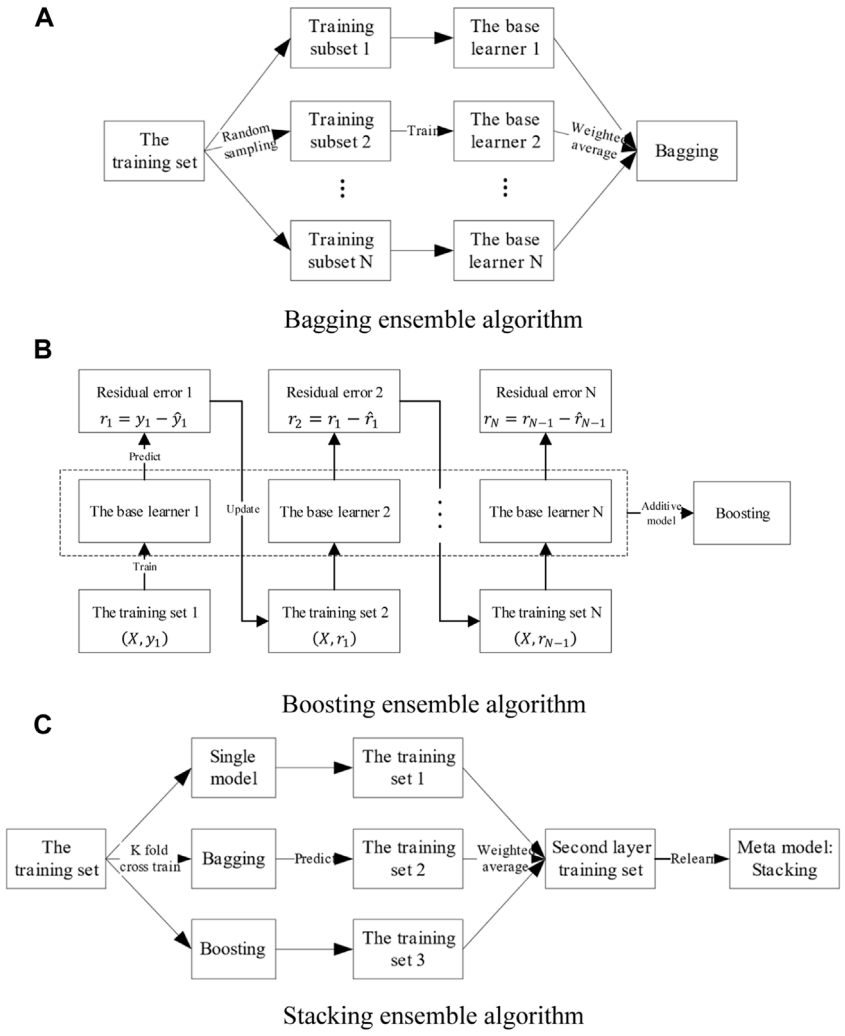

FIGURE 16
Concept schematic of three ensemble algorithm models. **(A)** Bagging ensemble algorithm, **(B)** Boosting ensemble algorithm, **(C)** Stacking ensemble algorithm.

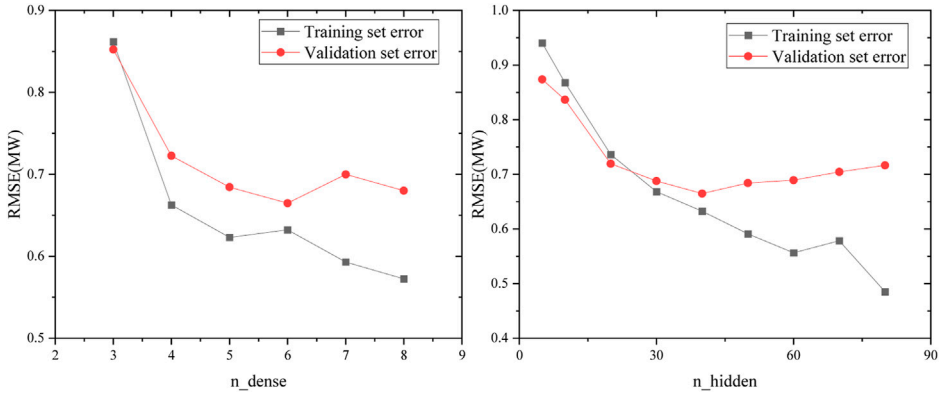

FIGURE 17
Influence of the neural network depth and width on overfitting.

4 Optimization and evaluation of artificial neural network model

The artificial neural network can model non-linear relationships between variables. Macroscopically, it partitions the data space by progressive decomposition and relies on the scale of the model to obtain better performance. The artificial neural network has a wide range of applications. However, the relationship between targets and features varies so much in datasets of different scenarios that it is difficult to use the comparative results on one dataset as a guide to another. This paper is more interested in how the ANN performs in the specific application scenario of the heat pipe cooled reactor's start-up and power-up processes and how to comprehensively evaluate the neural network's applicability.

Therefore, this section builds a peak power prediction model for the heat pipe cooled reactor's start-up and power-up processes based on an artificial neural network, optimizes the model by adjusting the model structure, and evaluates the model's performance in terms of cost, accuracy, interpretability, and uncertainty using a comprehensive framework.

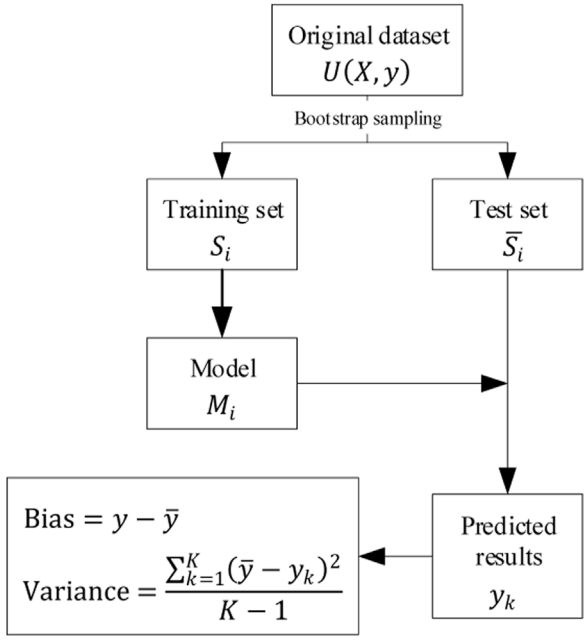

FIGURE 18
Flowchart of bias and variance calculation method.

4.1 Model optimization

The accuracy of neural network models is affected by numerous factors. The hyperparameters affect the prediction ability by determining the complexity of the model, the training data directly affect the effect of model learning, and the ensemble algorithms can achieve performance improvement through the combination of multiple models.

4.1.1 Hyperparameters optimization

The hyperparameters determine the complexity of the model. The learning ability of a simple model is limited, but as the complexity increases, the model overfits, i.e., gradually learns some properties of the training set and loses good generalization performance. Taking the power-up dataset as an example, the complexity of the model can be represented by hyperparameters that indicate the model structure size, such as the depth (n_dense) and width (n_hidden). The neural network will directly determine the size of the model. This section uses the training set to calculate the model parameters and the validation set to determine the degree of overfitting. Figure 17 shows the effect of hyperparameters on the overfitting of the neural network model.

The overfitting phenomenon can be observed in the training of the neural network. Although each neuron can use the complete samples, the increase in width due to the different weights still causes the effect of further division of the data space. The neural network that is too deep may cause parameters instability with vanishing gradient problems or exploding gradient problems due to the continued multiplication of multiple activation functions. Therefore, the hyper parameters should be tuned to alleviate the overfitting situation to get the prediction model with the best results.

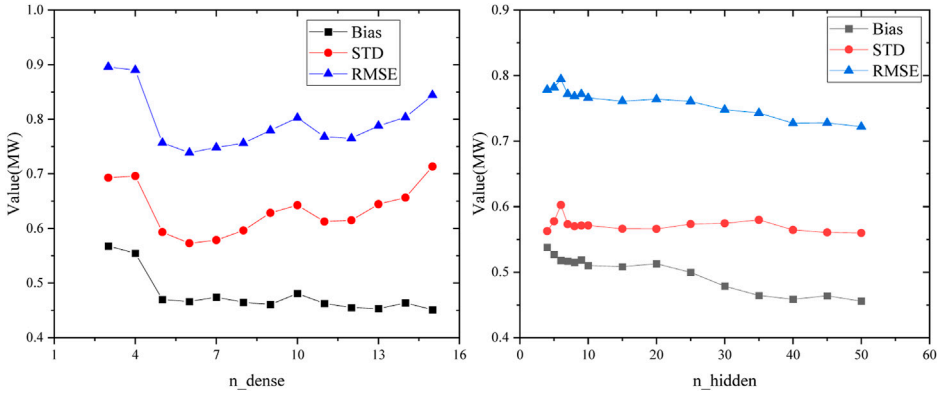

FIGURE 19
Influence of the neural network depth and width on bias and variance.

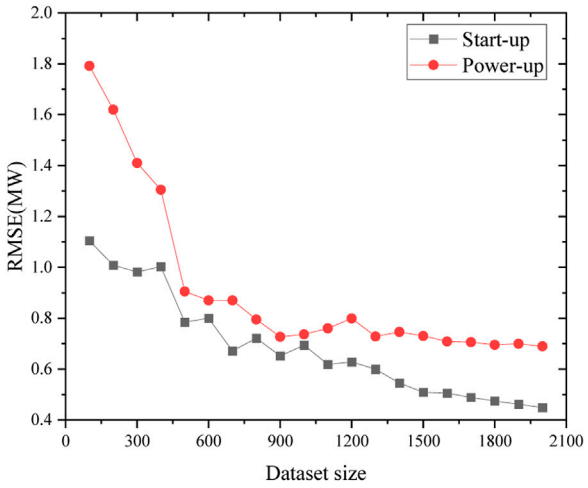

FIGURE 20
Influence of dataset capacity on RMSE in start-up and power-up processes.

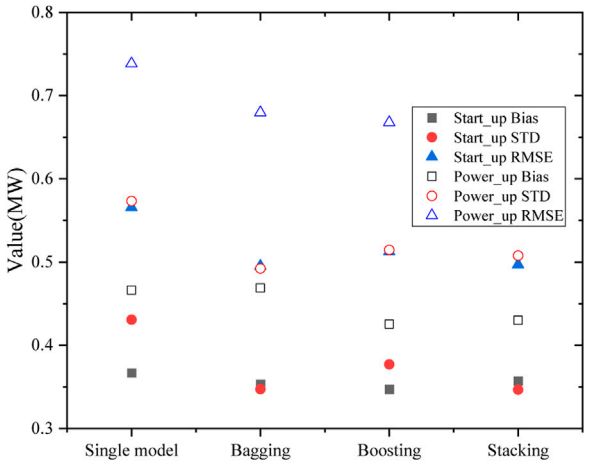

FIGURE 21
Effect of ensemble models in start-up and power-up processes.

This overfitting phenomenon of the model can be explained by the bias-variance dilemma, where the model complexity makes a difference in the effect of the bias and variance, thus leading to a change in the generalization error of the model, as shown in Figure 15. A model's generalization error can always be decomposed into bias and variance, and the effect of hyperparameters on overfitting is a combination of the effects on bias and variance, respectively. The bias and variance are averaged over all possible datasets computed by the model and are only relevant to the model and not to the specific dataset.

In cases where datasets are difficult to obtain, the bias and variance of the model can be computed on the multiple datasets obtained by bootstrap replicates from the original dataset as shown in Figure 18 (Sofus et al., 2008).

Overfitting can be alleviated by adjusting the model hyperparameters and controlling the bias and variance in a suitable position. It is found that the bias of the neural network always decreases monotonically with the increase of depth or width. However, as the width increases, the variance is unimodal, and it is found that deeper models increase variance. Thus, the trend of the generalization error of the neural network with model complexity depends on the relative magnitude of bias and variance (Yang et al., 2020).

The artificial neural network is a low bias but high variance model and the generalization error depends mainly on the control of variance. For the neural network, the variance will increase if the model is too deep. The effect of width on variance is still unimodal, as shown in Figure 19, and performance can be further improved by widening.

4.1.2 Dataset size

This section investigates the effect of dataset size on model error. Figures 20, 21 shows that the relationship between dataset size and model error has basically converged during the start-up and power-up processes, indicating that it is appropriate to use both datasets to train the neural network model. However, both datasets still have room for expansion to reduce the error. The neural network has many parameters. It is difficult for a small amount of data to learn more accurate parameters in the error back propagation process, so it is usually suitable for large datasets such as picture and text recognition.

4.1.3 Ensemble algorithms

Finally, the performance improvements of the three ensemble algorithms on the neural network model were compared. The results show that all three ensemble algorithms effectively reduce the generalization error of the models compared to single models.

The reduction effect on the variance and the bias is consistent with the theoretical analysis, with Bagging mainly reducing the variance and Boosting mainly reducing the bias. Considering that the neural network is a high variance but low bias model, the gains are more significant using Bagging than Boosting. While Stacking may obtain better results by relearning based on a simultaneous ensemble of a single model, Bagging and Boosting simultaneously.

5 Conclusion

The following research has been conducted in this paper. Firstly, the Monte Carlo sampling method and the deterministic model are combined to generate the heat pipe cooled reactor datasets in start-up and power-up processes. Then, the peak power prediction model based on the artificial neural network is established. Next, the influence of hyperparameters, dataset size, and ensemble algorithms on the model performance is studied. Finally, the following conclusions were obtained.

(1) The neural network model has a high prediction accuracy. The prediction error of the peak power in the heat pipe cooled reactor is 0.5658 MW for the start-up process and 0.7385 MW for the power-up process. It has a low uncertainty, and the predictive percentage errors of most samples are less than 20 percent.
(2) The neural network is a model with high variance and low bias. Thus, ensemble algorithms are mainly used to improve performance by reducing the variance of the model. The dataset size also impacts the model, and there is room for further expansion.
(3) The training and tuning costs of the neural network are high; the training time is 120 s on the start-up process dataset and 139 s on the power-up process dataset. But it has a relatively low prediction cost. The interpretability is weak too. It can be partially explained by passive interpretation, such as attribution interpretation and distance interpretation. It could be improved by combing neural networks and other algorithms in the future. Applying the neural network in scenarios that do not require high interpretability is more advantageous.

Data availability statement

The raw data supporting the conclusion of this article will be made available by the authors, without undue reservation.

Author contributions

YL: Methodology, software, writing—original draft. MH: Investigation, formal analysis. CP: Conceptualization, methodology, supervision. ZD: Software, Writing—original draft. ZW: Formal analysis.

Funding

The work described in this paper was supported by the Sichuan Province's Outstanding Young Scientific and Technological Talent Project (2021JDJQ0034) and Science and Technology Innovation Team Program of Key Laboratory of NPIC (ZDSY-CXTD-21-04-001).

Conflict of interest

The authors declare that the research was conducted in the absence of any commercial or financial relationships that could be construed as a potential conflict of interest.

Publisher's note

References

Bae, J., Kim, G., and Lee, S. J. (2021). Real-time prediction of nuclear power plant parameter trends following operator actions. *Expert Syst. Appl.* 186, 115848. doi:10.1016/j.eswa.2021.115848

Dias, A. M., and Silva, F. C. (2016). Determination of the power density distribution in a PWR reactor based on neutron flux measurements at fixed reactor incore detectors. *Ann. Nucl. Energy* 90, 148–156. doi:10.1016/j.anucene.2015.12.002

Geman, S., Bienenstock, E., and Doursat, R. (1992). Neural networks and the bias/variance dilemma. *Neural Comput.* 4, 1–58. doi:10.1162/neco.1992.4.1.1

Gurgen, A. (2021). *Development and assessment of physics-guided machine learning framework for prognosis system*. Ann Arbor: North Carolina State University, 181.

Hornik, K. (1991). Approximation capabilities of multilayer feedforward networks. *Neural Netw.* 4, 251–257. doi:10.1016/0893-6080(91)90009-t

Ikonen, T. (2016). Comparison of global sensitivity analysis methods -Application to fuel behavior modeling. *Nucl. Eng. Des.* 297, 72–80. doi:10.1016/j.nucengdes.2015.11.025

Ma, Y., Liu, J., Yu, H., Tian, C., Huang, S., Deng, J., et al. (2022). Coupled irradiation-thermal-mechanical analysis of the solid-state core in a heat pipe cooled reactor. *Nucl. Eng. Technol.* 54, 2094–2106. doi:10.1016/j.net.2022.01.002

Ma, Y., Tian, C., Yu, H., Zhong, R., Zhang, Z., Huang, S., et al. (2021b). Transient heat pipe failure accident analysis of a megawatt heat pipe cooled reactor. *Prog. Nucl. Energy* 140, 103904. doi:10.1016/j.pnucene.2021.103904

Ma, Y., Yang, X., and Liu, Y. (2021a). Reactivity feedback characteristic and reactor startup analysis of megawatt heat pipe cooled reactor[J]. *Atomic Energy Sci. Technol.* 50, 213–220. doi:10.7538/yzk.2021.zhuankan.0121

Mcclure, P., Poston, D., and Rao, D. (2015). *Design of megawatt power level heat pipe reactors[R]*. Los Alamos: Los Alamos National Lab.

Song, S. (2002). Heat balance test for determined reactor core power. *Nucl. Power Eng.* 23, 82–86. doi:10.3969/j.issn.0258-0926.2002.02.018

Sterbentz, J. W., Werner, J. E., and Mckellar, M. G. (2017). *Special purpose nuclear reactor (5MW) for reliable power at remote sites assessment report[R]. Idaho Falls*. United States: Idaho National Lab.

Wan, A., Dunlap, L., Ho, D., Jihan, Y., Lee, S., and Jin, H. (2020). NBDT:Neural-Based decision trees arXiv. arXiv (USA), 14.

Xi, X., Xiao, Z. J., Yan, X., Li, Y. L., and Huang, Y. P. (2013). The axial power distribution validation of the SCWR fuel assembly with coupled neutronics-thermal hydraulics method. *Nucl. Eng. Des.* 258, 157–163. doi:10.1016/j.nucengdes.2013.01.031

Zhang, X. Y., Trame, M. N., Lesko, L. J., and Schmidt, S. (2015). Sobol sensitivity analysis: A tool to guide the development and evaluation of systems pharmacology models. *CPT pharmacometrics Syst. Pharmacol.* 4, 69–79. doi:10.1002/psp4.6

Zhong, R., Ma, Y., and Deng, J. (2021). Reactor startup characteristics of heat pipe cooled reactorwith multiple FeedbackMechanism[J]. *Nucl. Power Eng.* S2, 104–108. doi:10.13832/j.jnpe.2021.S2.0104

Zhou, Z. H. (2016). *Machine learning*. Beijing: Tsinghua University Press.

frontiers | Frontiers in Energy Research

TYPE Original Research
PUBLISHED 13 January 2023
DOI 10.3389/fenrg.2022.1042391

OPEN ACCESS

EDITED BY
Mingjun Wang,
Xi'an Jiaotong University, China

REVIEWED BY
Haochun Zhang,
Harbin Institute of Technology, China
Zhuqiang Yang,
Dalian University of Technology, China

*CORRESPONDENCE
Shanfang Huang,
sfhuang@mail.tsinghua.edu.cn

SPECIALTY SECTION
This article was submitted to Nuclear Energy, a section of the journal Frontiers in Energy Research

RECEIVED 12 September 2022
ACCEPTED 14 November 2022
PUBLISHED 13 January 2023

CITATION
Liu M, Liu S, Xi D, Huang S and Huang Y (2023), Analysis of heat transfer mechanism in supercritical fluids from the aspect of pool heating.
Front. Energy Res. 10:1042391.
doi: 10.3389/fenrg.2022.1042391

Analysis of heat transfer mechanism in supercritical fluids from the aspect of pool heating

Minyun Liu[1,2], Shenghui Liu[3], Dapeng Xi[1], Shanfang Huang[2]* and Yanping Huang[1]

[1]CNNC Key Laboratory on Nuclear Reactor Thermal Hydraulics Technology, Nuclear Power Institute of China, Chengdu, China, [2]Department of Engineering Physics, Tsinghua University, Beijing, China, [3]Key Laboratory of Energy Thermal Conversion and Control of Ministry of Education, School of Energy and Environment, Southeast University, Nanjing, China

For the special phenomena of heat transfer deterioration or enhancement in supercritical fluid heat transfer, existing research still presents inconsistent opinions. In this study, we perform an analysis of the property changes, and present new understandings for pseudo-boiling theory. More importantly, essential differences between subcritical boiling and supercritical pseudo-boiling are highlighted; the critical factors being thermodynamic instability and stability. For isothermal heating cases, pseudo film boiling can be regarded as an extension of near-critical boiling. Moreover, pseudo nucleate boiling only appears in non-isothermal heating cases and is strongly dependent on the heater geometry, materials, etc. A coupled level-set and volume-of-fluid method is used to simulate the near-critical film boiling of carbon dioxide at pressures of 7.0 and 7.37 MPa. In comparison, supercritical cases at a pressure of 7.5 MPa are the natural convections of single-phase fluid with variable physical properties. The numerical results indicate the similar motions of low-density fluids in subcritical and supercritical cases. All results are consistent with prior experiments, providing a better understanding of the special features of supercritical fluid heat transfer.

KEYWORDS

supercritical fluids, pseudo-boiling, boiling, natural convection, heat transfer

1 Introduction

Fourth-generation nuclear energy systems are safer and more economical, and their use has gradually spread worldwide. Among different reactor designs, system simplification and the realization of a higher core outlet temperature is easier in gas-cooled reactors. Recently, supercritical carbon dioxide cooled reactors have aroused widespread attention because of advantages in efficiency, small size, and weight (Ahn et al., 2015). These advantages are due to the peculiar physicochemical properties of supercritical fluids (SCF), especially in the pseudo-critical region (Brun et al., 2017). However, special heat transfer mechanisms have also been found, which pose numerous risks to the system (Duffey and Pioro, 2005) and should be carefully studied. Similar problems exist in supercritical water reactors.

In the vicinity of the critical point, SCFs are very compressible and dense. For such fluids in heated enclosures, the rapid establishment of thermal equilibration, observed in microgravity experiments, cannot be explained by convection and conduction (Shen and Zhang, 2013). Onuki et al. (1990) (Boukari et al., 1990; Zappoli et al., 1990) studied dominant thermo-acoustic heating (piston effect) and successfully explained microgravity experiments through numerical models. However, for most industrial applications of SCF heat transfer, systems are maintained at a constant pressure using a pressurizer. In this condition, expansion of the thermal boundary layer cannot cause adiabatic compression of bulk materials, unlike a moving piston. Meanwhile, unlike the study of the piston effect at small temperature differences (dozens of milli Kelvins), fluid states are usually much removed from the critical point. These factors together make the piston effect negligible.

Therefore, buoyancy driven convection, including natural convection and mixed convection, is still the key driver of SCF heat transfer. Large-scale variations of SCF properties within the pseudo-critical region make the transfer mechanism complex, indicated by various experimental studies (Swenson et al., 1965; Li et al., 2010; Jiang et al., 2013). For heat transfer of SCFs flowing inside channels, Pioro and Duffey (2005) (Duffey and Pioro, 2005) reviewed more than 450 experimental papers on supercritical water and supercritical carbon dioxide spanning from the 1950s to the 2000s. The results verify that three different heat transfer modes dominate (Mokry et al., 2010): normal heat transfer, improved heat transfer, and deteriorated heat transfer. These modes are mainly influenced by the pressure, pipe diameter, mass flow rate, heat flux, bulk temperature, and flow direction. Similar phenomena are also observed in other SCFs, for example, methane (Gu et al., 2013) and kerosene (Fu et al., 2017). For natural convection of SCFs, Knapp and Sabersky (Knapp and Sabersky, 1966) designed an experiment employing horizontal wires heated in supercritical carbon dioxide. In the experiment, three general types of flow modes were observed: laminar flow, oscillation flow, and bubble-like flow, which are similar to subcritical pool boiling. Since then, many studies (Goldstein and Aung, 1968; Nishkawa and Ito, 1969; Abadzic and Goldstein, 1970; Neumann and Hahne, 1980) have attempted to repeat Knapp's work, and it was finally determined that the last two modes only appear in experiments that heat thin, low thermal diffusivity wires (Hahne and Neumann, 1981).

From a theoretical perspective, the mechanisms for improved heat transfer and deteriorated heat transfer are still controversial. According to observations of bubble-like structures and flow noise such as subcritical boiling, some studies (Ackerman, 1970; Banuti and Hannemann, 2014; Nasuti and Pizzarelli, 2020; Xu et al., 2020) proposed a pseudo-boiling theory and likened the improved heat transfer to nuclear boiling, and the deteriorated heat transfer to film boiling. Another theory focused on the buoyancy and flow acceleration effects caused by changes in the properties (McEligot et al., 1970; Petukhov et al., 1972; Hiroaki et al., 1973; Liu et al., 2017; Xu et al., 2017). This theory considers the force on near-wall fluids and explains experiment results very well. Nevertheless, the two theories have limitations. Existing research still presents inconsistent results, especially regarding the onset of heat transfer deterioration. For the pseudo-boiling theory, differences between the subcritical gas-liquid transition and pseudo-critical phenomena should be carefully considered. For the buoyancy and flow acceleration theory, effects of peculiar properties on the boundary layer are important and difficult to elucidate, requiring further studies.

Many researchers have carried out both experimental and theoretical studies on SCF heat transfer, particularly on flow and heat transfer in tubes. However, the existing research still yields inconsistent results due to complex turbulence flows. In contrast, it is much simpler to conduct visual experiments on, and to analyze the mechanism in pool heating cases; rarely reported in existing SCF studies. Moreover, basic analyses of the property distortions, especially comparisons of the subcritical gas-liquid transition, can also provide important information. Therefore, in the present study, the similarities of, and differences between the subcritical gas-liquid transition and pseudo-critical phenomena are studied using theoretical analyses and numerical simulations. A coupled level-set and volume-of-fluid method is used to analyze bubble growth in the film boiling of carbon dioxide near its critical point. For cases above the critical point, the natural convection of single-phase fluid with variable properties is considered. Through comparisons of these cases, the pseudo-boiling heat transfer mechanism in supercritical fluids has been improved.

2 Analysis of heat transfer characteristics of supercritical fluid in pool heating cases

The original pseudo-boiling theory was advanced by experimental observations, and can partly be proved by comparing gas-liquid transitions and pseudo-critical transitions, especially similarities in property changes. However, more importantly, the discrepancies in thermodynamic stabilities between these transitions lead to essential differences; thus, the original pseudo-boiling theory must be modified.

2.1 Similarities between the subcritical gas-liquid transition and the pseudo-critical transition

Taking water as an example, Figure 1 displays several properties at different pressures, including the density ρ, isobaric heat capacity c_P, thermal conductivity λ, viscosity μ, isothermal compressibility κ_T and thermal expansion rate α_P.

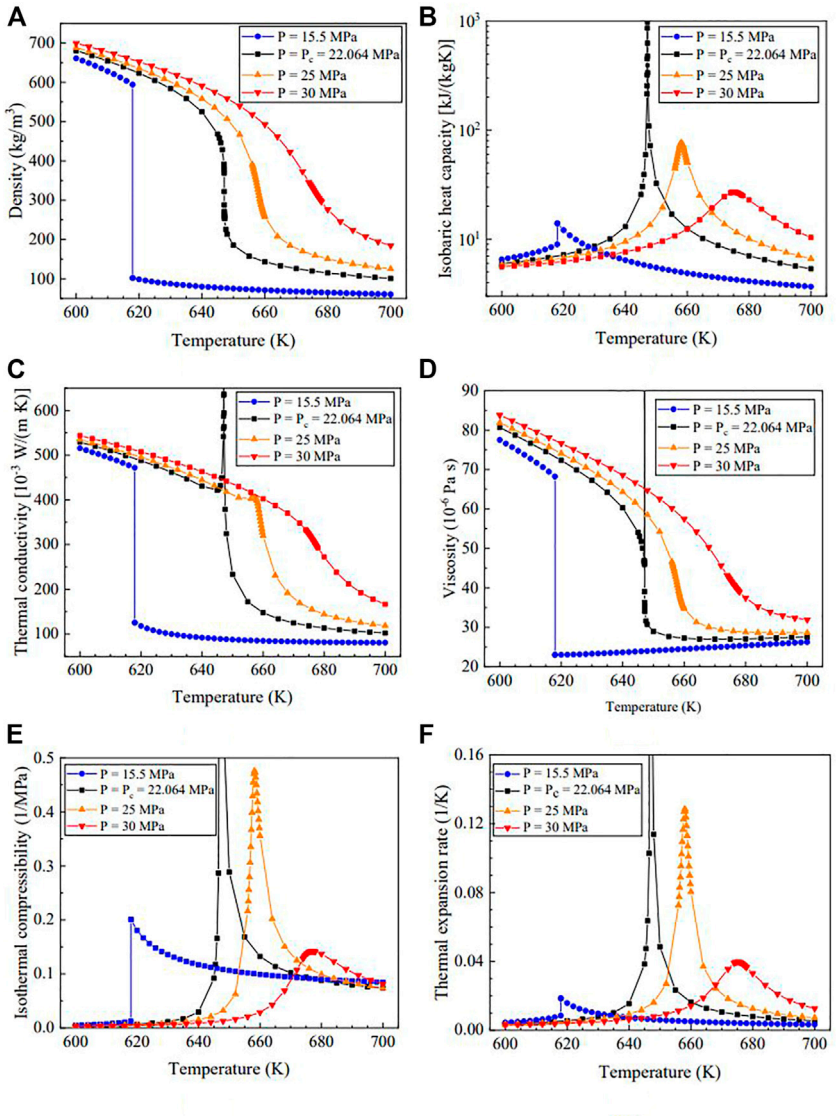

FIGURE 1
Different properties of water at different pressures.

The dotted line corresponds to the subcritical condition and the other three correspond to supercritical conditions. Many similarities between the subcritical gas-liquid transition and the pseudo-critical transition can be found from comparisons of the property changes.

Similar to the stepwise change during the subcritical gas-liquid transition, the fluid density changes dramatically in the pseudo-critical region. At a constant pressure of $P = 25$ MPa, the density of supercritical water changes from 400 kg/m^3 to 200 kg/m^3 over a 10 K temperature range. Meanwhile, the critical point is special where the first derivative $(\partial\rho/\partial T)_P$, and second derivative $(\partial^2\rho/\partial T^2)_P$, of the fluid density with respect to temperature are infinite.

For the isobaric heat capacity c_P, similarities also exist, but are more complex. The subcritical transition from the gas phase to liquid phase is accompanied by a jump in c_P. In the pseudo-critical transition, this phenomenon can also be observed, but is accompanied by a peak in c_P. Within the pseudo-critical region, c_P increases rapidly and then decreases as the temperature increases at a constant pressure. Specially, the unusual change of c_P at the critical pressure follows the power law $\Delta c_P \propto (T - T_C)^{-1.24}$, which is well explained by the scaling law (Kadanoff et al., 1967) and renormalization group (RG) theory (Wilson, 1971; Cardy, 1996). At the critical point, c_P is infinite. Away from the critical point, the c_P peak still exists, which corresponds to an additional energy demand for the

transition from high-density fluid to low-density fluid. The additional energy demand is quite similar to the latent heat of vaporization h_{lg}, in the subcritical gas-liquid transition, and can be quantitatively described by an integral of c_P with respect to T.

The isothermal compressibility, κ_T, and thermal expansion rate, α_P, are measures of the fluid density change as a response to a pressure or temperature change. The values of κ_T and α_P for a low-density fluid including the gas phase in subcritical states and gas-like fluid in supercritical states, are always higher than those for high-density fluids. Meanwhile, the peaks in κ_T and α_P in the pseudo-critical region refer to the peculiar change in fluid density.

The changes in the thermal conductivity, λ, and viscosity, μ, in supercritical states are similar to those in subcritical states. Compared with low-density fluids, a high-density fluid presents higher values of λ and μ. However, critical enhancement areas exist in the pseudo-critical region, corresponding to the peaks in Figures 1C,D. As the pressure increases away from the critical point, the dramatic changes in these properties are mild. Compared with those of c_P, the effects of the critical enhancement areas on λ and μ are much weaker and diminish quicker, and are usually negligible.

In the supercritical region, the maximum of the isobaric specific heat, c_p, at a constant pressure is called the pseudo-critical point, and is determined by the pseudo-critical pressure, P_{pc}, and the pseudo-critical temperature, T_{pc}. The pseudo-critical line connects these points and is also called the Widom line. In this context, the pseudo-critical line seems to be an extension of the gas-liquid coexistence line.

These phenomena are also present in other fluids, indicating the correlation between the subcritical gas-liquid transition and the pseudo-critical transition. Meanwhile, inelastic X-ray scattering experiments (Gorelli et al., 2006; Simeoni et al., 2010; Fomin et al., 2015) confirm the transitions between liquid-like and gas-like structures in SCFs, which are well reproduced by molecular dynamics simulations. Many studies (Ha et al., 2018; Yoon et al., 2019; Maxim et al., 2020) have examined structure-property correlations and have proposed the theory "supercritical gas-liquid coexistence" on a micro level. For different fluids in different states, intermolecular attraction and repulsion leads to different macro behaviors.

2.2 Differences between the subcritical gas-liquid transition and the pseudo-critical transition

Although many similarities between the two phenomena are presented above, the subcritical gas-liquid transition is still fundamentally different from the pseudo-critical transition (Liu et al., 2022). In the subcritical gas-liquid transition, phase separation occurs between gas and liquid phases and surface tension plays an important role in boiling. However, in the whole

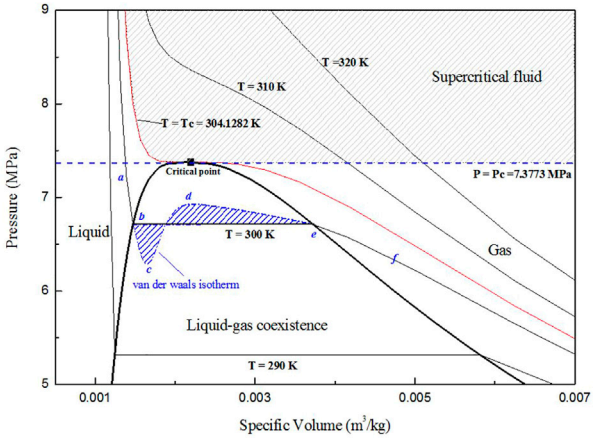

FIGURE 2
P-V diagram for carbon dioxide.

supercritical region, the two phases are indistinguishable, and phase separation does not occur. These differences can be explained by the thermodynamic stability theory and different heat transfer mechanisms.

According to the well-known van der Waals model, the isotherm is represented by "*abcdef*" in Figure 2. For *cd*, $(\partial P/\partial V)_T > 0$, which means that the pressure increases when the fluid volume increases. The states are unstable, leading to the separation and coexistence of gas and liquid phases. *bc* and *de* correspond to superheated liquid and subcooled gas, respectively, which are semi-stable and easily transition to the gas-liquid coexistence state. Therefore, for $T - T_C < 0$, the middle of the isotherm is a straight line, *be*. For $T - T_C > 0$, the isotherm is a monotonically decreasing function and $(\partial P/\partial V)_T < 0$. The states are always stable and the predictions of the van der Waals model are consistent with the experimental data.

In the subcritical pool boiling case, with heating from the bottom, the temperature of the heated wall is higher than the saturated temperature. At this condition, fluid near the wall is superheated. However, most of the superheated liquid cannot transform into gas as the formation of bubbles is conditional and random. The appearance of the gas phase in superheated liquid originates from density fluctuations caused by random movement of molecules. As illustrated in Figure 3A, density fluctuations cause a pressure increase, ΔP, in a region. If ΔP is large enough to overcome the surface tension, this region expands. As $(\partial P/\partial V)_T > 0$, expansion leads to a further increased pressure and the expansion continues until a stable, low-density state (a bubble) is formed. Generally, the initial unstable region (called a nucleation site) appears on the surface of the heated wall, where the effect of surface tension is relatively small.

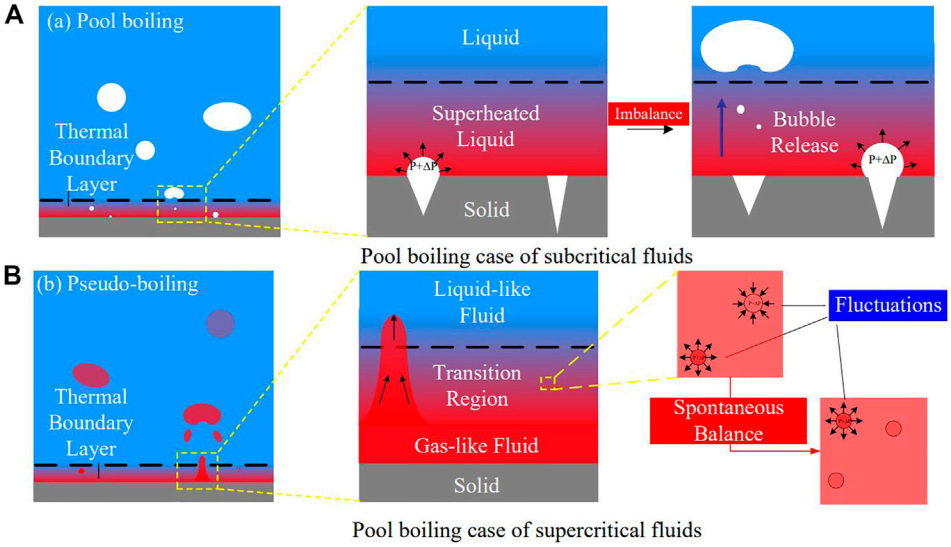

FIGURE 3
Different heat transfer mechanisms of the **(A)** subcritical gas-liquid transition and **(B)** pseudo-critical transition.

The pseudo-boiling case is referred to as the subcritical boiling case, where the bulk temperature is less than the pseudo-critical temperature, T_{pc}, and the wall temperature is higher. As illustrated in Figure 3B, fluid near the wall is low-density and the bulk is high-density. In the transition region between gas-like fluid and liquid-like fluid, the fluid density rapidly changes, corresponding to the pseudo-critical transition. Under the effect of buoyancy, the low-density fluid flows upward. The flow mode is similar to those of bubbles during boiling. However, the formation mechanisms of low-density fluids in pseudo-boiling and bubbles in boiling are different. As $(\partial P/\partial V)_T < 0$, fluctuations in SCFs dissipate spontaneously and do not destabilize the system. Gas-like and liquid-like structures are homogenously dispersed in the SCFs, originating from density fluctuations caused by the random movement of molecules. Thus, SCFs are always continuous and homogenous on a macro scale.

Subcritical gas-liquid transition depends on two key parameters: temperature and nucleation sites. Bubble formation is a stochastic process, dominated by density fluctuations and thermodynamic instability. Further, different modes of bubble formation and movement lead to different boiling modes, including nucleate boiling, transition boiling, and film boiling. The pseudo-critical transition depends on the temperature, and gas-like fluid formation is a deterministic process, although the movements of gas-like fluids are still stochastic. Different modes of gas-like fluid formation and movement also cause different pseudo-boiling modes. According to the prior similarity analyses, the pseudo-boiling modes are similar to the boiling modes. Natural convection induced by buoyancy, with a large density difference, is the common feature.

2.3 Mathematical description of hydraulic instability

For a typical subcritical horizontal film boiling case, a layer of vapor fully covers the heated wall and a layer of liquid is present above the vapor layer. The temperature of the heated wall is constant and higher than the saturation temperature. Due to density differences under gravity, the liquid-vapor interface is unstable, which is called Rayleigh-Taylor instability. Meanwhile, evaporation of the liquid and the generation of fresh vapor cause changes at the gas-liquid interface.

According to Taylor's theory (Taylor, 1950), the interface disturbance can be expressed through first-order perturbation analysis using the following equation:

$$\eta = \sum_k \eta_k e^{-in_k t} \cos kx = \sum_k \eta_k e^{b_k t} \cos kx \tag{1}$$

The growth coefficient, b_k, is related to the wave frequency, n_k; and the wavenumber, k, is related to the wavelength, l_k, by:

$$b_k = -in_k, \quad k = \frac{2\pi}{l_k} \tag{2}$$

Therefore, the interface disturbance is divided into several sub-disturbances with a particular wavelength l_k. When b_k is imaginary, the sub-disturbance is periodic in time and therefore

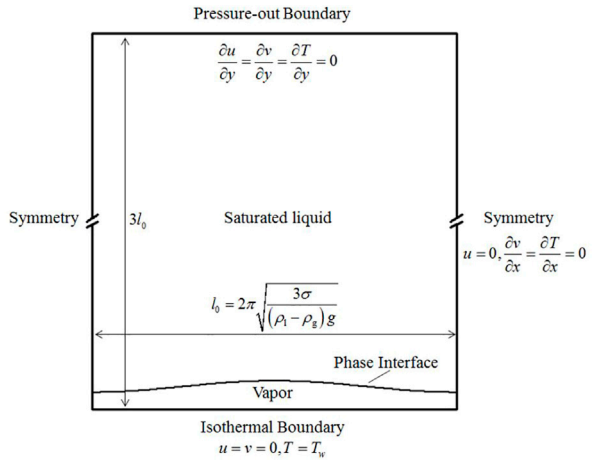

FIGURE 4
Computational domain and boundary conditions in subcritical cases.

stable. However, if b_m is real, the sub-disturbance grows exponentially with time and is therefore unstable.

For the horizontal film boiling with no forced convection, the irrotational flow kinematic equation, which yields the relations between wave number, gravity, surface tension, and the fluid properties, can be simplified to the following equation (Berenson, 1961):

$$k\rho_g\left(V_g-\frac{n_k}{k}\right)^2+k\rho_l\left(\frac{n_k}{k}\right)^2=g\sigma k^2-g\left(\rho_l-\rho_g\right) \tag{3}$$

If the vapor velocity, V_v, is negligible, then the equation for the grow coefficient b is:

$$b_k^2=-n_k^2,\ b_k=\left[\frac{g\left(\rho_l-\rho_g\right)k}{\rho_l+\rho_g}-\frac{g\sigma k^3}{\rho_l+\rho_g}\right]^{1/2} \tag{4}$$

According to the previous analysis, the larger the value of b_k, the more unstable the sub-disturbance, which corresponds to a greater growth rate of the boundary. Therefore, Eq. 4 indicates that the density difference and gravity play important roles in the hydraulic instability. On the contrary, surface tension tends to restrain the disturbances. When the wavelength l is small, b_k is imaginary and the corresponding disturbance will disappear.

$$\left(\frac{db_k}{dk}\right)=0\Rightarrow l=l_0=2\pi\left[\frac{3\sigma}{\left(\rho_l-\rho_g\right)g}\right]^{\frac{1}{2}} \tag{5}$$

As shown in Eq. 5, the value of b_k is a maximal real number when $l=l_0$. In this condition, the disturbance is most likely to develop into a visible bubble. This special wavelength is also called the "most dangerous wavelength".

However, the surface tension, σ, of supercritical fluids is always zero. For an arbitrary k, the value of b_k is real, which indicates that all disturbances will grow, leading to an unstable interface. Compared with the subcritical film boiling cases, the natural convection in supercritical fluid cases are more irregular and chaotic.

3 Numerical methods and models

To prove the prior theories, several numerical simulations are performed for both the subcritical and supercritical fluids. This section aims to demonstrate the numerical methods and models.

3.1 Horizontal film boiling of subcritical fluids

3.1.1 Macro-scale model

For the subcritical cases, the computational domain is a rectangular region. The domain width is the most dangerous wavelength, l_0, and the height is $3l_0$ (Figure 4). The bottom is a no-slip wall with a constant temperature. The left and right boundaries are both symmetrical. The top boundary is free, where the vapor is allowed to exit and the saturated liquid is allowed to enter.

In the initial condition, the liquid temperature is set as the saturated temperature. The gas-liquid interface is initialized as the original disturbance, which satisfies

$$y=\frac{l_0}{128}\left[4.0+\cos\left(\frac{2\pi x}{l_0}\right)\right] \tag{6}$$

Meanwhile, the vapor temperature increases linearly from the interface to the bottom, along the negative y direction.

3.1.2 Numerical methods

In order to simulate horizontal film boiling, the coupled level-set and volume-of-fluid method in FLUENT 17.2 is used to capture and track the interface. The continuum surface force model (CSF) (Brackbill et al., 1992) is used to consider the effect of surface tension in the momentum equation. As the fluid velocity is small, these cases only consider the laminar model. The governing equations for these models can be found in the help manual of Fluent.

The evaporation model is presented by Sun et al. (2012), and is developed specially for film boiling. In this model, heat transfer in the saturated liquid is ignored. Therefore, the thermal conductivity of the saturated liquid, λ_l, is set as 0, and the isobaric heat capacity of the saturated liquid is set to that of the gas. To calculate the heat flux on the interface q_S, assuming Assuming the fraction of the gas is α_g and the latent heat of vaporization is h_{lg}, then

$$q_S=2\lambda_g\left(\nabla\alpha_g\cdot\nabla T\right) \tag{7}$$

The mass transfer from the gas to liquid, $\dot{m}_l$, is calculated in Eq. 8, opposite to the mass transfer from the liquid to gas, $\dot{m}_g$.

TABLE 1 Numerical simulation cases.

Case	Fluid	Pressure/MPa	l_0/m	ΔT/K
Case 1	Water	—	0.0768	5
Case 2	Carbon dioxide	7.0	0.0025	80
Case 3	Carbon dioxide	7.37	0.0004	80

$$\dot{m}_l = -\dot{m}_g = \frac{2\lambda_g\left(\nabla\alpha_g \cdot \nabla T\right)}{h_{lg}} \tag{8}$$

Finally, through the used defined functions (UDFs) of FLUENT, $\dot{m}_l$ and $\dot{m}_g$ are respectively added to the mass conservation equations of the liquid and gas as the mass source terms. q_S is added to the energy conservation equation as an energy source term.

The numerical simulations of the cases are shown in Table 1 and the properties of the saturated liquid and vapor are listed in Table 2.

3.1.3 Grid independence tests

To obtain grid-independent results, three different grid systems of 32×96, 64×192 and 128×384 in Case 1 are considered. Figure 5A shows the bubble shapes computed on the three grids at the same time, $t = 0.6\,s$. Figure 5B presents the computed space-averaged Nusselt number changes over time on the three grids with a characteristic length $l = [\sigma/(\rho_l - \rho_g)g]^{1/2}$. According to these figures, the 64×192 grid system is suitable for this case, and is selected for the later simulations of film boiling. The time step, Δt, in all the cases is $1 \times 10^{-5}s$, as the relative difference in time- and space-averaged Nusselt numbers for $\Delta t = 5 \times 10^{-6}$ s is less than 5%.

As a verification, the results are compared with Klimenko's analyses (dashed line in Figure 5B). In Case 1, the space- and time-averaged Nusselt number is 1.70, whereas it is 1.91 according to Klimenko's correlation. The difference between them is 10% and thus the results are comparable and consistent with the prior work.

TABLE 2 Properties database for cases 1–3.

Case	-	ρ	c_P	λ	μ	σ	h_{lg}
		kg/m^3	J/(kg · K)	W/(m · K)	Pa · s	N/m	J/kg
1	Liquid	200	200.0	0	0.1	0.1	10^4
	Vapor	5	200.0	1.0	0.005		
2	Liquid	638.3	2.19×10^4	0	4.84×10^{-5}	1.72×10^{-6}	8.3×10^4
	Vapor	304.0	2.19×10^4	0.0688	2.3×10^{-5}		
3	Liquid	512.1	1.83×10^6	0	3.65×10^{-5}	1.17×10^{-6}	2.06×10^4

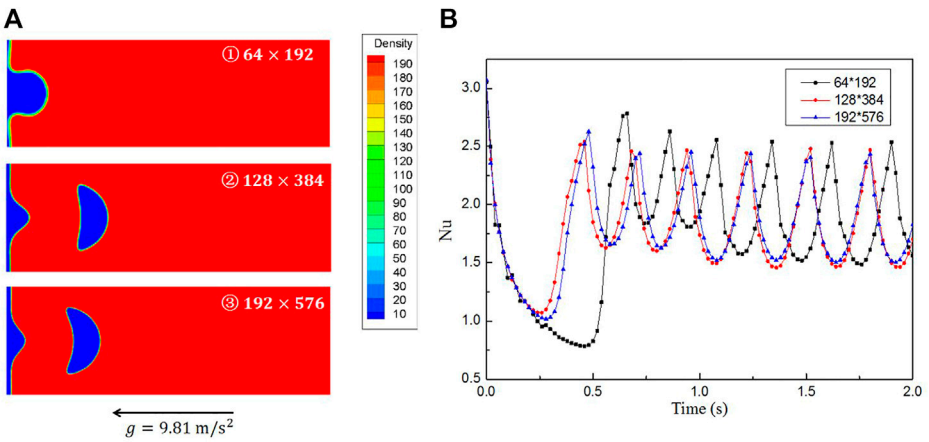

FIGURE 5
Results for three grid systems. **(A)** Bubble shapes at t = 0.6 s and **(B)** time-dependent, space-averaged Nusselt numbers.

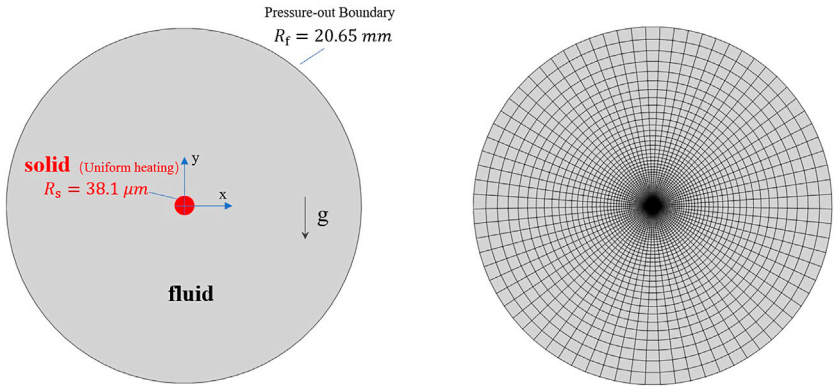

FIGURE 6
Computational domain and boundary conditions in supercritical cases.

3.2 Pseudo-boiling of supercritical fluids

3.2.1 Macro-scale model

In the pseudo-boiling cases, the bulk temperature and the heating wall temperature are below and above the pseudo-critical temperature, T_{pc}, respectively. Referring to Rousselt's experiments (Rousselet et al., 2013), the heat transfer characteristics of supercritical carbon dioxide in a simplified two-dimensional cylindrical model are studied (Figure 6).

In the model, a uniformly heated wire is present in the center, and the outer boundary is free. The computational domain is large enough so as to not affect the flow field near the wire. The radius of the wire and the domain are 38.1 μm and 20.65 mm, respectively. The pressure and temperature of the initial fluids and backflows are 7.5 MPa and 10°C, respectively.

3.2.2 Numerical methods

According to the statement in Section 2, supercritical fluids are always homogeneous with no phase transition. However, property changes with temperature in the pseudo-critical region, especially the density change, are not linear. The density can be doubled within a small temperature range, and the density change is certainly not small. Therefore, distinct from normal, natural convection simulations of single-phase fluids, the two main assumptions that the well-known Boussinesq approximation relied on are no longer valid in pseudo-boiling cases. It is thus necessary to solve the Navier-Stokes equations directly, with variable properties.

The change of the carbon dioxide properties with pressure is ignored, and only the effect of temperature is considered. The properties are described by a piecewise-linear profile consisting of 50 data points given by REFPROP. In the region where physical properties change dramatically, the temperature interval between adjacent data points is small. Similar to the subcritical boiling cases, only the laminar model is considered.

3.2.3 Independence tests

The independence tests study the effects of the number of circumferential and radial meshes and time steps. As shown in Table 3, the 76 × 120 grid system is suitable for this case, and is selected for the later simulations. Meanwhile, the wall temperature curves calculated at different time steps are almost identical (Figure 7A). The time step, Δt, of 2×10^{-4} s is suitable.

As a verification, the results are compared with Rousselt's experiments (dots in Figure 7B). For the 22 calculated conditions, the maximum relative difference of the wall temperature is approximately 18% and the mean relative difference is only 6%. Therefore, the model used in this section is reliable.

4 Results and discussions

4.1 Results of horizontal film boiling cases

Figure 8 presents six typical bubble shapes during the bubble release process for Case 2. For saturated carbon dioxide at 7 MPa, when the overheat temperature is high enough, the generated gas gathers into a stable film and film boiling occurs. With a given initial interface, the bubble formed at the center rises under the effect of buoyancy. The neck of the bubble becomes thinner until detachment. After detaching, the bubble continues to rise and leaves a packet at the detachment point (Figure 8C). This packet is pulled back into the gas film under the effect of surface tension. Further, the packet is finally absorbed and becomes a disturbance that propagates to both sides (Figure 8D). Meanwhile, the shape of the rising bubble constantly changes. As shown in Figures 8E,F, new bubble release processes occur at the original antinodes. If the flow field is undisturbed, this cycle is periodic. These results are consistent with experimental observations (Figure 9A). The photos are reproduced with permission from Abadzic and Goldstein (1970).

TABLE 3 Mesh independence tests.

Grid No.	Circumferential mesh number	Radial mesh number	T_w	Relative error (%)
1	16	120	377.7	−3.35
2	36	120	388.5	−0.59
3	76	120	390.8	0
4	116	120	391.2	0.10
5	76	80	390.3	−0.13
6	76	100	390.7	−0.03
7	76	200	390.4	−0.10

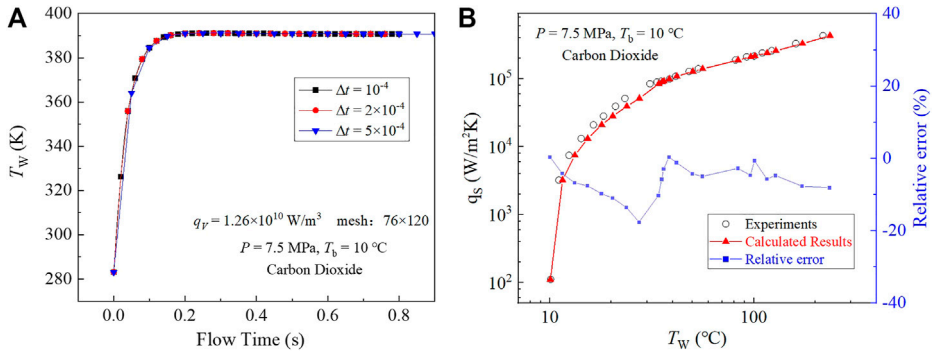

FIGURE 7
Independence tests and verifications. **(A)** Time step independence tests. **(B)** Comparisons with the experiments (Rousselet et al., 2013).

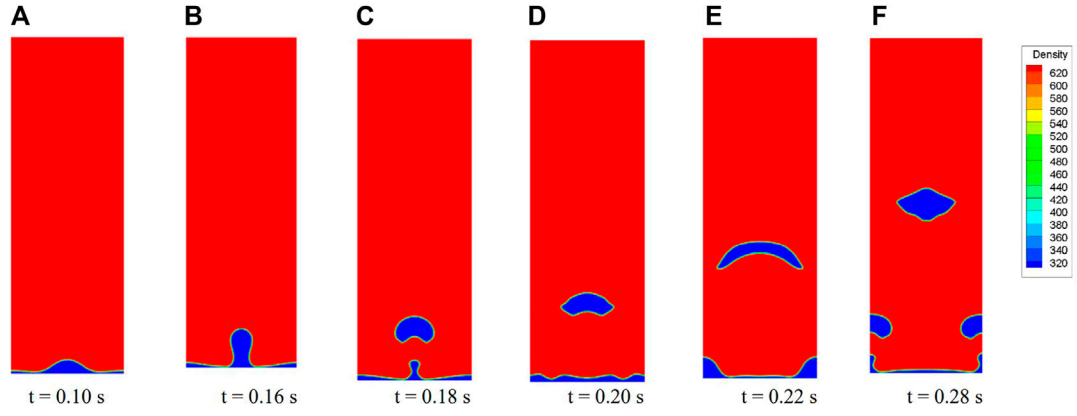

FIGURE 8
Density contours of carbon dioxide at 7.0 MPa with 80 K overheat, at different times.

In this process, the overheat condition provides the necessary energy for bubble formation and affects the frequency of bubble detachment. Specifically, when the overheat temperature is low, the whole gas film may form a bubble and the bubble then detaches from the wall. At this time, the wall is no longer covered by the vapor, and the

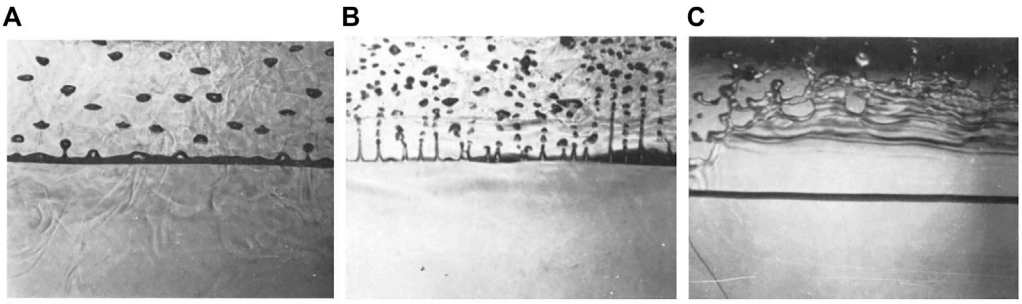

FIGURE 9
Film boiling experimental results for carbon dioxide at different cases. **(A)** 80 K overheat; **(B)** 110 K overheat; **(C)** 400 K overheat.

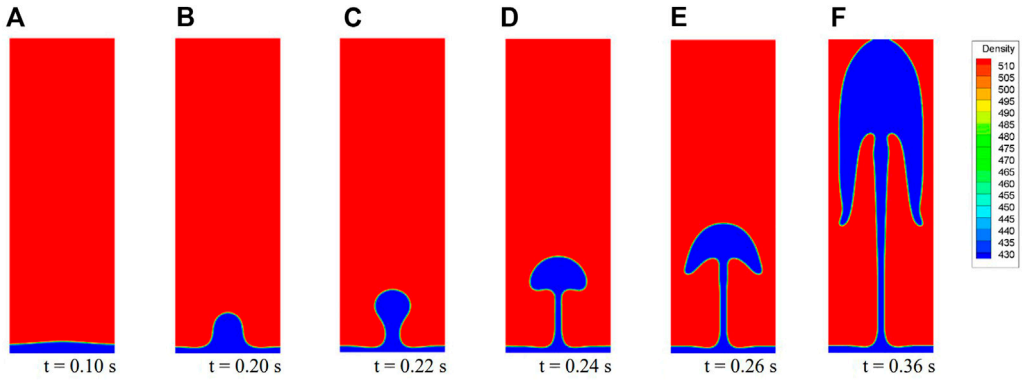

FIGURE 10
Density contours of carbon dioxide at 7.37 MPa with 80 K overheat, at different times.

boiling mode is nucleate boiling. The surface tension effect tends to generate a "smooth" interface as the surface energy decreases. According to Eq. 4, a larger value of σ leads to a smaller or even non-real value of b, corresponding to slower development of the disturbance or spontaneous decay.

When approaching the critical point, the differences between the two phases, in terms of latent heat and surface tension decrease rapidly. In Case 3, for saturated carbon dioxide at 7.37 MPa, the interface (Figure 10) is a slender column rather than individual bubbles as seen in Case 2, although the overheat temperature in the two cases are identical. At this condition, vapor formation becomes easier and numerous vapors are generated at a moderate overheat temperature. The slender vapor column becomes taller and accumulates most of the vapor at the top. Upon disturbance, the top of the vapor column may break into many small

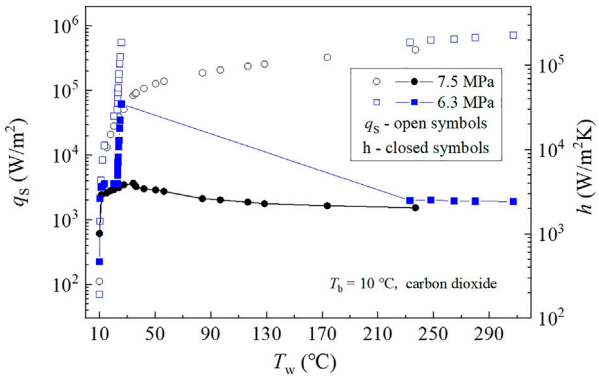

FIGURE 11
Surface heat flux and heat transfer coefficient at different wall temperatures.

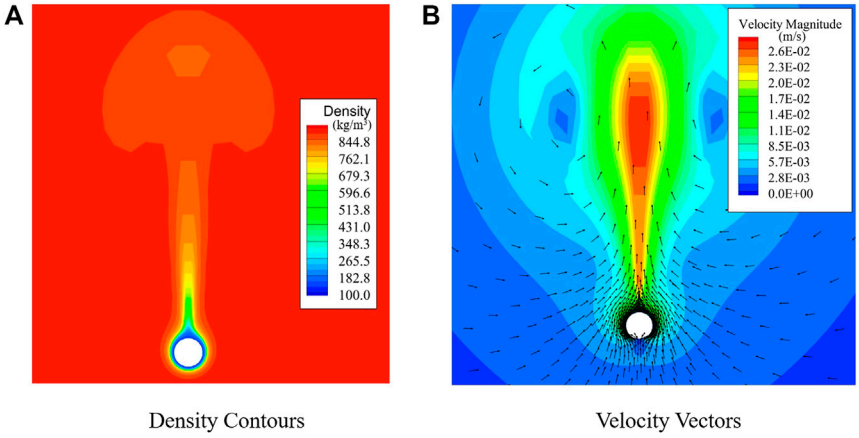

FIGURE 12
(A) Density contour and **(B)** velocity contour and vectors at 7.5 MPa with 90 K overheat.

bubbles (Figure 9B). In this context, the numerical result is too idealistic to observe.

If the vapor is produced faster, the vapor columns may converge to form a vapor sheet, which has been verified by experiment (Figure 9C).

4.2 Results of the pseudo-boiling cases

Figure 11 compares the surface heat flux, q_S, and the heat transfer coefficient, h, in supercritical and subcritical cases. The results at $P = 6.3$ MPa are from the experiments (Rousselet et al., 2013), whereas the results at $P = 7.5$ MPa are calculated based on the above proven models.

When the bulk is liquid-like, the heat transfer curve, $T_W - h$, of the supercritical carbon dioxide can be regarded as a continuation of the subcritical boiling curve. The main phenomenon is that the heat transfer mode rapidly evolves from single-phase, natural convection to "film-like boiling", while the nucleate boiling mode disappears. For similar bulk properties, the curves for the heat flux, q_S, and the heat transfer coefficient, h, in subcritical and supercritical cases, approximately overlap in some regions.

Figure 12 presents the density and velocity contours of the fully-developed pseudo-boiling case. The surface heat flux q_S is 2.14×10^5 W/m^2 and the calculated mean wall temperature is approximately 100°C, which differs from the experiment by less than 1°C.

The density profile displays a three-layer structure: the gas-like fluid layer, the transition layer, and the liquid-like fluid layer. Owing to the hydrodynamic instability, a number of initial disturbances appear in the transition layer and develop into the thermal plumes.

Thermal plumes are the key and are similar to bubbles in the subcritical cases. A typical plume exhibits a mushroom-like structure, consisting of a central rising column with vortexes on both sides. In the growth process, the upper high-density fluids are pushed away by the plume and flow downward along the sides. Some of the high-density fluid flows into the bottom low-density layer and is then heated, finally rising along the central column. The plumes may collide and merge with one another. The plumes cool as they rise, and their shapes change constantly. Specifically, the vertexes on both sides of the plumes are easily broken away, while the generated disturbances further affect the flow field.

4.3 Comparison of the pseudo-boiling and boiling cases

Thermal plumes in pseudo-boiling cases act like bubbles and vapor columns, and the near-wall low-density fluid layer is similar to the vapor film. Significant similarities exist between pseudo-boiling cases and film boiling cases, especially for the near-critical film boiling cases (Figure 10). However, in supercritical conditions, phase interfaces are non-existent, and the surface tension, σ, is reduced to zero. According to Eq. 4, at this time, b is always a real number for an arbitrary wave number m. Therefore, at an arbitrary wavelength, fluctuations will develop, and the most dangerous wavelength is non-existent. The distance between adjacent plumes can be small without restricting the subcritical conditions. Thus, the flow modes are more irregular and disordered than those in subcritical film boiling. Figure 13A (Abadzic and Goldstein, 1970) presents a visual observation of the horizontal wire heating experiment in supercritical carbon dioxide. The plume structures and the similarity to film boiling are evident.

Heat transfer in these two cases is enhanced by convection as the boundary layers are disturbed by the rising vapor or gas-like fluids. Certainly, the degree of heat transfer enhancement is

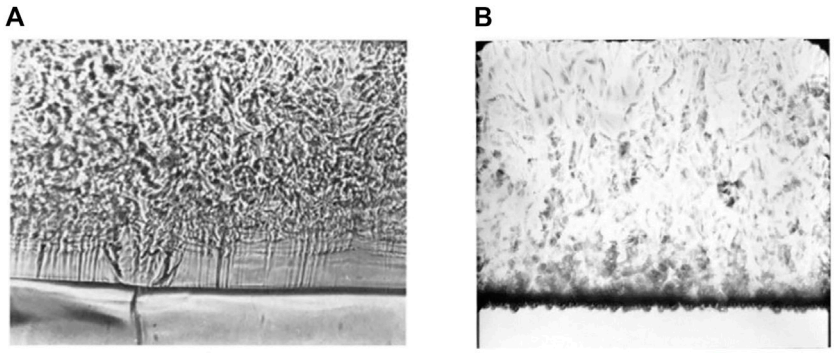

FIGURE 13
Pseudo-boiling experiments on a wire. **(A)** Pseudo film boiling **(B)** Pseudo nucleate boiling.

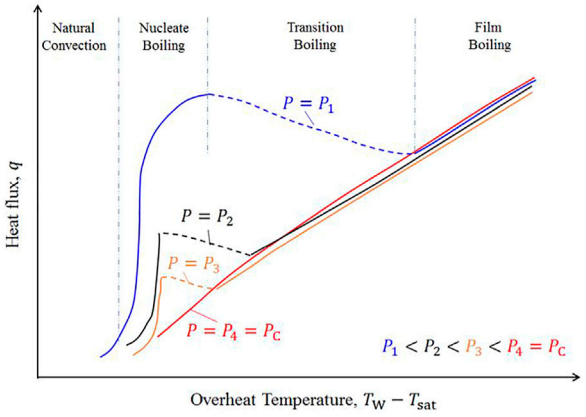

FIGURE 14
Schematic of boiling curves at different pressures.

much lower than for nucleate boiling. The low-density, near-wall fluid layer severely limits heat transfer. In applications, film boiling is regarded as the cause of heat transfer deterioration. It is desirable to avoid the transition from nucleate boiling to film boiling, which is called boiling crisis.

Many experiments have verified that heat fluxes when nucleate boiling occurs are reduced as the critical point is approached, and film boiling occurs more readily (Figure 14) (Hall and Jackson, 1978). The nucleate boiling and transition boiling areas in the boiling curve shrink, while the film boiling area expands. In this context, if only these isothermal heating cases are considered, pseudo film boiling can be regarded as an extension of near-critical boiling.

In subcritical boiling, an isothermal heating wall may lead to different boiling modes, which also depend on the heat flux, the number of vaporized cores, etc. However, according to the above analyses, pseudo film boiling is the only likelihood for an isothermal heating wall in pseudo-boiling cases. In order to prevent the formation of a low-density fluid layer, a heating wall with an inhomogeneous temperature profile is required.

Prior experiments have proved pseudo nucleate boiling, which is called bubble-like flow, and corresponds to a considerable increase in the heat transfer coefficient (Figure 13B). Pseudo nucleate boiling in the horizontal heating cases is only observed when the heaters are very fine wires with low thermal diffusion coefficients, for example, a nichrome wire with diameter of 0.1 mm (Knapp and Sabersky, 1966). Theoretically, a material with a low thermal diffusion coefficient is more likely to have an inhomogeneous surface temperature. Bubble-like structures are generated and released from hotspots. The hotspots are then covered and cooled by the high-density and low-temperature bulk. Nevertheless, the explanation provided in this paper is not insufficient. More experiments with wires of different diameters and materials are required to provide further evidence for our theory.

5 Conclusion

This paper theoretically analyses the similarities and differences between the subcritical gas-liquid transition and the pseudocritical transition. The heat transfer characteristics in the subcritical gas-liquid transition and the pseudocritical transition are compared through theory and numerical simulations.

Property changes during the subcritical phase transition and the pseudocritical transition are similar, leading to similar heat transfer characteristics. The similarities are the result of the hydraulic instability of the low-density bulk under the effects of gravity. However, thermodynamic stability prevents the phase separation of supercritical fluids. Pseudocritical transition only depends on the temperature; the formation of low-density bulk in supercritical cases is a deterministic process. On the contrary,

vapor formation in subcritical cases is a stochastic process which relies on the initial nucleation sites.

The random distribution of nucleation sites means that the heating wall may not necessarily be completely covered by the low-density fluid during boiling. For an isothermal heating wall, different boiling modes may appear in subcritical cases, whereas only pseudo film boiling is observed in supercritical cases. For isothermal heating cases, pseudo-boiling cases can be regarded as an extension of near-critical boiling. However, pseudo nucleate boiling may appear in non-isothermal cases, which strongly depends on the heater geometry, materials, etc.

Data availability statement

The original contributions presented in the study are included in the article/Supplementary Material, further inquiries can be directed to the corresponding author.

Author contributions

ML: software, methodology, writing-original draft; SL: methodology; DX: analysis; SH: methodology, supervision, YH: conceptualization, funding acquisition, supervision.

Funding

This work was supported by the National Natural Science Foundation of China (Grant No. U1867218) and the Nuclear Power Technology Innovation Center in the National Defense Science and Technology Industry of China.

Conflict of interest

The authors declare that the research was conducted in the absence of any commercial or financial relationships that could be construed as a potential conflict of interest.

Publisher's note

All claims expressed in this article are solely those of the authors and do not necessarily represent those of their affiliated organizations, or those of the publisher, the editors and the reviewers. Any product that may be evaluated in this article, or claim that may be made by its manufacturer, is not guaranteed or endorsed by the publisher.

References

Abadzic, E., and Goldstein, R. J. (1970). Film boiling and free convection heat transfer to carbon dioxide near the critical state. *Int. J. Heat Mass Transf.* 13 (7), 1163–1175. doi:10.1016/0017-9310(70)90006-2

Ackerman, J. (1970). Pseudoboiling heat transfer to supercritical pressure water in smooth and ribbed tubes. *J. Heat. Transf.* 92 (3), 490–497. doi:10.1115/1.3449698

Ahn, Y., Bae, S. J., Kim, M., Cho, S. K., Baik, S., Lee, J. I., et al. (2015). Review of supercritical CO2 power cycle technology and current status of research and development. *Nucl. Eng. Technol.* 47 (6), 647–661. doi:10.1016/j.net.2015.06.009

Banuti, D. T., and Hannemann, K. (2014). "Supercritical pseudo-boiling and its relevance for transcritical injection," in 50th AIAA/ASME/SAE/ASEE Joint Propulsion Conference, Cleveland, OH, July 28-30, 2014.

Berenson, P. J. (1961). Film-boiling heat transfer from a horizontal surface. *J. Heat Transf.* 83 (3), 351–356. doi:10.1115/1.3682280

Boukari, H., Shaumeyer, J. N., Briggs, M. E., and Gammon, R. W. (1990). Critical speeding up in pure fluids. *Phys. Rev. A . Coll. Park.* 41 (4), 2260–2263. doi:10.1103/physreva.41.2260

Brackbill, J. U., Kothe, D. B., and Zemach, C. (1992). A continuum method for modeling surface tension. *J. Comput. Phys.* 100 (2), 335–354. doi:10.1016/0021-9991(92)90240-y

Brun, K., Friedman, P., and Dennis, R. (2017). *Fundamentals and applications of supercritical carbon dioxide (sCO2) based power cycles*. Sawston, United Kingdom: Woodhead publishing.

Cardy, J. (1996). *Scaling and renormalization in statistical physics*. NewYork: Cambridge University Press.

Duffey, R. B., and Pioro, I. L. (2005). Experimental heat transfer of supercritical carbon dioxide flowing inside channels (survey). *Nucl. Eng. Des.* 235 (8), 913–924. doi:10.1016/j.nucengdes.2004.11.011

Fomin, Y. D., Ryzhov, V., Tsiok, E., and Brazhkin, V. (2015). Dynamical crossover line in supercritical water. *Sci. Rep.* 5, 14234. doi:10.1038/srep14234

Fu, Y., Huang, H., Wen, J., Xu, G., and Zhao, W. (2017). Experimental investigation on convective heat transfer of supercritical RP-3 in vertical miniature tubes with various diameters. *Int. J. Heat Mass Transf.* 112, 814–824. doi:10.1016/j.ijheatmasstransfer.2017.05.008

Goldstein, R. J., and Aung, W. (1968). Heat transfer by free convection from a horizontal wire to carbon dioxide in the critical region. *J. Heat Transf.* 90 (1), 51–55. doi:10.1115/1.3597459

Gorelli, F., Santoro, M., Scopigno, T., Krisch, M., and Ruocco, G. (2006). Liquidlike behavior of supercritical fluids. *Phys. Rev. Lett.* 97 (24), 245702. doi:10.1103/PhysRevLett.97.245702

Gu, H., Li, H., Wang, H., and Luo, Y. (2013). Experimental investigation on convective heat transfer from a horizontal miniature tube to methane at supercritical pressures. *Appl. Therm. Eng.* 58 (1-2), 490–498. doi:10.1016/j.applthermaleng.2013.04.049

Ha, M. Y., Yoon, T. J., Tlusty, T., Jho, Y., and Lee, W. B. (2018). Widom delta of supercritical gas–liquid coexistence. *J. Phys. Chem. Lett.* 9 (7), 1734–1738. doi:10.1021/acs.jpclett.8b00430

Hahne, E., and Neumann, R. (1981). Boiling-like phenomena in free-convection heat transfer at supercritical pressures. *Warme- Stoffubertragung* 15 (3), 171–180. doi:10.1007/BF01376829

Hall, W. B., and Jackson, J. D. (1978). Heat transfer near the critical point. *Adv. Heat. Transf.* 7, 1–86. doi:10.1016/S0065-2717(08)70016-9

Hiroaki, T., Ayao, T., Masaru, H., and Nuchi, N. (1973). Effects of buoyancy and of acceleration owing to thermal expansion on forced turbulent convection in vertical circular tubes—Criteria of the effects, velocity and temperature profiles, and reverse transition from turbulent to laminar flow. *Int. J. Heat Mass Transf.* 16 (6), 1267–1288. doi:10.1016/0017-9310(73)90135-x

Jiang, P., Liu, B., Zhao, C., and Luo, F. (2013). Convection heat transfer of supercritical pressure carbon dioxide in a vertical micro tube from transition to turbulent flow regime. *Int. J. heat mass Transf.* 56 (1-2), 741–749. doi:10.1016/j.ijheatmasstransfer.2012.08.038

Kadanoff, L. P., Götzes, W., Hamblen, D., Hecht, R., Kane, J., Palciauskas, V. V., et al. (1967). Static phenomena near critical points: Theory and experiment. *Rev. Mod. Phys.* 39 (2), 395–431. doi:10.1103/RevModPhys.39.395

Knapp, K. K., and Sabersky, R. H. (1966). Free convection heat transfer to carbon dioxide near the critical point. *Int. J. Heat Mass Transf.* 9 (1), 41–51. doi:10.1016/0017-9310(66)90055-x

Li, Z., Jiang, P., Zhao, C., and Zhang, Y. (2010). Experimental investigation of convection heat transfer of CO2 at supercritical pressures in a vertical circular tube. *Exp. Therm. fluid Sci.* 34 (8), 1162–1171. doi:10.1016/j.expthermflusci.2010.04.005

Liu, M., Tang, J., Liu, S., Xi, D., Min, L., Zang, J., et al. (2022). Modified landau model for fluids: A rethink of pseudoboiling theory for supercritical fluids. *J. Supercrit. Fluids* 183, 105554. doi:10.1016/j.supflu.2022.105554

Liu, S., Huang, Y., Liu, G., Wang, J., and Leung, L. K. (2017). Improvement of buoyancy and acceleration parameters for forced and mixed convective heat transfer to supercritical fluids flowing in vertical tubes. *Int. J. Heat Mass Transf.* 106, 1144–1156. doi:10.1016/j.ijheatmasstransfer.2016.10.093

Maxim, F., Karalis, K., Boillat, P., Banuti, D. T., Marquez Damian, J. I., Niceno, B., et al. (2020). Thermodynamics and dynamics of supercritical water pseudo-boiling. *Adv. Sci. (Weinh).* 8, 2002312. doi:10.1002/advs.202002312

McEligot, D., Coon, C., and Perkins, H. (1970). Relaminarization in tubes. *Int. J. Heat Mass Transf.* 13 (2), 431–433. doi:10.1016/0017-9310(70)90118-3

Mokry, S., Pioro, I., Kirillov, P., and Gospodinov, Y. (2010). Supercritical-water heat transfer in a vertical bare tube. *Nucl. Eng. Des.* 240 (3), 568–576. doi:10.1016/j.nucengdes.2009.09.003

Nasuti, F., and Pizzarelli, M. (2020). Pseudo-boiling and heat transfer deterioration while heating supercritical liquid rocket engine propellants. *J. Supercrit. Fluids* 168, 105066. doi:10.1016/j.supflu.2020.105066

Neumann, R. J., and Hahne, E. W. (1980). Free convective heat transfer to supercritical carbon dioxide. *Int. J. Heat Mass Transf.* 23 (12), 1643–1652. doi:10.1016/0017-9310(80)90223-9

Nishkawa, K., and Ito, T. (1969). An analysis of free-convective heat transfer from an isothermal vertical plate to supercritical fluids. *Int. J. Heat Mass Transf.* 12 (11), 1449–1463. doi:10.1016/0017-9310(69)90027-1

Onuki, A., Hao, H., and Ferrell, R. A. (1990). Fast adiabatic equilibration in a single-component fluid near the liquid-vapor critical point. *Phys. Rev. A . Coll. Park.* 41 (4), 2256–2259. doi:10.1103/physreva.41.2256

Petukhov, B., Protopopov, V., and Silin, V. (1972). Experimental investigation of worsened heat-transfer conditions with the turbulent flow of carbon dioxide at supercritical pressure. *High. Temp.* 10 (2), 304–310.

Pioro, I. L., and Duffey, R. B. (2005). Experimental heat transfer in supercritical water flowing inside channels (survey). *Nucl. Eng. Des.* 235 (22), 2407–2430. doi:10.1016/j.nucengdes.2005.05.034

Rousselet, Y., Warrier, G. R., and Dhir, V. K. (2013). Natural convection from horizontal cylinders at near-critical pressures—part I: Experimental study. *J. Heat Transf.* 135 (2). doi:10.1115/1.4007672

Shen, B., and Zhang, P. (2013). An overview of heat transfer near the liquid–gas critical point under the influence of the piston effect: Phenomena and theory. *Int. J. Therm. Sci.* 71, 1–19. doi:10.1016/j.ijthermalsci.2013.04.010

Simeoni, G., Bryk, T., Gorelli, F., Krisch, M., Ruocco, G., Santoro, M., et al. (2010). The Widom line as the crossover between liquid-like and gas-like behaviour in supercritical fluids. *Nat. Phys.* 6 (7), 503–507. doi:10.1038/nphys1683

Sun, D., Xu, J., and Wang, L. (2012). A vapor-liquid phase change model for two-phase boiling and condensation. *J. Xi'an Jiaot. Univ.* 46 (7), 7–11.

Swenson, H., Carver, J., and Kakarala, C. d. (1965). Heat transfer to supercritical water in smooth-bore tubes. *J. Heat Transf.* 87 (4), 477–483. doi:10.1115/1.3689139

Taylor, G. I. (1950). "The instability of liquid surfaces when accelerated in a direction perpendicular to their planes. I," in Proceedings of the Royal Society of London. Series A. Mathematical and Physical Sciences, Taylor, Geoffrey, March 1950.

Wilson, K. G. (1971). Renormalization group and critical phenomena. I. Renormalization group and the kadanoff scaling picture. *Phys. Rev. B* 4 (9), 3174–3183. doi:10.1103/PhysRevB.4.3174

Xu, J., Zhang, H., Zhu, B., and Xie, J. (2020). Critical supercritical-boiling-number to determine the onset of heat transfer deterioration for supercritical fluids. *Sol. Energy* 195, 27–36. doi:10.1016/j.solener.2019.11.036

Xu, R.-N., Luo, F., and Jiang, P.-X. (2017). Buoyancy effects on turbulent heat transfer of supercritical CO2 in a vertical mini-tube based on continuous wall temperature measurements. *Int. J. heat mass Transf.* 110, 576–586. doi:10.1016/j.ijheatmasstransfer.2017.03.063

Yoon, T. J., Ha, M. Y., Lee, W. B., and Lee, Y.-W. (2019). A corresponding-state framework for the structural transition of supercritical fluids across the Widom delta. *J. Chem. Phys.* 150 (15), 154503. doi:10.1063/1.5086467

Zappoli, B., Bailly, D., Garrabos, Y., Neindre, B. L., Guenoun, P., and Beysens, D. (1990). Anomalous heat transport by the piston effect in supercritical fluids under zero gravity. *Phys. Rev. A . Coll. Park.* 41 (4), 2264–2267. doi:10.1103/physreva.41.2264

Nomenclature

P pressure, MPa
T temperature, K
V volume, m^3
m mass, kg
t time, s
ρ density, kg/m^3
c_P isobaric heat capacity, $kJ/(kg \cdot K)$
λ thermal conductivity, $W/(m \cdot K)$
μ viscosity, Pa·s
κ_T isothermal compressibility, 1/MPa
α_P thermal expansion rate, 1/K
σ surface tension, N/m
h_{lg} latent heat of vaporization, J/kg
η distance perpendicular to liquid-vapor interface, m
k wave number, 1/m
l wavelength, m
n wave frequency, 1/s
b -in growth coefficient, 1/s
l_0 most dangerous wavelength, m
q heat flux, W/m^2
q_S heat flux on the interface, W/m^2
α volume fraction of vapor
Nu Nusselt number
h heat transfer coefficient

Subscripts

pc pseudocritical
C critical
l liquid
g vapor or gas
b bulk
w wall
sat saturation

frontiers | Frontiers in Energy Research

TYPE Original Research
PUBLISHED 26 January 2023
DOI 10.3389/fenrg.2022.1097023

OPEN ACCESS

EDITED BY
Shanfang Huang,
Tsinghua University, China

REVIEWED BY
Yuan Zhou,
Sichuan University, China
Haochun Zhang,
Harbin Institute of Technology, China

*CORRESPONDENCE
Yanping Huang,
hyanping007@163.com

SPECIALTY SECTION
This article was submitted to Nuclear Energy, a section of the journal Frontiers in Energy Research

RECEIVED 13 November 2022
ACCEPTED 25 November 2022
PUBLISHED 26 January 2023

CITATION
Liu X, Huang Y, Liu M, Min L, Zhang T, Li X and Zhuo W (2023), Analysis of the Brayton cycle coupled with a small fluoride salt-cooled high-temperature reactor.
Front. Energy Res. 10:1097023.
doi: 10.3389/fenrg.2022.1097023

Analysis of the Brayton cycle coupled with a small fluoride salt-cooled high-temperature reactor

Xiuting Liu[1], Yanping Huang[1]*, Minyun Liu[1], Luyue Min[1], Ting Zhang[1], Xinyu Li[2] and Wenbin Zhuo[1]

[1]Nuclear Power Institute of China (NPIC), Chengdu, China, [2]School of Energy and Power Engineering, Xi'an Jiaotong University, Xi'an, China

Considering the environmental conditions and transportation conditions of remote areas, an inherently safe integrated energy conversion system featuring miniaturization, modularization, and high environmental adaptability is needed. The small fluoride salt-cooled high-temperature reactor (FHR) coupled with the Brayton cycle is a promising design. In this paper, the efficiency, exergy efficiency, and exergy loss of four different configurations of the supercritical carbon dioxide (S-CO_2) Brayton cycle coupled with a new small fluoride salt-cooled high-temperature reactor are compared. The S-CO_2 recompressor Brayton cycle has the best overall performance. Meanwhile, the effects of the cooling conditions on the thermal efficiency and exergy efficiency of different cycle configurations are discussed. When the core outlet temperature is 700°C, the efficiency of the designed S-CO_2 recompressor Brayton cycle is approximately 42–44% when the cycle minimum temperature is 20–40°C. In conclusion, the designed small FHR coupled with the Brayton cycle system offers interesting performances in power generation, mineral mining, industrial steam supply, molten salt energy storage, and high-temperature hydrogen production in remote areas.

KEYWORDS

fluoride salt-cooled reactor, Brayton cycle, supercritical carbon dioxide, exergy, efficiency

1 Introduction

Regarding the fourth-generation nuclear power systems, six candidate reactor types, including the ultrahigh temperature reactor, supercritical water reactor (Pegallapati et al., 2020; Deev et al., 2021), gas-cooled fast reactor (Matozinhos et al., 2022; Lima-Reinaldo and François, 2023), lead-cooled fast reactor (Massone et al., 2022; Lima-Reinaldo and François, 2023), sodium-cooled fast reactor (Tak et al., 2022), and molten salt reactor (Ingersoll et al., 2004; Delpech, 2013), have been proposed. Studies of new reactors and coupled power systems have been a research focus worldwide. Among them, the molten salt reactor (MSR) is a kind of

nuclear fission reactor, and its primary coolant is a kind of molten mixed salt. The MSR can maintain a lower pressure when working at high temperatures (higher thermal efficiency can be obtained), thus reducing the mechanical stress and improving the safety.

From 2001 to 2003, the Oak Ridge National Laboratory (ORNL) (Ingersoll and Forsberg, 2006; Forsberg et al., 2013), Sandia National Laboratories (SNL), and the University of California, Berkeley (UCB), jointly developed the concept of a fluoride salt-cooled high-temperature reactor (FHR) (Haubenreich et al., 1964; Scott and Grindell, 1967). In 2007, the UCB carried out simulations of the PB-AHTR (Bardet et al., 2008) by RELAP5-3D and believed that it had a higher power density than the high-temperature helium-cooled reactor.

The ORNL proposed a new FHR concept called the SmAHTR (Greene et al., 2010), which is based on the research on the AHTR in 2006. The SmAHTR adopted the modular design concept with a 125-MW thermal power and a 60-year design life. The core inlet and outlet temperatures are 670°C and 700°C, respectively (Ilas et al., 2014).

Meanwhile, the Shanghai Institute of Applied Physics of the Chinese Academy of Sciences has built platforms for molten salt chemistry experiments and started the construction of a 2-MWt liquid fuel thorium-based molten salt reactor (Ruan Jian, 2017). Xi'an Jiaotong University (Qin Hao, 2018) also built an experimental platform for molten salt flow heat transfer and passive residual heat removal systems and carried out a series of studies in core physical and thermal design, safety analysis, etc.

In conclusion, the development of the FHR is still in the stage of a concept proposal, basic theory, and experimental research. Research on the coupled power conversion system of molten salt reactors is still limited. Compared with the light water reactor, the outlet temperature of the FHR is much higher and is potentially compatible with several highly efficient power conversion technologies. A particularly appealing option for the system is the high-efficiency S-CO_2 Brayton cycle. In recent years, with the breakthrough of key technologies such as heat exchangers and turbines, the supercritical carbon dioxide cycle has received extensive attention. However, there are few studies on the cycles coupled with the FHR, which is important for designing an integrated energy conversion system.

In this paper, an innovative and modular advanced nuclear power system, which consists of a small modular FHR and an S-CO_2 Brayton cycle, is proposed. Based on the thermal–hydraulic design of the proposed FHR, different configurations of the S-CO_2 Brayton cycle are discussed from the perspective of energy analysis and exergy analysis. Considering the probable climate in remote regions, the effects of the cooling conditions are further analyzed.

2 Small modular advanced nuclear power systems

2.1 System layouts

Considering the compact and integrated design requirements of the small modular FHR, helical cruciform fuel made of TRISO was selected. The fuel cladding is made of a special carbon–carbon (C–C) material (Greene et al., 2010), and the moderator is made of graphite (Jiang et al., 2022). A three-dimensional continuous energy Monte Carlo particle transport program was adopted in neutronic analyses. The computational fluid dynamics software Fluent and STAR-CCM+ based on the Euler method were used in the thermal–hydraulic calculations.

The FLiBe (Sehgal, 2012) coolant is heated when flowing through the core, and then, it flows upward along the ascending segment. After leaving the ascending segment, the coolant is deflected at the top and flows downward into the intermediate heat exchanger to release heat. The coolant enters the main pump for pressurization. In the pump outlet, most of the coolant returns to the core along the downcomer, and the other small part returns to the direct heat exchanger (DHE) for waste heat discharge. After meeting with the main coolant from the core, it enters the FLiBe–FLiNaK intermediate heat exchanger again, forming a primary loop. The diagram of the primary loop is shown in Figure 1. The FLiNaK–CO_2 intermediate heat exchangers were set between the reactor core coolant and the supercritical carbon dioxide (S-CO_2) power cycle system. The FLiNaK–CO_2 intermediate heat exchangers transfer the reactor heat to the power conversion cycle and finally realize the conversion of heat energy to electric energy.

The advantages and disadvantages of different pellet materials are compared, as shown in Table 1. The comparative analysis results show that UZr fuel and TRISO fuel both have a high thermal conductivity and a small temperature gradient; thus, the temperature of the fuel and cladding can meet the requirements of the temperature limits under normal operation and during accidents (Haynes-International, 2002; Clarno et al., 2007), and both fuels can contain fission gas, thus reducing the possibility of a large-scale release of radioactive materials. It can be used as a candidate material for high-safety fuel schemes. HT9 stainless steel and C–C composites were selected as candidate cladding materials for the high-safety fuel scheme. Between them, HT9 is used as a UZr fuel cladding, and the C–C composite is used as a TRISO-type fuel cladding. After comparing and analyzing the slowing properties of light water, heavy water, graphite, and

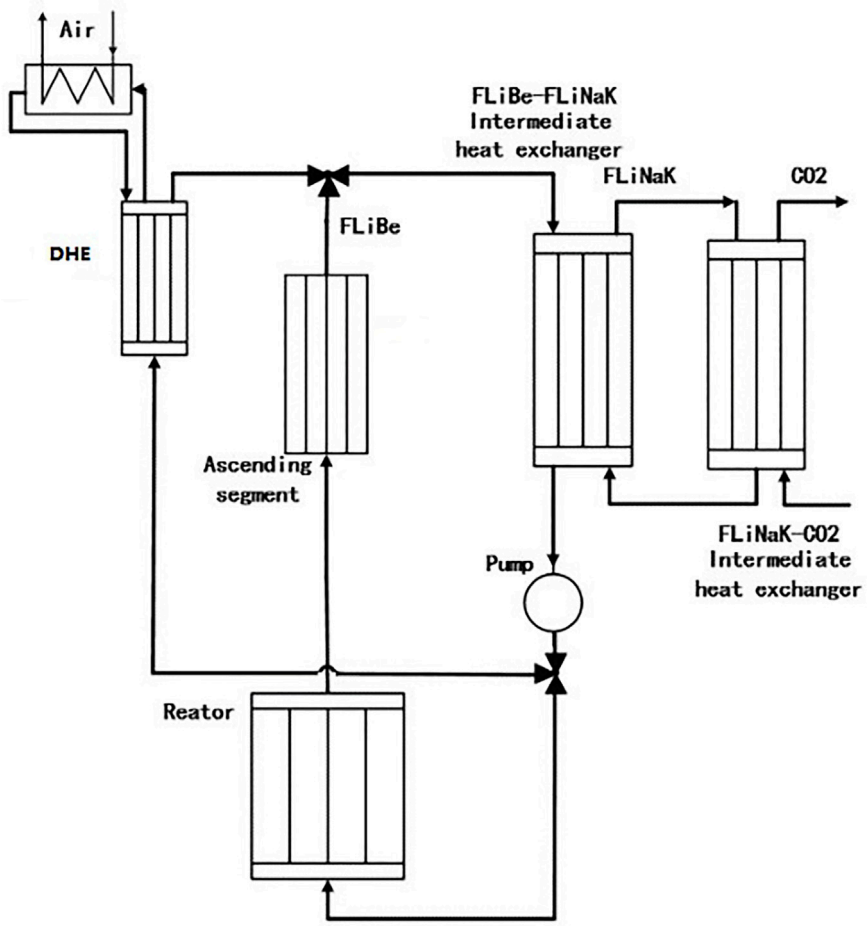

FIGURE 1
Diagram of the primary loop of the FHR.

TABLE 1 Advantages and disadvantages of different pellet materials.

	Ceram	UZr	TRISO
Advantages	High melting point	High thermal conductivity	High melting point
	Strong irradiation stability	High effective density	High thermal conductivity
	Good chemical compatibility	Lattice structure can contain the fission gas	Buffer layer can contain the fission gas
	Mature technology and low cost	No gaps and reduces the temperature gradient	No gaps and reduces the temperature gradient
Disadvantages	Low thermal conductivity	Low melting point	Low effective density of fuels
	Large temperature difference		
	Poor radioactive tolerance	At high temperatures, the crystalline phase changes	

beryllium and considering the chemical stability, thermal conductivity, and mechanical properties, the two candidate schemes of no slowing and graphite were finally selected. Between them, no slowing was used as the moderator scheme of the UZr fuel, and graphite was used as the moderator scheme of the TRISO fuel. Combined with the chemical stability, flow heat transfer characteristics, and neutron effect, FLiBe with a low viscosity, good thermal conductivity, and better neutron

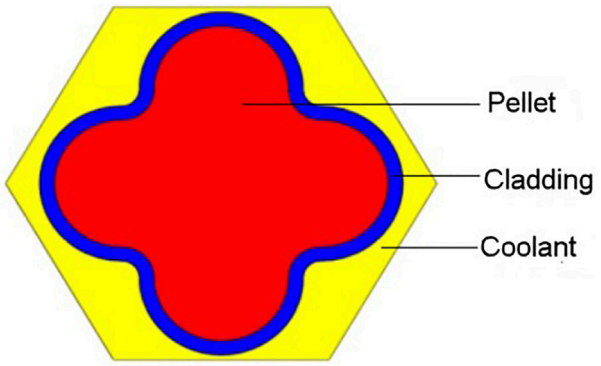

FIGURE 2
Single-channel geometric model.

performance was selected as the coolant. The molar ratio of LiF to BeF_2 was 2:1, and the Li-7 enrichment was 99.99%. Molten FLiNaK salt is used as the heat transfer medium in the primary loop and the passive residual heat removal system, which has the characteristics of low cost, moderate viscosity, and benefits from natural circulation. The helical cruciform fuel, which is superior to traditional PWR fuel in terms of convective heat transfer, cladding damage, radiation swelling, and other indicators, is finally adopted to determine the helical cruciform fuel, dispersion core material, C–C composite cladding, graphite slowing, and multicomponent compact core designs. Figure 2 shows the single-channel geometric model of the helical cruciform fuel.

The non-thermal equilibrium porous medium model of STAR-CCM+ simulating the physical velocity is used to carry out the thermal–hydraulic calculation of the one-sixth core of the FHR reactor. The equation of single-phase incompressible non-thermal equilibrium porous media simulating physical velocity in STAR-CCM+ is as follows:

$$\frac{\partial}{\partial t}(\rho\chi) + \nabla \cdot (\rho\chi U) = 0, \tag{1}$$

$$\begin{aligned}\frac{\partial}{\partial t}(\rho\chi U) &+ \nabla \cdot (\rho\chi U \otimes U) \\ &= -x\nabla P + \nabla \cdot [\chi\mu(\nabla U + \nabla U^T)] \\ &\quad - \chi P_v \otimes U_s - \chi P_i |U_s| U_s + S,\end{aligned} \tag{2}$$

$$\begin{aligned}\frac{\partial}{\partial t}(\chi\rho_{\text{fluid}} e_{\text{fluid}}) &+ \nabla \cdot (\chi\rho_{\text{fluid}} h_{\text{fluid}} U) \\ &= -\chi\nabla \cdot q_{\text{fluid}} + \nabla \cdot [\chi\mu(\nabla U + \nabla U^T) \cdot U] \\ &\quad + ah(T_{\text{fluid}} - T_{\text{solid}}) + S_e,\end{aligned} \tag{3}$$

$$\begin{aligned}\frac{\partial}{\partial t}[(1-\chi)\rho_{\text{solid}} E_{\text{solid}}] &= -\nabla \cdot [(1-\chi) q_{\text{solid}}] \\ &\quad + aHTR(T_{\text{fluid}} - T_{\text{solid}}).\end{aligned} \tag{4}$$

Figure 3B shows the physical calculation model of a one-sixth core. This calculation model has the same structure size as the calculation model of the whole core; the only difference is that the one-sixth of the whole core is selected, and a reflective boundary is set. The material layout and component number are shown in Figure 3. Figure 4 shows the longitudinal section and cross section of the one-sixth core model of the FHR established by using the MCNP modeling method. Based on the actual fission power distribution of each component calculated by the MCNP, the mass flow distribution of the coolant in each component is calculated as the inlet boundary condition for the CFD calculation. Thermal–hydraulic analyses and calculations are carried out using STAR-CCM+. The geometric model and CFD calculation model are shown in Figure 5. During the CFD calculation, the coolant, fuel, and cladding inside each hexagon assembly are set as the porous media area, the component graphite box and radial graphite reflector are set as the solid, and the turbulence model is the *k-SST* model. The design parameters of the S-CO_2 power cycle system are shown in Table 2.

2.2 Thermodynamic analyses

Considering the differences in the cycle configurations, the thermodynamic analysis conclusions, equipment operating parameters, optimal configurations, cycle performance evaluation criteria, and optimization results are different. The following is a comparative analysis of the Brayton cycle configurations to provide theoretical and data references for the preliminary design of small fluoride reactor systems. A small fluoride-cooled high-temperature reactor can be matched with a variety of Brayton cycle configurations. Taking the recompression Brayton cycle as an example, the cycle flow chart is shown in Figure 6.

After heat absorption occurs in the 1–2 processes, the working medium enters the turbine to complete the 3–4 work processes. The exhaust gas after work is discharged through the low-pressure side of the 5–6 high-temperature recuperator and the low-pressure side of the 6–7 low-temperature recuperator. It is divided from the outlet of the low-temperature recuperator. One enters the cooler and the main compressor after the 8–9 heat release process. After the 10–12 pressurization of the main compressor, it enters inlet 14 at the cold side of the low-temperature recuperator; the other enters the recompressor for the 11–13 repressure process directly. The working fluid from the recompressor joins the working fluid passing through the high-pressure side of the low-temperature regenerator, enters the high-pressure side of the high-temperature regenerator to complete the

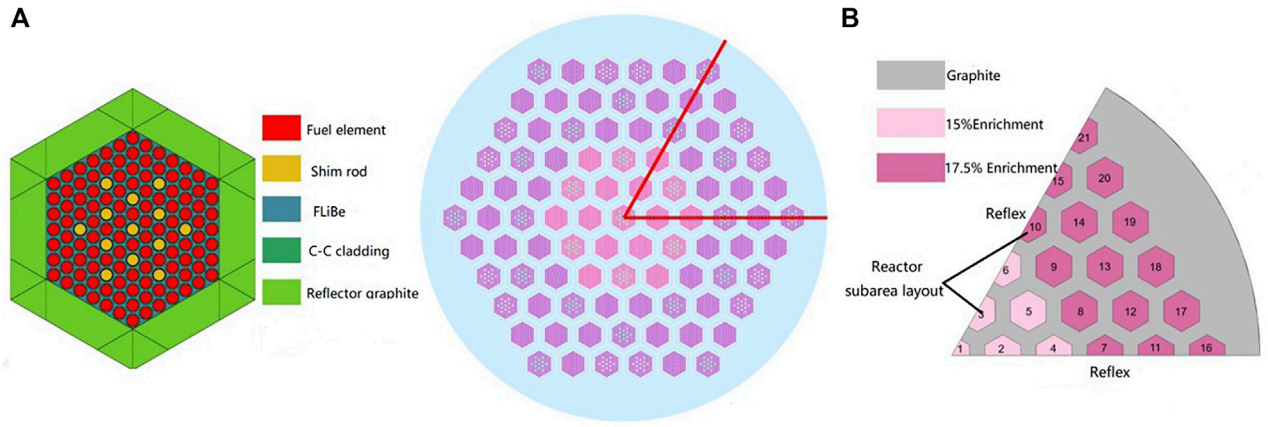

FIGURE 3
FHR core model. **(A)** Full-core model and **(B)** 1/6 core model.

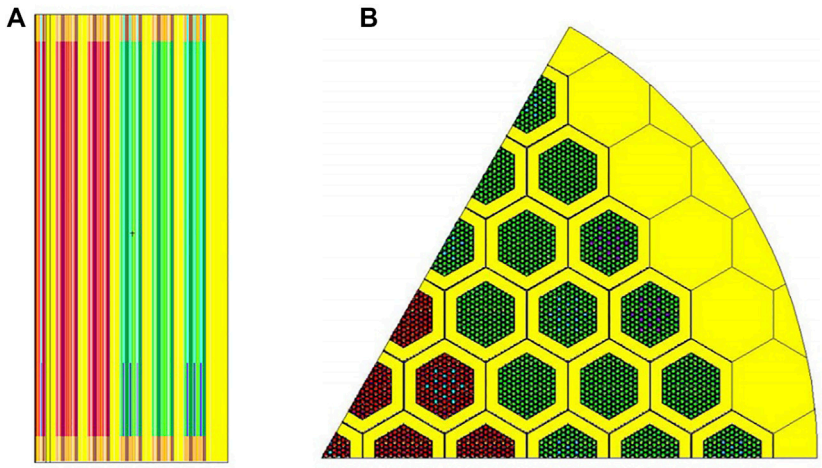

FIGURE 4
Core model in the MCNP. **(A)** Longitudinal section and **(B)** cross section.

15–1 heat absorption process, and finally enters the 1–2 intermediate heat exchanger to absorb heat, completing the whole cycle.

To carry out the thermodynamic analysis and analytical modeling of the system (Liu et al., 2020; Yourong, 2020), the initial assumptions are as follows:

1) The system components operate stably under various working conditions without considering the potential energy and the kinetic energy.
2) Ignoring the pressure drop of the pipeline, the pressure drop of the system is only the pressure drop of the heat exchanger.
3) The working process of the turbomachinery is adiabatic but not isentropic. Based on the first law of thermodynamics and the second law of thermodynamics, the energy balance relationship is established. The basic formula of the thermodynamics law can be expressed as follows:

$$\sum m_{\text{in}} = \sum m_{\text{out}}, \tag{5}$$

$$\sum Q - \sum W = \sum m_{\text{out}} \cdot h_{\text{out}} - \sum m_{\text{in}} \cdot h_{\text{in}}, \tag{6}$$

$$h, T = f(p, s). \tag{7}$$

The heat input of the fluorine salt-cooled high-temperature reactor core can be expressed as follows:

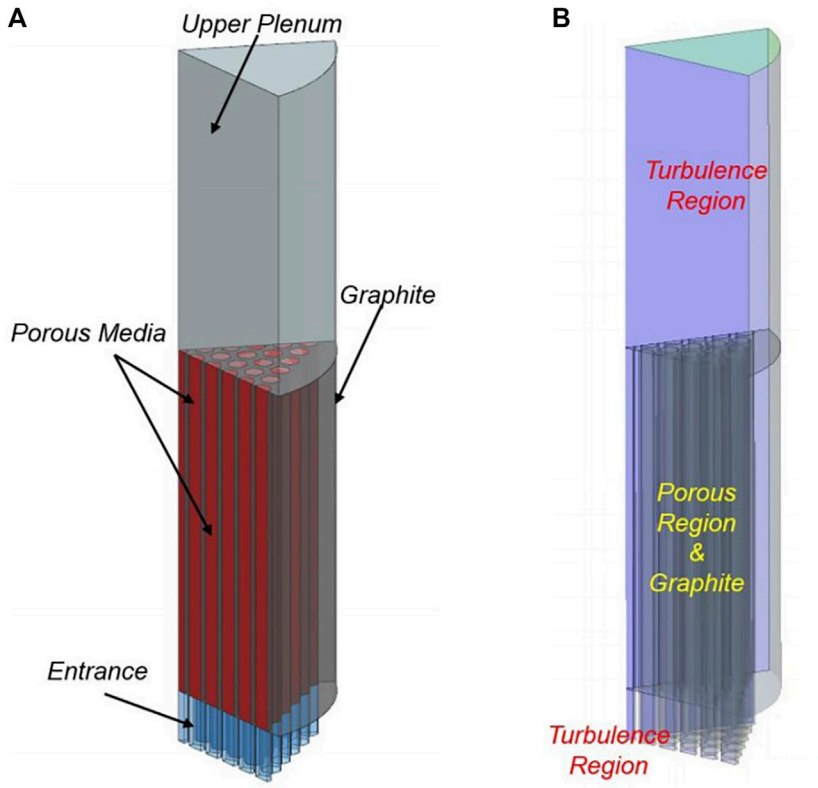

FIGURE 5
Core thermal–hydraulic model. **(A)** the geometric model **(B)** the CFD calculation model.

TABLE 2 Cycle parameter settings.

Parameter	Value
Core thermal power (MW)	10
Core inlet temperature (°C)	600
Core outlet temperature (°C)	700
Environment temperature (°C)	15
Heat exchanger pressure drop (kPa)	1%
Isentropic efficiency of the compressor (%)	80
Isentropic efficiency of the turbines (%)	83
End difference of heat exchangers (°C)	10
Efficiency of generators (%)	97
Heat loss	1%
Turbomechanical loss (kw)	200

$$Q_{in} = m_{in}(h_1 - h_2). \tag{8}$$

The isentropic work of the compressor and turbine can be determined by the following relationships:

$$W_i = m(h_{in} - h_{out,i}), \tag{9}$$

$$W_C = \frac{W_i}{\eta_{isen,C}}, \tag{10}$$

$$W_T = W_i \eta_{isen} \tag{11}$$

.

The network of the cycle system can be expressed as follows:

$$W_{net} = W_T - W_{MC} - W_{RC}. \tag{12}$$

The thermoelectric conversion efficiency of the system can be expressed as follows:

$$\eta_{th} = \frac{W_{net}}{Q_{in}}. \tag{13}$$

Exergy analysis is an effective tool to describe energy quality and reduce irreversibility. It can measure the energy conversion and work carried out by a system or equipment from the perspective of energy availability. Based on thermodynamic exergy analysis, a balance equation of the available energy can be established. The basic equation of physical exergy at a certain point can be expressed as follows:

$$\dot{E}_i = m_i[(h_i - h_{env}) - T_{env}(s_i - s_{env})] \tag{14}$$

.

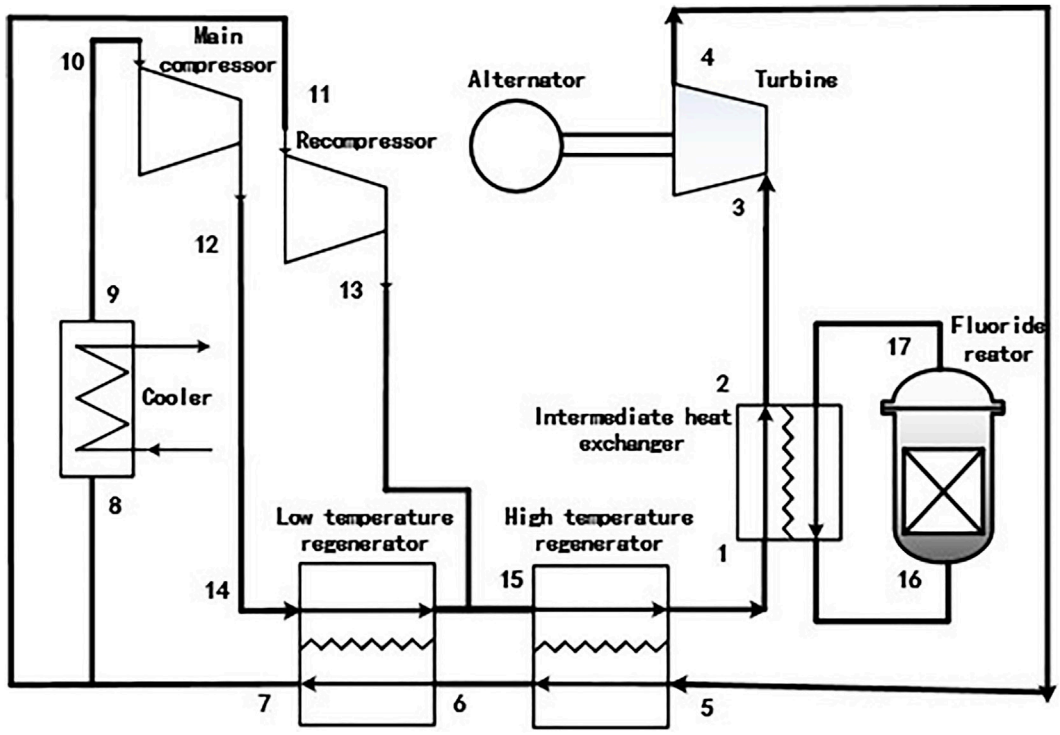

FIGURE 6
Flow chart of the recompression Brayton cycle.

The efficiency is expressed as follows:

$$\eta_{ex} = \frac{\dot{E}_{core} - \dot{I}_{total}}{\dot{E}_{core}}, \tag{15}$$

$$\dot{E}_{core} = Q_{core}\left(1 - \frac{T_{env}}{T_{core}}\right). \tag{16}$$

The total loss of each component can be expressed as the total loss of all key components, and the loss of each component can be calculated by Table 1.

$$\dot{I}_{total} = \sum \dot{I}_i. \tag{17}$$

3 Small modular advanced nuclear power system

The most typical S-CO_2 Brayton cycle is the simple regenerative cycle. In the simple regenerative cycle, the working medium directly enters the turbine for work after heating in the intermediate heat exchanger. The exhaust gas after work flows through the regenerator and the cooler for cooling and finally enters the compressor. After being pressurized by the compressor, the working medium returns to the regenerator, is heated by the working medium on the low-pressure side, and finally enters the intermediate heat exchanger to form a whole cycle.

In the recompression cycle, an additional compressor and an additional regenerator are introduced based on a simple regenerative cycle to split the flow. Based on the recompression cycle, inter-stage cooling is introduced to form an intermediate cooling structure, which is called the recompression intermediate cooling cycle. The reheating structure increases the multi-stage reheating between the turbine stages to increase the turbine output power, which is called the reheating cycle. Figure 6, Figure 7, Figure 8, and Figure 9 show the flow chart of the recompression cycle, simple regenerative cycle, intermediate cooling recompression cycle, and reheat recompression intermediate cooling cycle.

3.1 Analysis of different cycle configurations

To discuss the compatibility with a small fluoride-cooled high-temperature reactor, four typical supercritical carbon dioxide Brayton cycles, including the single-stage regenerative cycle, recompression cycle, main pressure intercooling cycle, and

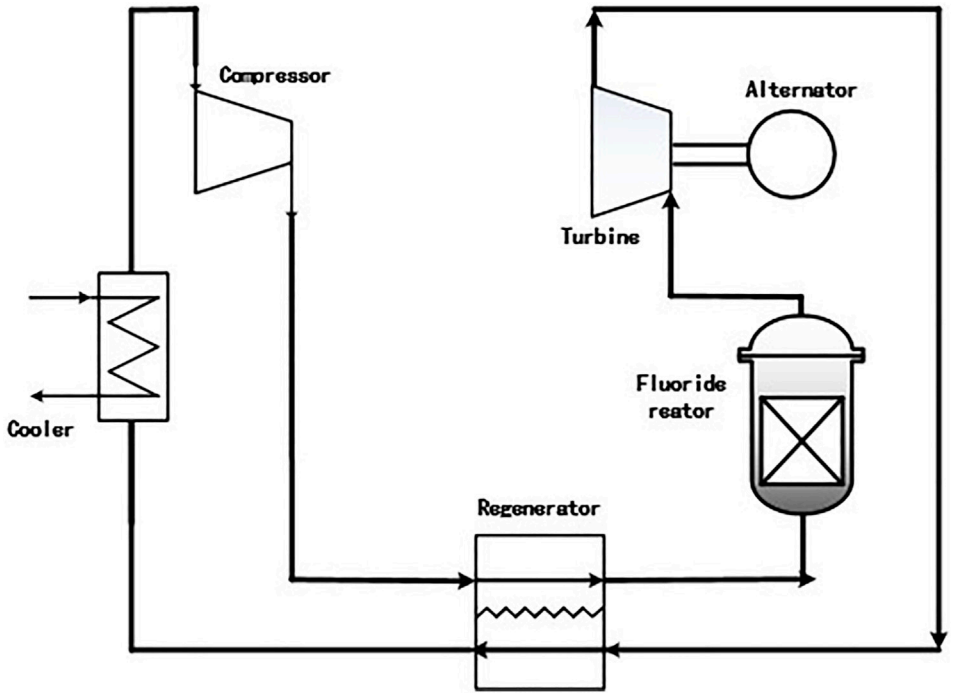

FIGURE 7
Flow chart of the simple regenerative cycle.

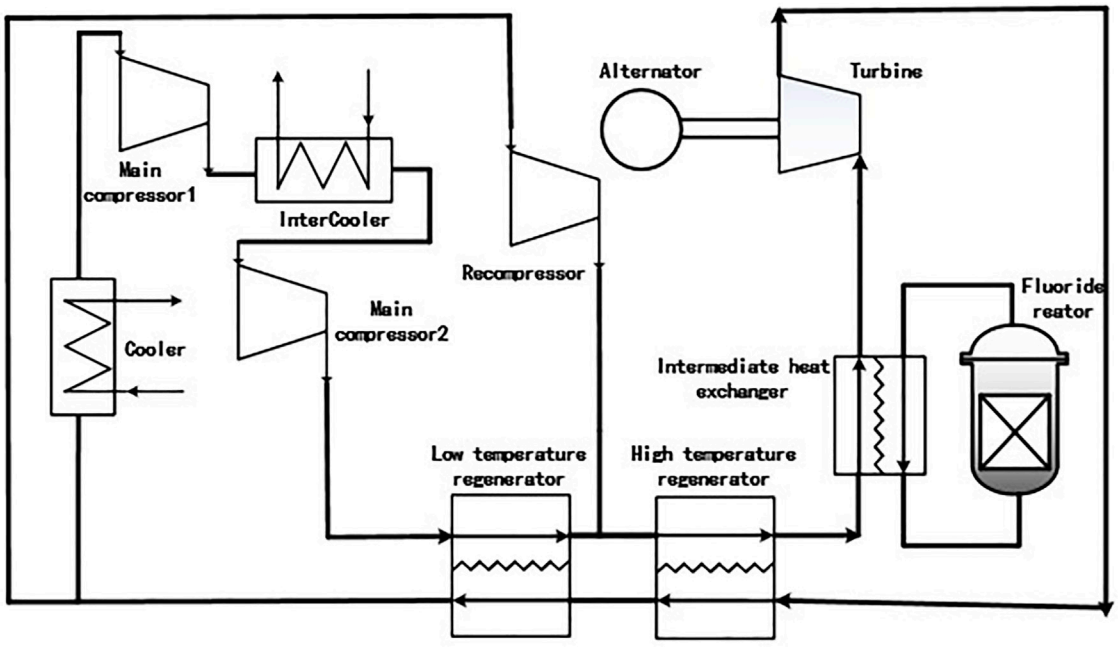

FIGURE 8
Flow chart of the intercooling recompression cycle.

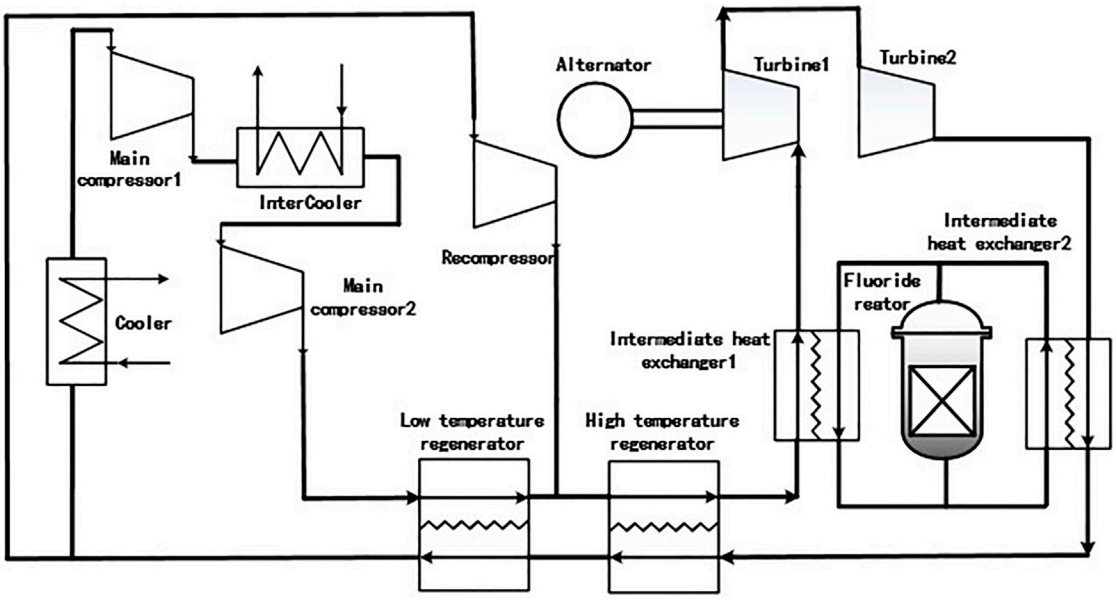

FIGURE 9
Flow chart of the reheat recompression intermediate cooling cycle.

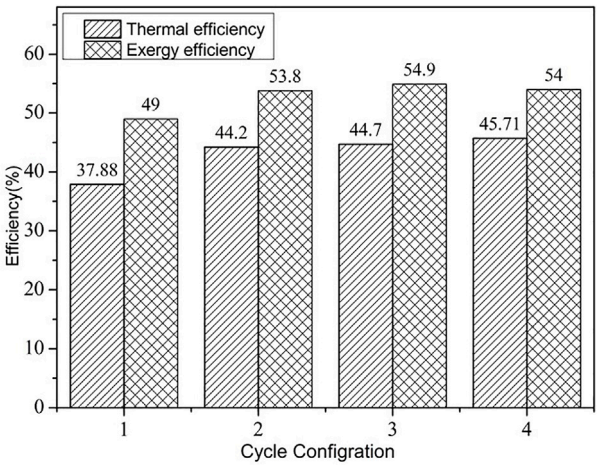

FIGURE 10
Comparison of the thermal efficiency and exergy efficiency of different cycle configurations.

reheat recompression cycle, are selected for comparative analyses. The initial parameters of the selected cycle are listed in Table 2.

The application background of small fluoride-cooled high-temperature reactors is remote areas in western China. Considering the adaptability of the environment, the circulating cooling mode is air-cooling circulation, and the ambient temperature is 25°C.

According to the aforementioned assumptions, the system input parameters, energy balance, and exergy balance are used to calculate the thermoelectric conversion efficiency, exergy efficiency, and exergy loss distribution of the four configurations.

Figure 10 shows that with the introduction of the split flow recompression, and intercooling and reheating structures, the thermoelectric conversion efficiency of the supercritical carbon dioxide Brayton cycle gradually increases. Compared with the simple regenerative cycle, the thermal efficiency of the recompression cycle increases by approximately 5%, while that of the intercooling recompression cycle and the reheating intercooling recompression cycle increases by approximately 0.5%, which is far less than the increase in the efficiency of the recompression cycle compared with the simple regenerative cycle. The cycle efficiency increases gradually with the introduction of the recompression split flow and intercooling structure, while the cycle efficiency decreases slightly with the introduction of the reheat structure. In summary, with the introduction of intercooling and reheating structures, the cycle thermoelectric conversion efficiency has been improved. However, the extent of improvement is limited, and the volume of the system complexity level has gradually increased. In the recompression Brayton cycle, due to the introduction of the additional compressor and the low-temperature regenerator, the energy utilization rate is improved, and the existence of the split flow effectively reduces the heat exchange pinch point problem of the low-temperature regenerator. The introduction of an intercooling structure can play an effective cooling role between the compressor stages and greatly reduce the power

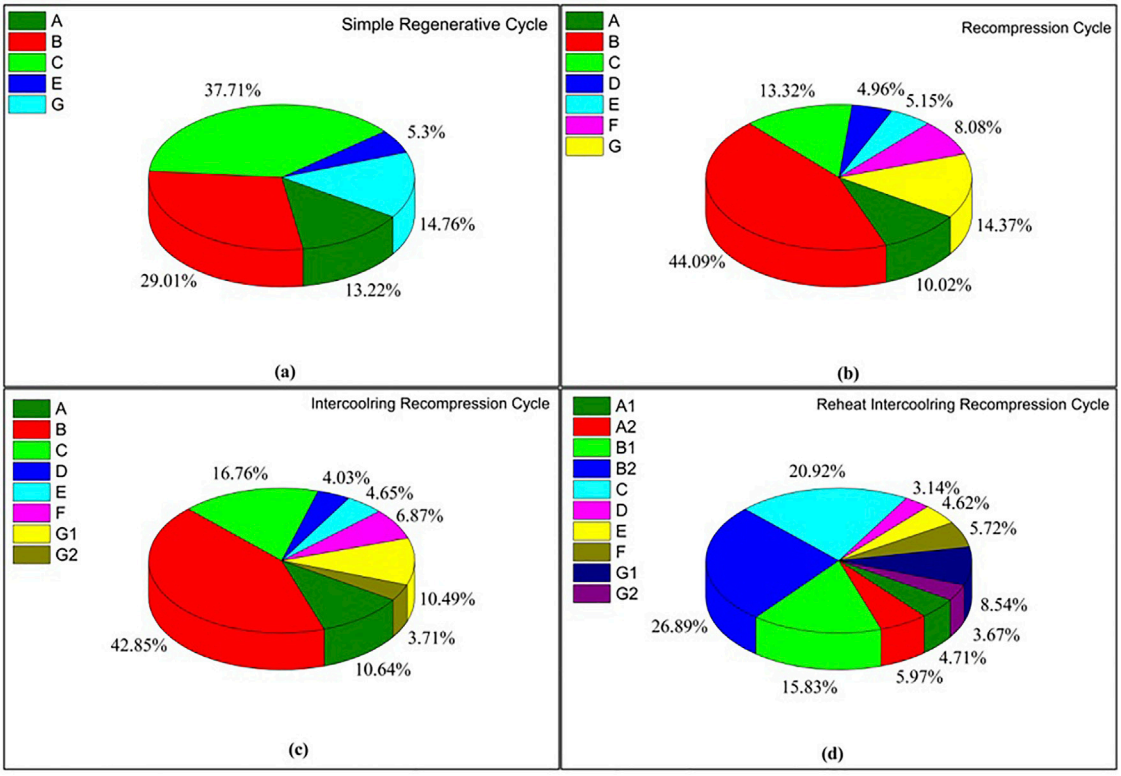

FIGURE 11
Exergy loss distribution of different cycle configurations. **(A)** Simple Regenerative Cycle **(B)** Recompression Cycle **(C)** Intercooling Cycle **(D)** Reheat Intercooling Recompression Cycle.

consumption of the compressor. The introduction of a reheat structure between turbine stages can increase the output work of the turbine, increase the average heat absorption temperature, and thus improve the thermal efficiency.

Figure 11A–D shows the loss distribution of four typical supercritical carbon dioxide reprocessing Brayton cycles. It can be seen from the loss distribution that the turbine loss is large in all four configurations. It can be seen from a) that in the simple regenerative Brayton cycle, the loss of the regenerator link is the largest and even exceeds the loss of the turbine. This is because the regenerator may have pinch points, the regeneration is insufficient, and the available energy is reduced. From B–C, the loss of the compressor is greatly reduced when the reheater is introduced into the recompression structure, and the loss of the compressor is reduced after the introduction of the intercooling structure. This also explains the perspective of exergy analysis that the split flow recompression structure can effectively reduce the pinch point of the regenerator and that the introduction of an intercooling structure can reduce the power consumption of the compressor to improve the cycle thermal efficiency and exergy efficiency. It can be seen from D that the total loss of the turbine is still the largest. However, compared with the recompression cycle and the main pressure intercooling recompression cycle, the loss of the intermediate heat exchanger has increased, which also explains why the efficiency of the reheating intercooling recompression cycle is slightly lower than that of the intercooling recompression cycle.

3.2 Effects of different cooling conditions

Considering the environmental characteristics of the western region, the air-cooling mode of anhydrous cooling is adopted for the S-CO_2 Brayton cycle cooling of a small fluoride-cooled high-temperature reactor. Taking the typical climate data on western China as the input, the influence of the cycle minimum temperature on the thermal efficiency and exergy efficiency of different cycle configurations was discussed. The typical climate data are shown in Table 3. Considering the annual maximum air temperature in the typical areas, the calculation results of

TABLE 3 Energy balance and exergy balance relationship.

Part	Energy balance	Exergy loss
Core	$Q_{core} = 125MW$	$\dot{I}_{core} = \dot{E}_{10} - \dot{E}_9 + \dot{E}_{core}$
Intermediate heat exchanger	$Q_{INH} = (h_8 - h_1)m_1$	$\dot{I}_{INH} = \dot{E}_8 + \dot{E}_9 - \dot{E}_1 - \dot{E}_{10}$
Turbine	$W_{TU} = (h_1 - h_2)m_1$	$\dot{I}_{TU} = \dot{E}_1 - \dot{E}_2 - \dot{W}_{TU}$
High-temperature regenerator	$W_{HTR} = (h_2 - h_3)m_2 = (h_{7a} - h_8)m_{7a}$	$\dot{I}_{HTR} = \dot{E}_{7a} + \dot{E}_2 - \dot{E}_3 - \dot{E}_8$
Low-temperature regenerator	$W_{LTR} = (h_3 - h_2)m_3 = (h_{7b} - h_6)m_6$	$\dot{I}_{LTR} = \dot{E}_3 + \dot{E}_6 - \dot{E}_4 - \dot{E}_{7b}$
Main compressor	$W_{MC} = (h_6 - h_5)m_5$	$\dot{I}_{MC} = \dot{E}_5 - \dot{E}_6 - \dot{W}_{MC}$
Recompressor	$W_{RC} = (h_7 - h_4)m_7$	$\dot{I}_{RC} = \dot{E}_4 - \dot{E}_7 - \dot{W}_{RC}$
Cooler	$Q_{cooler} = (h_4 - h_5)m_5$	$\dot{I}_{cooler} = \dot{E}_{11} + \dot{E}_4 - \dot{E}_{12} - \dot{E}_5$

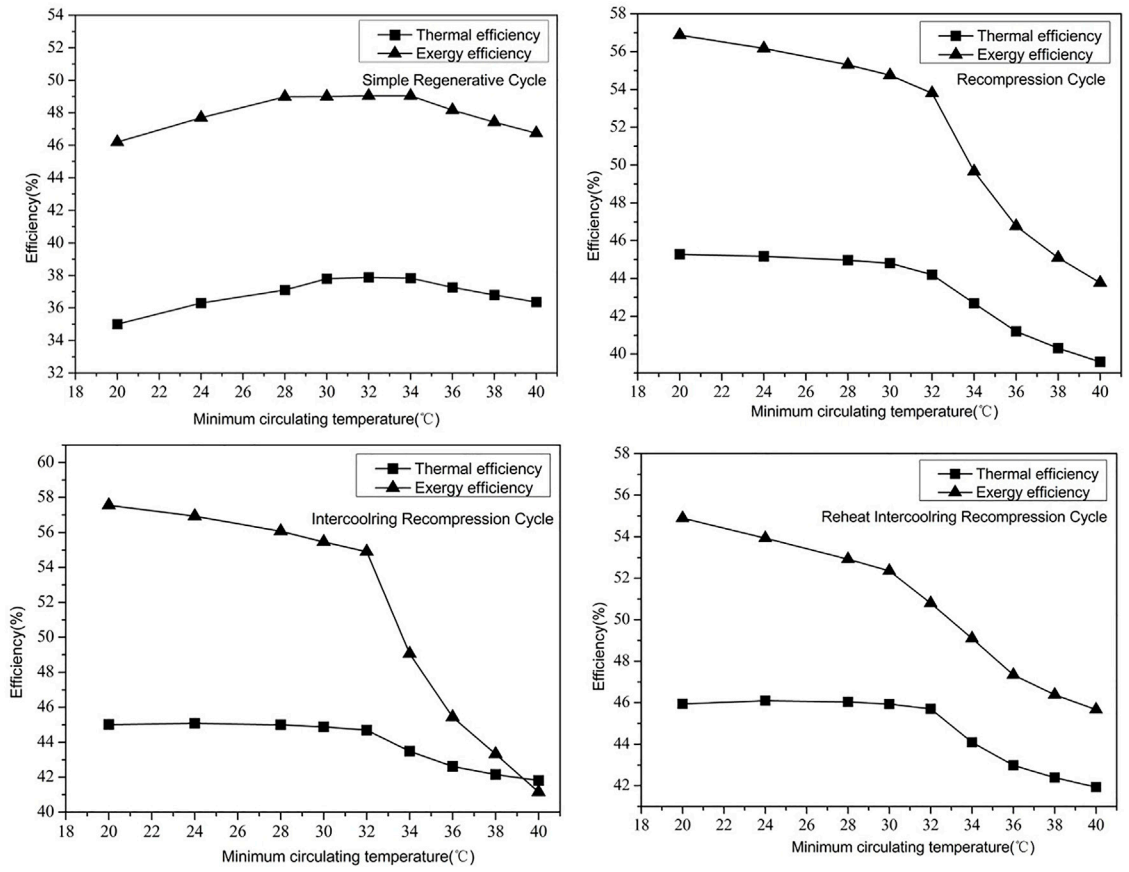

FIGURE 12
Efficiency of different configurations at different cycle minimum temperatures.

TABLE 4 Typical climate data.

Typical area	Pingliang, Gansu	Qingyang, Gansu	Baiyin, Qinghai	Haixi, Ningxia	Yinchuan, Ningxia	Tiemenguan, Xinjiang
Annual minimum temperature/°C	−24.3	−21.4	−22.1	−16.8	−30.6	−28
Annual maximum temperature/°C	36	36.4	39.1	23	39.3	35
Annual average temperature/°C	8.5	10	7.2	0	9	11.4

different cycle configurations between 32°C and 40°C are analyzed. Figure 12A–Dshows that the ambient temperature is very important to the temperature of the compressor inlet working medium. The higher the regional temperature is, the worse the cooling conditions are (Table 4). The higher the temperature of the compressor inlet working medium is, the worse the effect of the compressor inter-stage cooling is. The greater the power consumption of the compressor, the lower the circulating thermal efficiency and efficiency are. It can be seen from the analysis results that, considering the temperature environment in the western region, the optimal configuration for matching the small fluoride-cooled high-temperature reactor is the cycle without the intercooling structure, and the recommended recompression cycle configuration with high efficiency and compactness is the optimal configuration for matching the supercritical carbon dioxide cycle.

4 Conclusion

Based on the energy demand and utilization in western China, the S-CO_2 Brayton thermoelectric conversion system that matches the small fluoride-cooled high-temperature reactor is modeled in this paper. Moreover, the cycle efficiency of four typical configurations, such as a simple regenerative cycle, is compared using the methods of energy analysis and exergy analysis, and the thermoelectric conversion system matching the small fluoride-cooled high-temperature reactor is obtained. The following conclusions are then developed.

The introduction of the split flow recompression structure reduces the loss of the regenerator, thereby improving the circulation efficiency. The introduction of the intercooling structure reduces the power consumption of the compressor, thus improving the cycle thermal efficiency. However, the efficiency is greatly affected by the ambient temperature, especially in air-cooling conditions.

The S-CO_2 recompression Brayton cycle has a high compactness and high thermoelectric conversion efficiency. Compared with the indirect cooling cycle, the efficiency of the recompression cycle is less affected by the environmental temperature. Meanwhile, the recompression cycle is much simpler than the reheat cycle, which reduces the cost and control difficulty. Considering the climate factors and transportation conditions in the western region, the supercritical carbon dioxide recompression cycle has the highest adaptability to the small fluoride-cooled high-temperature reactor and is conducive to the realization of future mobile power supplies.

Data availability statement

The raw data supporting the conclusions of this article will be made available by the authors, without undue reservation.

Author contributions

XL: software, methodology, and writing—original draft; ML: methodology and analysis; LM: analysis; XL: analysis; WZ: methodology and supervision; and YH: conceptualization, funding acquisition, and supervision. All authors contributed to the article and approved the submitted version.

Funding

This work was supported by the National Key Research and Development program of China (2020YFB1902000).

Conflict of interest

The authors declare that the research was conducted in the absence of any commercial or financial relationships that could be construed as a potential conflict of interest.

Publisher's note

References

Bardet, P., Blandford, E., Fratoni, M., Niquille, A., Greenspan, E., and Peterson, P. F. (2008). Design, analysis and development of the modular PB-AHTR. Proceedings of the International Conference of Asian Political Parties. Anaheim, CA USA.

Clarno, K., Forsberg, C., Gehin, J., Slater, C., Carbajo, J., Williams, D., et al. (2007). Trade studies for the liquid-salt-cooled very high-temperature reactor: Fiscal year 2006 progress report. ORNL/TM- 140, 35 .

Deev, V., Kharitonov, V., Baisov, A., and Churkin, A. (2021). Hydraulic resistance of supercritical pressure water flowing in channels–A survey of literature. *Nucl. Eng. Des.* 380, 111313. doi:10.1016/j.nucengdes.2021.111313

Delpech, S. (2013). *Molten salts for nuclear applications* molten salts chemistry. Elsevier, 497–520. Amsterdam, Netherlands.

Forsberg, C., Hu, L.-W., Peterson, P. F., and Sridharan, K. (2013). *Fluoride-salt-cooled high-temperature reactors (FHRs) for base-load and peak electricity, grid stabilization, and process heat*. Cambridge, MIT-ANP-: Massachusetts Institute of Technology: Center for Advanced Energy Systems. *TR-147*.

Greene, S. R., Gehin, J. C., Holcomb, D. E., Carbajo, J. J., Ilas, D., Cisneros, A. T., et al. (2010). *Pre-conceptual design of a fluoride-salt-cooled small modular advanced high-temperature reactor (SmAHTR)*. Oak Ridge National Laboratory. *ORNL/TM-2010/199*.

Haubenreich, P., Engel, J., Prince, B., and Claiborne, H. (1964). *MSRE design and operations report. Part III. Nuclear analysis*. Retrieved from.

Haynes-International. (2002). *USA patent No.: i. H. N. alloy*.

Ilas, D., Holcomb, D. E., and Gehin, J. C. (2014). *SmAHTR-CTC neutronic design*. Retrieved from.

Ingersoll, D., Forsberg, C., Ott, L., Williams, D., Renier, J., Wilson, D., et al. (2004). Status of preconceptual Design of the advanced high-temperature reactor (AHTR): *United States*. Department of Energy.

Ingersoll, D., and Forsberg, C. (2006). Overview and status of the advanced high-temperature reactor," in *Proceedings of the international congress on advanced nuclear power plants*. Reno, Nevada. Paper presented at theJune 4–8.

Jiang, D., Zhang, D., Li, X., Wang, S., Wang, C., Qin, H., et al. (2022). Fluoride-salt-cooled high-temperature reactors: Review of historical milestones, research status, challenges, and outlook. *Renew. Sustain. Energy Rev.* 161, 112345. doi:10.1016/j.rser.2022.112345

Lima-Reinaldo, Y., and François, J.-L. (2023). Fuel loading pattern optimization of ALLEGRO fast reactor using genetic algorithms. *Ann. Nucl. Energy* 180, 109451. doi:10.1016/j.anucene.2022.109451

Liu, X., Zhang, H., Yin, D., Chai, X., and Xiu, Z. (2020). *Based on SCO2 Performance analysis of dual-mode nuclear thermal propulsion system of Brayton cycle* Nuclear Power Engineering. doi:10.13832/j.jnpe.2020.S2.0102

Massone, M., Abrate, N., Nallo, G. F., Valerio, D., Dulla, S., and Ravetto, P. (2022). Code-to-code SIMMER/FRENETIC comparison for the neutronic simulation of lead-cooled fast reactors. *Ann. Nucl. Energy* 174, 109124. doi:10.1016/j.anucene.2022.109124

Matozinhos, C. F., Carroll, A. D., Menezes, C., Vaghetto, R., and Hassan, Y. (2022). Experimental measurements of fluid flow in an 84-pin hexagonal rod bundle with spacer grid for a gas-cooled fast modular reactor. *Int. J. Heat Fluid Flow* 97, 109014. doi:10.1016/j.ijheatfluidflow.2022.109014

Pegallapati, A. S., Banoth, P., and Maddali, R. (2020). Dynamic model of supercritical CO2 based natural circulation loops with fixed charge. *Appl. Therm. Eng.* 169, 114906. doi:10.1016/j.applthermaleng.2020.114906

Qin Hao, W. C., and Zhang, D. (2018). Numerical study on tritium transport characteristics of fluoride cooled high-temperature reactor. *Sci. Technol. Atomic Energy* 52 (3), 6.

Ruan Jian, Z. Y., Li, M., Zhou, B., Zhu, G., and Xu, H. (2017). Study on the transient behavior of the air Brayton cycle system for fluoride salt cooled high-temperature reactor. *Nucl. Power Eng.* 38 (4), 22–26.

Scott, D., and Grindell, A. (1967). *Components and systems development for molten-salt breeder reactors*. Retrieved from.

Sehgal, B. R. (2012). Chapter 1 - light water reactor safety: A historical review," in *Nuclear safety in light water reactors*. Editor B. R. Sehgal (Boston: Academic Press), 1–88.

Tak, N.-i., Sik Lim, H., Hong, J., Yoon, J., Ha Park, B., and Eoh, J. (2022). Improvement of GAMMA+ code for system transient and thermo-fluid safety analysis of sodium-cooled fast reactors. *Nucl. Eng. Des.* 399, 112002. doi:10.1016/j.nucengdes.2022.112002

Yourong, L. (2020). Theory and Application of thermoeconomics *beijing China*. Science Press.

Glossary

Nomenclature

m mass flow

p pressure

T temperature

h enthalpy

s entropy

W work

Q thermal power

η_{th} thermoelectric conversion efficiency

η_{th} exergy efficiency

$\dot{E}$ calculated exergy

$\dot{I}_{total}$ total exergy loss

$\dot{I}_i$ exergy loss of each component

U velocity

U_s apparent velocity

χ porosity

P_v viscosity tensor

P_i inertia tensor

q heat flux;

HTR heat transfer convection coefficient

a interface density

Subscripts

in inlet

out outlet;

net net work

core reactor core

env environment

T turbine

C compressor

MC main compressor

RC recompressor

frontiers | Frontiers in Energy Research

TYPE Original Research
PUBLISHED 13 April 2023
DOI 10.3389/fenrg.2023.1175254

OPEN ACCESS

EDITED BY
Yugao Ma,
Nuclear Power Institute of China (NPIC), China

REVIEWED BY
Luteng Zhang,
Chongqing University, China
Jingang Liang,
Tsinghua University, China

*CORRESPONDENCE
Po Hu,
pohu@sjtu.edu.cn

SPECIALTY SECTION
This article was submitted to Nuclear Energy, a section of the journal Frontiers in Energy Research

RECEIVED 27 February 2023
ACCEPTED 29 March 2023
PUBLISHED 13 April 2023

CITATION
Ma K and Hu P (2023), Analysis of Th and U breeding in a heat pipe cooled traveling wave reactor.
Front. Energy Res. 11:1175254.
doi: 10.3389/fenrg.2023.1175254

Analysis of Th and U breeding in a heat pipe cooled traveling wave reactor

Kunfeng Ma and Po Hu*

School of Nuclear Science and Engineering, Shanghai Jiao Tong University, Shanghai, China

Introduction: Heat pipe cooled traveling wave reactor (HPTWR) is a newly proposed heat pipe reactor. The HPTWR can achieve the low enrichment of loaded fuel, small reactivity swing, and long-term continuous operation for the power supply of decentralized electricity markets. Due to the excellent breeding capability of the HPTWR, the Th fuel is also added into the breeding fuel region of the reactor to achieve the Th-U fuel cycle in this work.

Methods: The Monte Carlo code RMC is used to obtain the reactivity swing, propagation of axial power peak, burnup, and productions of bred fissile nuclides for the HPTWR with Th and U fuels.

Results and Discussion: The results indicate that the HPTWR with 13.6% ^{235}U enrichment of ignition fuel and 20% ^{235}U enrichment of breeding fuel can continuously operate for 18.1 years without refueling when the mass fraction of ^{232}Th in heavy metals of breeding fuel region is 33%. The propagation velocity of axial power peak and total burnup for the HPTWR with Th and U fuels is about 0.5525 cm/years and 24.72 GWd/THM during the 18.1 years operation respectively. The corresponding productions of bred ^{239}Pu, ^{241}Pu and ^{233}U are about 212.99 kg of ^{239}Pu, 0.19 kg of ^{241}Pu and 81.58 kg of ^{233}U at the end of cycle (EOC) respectively. The obtained results in this study demonstrate that the HPTWR can achieve the Th fuel breeding in the case of the low ^{235}U enrichment loading (≤ 20%).

KEYWORDS

heat pipe, traveling wave reactor, breeding, Monte Carlo code, thorium

1 Introduction

To achieve the sustainable development of nuclear energy, it is necessary to solve the problem of nuclear fuel shortage. As an alternative nuclear fuel resource, thorium is estimated to be 3 to 4 times as abundant in Earth's crust as uranium, with a lower mining cost (Wickleder, 2006). Sustainable supply of nuclear fuel can be achieved by the Th–U fuel cycle, which attracts more and more attention to ensure sustainable energy generation (IAEA-TECDOC-1319, 2002; IAEA-TECDOC-1450, 2005). So, up to now, the Th fuel cycle has been applied to many breeding reactors (Fomin et al., 2011; Zhang et al., 2011; Liem et al., 2016), which show great potential and advantages in realizing efficient utilization of thorium resources.

The micro heat pipe cooled reactor can be applied to the energy systems of decentralized electric markets (such as remote regions, island communities, and military bases) because it has a more compact structure, simple design, safety features, longer lifetime, and higher power output (Yan et al., 2020; Zohuri, 2020). The mass and volume of the designed heat pipe cooled reactor

usually are lighter and smaller, respectively, for better mobility (Wang et al., 2020). Thus, fuel enrichment of the heat pipe cooled reactor is usually much higher than that of the large PWR. The original concepts of heat pipe cooled reactors were pioneered at Los Alamos National Laboratory (LANL) for space applications during the 1960s (Niederauer and Lantz, 1970). In the 21st century, many space heat pipe cooled reactors have been proposed (Sun et al., 2018; Liu et al., 2020; McClure et al., 2020; Zhang et al., 2020; Ma et al., 2021a; Cui et al., 2021; Xiao et al., 2022). In addition, the continual development of heat pipes has led to many research institutes developing high-power heat pipe cooled reactors in decentralized electric markets. Recently, Alawneh et al. (2022) proposed a 3 MW yttrium hydride moderated heat pipe cooled microreactor with UO_2 fuel, which can be operated safely for more than 11 years. LANL (McClure et al., 2015) proposed a 5 MW_{th} heat pipe cooled mobile nuclear reactor (Megapower), which can continuously operate for more than 12 years in the case of 19.75% enriched UO_2 fuel. Guo et al. (2021) analyzed the neutronic characteristics of the Megapower. The results show that the influence of the cross-section library can be >750 pcm and the addition of the axial structure zone can lead to a >300 pcm reactivity increase. Zirconium hydride is introduced in the Meagpower to design a moderated megawatt-class HPR core (Feng et al., 2022). The results show that the moderation of the core can decrease the maximum neutron flux and is beneficial to reducing the thickness and weight of the shield. In addition, many studies (Ma et al., 2020a; Ma et al., 2021b; Ma et al., 2022a; Ma et al., 2022b) focused on thermal-hydraulic analyses of the Megapower. In order to improve the power output of the reactor, Westinghouse Electric Company (2017) proposed a 15 MWe eVinci reactor with UN fuel, which can operate for more than 10 years without refueling. Based on the eVinci-like heat pipe cooled reactor, Hernandez et al. (2019) found that the neutron leakage impact for the small-sized heat pipe reactor is the most limiting factor on the fuel cycle performance. To improve the lifetime of the reactor, the KAIST (Choi et al., 2020) proposed an 18 MW_{th} H-MMR with UN fuel, which provides continuous operation for about 56 years in the case of 12.1% ^{235}U enrichment. In addition, Ehud (2008) proposed a 125 MWth HP-ENHS core, which can achieve at least 20 years of core lifetime by loading the depleted uranium and TRUs.

The neutron breeding wave has been applied in the liquid metal-cooled reactor (Fomin et al., 2011), water-cooled reactor (Zhang et al., 2011), and gas-cooled reactor (Liem et al., 2016), and the breeding of thorium fuel has been achieved in those reactors due to their higher breeding capability. Compared to traditional larger reactors, the heat pipe reactor has a smaller volume of core, and thus, a higher enrichment of fuel is required. Thus, the application of the neutron traveling wave in the heat pipe reactor can reduce the enrichment of fuel and extend the lifetime of the core. The neutron breeding traveling wave has been applied in the heat pipe cooled reactor in our previous work (Ma and Hu, 2022). Figure 1 shows the burnup strategy of the heat pipe cooled traveling wave reactor (HPTWR) power source, which consists of a reactor, shield, and heat exchanger. In the HPTWR, the channels of cooling are inserted into the heat pipe. The fission heat of the reactor is transferred to the heat exchanger by the heat pipe. In the beginning cycle, the reactor usually consists of an ignition fuel region (burnup region) and a breeding fuel region. In the depletion process, the burnup region is transformed axially, in wave form, through the reactor length. The proposed heat pipe cooled traveling wave reactor (HPTWR) consists of an ignition fuel region with 14% ^{235}U enrichment and a breeding fuel region with 8.5% ^{235}U enrichment, which can continuously operate for 59 years with a 1.2% variation range of k_{eff} in the case of U–Pu fuel cycle. Due to its high breeding capability, the breeding of Th fuel is also explored in the HPTWR. However, the more neutrons will be consumed for the ^{232}Th breeding in the reactor relative to the ^{238}U breeding because it has a longer breeding chain of Th–U. Therefore, ^{232}Th is loaded into the breeding fuel region, and the ^{235}U enrichment of the breeding fuel must not be higher than 20% due to non-proliferation and safeguards. In addition, based on the HPTWR with only U fuel, a part of U fuel must be loaded into the breeding fuel to compensate for the reactivity and achieve the axial propagation of the neutron breeding wave. Section 2 will describe the reactor model. Section 3 will discuss the main burnup results of this model, including the reactivity, axial power distribution, burnup, and breeding capability of the Th–U fuel cycle. Finally, Section 4 will present the conclusion of this paper.

2 Model description

The HPTWR is a heat pipe cooled reactor with 65.5 MW_{th}, which has a total of 1,008 heat pipe fuel elements with ignition and breeding fuel regions (Ma and Hu, 2022). A central heat pipe in each fuel element is surrounded by a uranium nitride (UN) fuel pellet with cladding on both radial sides of the pellet (inner and outer claddings) (Sterbentz et al., 2018). Lithium heat pipes with a radius of 0.71 cm are used for the reactor cooling, where the ^{7}Li enrichment and Li density are 99.9% and 0.414 g/cm^3, respectively (Sun et al., 2018). Figure 2 shows the cross-sections of the fuel element (a) and heat pipe (b). Both the operation temperatures of UN fuel and Li heat pipe in the neutroncis calculation are set to 1,600 K. The Li heat pipe can be replaced during long-term continuous reactor operation due to its high-temperature life limit (Rosenfeld et al., 2004; Choi et al., 2020). The 1,008 fuel elements are surrounded by the axial and radius reflectors to keep the criticality of the reactor. A shutdown/safety rod is located at the center of the reactor. The schematic arrangement and main parameters of the HPTWR are shown in Figure 3 and Table 1, respectively.

All the computational results are performed by the Monte Carlo program RMC (Reactor Monte Carlo code), which is a 3D stochastic neutron transport simulation developed by Tsinghua University (Wang et al., 2015; Ma et al., 2019). The continuous-energy cross-section based on the ENDF/B-VII library is used for the different materials in this study (Chadwick et al., 2006). The calculations of fuel depletion in the HPTWR are based on using 15,000 particles per cycle, with 50 inactive cycles and 200 active cycles (computational uncertainty of less than 30 pcm). In order to simulate the neutron breeding wave of the reactor, the core is divided into 18 smaller zones axially, and each zone is 5 cm long in the axial direction (Shrestha and Rizwan-uddin, 2014; Huang et al., 2015).

3 Results and discussion

3.1 Core lifetime

Owing to the larger neutron capture cross-section (0.15 b at 0.3 MeV) of ^{232}Th compared with its fission cross-section (7.2×10^{-7} b at 0.3 MeV), some enriched ^{235}U fuel is required to maintain the

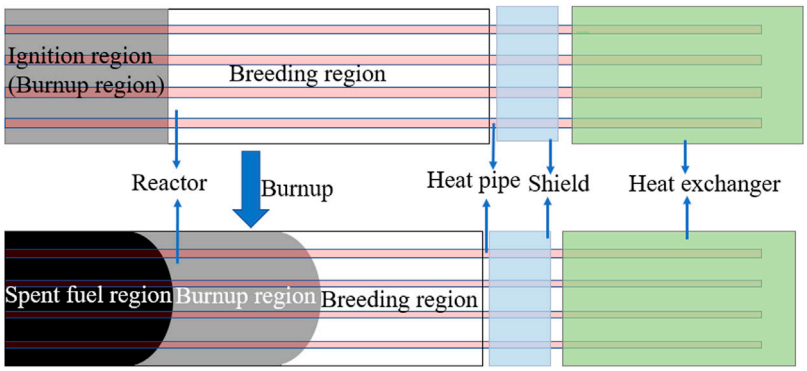

FIGURE 1
Burnup strategy of the heat pipe cooled traveling wave reactor.

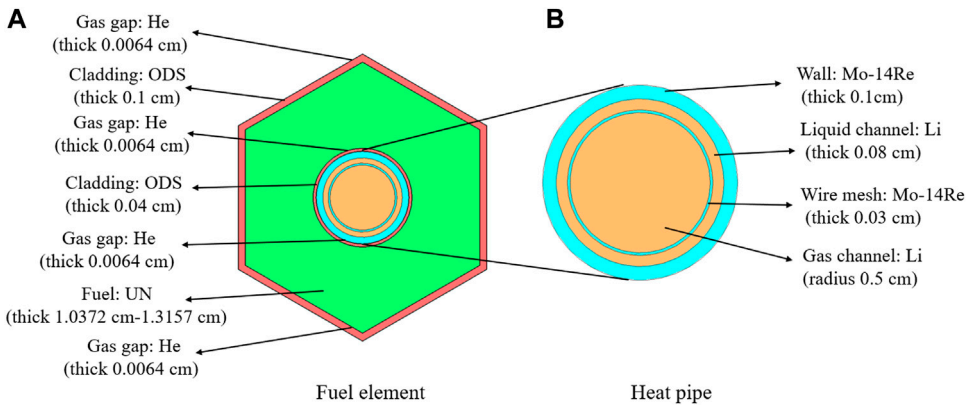

FIGURE 2
Cross-sections of the fuel element **(A)** and heat pipe **(B)**.

reactor criticality in the breeding fuel region during the reactor operation. In order to achieve the breeding of Th fuel, U fuel with 20% enrichment of ^{235}U is adopted in the breeding fuel region because of non-proliferation and safeguards. Therefore, both the enrichment of ^{235}U in the ignition fuel region and the mass fraction of Th fuel in the breeding fuel region require to be adjusted to achieve propagation of the neutron traveling wave. Table 2 shows three scenarios to study the effect of the loaded ^{232}Th amount on the reactor reactivity. Figure 4 shows the k_{eff} of the reactor for three scenarios during the operation. The three scenarios have the same initial k_{eff} (about 1.002). The k_{eff} for scenarios 2 and 3 gradually increase during the first 25 years because the bred fissile ^{239}Pu and ^{241}Pu in the reactor provide a higher positive reactivity. Then, the k_{eff} gradually decreases during the next operation time because a large number of nuclear fuel gets consumed in the reactor. The k_{eff} for scenario 1 gradually decreases during the whole operation because it is loaded into a large number of ^{232}Th in the breeding fuel region. It can be seen that the lifetime of scenarios 1, 2, and 3 are about 11.3 years, 18.1 years, and 18.8 years, respectively, and the corresponding k_{eff} ranges of variation (swing) remain about 0.2%, 0.35%, and 0.4%, respectively. The breeding chain of the Th–U fuel cycle is longer than that of the U–Pu fuel cycle, and the half-life of ^{233}Pa (about 27 days) produced by the neutron capture and the decay of ^{232}Th is longer than that of ^{239}U (about 23 min) produced by the neutron capture of ^{238}U (Jiang et al., 2012). Therefore, the consumed fission neutron amount for the ^{232}Th breeding is higher than that for the ^{238}U breeding, which decreases the lifetime of the HPTWR with only U fuel (about 59 years).

In order to investigate the propagation of neutron breeding wave, Figure 5 shows the spacial and temporal profiles of axial power density distributions for scenarios 1, 2, and 3. The power density peak for scenario 1 is always in the ignition fuel region during the whole operation because it has a shorter lifetime of the reactor. The power density peak for scenario 3 is in the breeding fuel region at the BOC because the ignition and breeding fuel regions have lower and higher ^{235}U enrichments, respectively. In addition, the axial power density peak is always in the 47.5 cm axial position during the whole operation, which has the higher radiation damage for the structural materials in the 47.5 cm axial position. In addition, higher Th fuel loading can achieve a higher ^{233}U production rate in the reactor,

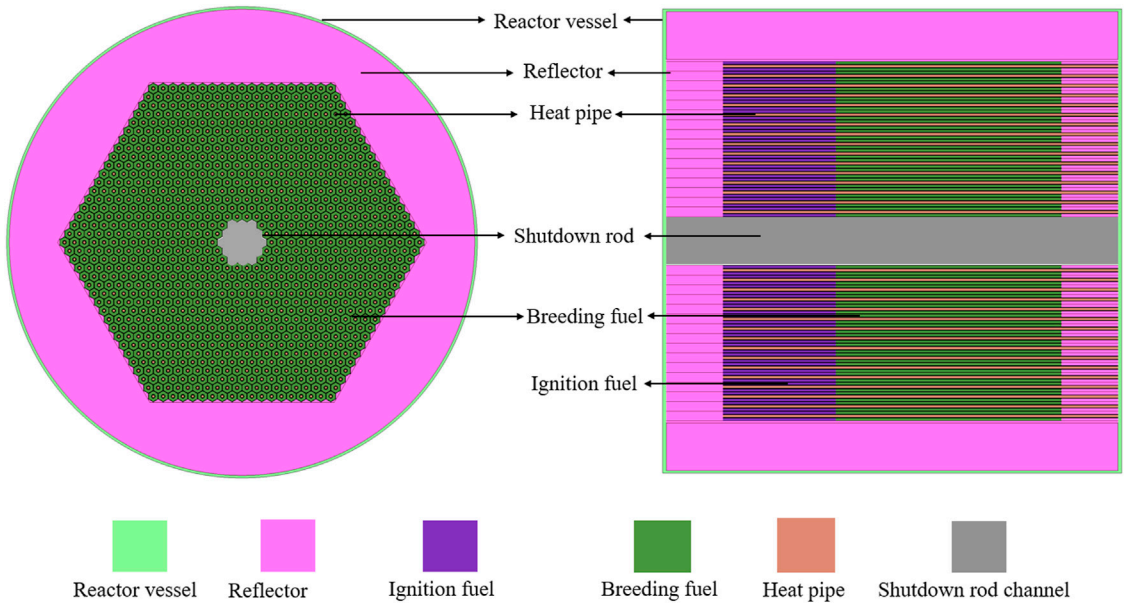

FIGURE 3
Cross-section view and longitudinal cross-section view of the HPTWR.

TABLE 1 Main parameters for the HPTWR with Th and U fuels.

Parameters	Value	Parameters	Value
Power (MW_{th})	65.5	Heat pipe wall material	Mo-14Re
Total number of heat pipes	1,008	Density of Mo-14Re (g/cm^3)	12
Fuel	UN	Wick material	Mo-14Re
^{15}N enrichment in fuel (%)	99.9	Heat pipe outer radius (cm)	0.71
Density of fuel (g/cm^3)	13.59	Heat pipe wall thickness (cm)	0.1
^{235}U enrichment of ignition fuel (wt%)	13.6	Liquid lithium channel thickness (cm)	0.08
^{235}U enrichment of breeding fuel (wt%)	20	Wick thickness (cm)	0.03
Mass fraction of ^{232}Th in heavy metals of breeding fuel region	33%	Gas lithium channel radius (cm)	0.5
Ignition region length (cm)	30	Reflector material	Al_2O_3
Breeding region length (cm)	60	Density of reflector (g/cm^3)	3.9
Mass of heavy metal (t)	10.90	Temperature of reflector (K)	900
Element to element pitch (cm)	3.8256	Side reflector outer radius (cm)	77.8
Fuel cladding material	Mo-14Re	Radial reflector thickness (cm)	18.71–28.30
Outer cladding thickness (cm)	0.1	Axial reflector length (cm)	15
Inner cladding thickness (cm)	0.04	Safety rod channel outer radius (cm)	8

which has been shown in our previous works (Ma et al., 2020b; Ma et al., 2020c). Therefore, scenario 2 is recommended for ^{232}Th fuel breeding in the HPTWR.

For scenario 2, the ignition fuel region has the higher power distribution relative to the breeding fuel region at the beginning of cycle (BOC) because the ignition fuel region has the higher ^{235}U fuel density. The total power density of ignition and breeding fuel regions are about 527.12 MW_{th}/m^3 and 855.2 MW_{th}/m^3 at the BOC, respectively. The power distributions in the ignition and breeding fuel regions continuously decrease and increase during the reactor operation, respectively, because many ^{235}U are consumed in the ignition fuel region, and many new fissile nuclides are bred in

TABLE 2 Th and U breeding scenarios under different conditions.

	Ignition fuel	Breeding fuel	
Scenario	^{235}U enrichment (%)	^{235}U enrichment (%)	^{232}Th mass fraction in heavy metals (%)
1	14.23	20	35
2	13.6	20	33
3	11.9	20	30

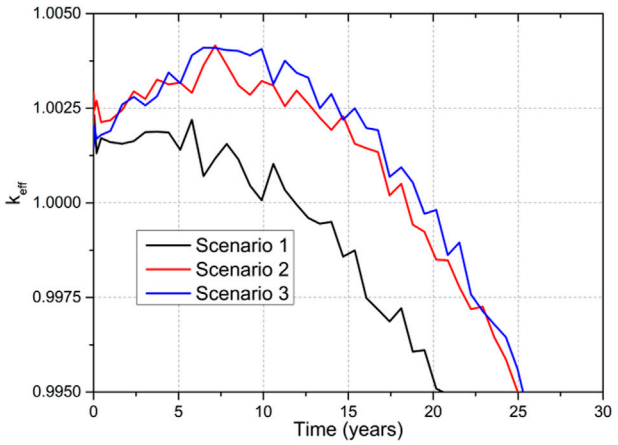

FIGURE 4
Evolutions of k_{eff} for scenarios 1, 2, and 3.

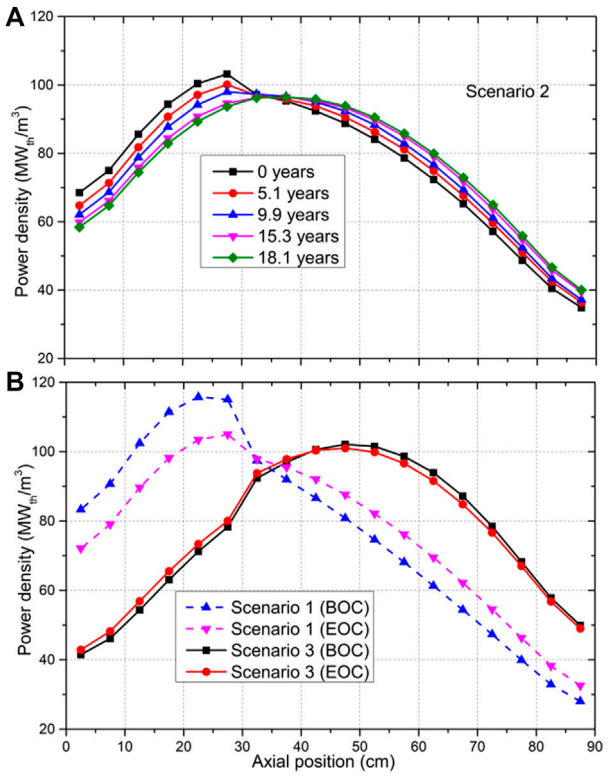

FIGURE 5
Axial power profiles of scenarios 2 **(A)**, 1 and 3 **(B)**.

the breeding fuel region. It can also be seen that the axial position of the power peak has been shifted to the breeding fuel region at the end of cycle (EOC). The axial power density peak is decreased from about 103.21 MW_{th}/m^3 at the BOC to about 96.45 MW_{th}/m^3 at the EOC due to the flattening of axial power distribution. The axial peak locations of power distribution at the BOC and EOC are about 27.5 and 37.5 cm in Figure 5, respectively. The resulting traveling wave speed is about 0.5525 cm/year, which is higher than that of the U–Pu fuel cycle (0.5085 cm/year) because the ^{235}U mass densities between the ignition fuel region and breeding fuel region have a relatively smaller difference.

The shift of the axial power peak has a significant influence on the local burnup of scenario 2 during the reactor operation. The core was divided into six subregions to analyze the local burnup of fuel, which is shown in Table 3. Figure 6 shows the burnups for subregions of scenario 2 during the 18.1 years of operation. Subregions 2 and 3 have higher burnup rates because they have higher local powers during operation. Subregions 5 and 6 have lower burnups of fuel because the axial power peak is only shifted to subregion 3 at the EOC. The burnups for subregions 1, 2, 3, 4, 5, and 6 are increased to about 38.07 GWd/THM, 50.50 GWd/THM, 51.49 GWd/THM, 46.76 GWd/THM, 36.83 GWd/THM, and 23.79 GWd/THM, respectively, at the EOC. In addition, the burnups per small zones at the EOC are shown in Figure 7. The maximum burnup of small zones in the ignition fuel region is about 52.84 GWd/THM at the EOC, whose corresponding axial position is 27.5 cm because it has the highest power value during the whole reactor operation. The maximum burnup of small zones in the breeding fuel region is about 52.09 GWd/THM at the EOC, whose corresponding axial position is 32.5 cm because its axial position is close to the ignition fuel region and has a relatively higher power value during the whole reactor operation. The minimum burnups of small zones in the ignition and breeding fuel regions are about 33.93 GWd/THM and 19.99 GWd/THM, respectively, whose axial positions are 2.5 and 87.5 cm, respectively, because their axial positions are close to the axial reflector and have relatively lower power value during the whole reactor operation. The total burnup for the HPTWR with Th and U fuels is about 24.72 GWd/THM at 18.1 years.

3.2 Breeding capability

The continuous operation time of the HPTWR with Th and U fuels is about 18.1 years, which is about 40.9 years less than that with only U fuel (about 59 years). Thus, the nuclear fuel consumption

TABLE 3 Designation of subregions for the HPTWR with Th and U fuels.

Zones	Subregion
1–3	1 (Ignition region)
3–6	2 (Ignition region)
6–9	3 (Breeding region)
9–12	4 (Breeding region)
13–15	5 (Breeding region)
15–18	6 (Breeding region)

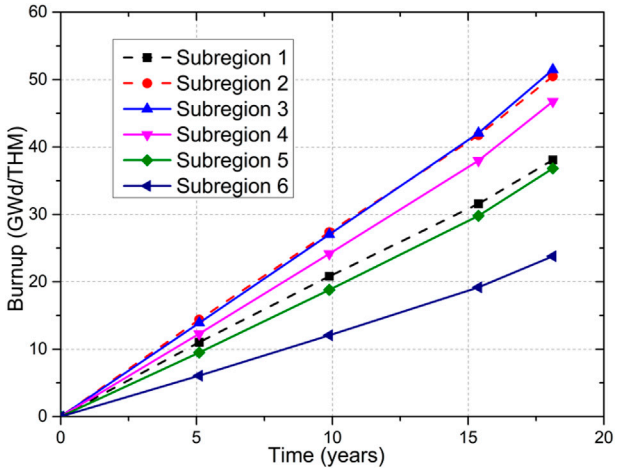

FIGURE 6
Local burnups for scenario 2 in the subregions.

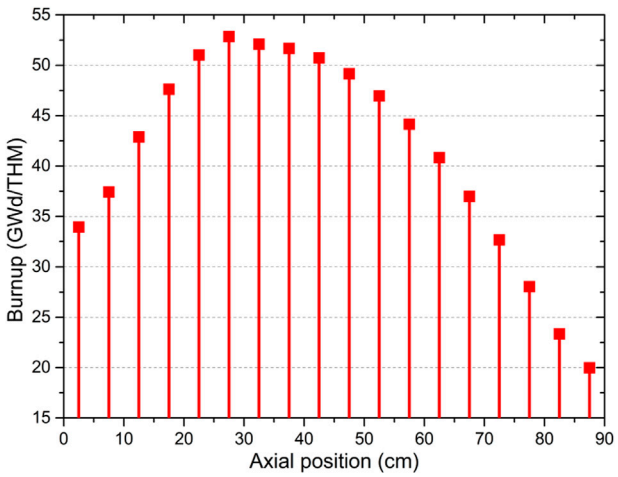

FIGURE 7
Burnup per small zones for scenario 2 at the EOC.

amount and Th–U breeding capability of the HPTWR will be evaluated during the reactor operation. In order to investigate the amount of consumed nuclear fuel, Figures 8–10 show the

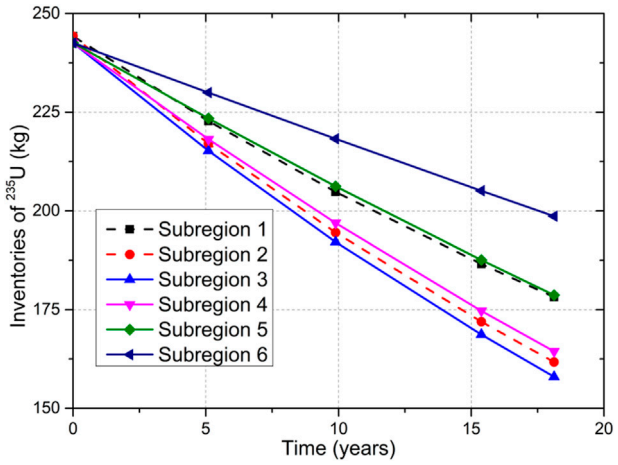

FIGURE 8
Time evolutions of ^{235}U inventories in the subregions.

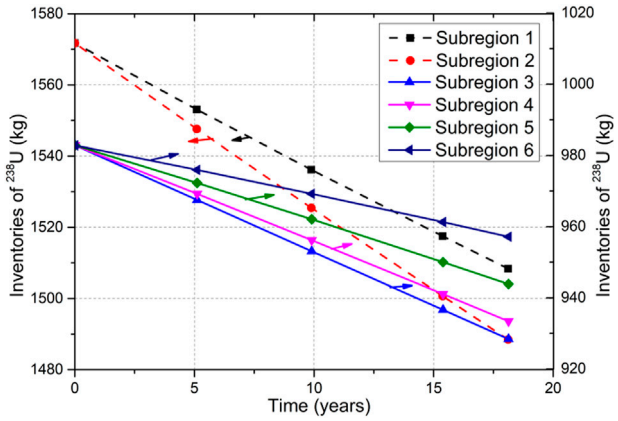

FIGURE 9
Time evolutions of ^{238}U inventories in the subregions.

inventories of ^{235}U, ^{238}U, and ^{232}Th in the six subregions of the HPTWR with Th and U fuels, respectively. Figures 11–13 show the inventories of the main bred fissile nuclides in the six subregions of the reactor.

The reactivity of the core mainly comes from the fission reaction of ^{235}U at the early operation of the core since the newly produced fissile nuclides are smaller in the reactor. The inventories of ^{235}U in subregions 2 and 3 have faster consumption rates in the ignition and breeding regions during the operation, respectively, because they have higher local powers. In addition, subregion 6 has the highest ^{235}U inventory at the EOC due to its lowest power during the whole operation. The inventories of ^{235}U in subregions 1 and 2 are decreased from 244.28 kg to about 178.18 and 161.72 kg, respectively, and the decreased amounts are about 66.1 and 82.56 kg, respectively. The inventories of ^{235}U in subregions 3, 4, 5, and 6 are about 157.98, 164.4, 178.68, and 198.63 kg, respectively, at the EOC, and the corresponding decreased amounts are about

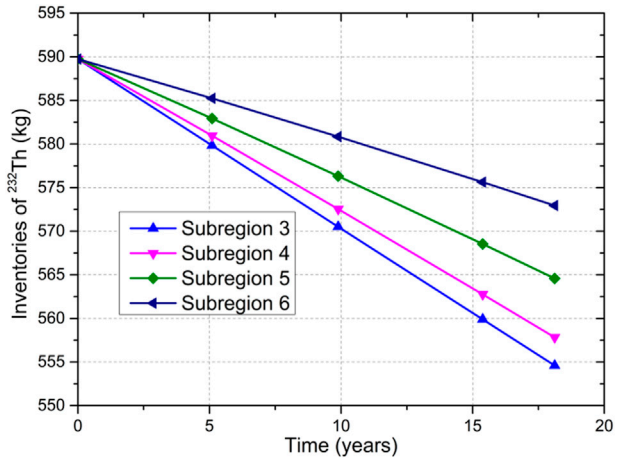

FIGURE 10
Time evolutions of ^{232}Th inventories in the subregions.

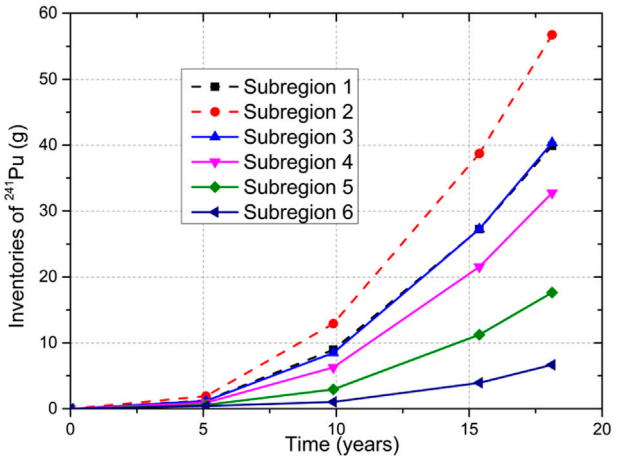

FIGURE 12
Time evolutions of ^{241}Pu inventories in the subregions.

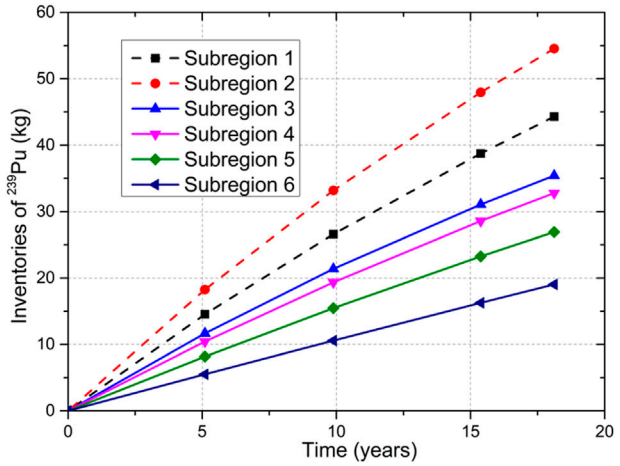

FIGURE 11
Time evolutions of ^{239}Pu inventories in the subregions.

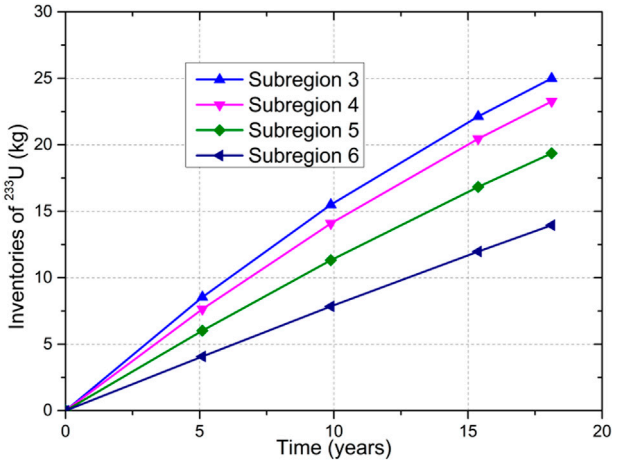

FIGURE 13
Time evolutions of ^{233}U inventories in the subregions.

84.61, 78.19, 63.91, and 43.96 kg, respectively (242.59 kg at BOC). The higher local power has a higher neutron flux in the HPTWR. Therefore, more ^{238}U and ^{232}Th will be transformed into ^{239}Pu and ^{233}U in the higher local power position of the HPTWR, respectively. The ^{238}U inventories in subregions 1 and 2 have higher consumption rates because they have higher initial ^{238}U loading inventories. The inventories of ^{238}U in subregions 1 and 2 are decreased from about 1571.74 kg at the BOC to about 1508.35 kg and 1488.48 kg at the EOC, respectively, and the corresponding decreased amounts are about 63.39 and 83.26 kg, respectively. The consumption rates of ^{238}U for subregions 3, 4, 5, and 6 sequentially decrease during operation due to their decrease of power distribution. The amounts of consumed ^{238}U in subregions 3, 4, 5, and 6 are about 54.38, 49.37, 38.93, 25.64, and 85.97 kg, respectively, during the 18.1 years of operation. Similar to ^{238}U inventories in the breeding fuel region, the amounts of consumed ^{232}Th in subregions 3, 4, 5, and 6 are about 35.14, 31.9, 25.17, and 16.80 kg, respectively, during the 18.1 years of operation (from about 589.74 kg to about 554.60, 557.84, 564.58, and 572.94 kg, respectively).

The breeding capability of the HPTWR can be evaluated by the productions of the newly produced fissile nuclides. The produced fissile nuclides in the U–Pu fuel cycle and Th–U fuel cycle consist of Pu isotopes (^{239}Pu and ^{241}Pu) and U isotope (^{233}U) in the traveling wave reactor, respectively. Figures 11–13 show the main inventories of produced fissile nuclides (^{239}Pu, ^{241}Pu, and ^{233}U). The bred ^{239}Pu inventories in subregions 1 and 2 are higher than those in subregions 3, 4, 5, and 6 because they have higher initial ^{238}U loading inventories. The productions of ^{239}Pu for subregions 3, 4, 5, and 6 sequentially decrease during the operation due to their decrease of power distribution. The productions of accumulated ^{239}Pu in subregions 1, 2, 3, 4, 5, and 6 are about 44.29, 54.54, 35.41, 32.78, 26.93, and 19.03 kg at

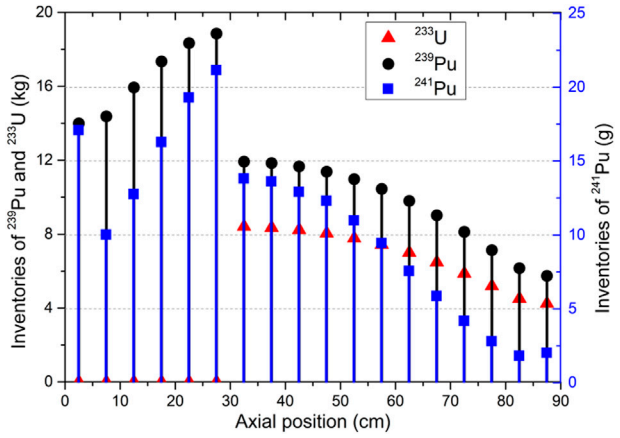

FIGURE 14
Productions of ^{239}Pu, ^{241}Pu, and ^{233}U per small zones at the EOC.

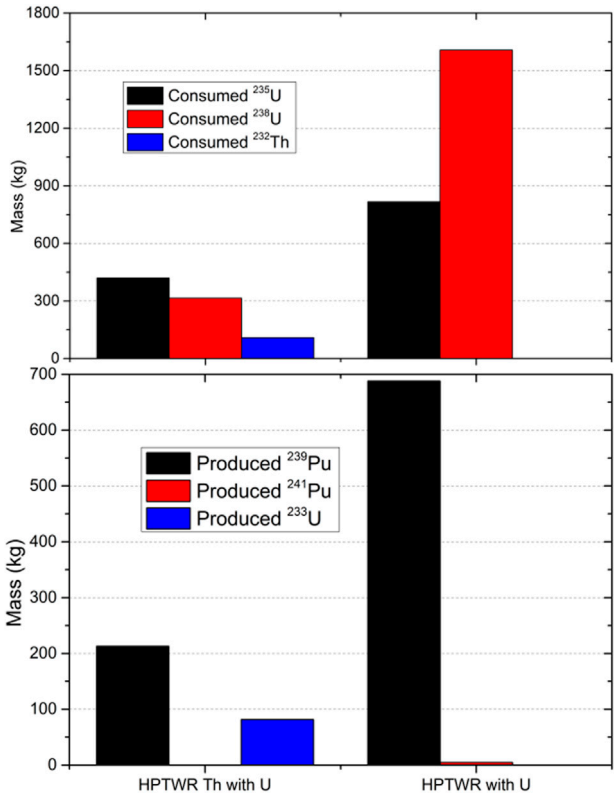

FIGURE 15
Consumed nuclear fuel amounts and produced fissile nuclide amounts in the HPTWR with two fuel loading scenarios.

the EOC, respectively. The corresponding productions of accumulated ^{241}Pu in subregions 1, 2, 3, 4, 5, and 6 are about 39.89, 56.75, 40.35, 32.75, 17.64, and 6.67 g at the EOC, respectively. The inventories of ^{241}Pu in the HPTWR are much less than those of ^{239}Pu because ^{241}Pu is produced by the sequence neutron captures of ^{239}Pu in the depletion process. The total productions of ^{239}Pu and ^{241}Pu in the HPTWR with U and Th fuels are about 212.99 kg and 194.05 g, respectively. In addition, the productions of accumulated ^{233}U in subregions 3, 4, 5, and 6 are about 25.00, 23.27, 19.36, and 13.94 kg at the EOC, respectively, and the total production of ^{233}U is about 81.58 kg.

The corresponding produced fissile nuclides per small zones of the HPTWR with U and Th fuels at the EOC are shown in Figure 14. The ^{239}Pu productions per small zones in the ignition fuel region are higher than those in the breeding fuel region at the EOC because it has a higher neutron flux, and more ^{238}U will be transformed into ^{239}Pu during the whole reactor operation. The highest ^{239}Pu production of small zones in the ignition fuel region is about 18.85 kg, whose axial position is 27.5 cm because it always has a relatively higher neutron flux during the reactor operation. Similar to ^{239}Pu production, the highest ^{241}Pu production of small zones in the ignition fuel region is about 21.15 g at the EOC in the axial position of 27.5 cm. It can be seen that the ^{241}Pu production of small zones in the 2.5 cm axial position (17.09 g) is also higher than that in the 7.5 cm axial position (10.04 g) because more thermal neutrons will be reflected from the reflector in the 2.5 cm axial position and ^{239}Pu has a much higher thermal neutron capture cross-section (about 271.0 b at 0.0253 MeV) relative to ^{238}U (about 8.4 b at 0.0253 MeV). The ^{233}U productions of small zones in the ignition fuel region are 0 kg because no ^{232}Th is loaded into the ignition fuel region. The productions of small zones for ^{239}Pu, ^{241}Pu, and ^{233}U in the breeding fuel region gradually decrease with the increase of axial position because of the decrease of power and neutron flux of small zones. The lowest productions of small zones for ^{239}Pu, ^{241}Pu, and ^{233}U are about 5.74 kg, 2.02 g, and 4.24 kg in the breeding fuel region, whose axial position is at 87.5 cm.

The lifetime of the HPTWR with Th and U fuels is decreased by about 40.9 years relative to the HPTWR with only U fuel. In order to investigate the amounts of consumed nuclear fuel and produced fissile nuclides, Figure 15 shows the consumed U and Th amounts and produced ^{239}Pu, ^{241}Pu, and ^{233}U amounts in the HPTWR with two fuel loading scenarios during the whole operation. The total amount of produced fissile Pu isotopes in the HPTWR with Th and U fuels during the 18.1 years of operation (about 212.99 kg of ^{239}Pu and 0.19 kg of ^{241}Pu) is 479.79 kg less than that in the HPTWR with only U fuel during the 59 years of operation (about 688.11 kg of ^{239}Pu and 4.86 kg of ^{241}Pu). However, the total amount of consumed U isotopes in the HPTWR with Th and U fuels (419.32 kg of ^{235}U and 314.98 kg of ^{238}U) during the 18.1 years of operation is about 1689.37 kg less than that in the HPTWR with only U fuel during the 59 years of operation (816.46 kg of ^{235}U and 1607.21 kg of ^{238}U). In addition, the HPTWR with Th and U fuels can consume about 109.01 kg of ^{232}Th and produce about 81.58 kg of ^{233}U.

4 Conclusion

In this work, the breeding capability and nuclear fuel consumption for a heat pipe cooled traveling wave reactor with Th and U fuels were investigated using the RMC code. The lifetime, propagation velocity of axial power peak, burnup, consumption of

nuclear fuel, and breeding capability of the reactor are discussed. The conclusion obtained can be summarized as follows:

1. The HPTWR loaded with 13.6% ^{235}U enrichment of ignition fuel and 20% ^{235}U enrichment of breeding fuel can continuously operate for about 18.1 years without refueling when the mass fraction of ^{232}Th in the heavy metals of the breeding fuel region is about 33%. The range of variation (swing) of k_{eff} remains within 0.35% during the 18.1 years of operation. The results indicate that the HPTWR can achieve utilization of Th fuel for better economy and sustainability.
2. The propagation velocity of the axial power peak and burnup for the HPTWR with Th and U fuels are about 0.5525 cm/years and 24.72 GWd/THM during the 18.1 years of operation, respectively. The burnup in the ignition fuel region is higher than that in the breeding fuel region at the EOC.
3. The HPTWR with Th and U fuels can produce about 212.99 kg of ^{239}Pu, 0.19 kg of ^{241}Pu, and 81.58 kg of ^{233}U at 18.1 years. The productions of ^{239}Pu and ^{241}Pu in the ignition fuel region are higher than those in the breeding fuel region at the EOC, and the productions of bred fissile nuclides (^{239}Pu, ^{241}Pu, and ^{233}U) in the breeding fuel region gradually decrease with the increase of the axial position of the reactor.

Data availability statement

The raw data supporting the conclusion of this article will be made available by the authors, without undue reservation.

Author contributions

PH and KM contributed to the conception and design of the study. KM performed the numerical analysis and wrote the first draft of the manuscript. All authors contributed to manuscript revision and read and approved the submitted version.

Funding

The authors thank the National Natural Science Foundation of China for their support through Grant No. 11205098.

Conflict of interest

The authors declare that the research was conducted in the absence of any commercial or financial relationships that could be construed as a potential conflict of interest.

Publisher's note

All claims expressed in this article are solely those of the authors and do not necessarily represent those of their affiliated organizations, or those of the publisher, the editors, and the reviewers. Any product that may be evaluated in this article, or claim that may be made by its manufacturer, is not guaranteed or endorsed by the publisher.

References

Alawneh, L. M., Vaghetto, R., Hassan, Y., and White, H. G. S. (2022). Conceptual design of a 3 MWth yttrium hydride moderated heat pipe cooled micro reactor. *Nucl. Eng. Des.* 397, 111931. doi:10.1016/j.nucengdes.2022.111931

Chadwick, M. B., Obložinský, P., Herman, M., Greene, N., McKnight, R., Smith, D., et al. (2006). ENDF/B-VII.0: Next generation evaluated nuclear data library for nuclear science and technology. *Nucl. data sheets* 107, 2931–3060. doi:10.1016/j.nds.2006.11.001

Choi, Y. J., Lee, S., Jang, S., Son, I. W., Kim, Y., et al. (2020). Conceptual design of reactor system for hybrid micro modular reactor (H-MMR) using potassium heat pipe. *Nucl. Eng. Des.* 370, 110886. doi:10.1016/j.nucengdes.2020.110886

Cui, D., Dai, Y., Cai, X., Fu, Y., Li, X., Zou, Y., et al. (2021). Preconceptual nuclear design of a 50 kWth heat pipe cooled micro molten salt reactor (micro-MSR). *Prog. Nucl. Energy* 134, 103670. doi:10.1016/j.pnucene.2021.103670

Ehud, G. (2008). Solid-core heat-pipe nuclear battery type reactor. Report No.: DE-FC07-05ID14706. Available at: https://www.osti.gov/servlets/purl/940911 (Accessed September 30, 2008).

Feng, K., Wu, Y., Hu, J., Jin, X., Gu, H., and Guo, H. (2022). Preliminary analysis of a zirconium hydride moderated megawatt heat pipe reactor. *Nucl. Eng. Des.* 388, 111622. doi:10.1016/j.nucengdes.2021.111622

Fomin, S. P., Fomin, O. S., Mel'nik, Yu.P., Pilipenko, V., and Shul'ga, N. (2011). Nuclear burning wave in fast reactor with mixed Th-U fuel. *Prog. Nucl. Energ* 53, 800–805. doi:10.1016/j.pnucene.2011.05.004

Guo, H., Feng, K., Gu, H., Yao, X., and Bo, L. (2021). Neutronic modeling of megawatt-class heat pipe reactors. *Ann. Nucl. Energy* 154, 108140. doi:10.1016/j.anucene.2021.108140

Hernandez, R., Todosow, M., and Brown, N. R. (2019). Micro heat pipe nuclear reactor concepts: Analysis of fuel cycle performance and environmental impacts. *Ann. Nucl. Energy* 126, 419–426. doi:10.1016/j.anucene.2018.11.050

Huang, J. F., Han, J. L., Cai, X. Z., Ma, Y., Li, X., Zou, C., et al. (2015). Breed-and-burn strategy in a fast reactor with optimized starter fuel. *Prog. Nucl. Energy* 85, 11–16. doi:10.1016/j.pnucene.2015.05.007

IAEA-TECDOC-1319 (2002). *Thorium fuel utilization: Options and trends*. Vienna, Austria: IAEA.

IAEA-TECDOC-1450 (2005). *Thorium fuel cycle-potential benefits and challenges*. Vienna, Austria: IAEA.

Jiang, M., Xu, H., and Dai, Z. (2012). Advanced fission energy program-TMSR nuclear energy system. *Bull. Chin. Acad. Sci.* 27 (3).

Liem, P. H., Tran, H. N., and Sekimoto, H. (2016). Burnup performance of small-sized long-life CANDLE high temperature gas-cooled reactors with U–Th–Pa fuel. *Ann. Nucl. Energy* 91, 36–47. doi:10.1016/j.anucene.2016.01.001

Liu, X., Zhang, R., Liang, L., Tang, S., Wang, C., Tian, W., et al. (2020). Core thermal-hydraulic evaluation of a heat pipe cooled nuclear reactor. *Ann. Nucl. Energy* 142, 107412. doi:10.1016/j.anucene.2020.107412

Ma, K., and Hu, P. (2022). Preliminary conceptual design and neutroncis analysis of a heat pipe cooled traveling wave reactor. *Ann. Nucl. Energy* 168, 108907. doi:10.1016/j.anucene.2021.108907

Ma, K., Yu, C., Cai, X., Zou, C. Y., and Chen, J. G. (2020). Transmutation of ^{129}I in a single-fluid double-zone thorium molten salt reactor. *Nucl. Sci. Tech.* 31 (1), 10. doi:10.1007/s41365-019-0720-1

Ma, K., Yu, C., Chen, J., and Cai, X. (2020). Transmutation of ^{135}Cs in a single-fluid double-zone thorium molten salt reactor. *Int. J. Energy Res.* 45, 12203–12214. doi:10.1002/er.6235

Ma, Y., Chen, E., Yu, H., Zhong, R., Deng, J., Chai, X., et al. (2020). Heat pipe failure accident analysis in megawatt heat pipe cooled reactor. *Ann. Nucl. Energy* 149, 107755. doi:10.1016/j.anucene.2020.107755

Ma, Y. G., Liu, S. C., Luo, Z., Huang, S., Li, K., Wang, K., et al. (2019). RMC/CTF multiphysics solutions to VERA core physics benchmark problem 9. *Ann. Nucl. Energy* 133, 837–852. doi:10.1016/j.anucene.2019.07.033

Ma, Y., Han, W., Xie, B., Yu, H., Liu, M., He, X., et al. (2021). Coupled neutronic, thermal-mechanical and heat pipe analysis of a heat pipe cooled reactor. *Nucl. Eng. Des.* 384, 111473. doi:10.1016/j.nucengdes.2021.111473

Ma, Y., Liu, J., Yu, H., Tian, C., Huang, S., Deng, J., et al. (2022). Coupled irradiation-thermal-mechanical analysis of the solid-state core in a heat pipe cooled reactor. *Nucl. Eng. Technol.* 54, 2094–2106. doi:10.1016/j.net.2022.01.002

Ma, Y., Tian, C., Yu, H., Zhong, R., Zhang, Z., Huang, S., et al. (2021). Transient heat pipe failure accident analysis of a megawatt heat pipe cooled reactor. *Prog. Nucl. Energy*. 140, 103904. doi:10.1016/j.pnucene.2021.103904

Ma, Y., Zhong, R., Yu, H., Huang, S., Tian, C., He, X., et al. (2022). Startup analyses of a megawatt heat pipe cooled reactor. *Prog. Nucl. Energy*. 153, 104405. doi:10.1016/j.pnucene.2022.104405

McClure, P., Poston, D., Rao, D. V., and Stowers, R. R. (2015). "Design of megawatt power level heat pipe reactors,". Report No.: LA-UR-15-28840. Available at: https://www.osti.gov/biblio/1226133 (Accessed November 12, 2015).

McClure, P. R., Poston, D. I., Gibson, M. A., Mason, L. S., and Robinson, R. C. (2020). Kilopower project: The KRUSTY fission power experiment and potential missions. *Nucl. Technol.* 206, 1–12. doi:10.1080/00295450.2020.1722554

Niederauer, G., and Lantz, E. (1970). "A split-core heat-pipe reactor for space power applications,". Report No.: NASA TM X-52918. Available at: https://www.osti.gov/biblio/7366283 (Accessed January 1, 1970).

Rosenfeld, J. H., Ernst, D. M., Lindemuth, J. E., and Sanzi, J. L. (2004). "An overview of long duration sodium heat pipe tests,". Report No.: NASA/TM-2004-212959. Available at: https://ntrs.nasa.gov/api/citations/20130013063/downloads/20130013063.pdf (Accessed February 8-12, 2004).

Shrestha, R., and Rizwan-uddin (2014). Modeling space-time evolution of flux in a traveling wave reactor. *Ann. Nucl. Energy* 70, 90–95. doi:10.1016/j.anucene.2014.03.011

Sterbentz, J. W., Werner, J. E., Hummel, A. J., Kennedy, J. C., O'Brien, R. C., Dion, A. M., et al. (2018). *Preliminary assessment of two alternative core design concepts for the special purpose reactor*. Idaho Falls, ID, USA: Idaho National Lab. INL.

Sun, H., Wang, C. L., Ma, P., Liu, X., Tian, W., Qiu, S., et al. (2018). Conceptual design and analysis of a multipurpose micro nuclear reactor power source. *Ann. Nucl. Energy* 121, 118–127. doi:10.1016/j.anucene.2018.07.025

Wang, D. Q., Yan, B. H., and Chen, J. Y. (2020). The opportunities and challenges of micro heat piped cooled reactor system with high efficiency energy conversion units. *Ann. Nucl. Energy* 149, 107808. doi:10.1016/j.anucene.2020.107808

Wang, K., Li, Z. G., She, D., Liang, J., Xu, Q., Qiu, Y., et al. (2015). RMC- A Monte Carlo code for reactor core analysis. *Ann. Nucl. Energy* 82, 121–129. doi:10.1016/j.anucene.2014.08.048

Westinghouse Electric Company, 2017. Westinghouse EVinci TM Reactor for Off-Grid Markets. Available at: https://www.researchgate.net/publication/329086061_Westinghouse_eVinciTM_Reactor_for_off-Grid_Markets. (Accessed July 2018).

Wickleder, M. S. (2006). "Thorium," in *The chemistry of the actinide and transactinide elements* (Berlin, Germany: Springer), 52.

Xiao, W., Li, X., Li, P., Zhang, T., and Liu, X. (2022). High-fidelity multi-physics coupling study on advanced heat pipe reactor. *Comput. Phys. Commun.* 270, 108152. doi:10.1016/j.cpc.2021.108152

Yan, B. H., Wang, C., and Li, L. G. (2020). The technology of micro heat pipe cooled reactor: A review. *Ann. Nucl. Energy* 135, 106948. doi:10.1016/j.anucene.2019.106948

Zhang, D. L., Chen, X. N., Gabrielli, F., Rineiski, A., Maschek, W., and Schulenberg, T. (2011). Numerical studies of nuclear traveling waves in a supercritical water cooled fast reactor. *Prog. Nucl. Energy* 53, 806–813. doi:10.1016/j.pnucene.2011.05.027

Zhang, W. W., Zhang, D. L., Wang, C. L., Tian, W., Qiu, S., and Su, G. (2020). Conceptual design and analysis of a megawatt power level heat pipe cooled space reactor power system. *Ann. Nucl. Energy* 144, 107576. doi:10.1016/j.anucene.2020.107576

Zohuri, B. (2020). *Nuclear micro reactors*. Cham Switzerland: Springer International Publishing. doi:10.1007/978-3-030-47225-2

frontiers | Frontiers in Energy Research

TYPE Original Research
PUBLISHED 20 April 2023
DOI 10.3389/fenrg.2023.1155294

OPEN ACCESS

EDITED BY
Yugao Ma,
Nuclear Power Institute of China (NPIC), China

REVIEWED BY
Shanfang Huang,
Tsinghua University, China
Minyun Liu,
Nuclear Power Institute of China (NPIC), China
Jiankai Yu,
Massachusetts Institute of Technology, United States

*CORRESPONDENCE
Yidan Yuan,
cheneh@cnpe.cc

RECEIVED 31 January 2023
ACCEPTED 03 April 2023
PUBLISHED 20 April 2023

CITATION
Chen E, Zhang H and Yuan Y (2023), POD-based reduced-order modeling study for thermal analysis of gas-cooled microreactor core.
Front. Energy Res. 11:1155294.
doi: 10.3389/fenrg.2023.1155294

POD-based reduced-order modeling study for thermal analysis of gas-cooled microreactor core

Erhui Chen, Huimin Zhang and Yidan Yuan*

China Nuclear Power Engineering Co., Ltd (CNPE), Beijing, China

Small modular reactors require multi-physics coupling calculations to balance economy and stability, due to their compact structures. Traditional tools used for light water reactors are not effective in addressing the several modeling challenges posed by these calculations. The lumped parameter method is commonly used in the thermal analysis for its high computational speed, but it lacks accuracy due to the thermal model is one-dimensional. While computational fluid dynamics software (CFD) can provide high-precision and high-resolution thermal analysis, its low calculation efficiency making it challenging to be coupled with other programs. Proper Orthogonal Decomposition (POD) is one of the Reduced Order Model (ROM) methods employed in this study to reduce the dimensionality of sample data and to improve the thermal modelling of gas-cooled microreactors. In this work, a non-inclusive POD with neural network method is proposed and verified using a transient heat conduction model for a two-dimensional plate. The method is then applied to build a reduced order model of the gas-cooled micro-reactor core for rapid thermal analysis. The results show that the root mean square error of the reactor core temperature is less than 1.02% and the absolute error is less than 8.2°C while the computational cost is reduced by several orders of magnitude, shortening the calculation time from 1.5-hour to real-time display. These findings proved the feasibility of using POD and neural network in the development of ROMs for gas-cooled microreactor, providing a novel approach for achieving precise thermal calculation with minimized computational costs.

KEYWORDS

proper orthogonal decomposition, reduced-order model, neural network, gas-cooled microreactor, thermal analysis

1 Introduction

Advanced small modular reactors (SMRs) have attracted extensive research due to their diverse applications, which were initially motivated by military needs and have been gradually expanded to many civilian fields. Due to their compact structures, SMRs require multi-physics coupling calculations to balance economy and stability during reactor designing, which presents several modeling challenges that cannot be addressed effectively by the traditional tools used for light-water reactors. Taking the integrated design of a gas-cooled microreactor as the example, the lumped-parameter method, which is based on one-dimensional models of physical transport phenomena, is typically used in the thermal-hydraulic analysis. Such a method has high computational efficiency but at the cost of accuracy and resolution. The computational fluid dynamics (CFD) software, on the other hand, is widely used to accurately simulate reactor cores

and handle complex geometries, but the enormous computational cost makes it difficult to be coupled with other programs. Therefore, this work focuses on developing a highly accurate thermal model with largely reduced computational cost to serve as a better alternative to the coarse thermal model currently used in integrated simulation.

Reduced-order modeling (ROM) is a powerful modeling technique that can significantly reduce the computational cost while maintaining accuracy. It works by creating a low-dimensional subspace, which is based on the dominant features extracted from the sample data, to approximate the full-state system. This leads to faster calculations from the reduced number of degrees of freedom in the subspace.

An efficient method for creating ROM is the proper orthogonal decomposition (POD)—also known as the Karhunen–Loève expansion, principal component analysis, or empirical orthogonal function (Lorenz, 1956). The POD was first proposed by Pearson (1901) for extracting the main components of big data. Sirovich (1987) used "snapshot" to reduce the dimensionality of the eigenvalue problem, making the POD more efficient and practical for use in various engineering problems, such as in signal analysis, pattern recognition, and fluid dynamics (Liang et al., 2002).

The POD-based ROM can be categorized into two methods: the inclusive and non-inclusive on the basis of whether they require the governing equation of the original system. ROM based on the POD and Galerkin projection is a representative intrusive method which projects the equation onto the subspace basis vector generated by the POD (Hazenberg et al., 2015; Zhang and Xiang, 2015; Gao et al., 2016; Stabile et al., 2017; German and Ragusa, 2019; Star et al., 2019; Sun et al., 2020). By contrast, the non-intrusive ROM is constructed by combining the POD with interpolation methods such as the RBF (Xiao et al., 2015b), Kriging (Chen et al., 2015), and Smolyak (Xiao et al., 2015a). With the rapid development of deep learning, the construction of non-intrusive reduced-order models using neural networks has become a research frontier in recent years. Although the intrusive method offers greater interpretability, its application is limited due to its requirement for accessing the full state equation, as well as instability and non-linear efficiency issues (Amsallem and Farhat, 2012; Washabaugh et al., 2012; Yu et al., 2018). Given the complexity of microreactors, the non-inclusive method based on neural networks is selected to build a reduced-order model in this study. Next is a brief overview of the research status of POD with neural networks.

Wang et al. (2018) applied the POD and long short-term memory (LSTM) to build a reduced-order model for ocean circulation and flow around a cylinder. The results showed that ROM provides high accuracy in numerical prediction, and the CPU time is greatly reduced. Similarly, Ooi et al. (2021) and Wu et al. (2020) used the convolutional neural network to study the flow around a cylinder and compared it with other machine learning methods, such as the regression tree, k-nearest neighbor, etc., which also proved the computational advantages. Unlike the inclusive method, the non-inclusive method can utilize the solution domain as an input parameter as well. For instance, Hasegawa et al. (2020) employed the POD and machine learning to study the unsteady flow around bluff bodies of variable cross sections and proved that these could predict the flow patterns of unknown shapes. To address the challenge of physical constraints in black box models, Swischuk et al. (2019) proposed combining a "particular solution" to modify the results obtained from machine learning to provide a new idea to improve the interpretability of the surrogate model.

In the nuclear industry, the application of ROM based on the POD can be divided into three categories: design and calculation, control optimization, and sensitivity analysis. In the design and calculation field, Sartori et al. (2016) used ROM to perform physical and thermal coupling calculations for a single channel of lead-cooled fast reactor. Star et al. (2021) coupled the RELAP code and ROM to conduct three-dimensional thermal coupling calculations for open and closed pipelines. Kang et al. (2022) used non-inclusive ROM to predict the flow field between reactor rod bundles. In control optimization, Lorenzi et al. (2017) utilized ROM to model the coolant pool of the lead-cooled fast reactor to demonstrate the application of ROM in system-level simulation code. Sensitivity analysis requires many repeated calculations that make it a suitable application for the low-cost calculation capabilities of ROM. For example, Alsayyari et al. (2020) used ROM to perform sensitivity analysis on a simplified molten salt reactor reference model to successfully obtain the relationship between various neutronics and thermal parameters of the system.

In the past three decades, the application of ROM in the nuclear industry has continued to improve with advancements in the model reduction theory and research on the applicability of the POD in heat transfer, Navier–Stokes equation, and neutron transport equations. However, most of the reduced-order models are still at the verification stage to demonstrate their great potential but with limited practical use, especially in the reactor core field. In light of this, this work aims to explore ROM for the gas-cooled microreactor core which balances accuracy and computational efficiency. This new approach could provide valuable insights and serve as the basis for reactor coupling calculations, simulation control, and intelligent operation and maintenance of nuclear power plants.

This article first briefly introduces the research background and previous progress. Section 2 covers the theory of ROM, which includes the calculation of basis and coefficients when using POD and neural network. The following two parts verify and apply ROM using a two-dimensional (2D) plate transient heat conduction problem and thermal analysis of a gas-cooled microreactor. The final part is the conclusion about this work.

2 Method of ROM based on POD

POD aims to find a set of optimal orthogonal basis vectors $\varphi_1(x), \varphi_2(x), \ldots, \varphi_k(x)$ (where $\varphi_i(x)$ is a column vector) in the least squares sense, such that the value to be solved of the original system at any time on any node can be expressed as a linear combination of this basis set (Chatterjee, 2000). For instance, considering the node temperature at the domain x, the representation is given as

$$\boldsymbol{T}(\boldsymbol{x},\boldsymbol{t}) = \boldsymbol{\alpha_1}(\boldsymbol{t})\boldsymbol{\varphi_1}(\boldsymbol{x}) + \boldsymbol{\alpha_2}(\boldsymbol{t})\boldsymbol{\varphi_2}(\boldsymbol{x}) + \cdots + \boldsymbol{\alpha_k}(\boldsymbol{t})\boldsymbol{\varphi_k}(\boldsymbol{x}), \quad (1)$$

where $\varphi_i(x)$ is the POD basis and $\alpha_i(t), i = 1, 2, \cdots, k$ are the corresponding coefficients.

In fact, the representation of Eq. 1 is not unique, as the function $\varphi_i(x)$ can be represented using different sets of basis functions, such as Legendre polynomials, Chebyshev polynomials, Fourier series, and so on. The sequence of time-functions $\alpha_i(t)$ is different for each kind of basis. For the POD, the basis vectors are especially orthogonal, which means this set of basis satisfies

$$\boldsymbol{\varphi}_{\boldsymbol{k_1}}(\boldsymbol{x}) \cdot \boldsymbol{\varphi}_{\boldsymbol{k_2}}(\boldsymbol{x}) = \begin{cases} \mathbf{1} & \text{if } \boldsymbol{k_1} = \boldsymbol{k_2} \\ \mathbf{0} & \end{cases}, \quad (2)$$

$$\boldsymbol{a_k}(\boldsymbol{t}) = \boldsymbol{T}(\boldsymbol{x},\boldsymbol{t}) \cdot \boldsymbol{\varphi_k}(\boldsymbol{x}). \tag{3}$$

Another characteristic of POD basis is that it consists of a set of ordered column vectors, which makes the approximate accuracy increase as more bases are selected.

Consider a physical field of interest q that is controlled by a mapping function: q: $\mathcal{X} \times \mathcal{T} \times \mathcal{P} \rightarrow \mathbb{R}$, where $\mathcal{X}$ represents the spatial domain, $\mathcal{T}$ represents the time domain, and $\mathcal{P}$ is the input parameter domain. Thus, field q is dependent on the input parameter and varies with time and space conditions. The mapping relationship is generally determined by the physical laws and governing equations, which are often in the form of complicated partial differential equations. These governing equations are discretized into a series of separated points to approximate the solution fields by most traditional numerical solutions that result in large degrees of freedom, especially for three-dimensional and time-varying systems. This leads to high computational requirements. By reducing the dimensionality of the spatial domain, the POD can effectively reduce the computational cost. Next is a brief introduction of the calculation of POD basis $\varphi_i(x)$ and coefficients $\alpha_i(t)$.

2.1 Calculation of POD basis

The calculation of POD basis relies on a method known as "snapshot," proposed by Sirovich (1987), which is only dependent on sample data. Consider a distribution $q(\cdot, t; \mathbf{p})$ of field q at time $t \in \mathcal{T}$ and parameter $\mathbf{p} \in \mathcal{P}$. $\mathbf{q}(t; \mathbf{p}) \in \mathbb{R}^{n_x}$, also known as "snapshot," is a finite dimensional approximation of $q(\cdot, t; \mathbf{p})$ with n_x as the dimension of discretization of the spatial domain. Snapshot is viewed as the true value that can be obtained from experiments or numerical models. A set of snapshots is collected at different times $t_1, \cdots, t_{n_t} \in \mathcal{T}$ and input parameters $\mathbf{p}_1, \cdots, \mathbf{p}_{n_p} \in \mathcal{P}$ to make up a matrix $S \in \mathbb{R}^{n_x \times n_s}$, which contains the snapshots as its columns, where $n_s = n_t n_p$ (Swischuk et al., 2019). Thus, each row of the matrix represents the value of each discrete point at different times or input parameters, while each column corresponds to the field distribution of all discrete points under the same condition, that is, the snapshot.

According to the theory of POD, the matrix can be written as

$$\boldsymbol{S} = \boldsymbol{U}\boldsymbol{\Sigma}\boldsymbol{V}^{\mathbf{T}}, \tag{4}$$

where

$$\boldsymbol{U}\boldsymbol{U}^{T} = \boldsymbol{I} \quad \boldsymbol{V}\boldsymbol{V}^{T} = \boldsymbol{I} \quad \boldsymbol{\Sigma} = \boldsymbol{diag}(\boldsymbol{\sigma_1}, \boldsymbol{\sigma_2}, \cdots, \boldsymbol{\sigma_p}), \tag{5}$$

with $\sigma_1 \geq \sigma \geq \cdots \geq \sigma_p \geq 0$ and $p = \min(n_x, n_s)$. U and V are the left and right singular vectors of S, respectively, and σ_i represents the singular values of S. The dimension of S will be reduced by selecting partial columns of U as basis vectors to form a new subspace to approximate S. The selection is determined by the value of the corresponding σ, which represents the contribution degree of the vector. Since the values of σ_i are arranged in the descending order, the first few vectors already contain the main features of the sample data. For example, by extracting the first k columns of U and the first rows of V, and retaining the corresponding σ, we can obtain an optimal approximation of S in the sense of square error, which is expressed as

$$\boldsymbol{S} \approx \boldsymbol{S_k} = \boldsymbol{U_k}\left(\boldsymbol{\Sigma}\boldsymbol{V}^{\mathbf{T}}\right)_{\boldsymbol{k}} \tag{6}$$

where $U_k = (\varphi_1, \varphi_2, \cdots, \varphi_k) \in R^{n_x \times k}$, which is called the POD basis. A typical approach (Holmes et al., 2012; JinXiu et al., 1998) to determine k is

$$\frac{\sum_{i=1}^{k} \boldsymbol{\sigma_i}}{\sum_{j=1}^{r} \boldsymbol{\sigma_j}} > \mathbf{99.9\%}, \tag{7}$$

where r is the rank of matrix S. The value is also called energy of the eigenvalue. Eq. 6 can also be written as

$$\boldsymbol{A} = \left(\boldsymbol{\Sigma}\boldsymbol{V}^{\mathbf{T}}\right)_{\boldsymbol{k}} = \boldsymbol{U}_{\boldsymbol{k}}^{\mathbf{T}}\boldsymbol{S}. \tag{8}$$

Matrix $A \in \mathbb{R}^{k \times n}$ is the projection coefficient of the sample data on the POD basis, then the original problem is transferred from solving $q(x, t, p)$ to $A(t, p)$. Since U_k is known, one can obtain the discretization results of S at the spatial domain if A with different times and input parameters is computed. The dimensionality or degree of freedom of $A(t, \boldsymbol{p})$ is k, which is much smaller than that of $q(x, t, \boldsymbol{p})$ (which is n_x), making it possible to realize rapid computation.

When the input conditions remain invariant, the field $\{\mathbf{q}(t_i) | i = 1, \ldots, n_t\}$ becomes a typical transient problem, which is only dependent on time. U_k represents the spatial mode of the sample while A contains time variations. The original system can be predicted by extrapolating the column vector of A. On the contrary, the problem becomes stable if the time variable remains invariant, which allows for quick calculation of results for different inputs.

2.2 Calculation of POD coefficients

The non-inclusive method is used to establish a surrogate model that maps input parameters, such as time, pressure, or power, to the coefficients of the POD basis through fitting, interpolation, or other methods, to avoid the need to access and discretize of the governing equation. In fact, Eq. 8 is used to project S onto the basis U_k, which gives a set of coefficients for the sample conditions. Thus, a map from the input to coefficients already exists. The coefficients for different parameters can be obtained by fitting this relationship, which is the main idea behind all kinds of non-inclusive methods, such as neural networks.

The artificial neural network, also called neural network in short, is a mathematical model in machine learning that imitates the structure of biological neural networks and can be used for function approximation or estimation. Neurons, which are the computing nodes in a neural network, are interconnected to form a network structure that enables non-linear, parallel, or local computation. A typical neural network comprises three parts:

1 Architecture. It refers to the variables and their topological relationships, which include excitation values and weights of neurons. Figure 1 shows a typical architecture of a neural network.
2 Activation rule. It refers to the functional relationship between the input and output of hidden and output layer nodes, which provides the non-linear ability of the neural network.
3 Learning rules. The learning process involves changing the topological relationship and weight values to reduce the output

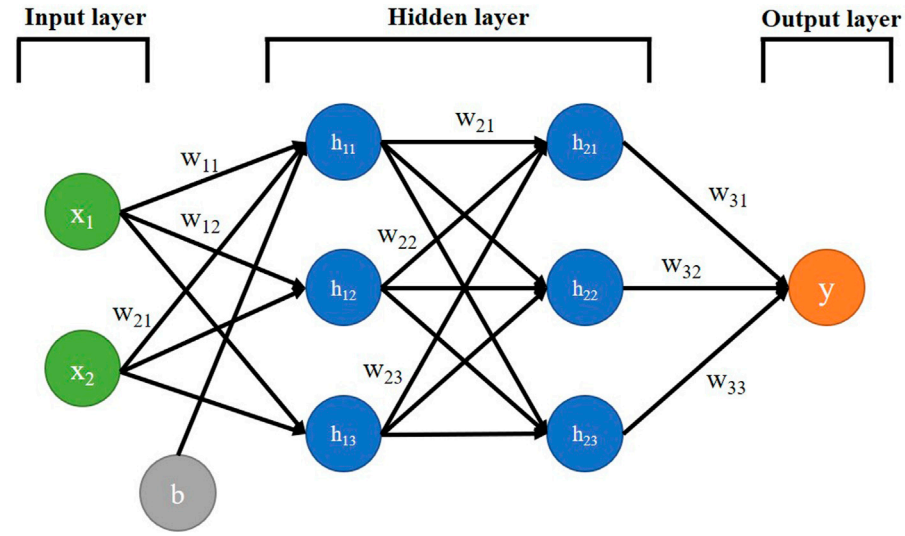

FIGURE 1
Neural network architecture.

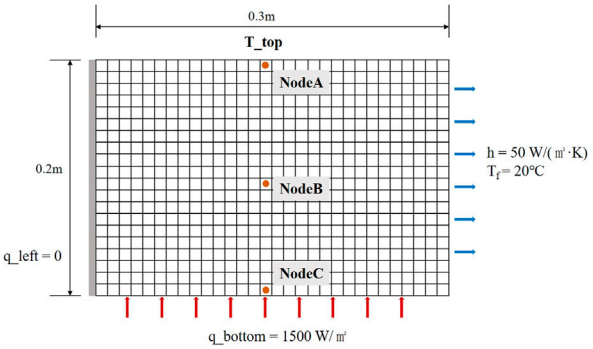

FIGURE 2
2D plate geometric diagram.

error within an acceptable range. The rule for modifying the variables is called the learning rule or learning algorithm. The error back propagation (BP) algorithm proposed by Rumelhart et al. (1986) has had the most extensive influence on learning rules and is also used in this work.

The architecture depicted in Figure 1 represents a fully connected feedforward neural network, where every node in each of the layers of the network is connected to all the nodes in the next layer (for simplicity, bias b is only connected to the first neuron of the first hidden layer). Information is transmitted from left to right in a feedforward network, with the input of each layer being the output of the previous layer. The green nodes make up the input layer, where the number of nodes equals the number of input parameters in the sample and is referred to as the input vector. The blue nodes represent the hidden layers, whose number of layers and nodes varies depending on the specific problem and is related to the non-linearity of the neural network. Typically, the number of hidden nodes is greater than the number of input nodes, such as 1.2 to 1.5 times the number of input nodes. Finally, the orange nodes form the output layer, where the number of nodes equals the number of output parameters in the model and is referred to as the output vector.

The data set is typically divided into three parts: the training set, validation set, and test set. The training set is used to train the algorithm, while the validation set is used to calculate the network's accuracy or error in order to optimize the model parameters. The final model is then evaluated on the test set to measure its error under real conditions.

In this work, a simple neural network and the long short-term memory (LSTM) network architecture are used to model stable and transient fields, respectively. The LSTM is a type of recurrent neural network that is specifically designed to prevent the output of the network for a given input from either decaying or exploding as it cycles through feedback loops (Yu et al., 2019). This architecture is applicable to a number of sequence learning problems, such as language modeling and translation, speech recognition, and timing problems. The underlying algorithms for these types of neural networks have not been reiterated in this study for they have already been developed in many open-source frameworks.

In summary, the calculation process consists of the following steps:

1 Collecting sample data through observations, numerical models, or other methods to form a snapshot matrix S
2 Performing POD on S using Eq. 4
3 Extracting the POD basis using principal Eq. 7
4 Calculating the coefficients using Eq. 8 to create a data set with input condition
5 Constructing a neural network model to learn from the data set and
6 Predicting results for different input conditions using Eq. 6.

The reduced order model is validated and analyzed by measuring its accuracy through deviation from the sample data

TABLE 1 Energy ratio of first k eigenvalues of case 1.

First k eigenvalues	1	2	3	4	5
Energy ratio	88.831%	98.818%	99.875%	99.934%	99.991%

and comparing its computational efficiency with the acquisition time of the sample data. Two methods are adopted in this work to measure the accuracy, one of which is the root-mean-square error (RMSE) of each snapshot, denoted as

$$\mathbf{RMSE}(\boldsymbol{n}) = \frac{\sqrt{\frac{1}{n_x}\sum_{m=1}^{n_x}\left(\mathbf{q}_m^{ROM} - \mathbf{q}_m\right)^2}}{\mathbf{max}(\mathbf{q}) - \mathbf{min}\ (\mathbf{q})}, \boldsymbol{n} = \mathbf{1}, \mathbf{2}, \ldots, \boldsymbol{N}. \quad (9)$$

Here, q^{ROM} is the result of ROM, q is the true value of snapshot, and n_x is the node number. N is the number of snapshots extrapolated using ROM. The maximum and average of all predicted snapshot errors are compared in the following sections. The other criterion is the absolute error between ROM and the true value.

In terms of calculation cost, a speed ratio is defined in this work, which is represented as

$$\boldsymbol{r} = \frac{\boldsymbol{t}}{\boldsymbol{t_{ROM}}}, \quad (10)$$

where t refers to the computational time required for obtaining the true value and t_{ROM} is the corresponding time for obtaining results using ROM. It should be noted that the time required for collecting the sample data and training the model is not considered in t_{ROM}, which means t_{ROM} refers to the test time.

3 Verification for 2D transient heat conduction

The method described in Section 2 is validated using a typical 2D plate transient heat conduction problem. As shown in Figure 2, the plate has a length of 0.3 m and a width of 0.2 m and is made of a material with density $\rho = 1000\ \mathrm{kg/m^3}$, and the specific heat $c = 1000\ \mathrm{J/(kg \cdot K)}$ and thermal conductivity $k_x = k_y = 100\ \mathrm{W/(m \cdot K)}$. The initial temperature of the plate is 300 K where its left boundary is adiabatic, bottom boundary has a heat flux of $q = 1500\ \mathrm{W/m^2}$, and right boundary has convection with a heat transfer coefficient $h = 50\ \mathrm{W/(m^2 \cdot K)}$ and bulk temperature $T_f = 20^{\circ}\mathrm{C}$. To verify the effectiveness of this method under different transient conditions, different top boundary conditions are employed in Case1 and Case2.

The finite volume method (FVM) is used to obtain the numerical solution, which is regarded as the true value. The mesh model is illustrated in Figure 2, with 30 grids in length and 20 grids in width, resulting in a model with 600 grids and 704 nodes. While the additional source method is used to deal with the boundary conditions, reducing the number of nodes to 600 finally. The time step is 10 s. Nodes A, B, and C are three specific locations selected for comparison with the FVM.

3.1 Case 1: time-varying boundary

In case 1, the upper edge temperature is the time-varying boundary condition with the representation as

$$\boldsymbol{T\_top} = \mathbf{400}\left(\mathbf{1} - \mathbf{0.5}\,\boldsymbol{sin}\,\frac{\boldsymbol{\pi}}{\mathbf{240}}\boldsymbol{t}\right). \quad (11)$$

A total of 400 snapshots are obtained by the finite volume model with $t = 10, 20, \cdots, 4000$ to generate sufficient sample data and constitute the snapshot matrix S. The matrix S is decomposed by Eq. 4, and the first four vectors are selected as the POD basis since they account for 99.9% of the energy, as listed in Table 1.

The coefficients $\alpha(t) \in \mathbb{R}^{400\times4}$ are obtained by projecting the snapshot matrix onto the POD basis, which is used as the training data set for the neural network model. In this work, the LSTM is selected to combine with POD and build the ROM, as it can fit or predict models using historical data, which is especially applicable to time-related variables. The architecture of the proposed POD-LSTM model is shown in Figure 3, which is implemented using Python and Keras. The input of the model are coefficients from the previous four steps and the output is the coefficient at time t. The term "DENSE" represents the fully connected layers. Therefore, the relation between the input and the output can be represented as

$$\boldsymbol{\alpha}(\boldsymbol{t}) = \boldsymbol{f}(\boldsymbol{\alpha}(\boldsymbol{t}-\mathbf{1}), \boldsymbol{\alpha}(\boldsymbol{t}-\mathbf{2}), \boldsymbol{\alpha}(\boldsymbol{t}-\mathbf{3}), \boldsymbol{\alpha}(\boldsymbol{t}-\mathbf{4})), \quad (12)$$

where $f(\cdot)$ is a mapping function.

In this case, the first 60% of the data (0 s–2,400 s) is selected as the training set and the last 40% (2,400 s–4,000 s) as the test set, and then 20% of the data in the training set is divided to be the verification data. The shape of the input vector is (4,4) and the number of nodes in the three hidden layers are 64, 32, and 4, with activation functions of Tanh, Tanh, and Linear, respectively. A batch size of 16 and 50 epochs is used, with the mean square error serving as the loss function, ADAM as the optimizer, and a learning rate of 0.0005 during training.

The temperature distribution of the plate at t = 4,000 s calculated by the reduced-order model as shown in Figure 4A. The temperatures of nodes A, B, and C are shown in Figure 4B to compare the errors, which vary with time. The maximum RMSE is 0.73% and the maximum absolute error is 1.82°C, which indicates that the results obtained from the reduced-order model are in good agreement with those from the finite volume model. As for the computational speed, the FVM model consumes 83.98 s while the training time of the reduced-order model is 9.63 s and the prediction time is 0.02 s, resulting in the speed ratio of $r = 4199$. It should be admitted that collecting the sample data is time-consuming and equivalent to the time required for the FVM model. However, once the reduced-order model is established, it can significantly reduce the computational cost.

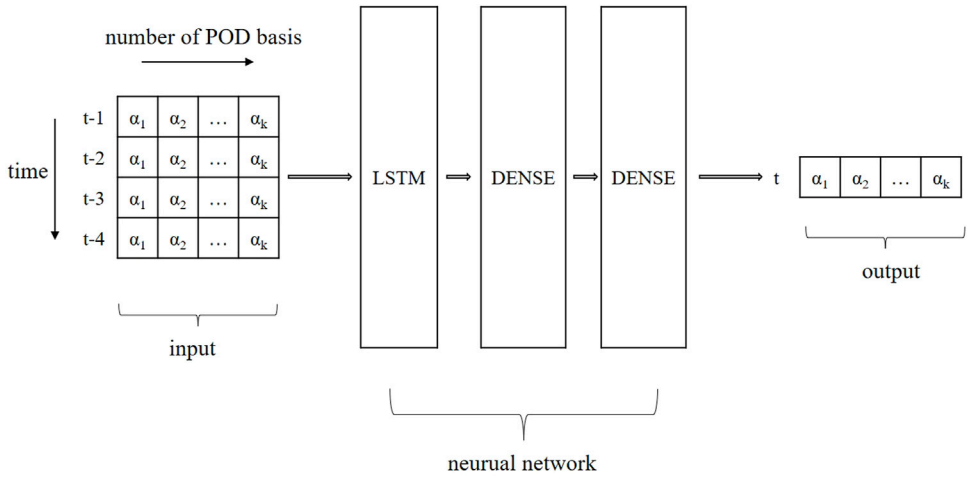

FIGURE 3
LSTM architecture for 2D plate heat conduction.

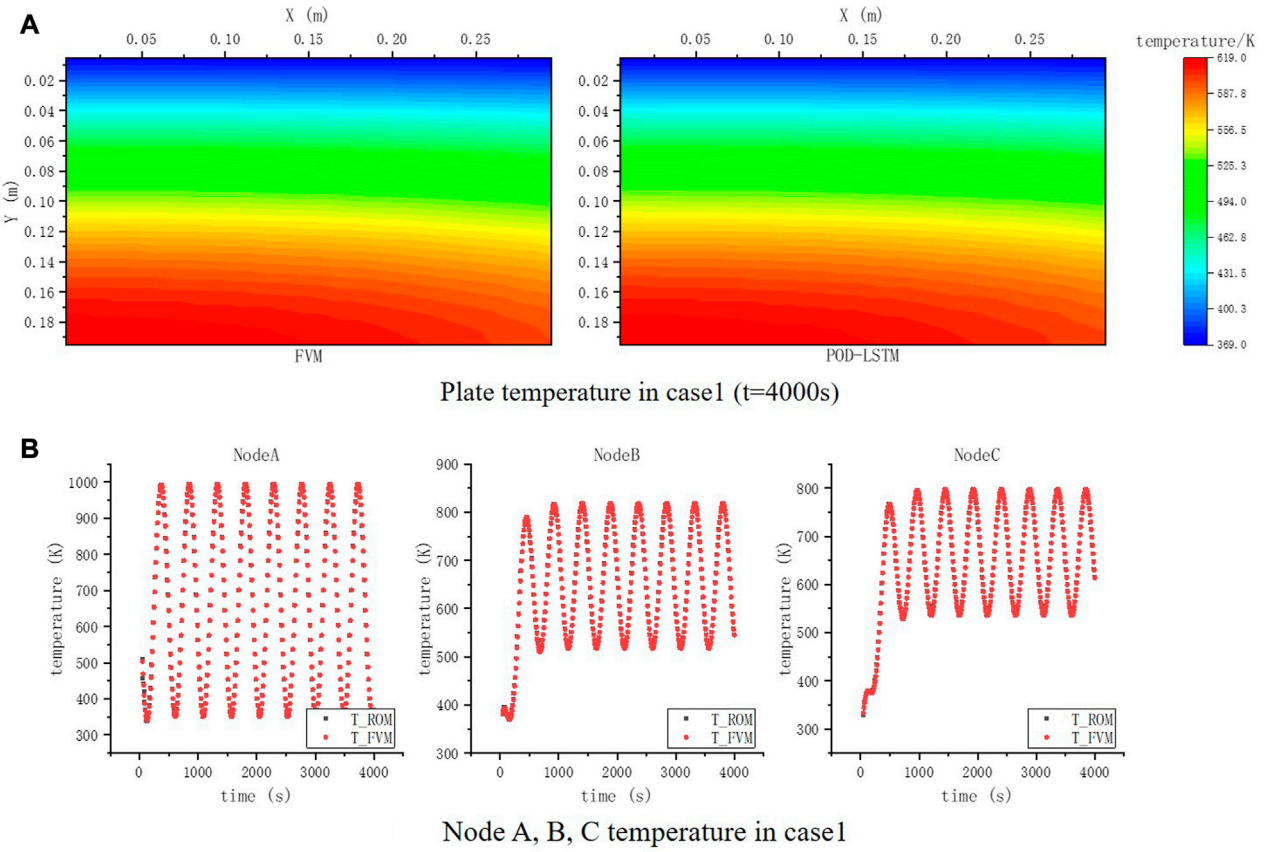

FIGURE 4
Temperature comparison in case 1. **(A)** Plate temperature in case 1 (t = 4,000 s). **(B)** Node A, B, and C temperature in case 1.

TABLE 2 Energy ratio of first k eigenvalues of case 2.

First k eigenvalues	1	2	3	4	5	6
Energy ratio	88.510%	98.639%	99.761%	99.887%	99.985%	99.996%

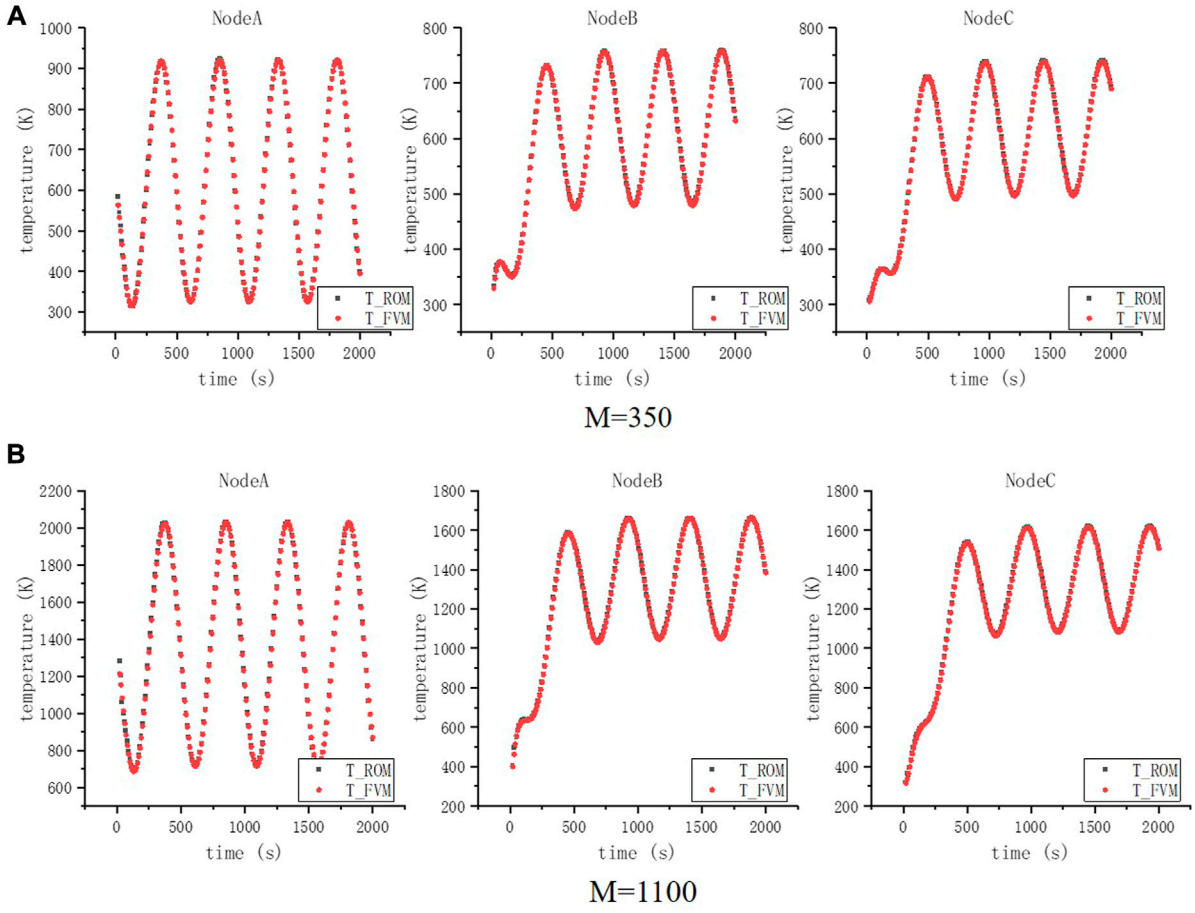

FIGURE 5
Node A, B, and C temperature in case 2. **(A)** M = 350 and **(B)** M = 1,100.

3.2 Case 2: multiple time-varying boundary

The upper boundary temperature in case 2 comprises nine different time-varying conditions, which can be expressed as

$$\boldsymbol{T\_top} = \boldsymbol{M}\left(\mathbf{1} - \mathbf{0.5}\,\boldsymbol{sin}\,\frac{\boldsymbol{\pi}}{\mathbf{240}}\boldsymbol{t}\right), \tag{13}$$

with $M = 200, 300, \ldots, 1,000$. The snapshot mentioned in Section 2.1 is only related to time, while the temperature in this case has two parameters: time t and amplitude M. Thus, the snapshot matrix is a combination of all sub-matrixes at the same M in the row vector direction, which is shown in Eq. 14. Subscript p represents different parameters, that is, different M in case 2. Then, the POD basis can be obtained using Eq. 4 as in the previous case.

$$\boldsymbol{S}_{p_1} = \begin{pmatrix} \boldsymbol{T}_{11}(\boldsymbol{t}_1, \boldsymbol{p}_1) & \cdots & \boldsymbol{T}_{11}(\boldsymbol{t}_n, \boldsymbol{p}_1) \\ \vdots & \ddots & \vdots \\ \boldsymbol{T}_{MN}(\boldsymbol{t}_1, \boldsymbol{p}_1) & \cdots & \boldsymbol{T}_{MN}(\boldsymbol{t}_n, \boldsymbol{p}_1) \end{pmatrix},$$

$$\boldsymbol{S} = \begin{pmatrix} \boldsymbol{S}_{p_1} & \cdots & \boldsymbol{S}_{p_J} \end{pmatrix} = \begin{pmatrix} \boldsymbol{T}_{11}(\boldsymbol{t}_1, \boldsymbol{p}_1) & \cdots & \boldsymbol{T}_{11}(\boldsymbol{t}_n, \boldsymbol{p}_J) \\ \vdots & \ddots & \vdots \\ \boldsymbol{T}_{MN}(\boldsymbol{t}_1, \boldsymbol{p}_1) & \cdots & \boldsymbol{T}_{MN}(\boldsymbol{t}_n, \boldsymbol{p}_J) \end{pmatrix}. \tag{14}$$

Unlike Eq. 12, the coefficients in case 2 include the influence of parameter M, thus the fitting relationship becomes

$$\boldsymbol{\alpha}(\boldsymbol{t}) = \boldsymbol{f}(\boldsymbol{\alpha}(\boldsymbol{t} - \mathbf{1}), \boldsymbol{M}, \boldsymbol{t}), \tag{15}$$

where $f(\cdot)$ is a mapping function.

The sample data consist of 1,800 snapshots with $t = 10, 20, \cdots, 2,000$ and $M = 200, 300, \ldots, 1,000$. The first five bases are retained for they meet principal Eq. 7 as shown in Table 2.

In total, 80% of the data set is used for training, and the remaining 20% is the validation set. The test data is the temperature when M = 350 and 1,100, which are not included

TABLE 3 Computational cost comparison in case 2.

Time/s	FVM	Data set generation	Training time	Prediction time	Speed ratio r
M = 350	72.59	288.45	25.76	0.010	7,259
M = 1,100	42.61	288.45	25.76	0.005	8,522

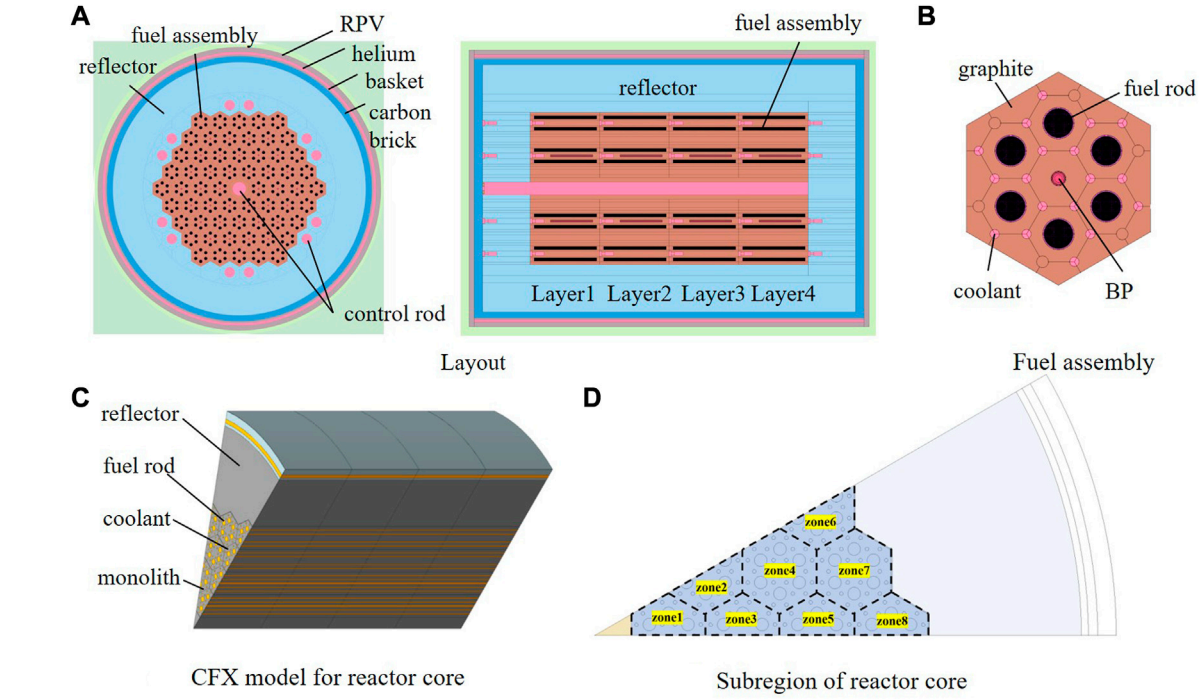

FIGURE 6
Layout and CFX model of reactor core. **(A)** Layout. **(B)** Fuel assembly. **(C)** CFX model for reactor core. **(D)** Subregion of reactor core.

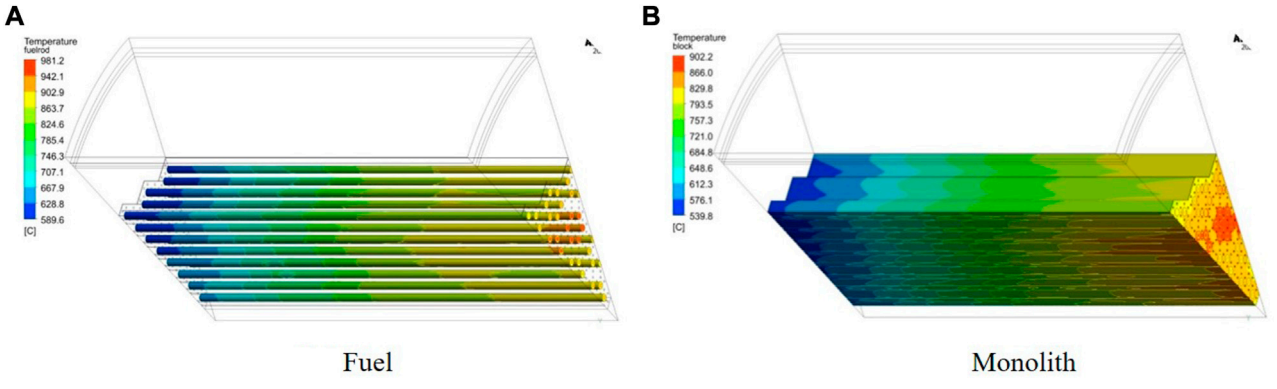

FIGURE 7
Temperature of core (1,000 EFPD, 488.7°C). **(A)** Fuel. **(B)** Monolith.

in the snapshot matrix. The shape of the input vector is (1,7) and the number of nodes in the three hidden layers are 100, 32, and 5 with activation functions of Tanh, Tanh, and Linear, respectively. The batch size is 8 and epoch is 100, loss function is the mean square error, optimizer is ADAM, and learning rate is 0.001. The temperature of the plate at t =

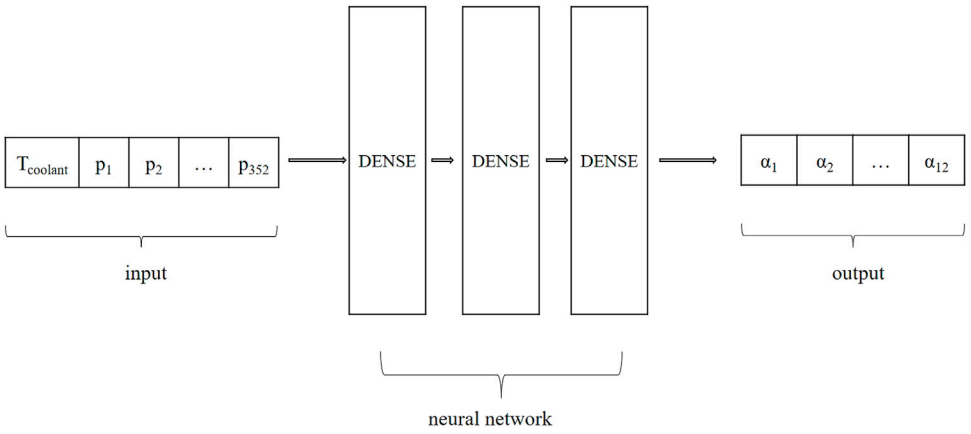

FIGURE 8
Neural network architecture for fuel rods zone.

TABLE 4 Comparison between ROM and CFX (fuel rods zone).

Input		RMSE (%)	Absolute error/°C	
EFPD	$T_{reactorInlet}$/°C		Maximum	Average
3.3	408	0.40	3.1	1.7
250	295	0.47	5.1	2.1
550	485	1.02	8.2	3.6
650	210	0.64	7.2	3.9
750	332	0.08	1.1	0.4
1,000	314	0.53	5.6	2.5

0–2,000 s is calculated using ROM and compared with the FVM results.

The temperature comparison is as shown in Figures 5A, B. The maximum RMSE is 5.63% and maximum absolute error is 4.07°C when M = 350, and the maximum RMSE is 5.50% and maximum absolute error is 12.72°C when M = 1,100. The accuracy of the temperature for M = 1,100 is slightly worse than that for M = 350, which indicates that the ability of extrapolation is not very satisfactory, as for all predictions are based on the known sample data. The computational cost comparison is represented in Table 3, which shows ROM can achieve fast calculations.

3.3 Analysis

In summary, the reduced-order model has demonstrated excellent accuracy and computational efficiency in case 1, while there is still room for improvement in accuracy for the more complex transient problem in case 2. It is worth noting that the distinction between transient and stable states is not evident, as they merely represent different input parameters for the neural network. Extrapolation remains a significant challenge for this method, as the neural network can only provide reasonable predictions based on known sample data. Despite being appropriate for time-series problems, even the LSTM model has limitations in addressing this challenge, as errors may accumulate gradually over prediction time. It is worth noting that the reduced-order model constructed using the POD and neural network method does not involve any governing equations or physical laws. Instead, it relies on a vast amount of sample data and optimization algorithms. Therefore, using different samples and algorithms to construct a reduced-order model could lead to better results for the two cases. But the acceleration effect of the reduced-order model underscores its potential for efficient predictions, once the model has been optimized to meet the desired accuracy requirements.

4 ROM for gas-cooled microreactor thermal analysis

4.1 CFD model for gas-cooled microreactor core

4.1.1 Layout of reactor core

This work presents the detailed modeling of a horizontal compact high-temperature gas-cooled reactor with a designed thermal power of 5 MWth. The reactor is composed of fuel assembly, control rod assembly, reflector, boron carbon brick, and other components. The core layout and fuel assembly configuration are illustrated in Figures 6A, B, respectively. The active zone of the horizontal core comprises hexagonal fuel assemblies that are organized into four layers in the axial direction, with each containing 60 fuel assemblies. As such, the entire reactor contains 240 fuel assemblies, with varying degrees of enrichment at different positions. The core has a total radial diameter (to the outer edge of the reflector) of 210 cm and a total axial length of 220 cm. The active zone has an equivalent diameter of 131 cm and a length of 164 cm. The core side reflector consists of 12 groups of regulating control rods, while a single group of control rods is located at the center. The coolant is single-phase helium, which is not coupled with reactivity and does not undergo any chemical reactions with the

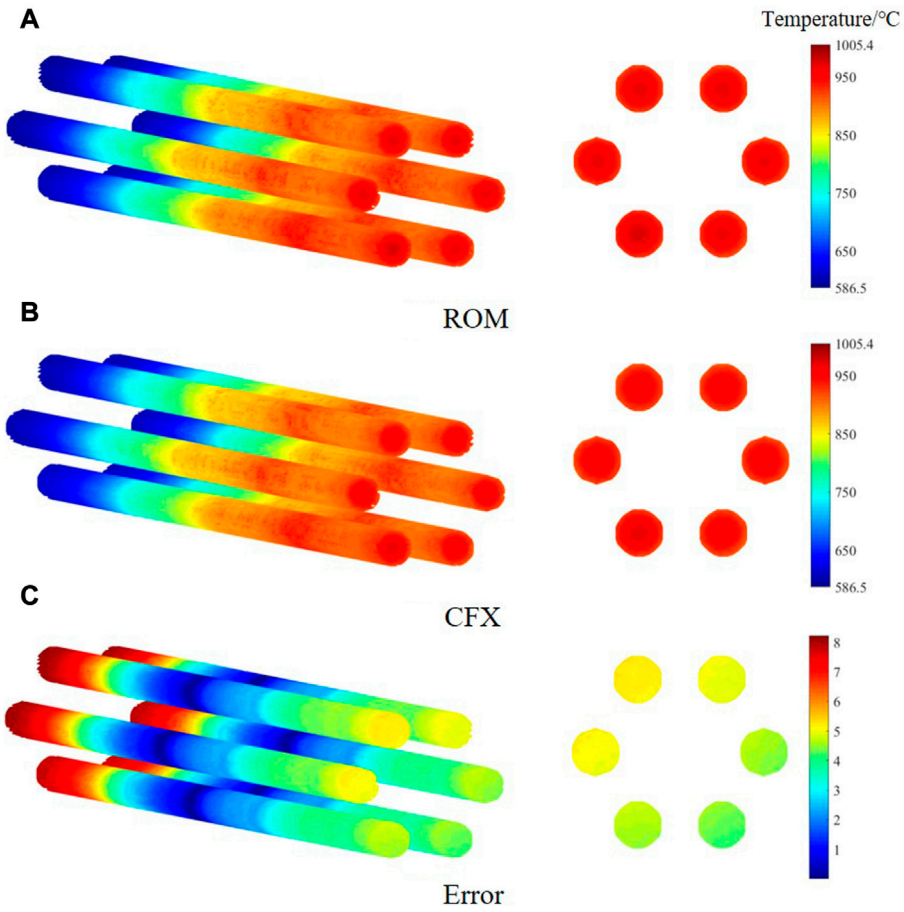

FIGURE 9
Temperature contour comparison for fuel rods zone. **(A)** ROM. **(B)** CFX. **(C)** Error.

TABLE 5 Comparison between ROM and CFX (monolith zone).

Input		RMSE (%)	Absolute error/°C	
EFPD	$T_{reactorInlet}$/°C		Maximum	Average
3.3	408	0.12	1.2	0.4
250	295	0.44	5.1	1.8
550	485	0.46	3.2	1.5
650	210	0.07	1.5	0.3
750	332	0.08	1.4	0.3
1,000	314	0.21	2.1	1.0

cladding and fuel structural materials. The reflectors are made of graphite, which also acts as the neutron moderator and core structure material.

4.1.2 Thermal analysis with CFX

A three-dimensional thermal modeling of the active zone in the reactor core is conducted using ANSYS CFX 2020. This model includes 1/12 of the entire core to take advantage of the symmetrical characteristic, as depicted in Figure 6C, with a mesh number of 2.77 million. Two significant boundary conditions are considered in this model. The first condition is the power density of fuel rods, denoted as S_{zonei}. The subscript "zone," shown in Figure 6D, refers to the different parts of the core. As mentioned, each fuel rod consists of four fuel assemblies in the axial direction, and one fuel assembly contains 11 fuel pellets. Therefore, the power distribution of each fuel rod has 44 points, resulting in the expression of power density $S_{zonei} \in \mathbb{R}^{8\times44}$, that is,

$$\boldsymbol{S_{zonei}} = \mathbf{1.0014}\boldsymbol{P_{zonei}} \cdot \frac{\boldsymbol{P_{total}}}{\mathbf{60} \times \boldsymbol{V_{zonei}}} \quad \boldsymbol{i} = \mathbf{1}, \mathbf{2}, \ldots, \mathbf{8}, \tag{16}$$

where 1.0014 is an empirical factor used in the thermal calculation of the CFX model to ensure energy conservation, $P_{zonei} \in \mathbb{R}^{8\times44}$ is the normalized power factor of each region, which is calculated by a neutronics model and is dependent on the lifetime of the reactor. P_{total} = 5MW is the design thermal power, and V_{zonei} is the volume of fuel rods in each region, which is directly stored in the CFX model. The number 60 represents the division of the core into four

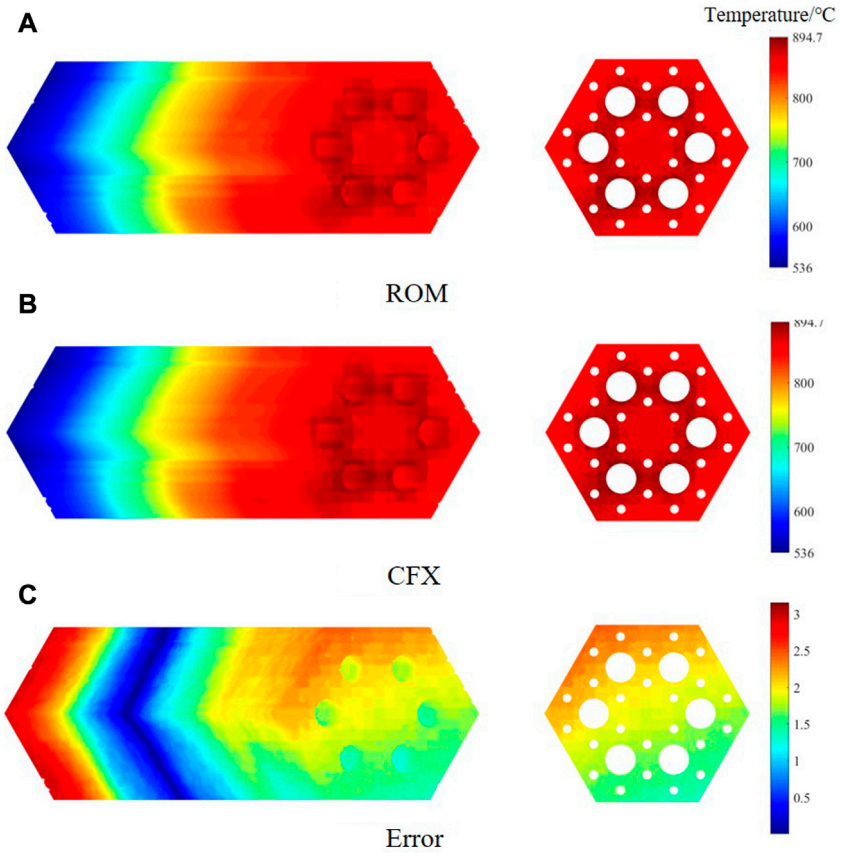

FIGURE 10
Temperature contour comparison for monolith zone. **(A)** ROM. **(B)** CFX. **(C)** Error.

layers in the axial direction, with each layer containing 60 fuel assemblies.

The other boundary is the flow of the coolant. The outlet of the reactor is at atmospheric pressure and outlet temperature is 750°C at load tracking operation. Therefore, the flow of the coolant can be represented as

$$Q = \frac{1}{12} \cdot \frac{P_{\text{total}}}{(T_{\text{reactorOutlet}} - T_{\text{reactorInlet}})C_{\text{p}}} \cdot \left(1 - Q_{\text{bypass}}\right), \tag{17}$$

where $T_{\text{reactorOutlet}} = 750^{\circ}\text{C}$, $C_{\text{p}} = 5195\text{J}/(\text{kg} \cdot \text{K})$ is the specific heat of helium, $Q_{\text{bypass}} = 0.12$ is the portion of the bypass flow, and the number 1/12 refers that only 1/12 of the core is considered.

In summary, the state of the core is dependent on the normalized power factor $P_{\text{zonei}} \in \mathbb{R}^{8\times44}$ (which is relies on the lifetime) and temperature of the coolant upon entering the reactor $T_{\text{reactorInlet}}$ .For example, considering a lifetime of 1000 EFPD (effective full-power days) and a coolant temperature of 488.7°C, the temperature of the core and monolith is shown in Figure 7. The maximum temperature of the fuel and monolith are 981.2°C and 902.2°C, respectively. It is worth noting that the temperature increases along the flow of the coolant in the axial direction and zone 4 is the hot zone.

4.2 ROM for thermal analysis of reactor core

4.2.1 Generation of sample data

Zone 4 is selected to build a reduced-order model as this area is a typical region. The first step is to collect sufficient sample data accruing to the abovementioned steps.

4.2.1.1 Power density

There are only seven different power density distributions calculated using the neutronics model due to computational limitations, where $EFPD = 0, 3.3, 250, 550, 650, 750,$ and $1,000$. To generate more input parameters, Hermite interpolation is adopted twice to the power factor, as it is a two-dimensional array. A small random variable is added to each power factor according to certain rules to ensure that the average power factor meets the normalization requirements. Finally, 100 different lifetimes, ranging from 5 EFPD–995 EFPD in iterations of 10 EFPD, are used as input parameters.

4.2.1.2 Temperature of inlet coolant

A trial calculation revealed that the effect of coolant temperature on the results is approximately linear, so it is not necessary to design too many different coolant temperatures. Considering the

maximum temperature limit of 550°C for the 316H stainless steel used in the reactor pressure vessel and basket, the range of the coolant inlet temperature is fixed at 200–500°C, with 50°C iteration.

To sum up, in combination with the distribution of power factor and coolant temperature, a total of 700 sets of different input conditions for core temperature are computed, which are taken as the sample data for ROM after format processing. The number of sample data is 36,774 and 19,602 for the fuel rods and monolith, respectively, by extracting nodes coordinates and temperatures in zone 4 (the nodes of the monolith are after selection). The following sections discuss ROM for fuel and monolith, respectively.

4.2.2 ROM for fuel rods zone

Based on the collected sample data, the size of the snapshot matrix is 36,774 × 700 with 700 corresponding eigenvalues, and the first 12 eigenvalues meet the selection principle, accounting for 99.90% of the total. Therefore, the input shape for the neural network is (700,353) and the output shape is (700,12). The training set is composed of 80% of the data, the test set is composed of 20%, and then 20% of data in the training set is divided to be the verification data. The architecture of the model is depicted in Figure 8, with three hidden layers having 64, 32, and 12 nodes, respectively, and activation functions of Tanh, Tanh, and Linear. A batch size of 32 and 150 epochs are used, with the mean square error serving as the loss function, ADAM as the optimizer, with a learning rate of 0.0005 during training.

To verify the accuracy of ROM, the results from six cases are compared with those obtained from the CFX model, as shown in Table 4. Figure 9 presents the temperature contour for the fuel rod in the case with maximum error. The results demonstrate that the average root-mean-square error is 1.02% and maximum absolute error is 8.2°C, indicating a good agreement between the ROM and CFX results. Furthermore, while CFX requires 1.5 h for a single computational core, the test time for the reduced-order model is less than 0.01 s, implying that ROM can achieve real-time display.

4.2.3 ROM for monolith zone

The reduced-order model building process for the monolith zone is similar to that of the fuel rods zone and is therefore not repeated here. But the number of bases for this case is nine. All other parameters are the same as for the previous fuel case, except that the epoch for the monolith model is 200. As shown in Table 5 and Figure 10, the maximum of RMSE is 0.46% and the maximum absolute error is 5.1°C, which also meets the accuracy requirements. The test time in this case is also less than 0.01 s.

5 Conclusion

This study introduces an approach to ROM that incorporates both POD and neural networks. The method is tested on a 2D transient heat conduction model, and the results demonstrate that ROM is effective in terms of both accuracy and computational speed, especially when dealing with time-varying boundaries. However, for more complex boundaries or problems that requires time-dependent predictions, the error rate increases due to the requirement for a large amount of historical data. Consequently, the model must be updated regularly to ensure accurate predictions. It is worth noting that the reduced-order model created using this approach does not distinguish between the time parameter in transient problems and other variables in steady-state problems. The key concept behind this approach is to reduce data dimensions by capturing the essential features of the sample data to enable fast calculations.

The Section 4 focuses on analyzing the thermal model of a gas-cooled microreactor core using load tracking operation as the reference condition, with future research aiming to consider more complex scenarios such as transient states and accidents. By employing a combination of POD and neural networks, a highly accurate reduced-order model is developed. The results demonstrate that ROM achieves a root-mean-square error of less than 1.02% and an absolute error of less than 8.2°C when predicting core temperature. Furthermore, the computational efficiency of the reduced-order model is greatly improved, reducing the calculation time from 1.5 h to real-time display. These findings provide compelling evidence for the feasibility of using POD and machine learning in the development of reduced-order models for gas-cooled microreactors, offering a novel approach to achieve precise thermal calculation while minimizing computational costs. The research thus holds significant implications for the intelligent operation and maintenance of nuclear power plants, as well as for the many coupled calculations involved in gas-cooled microreactors.

Data availability statement

The original contributions presented in the study are included in the article/Supplementary Material; further inquiries can be directed to the corresponding authors.

Author contributions

EC: methodology, calculation, and writing of the manuscript; HZ: resources and supervision; YY: project administration, resources, and supervision.

Conflict of interest

Authors EC, HZ, and YY were employed by China Nuclear Power Engineering Co., Ltd.

Publisher's note

References

Alsayyari, F., Tiberga, M., Perkó, Z., Lathouwers, D., and Kloosterman, J. L. (2020). A nonintrusive adaptive reduced order modeling approach for a molten salt reactor system. *Ann. Nucl. Energy* 141, 107321. doi:10.1016/j.anucene.2020.107321

Amsallem, D., and Farhat, C. (2012). Stabilization of projection-based reduced-order models. *Int. J. Numer. Methods Eng.* 91 (4), 358–377. doi:10.1002/nme.4274

Chatterjee, A. (2000). An introduction to the proper orthogonal decomposition. *Curr. Sci.* Available at: https://www.jstor.org/stable/24103957 78, 808–817.

Chen, X., Liu, L., and Yue, Z. (2015). Reduced order aerothermodynamic modeling research for hypersonic vehicles based on proper orthogonal decomposition and surrogate method. *Acta Aeronaut. Astronaut. Sin.* 36 (2), 462–472. doi:10.7527/S1000-6893.2014.0079

Gao, X., Hu, J., and Huang, S. (2016). A proper orthogonal decomposition analysis method for multimedia heat conduction problems. *J. Heat Transf.* 138 (7). doi:10.1115/1.4033081

German, P., and Ragusa, J. C. (2019). Reduced-order modeling of parameterized multi-group diffusion k-eigenvalue problems. *Ann. Nucl. Energy* 134, 144–157. doi:10.1016/j.anucene.2019.05.049

Hasegawa, K., Kai, F., Murata, T., and Fukagata, K. (2020). Machine-learning-based reduced-order modeling for unsteady flows around bluff bodies of various shapes. *Theor. Comput. Fluid Dyn.* 34, 367–383. doi:10.1007/s00162-020-00528-w

Hazenberg, M., Astrid, P., and Weiland, S. "Low order modeling and optimal control design of a heated plate," in Proceedings of the European Control Conference), Cambridge, UK, September 2015. doi:10.23919/ECC.2003.7085130

Kang, H., Tian, Z., Chen, G., Li, L., and Wang, T. (2022). Application of POD reduced-order algorithm on data-driven modeling of rod bundle. *Nucl. Eng. Technol.* 54 (1), 36–48. doi:10.1016/j.net.2021.07.010

Liang, Y., Lee, H., Lim, S., Lin, W., Lee, K., and Wu, C. (2002). Proper orthogonal decomposition and its applications—Part I: Theory. *J. Sound Vib.* 252 (3), 527–544. doi:10.1006/jsvi.2001.4041

Lorenz, E. N. (1956). *Empirical orthogonal functions and statistical weather prediction.* Cambridge, USA: Massachusetts Institute of Technology, Department of Meteorology.

Lorenzi, S., Cammi, A., Luzzi, L., and Rozza, G. (2017). A reduced order model for investigating the dynamics of the Gen-IV LFR coolant pool. *Appl. Math. Model.* 46, 263–284. doi:10.1016/j.apm.2017.01.066

Ooi, C., Le, Q. T., Dao, M. H., Nguyen, V. B., Nguyen, H. H., and Ba, T. (2021). Modeling transient fluid simulations with proper orthogonal decomposition and machine learning. *Int. J. Numer. Methods Fluids* 93 (2), 396–410. doi:10.1002/fld.4888

Pearson, K. (1901). LIII. On lines and planes of closest fit to systems of points in space. *Lond. Edinb. Dublin philosophical Mag. J. Sci.* 2 (11), 559–572. doi:10.1080/14786440109462720

Rumelhart, D. E., Hinton, G. E., and Williams, R. J. (1986). Learning representations by back-propagating errors. *Nature* 323, 533–536. doi:10.1038/323533a0

Sartori, A., Cammi, A., Luzzi, L., and Rozza, G. (2016). A multi-physics reduced order model for the analysis of Lead Fast Reactor single channel. *Ann. Nucl. Energy* 87, 198–208. doi:10.1016/j.anucene.2015.09.002

Sirovich, L. (1987). Turbulence and the dynamics of coherent structures. I. Coherent structures. *Q. Appl. Math.* 45 (3), 561–571. doi:10.1090/qam/910462

Stabile, G., Hijazi, S., Mola, A., Lorenzi, S., and Rozza, G. (2017). POD-galerkin reduced order methods for CFD using finite volume discretisation: Vortex shedding around a circular cylinder. *Commun. Appl. Industrial Math.* 8 (1), 210–236. doi:10.1515/caim-2017-0011

Star, S. K., Spina, G., Belloni, F., and Degroote, J. (2021). Development of a coupling between a system thermal–hydraulic code and a reduced order CFD model. *Ann. Nucl. Energy* 153, 108056. doi:10.1016/j.anucene.2020.108056

Star, S. K., Stabile, G., Georgaka, S., Belloni, F., Rozza, G., and Degroote, J. "POD-Galerkin reduced order model of the Boussinesq approximation for buoyancy-driven enclosed flows," in Proceedings of the International Conference on Mathematics and Computational Methods Applied to Nuclear Science and Engineering (M&C 2019), Portland, Oregon, August 2019 (American Nuclear Society (ANS).), 2452–2461.

Sun, Y., Yang, J., Wang, Y., Li, Z., and Ma, Y. (2020). A POD reduced-order model for resolving the neutron transport problems of nuclear reactor. *Ann. Nucl. Energy* 149, 107799. doi:10.1016/j.anucene.2020.107799

Swischuk, R., Mainini, L., Peherstorfer, B., and Willcox, K. (2019). Projection-based model reduction: Formulations for physics-based machine learning. *Comput. Fluids* 179, 704–717. doi:10.1016/j.compfluid.2018.07.021

Wang, Z., Xiao, D., Fang, F., Govindan, R., Pain, C. C., and Guo, Y. (2018). Model identification of reduced order fluid dynamics systems using deep learning. *Int. J. Numer. Methods Fluids* 86 (4), 255–268. doi:10.1002/fld.4416

Washabaugh, K., Amsallem, D., Zahr, M., and Farhat, C. (June 2012). "Nonlinear model reduction for CFD problems using local reduced-order bases," in Proceedings of the 42nd AIAA fluid dynamics conference and exhibit, New Orleans, Louisiana doi:10.2514/6.2012-2686

Wu, P., Sun, J., Chang, X., Zhang, W., Arcucci, R., Guo, Y., et al. (2020). Data-driven reduced order model with temporal convolutional neural network. *Comput. Methods Appl. Mech. Eng.* 360, 112766. doi:10.1016/j.cma.2019.112766

Xiao, D., Fang, F., Buchan, A. G., Pain, C. C., Navon, I. M., and Muggeridge, A. (2015a). Non-intrusive reduced order modelling of the Navier–Stokes equations. *Comput. Methods Appl. Mech. Eng.* 293, 522–541. doi:10.1016/j.cma.2015.05.015

Xiao, D., Fang, F., Pain, C., and Hu, G. (2015b). Non-intrusive reduced-order modelling of the Navier–Stokes equations based on RBF interpolation. *Int. J. Numer. Methods Fluids* 79 (11), 580–595. doi:10.1002/fld.4066

Yu, L., Baojing, Z., Xiaowei, G., Zeyan, W. U., and Feng, W. (2018). Reduced order model analysis method via proper orthogonal decomposition for nonlinear transient heat conduction problems. *Sci. Sinica(Physica,Mechanica Astronomica)* 48, 124603. doi:10.1360/sspma2018-00199

Yu, Y., Si, X., Hu, C., and Zhang, J. (2019). A review of recurrent neural networks: LSTM cells and network architectures. *Neural Comput.* 31 (7), 1235–1270. doi:10.1162/neco_a_01199

Zhang, X., and Xiang, H. (2015). A fast meshless method based on proper orthogonal decomposition for the transient heat conduction problems. *Int. J. Heat Mass Transf.* 84, 729–739. doi:10.1016/j.ijheatmasstransfer.2015.01.008

Holmes, P., Lumley, J. L., Berkooz, G., and Rowley, C. W. (2012). Turbulence, Coherent Structures, Dynamical Systems and Symmetry. *Cambridge: Cambridge University Press*. doi:10.1017/CBO9780511919701

JinXiu, H., BaoJing, Z., and XiaoWei, G. (2015). Reduced order model analysis method via proper orthogonal decomposition for transient heat conduction. *Sci Sin-Phys Mech Astron* 45(1), 014602. doi:10.1360/SSPMA2013-00041

frontiers | Frontiers in Energy Research

TYPE Original Research
PUBLISHED 05 June 2023
DOI 10.3389/fenrg.2023.1213000

OPEN ACCESS

EDITED BY
Jiankai Yu,
Massachusetts Institute of Technology,
United States

REVIEWED BY
Jingang Liang,
Tsinghua University, China
Xinyan Wang,
Massachusetts Institute of Technology,
United States

*CORRESPONDENCE
Hyoung Kyu Cho,
chohk@snu.ac.kr

RECEIVED 27 April 2023
ACCEPTED 24 May 2023
PUBLISHED 05 June 2023

CITATION
Jeong MJ, Im J, Lee S and Cho HK (2023), Multiphysics analysis of heat pipe cooled microreactor core with adjusted heat sink temperature for thermal stress reduction using OpenFOAM coupled with neutronics and heat pipe code. *Front. Energy Res.* 11:1213000. doi: 10.3389/fenrg.2023.1213000

Multiphysics analysis of heat pipe cooled microreactor core with adjusted heat sink temperature for thermal stress reduction using OpenFOAM coupled with neutronics and heat pipe code

Myung Jin Jeong, Jaeuk Im, San Lee and Hyoung Kyu Cho*

Department of Nuclear Engineering, Seoul National University, Seoul, Republic of Korea

Heat-pipe-cooled microreactors (HPRs) have advantages such as a compact design, easy transportation, and improved system reliability and stability. The core of an HPR consists of fuel rods and heat pipes in a monolith, which is a solid block structure containing many holes for the fuel rods and heat pipes. When designing the core of an HPR, high thermal stress and reactivity feedback owing to thermal expansion are important considerations. Therefore, a high-fidelity multiphysics analysis tool is required for accurately analyzing an HPR core. When performing a multiphysics analysis, it is necessary to couple the heat pipe thermal analysis code, thermal-structural analysis code, and neutronics code. To develop a multiphysics analysis tool, OpenFOAM, an open source Computational Fluid Dynamics (CFD) tool, and ANLHTP, a heat pipe thermal analysis code, were coupled. In this process, the structural analysis solver of OpenFOAM was verified, and its limitations were improved. To confirm the proper working of the code, the mini-core problem was analyzed using the OpenFOAM-ANLHTP coupled code. Next, to consider the reactivity feedback, coupling with PRAGMA, a GPU-based continuous-energy-Monte Carlo neutronics code was performed, and the multiphysics analysis capability of the OpenFOAM-ANLHTP-PRAGMA coupled code was confirmed through an analysis of the MegaPower reactor core. To reduce the temperature distribution within the monolith, the temperature distribution of the heat pipe sink was adjusted, and the reduced thermal stress of an HPR core was observed.

KEYWORDS

microreactor, heat pipe, multiphysics analysis, thermal stress, OpenFOAM, PRAGMA, ANLHTP

1 Introduction

A heat pipe cooled microreactor (HPR) is a nuclear reactor that passively removes heat from a core using heat pipes. The heat pipe is a passive heat-transfer device using the capillary force of the wick structure and phase transition. The heat pipe is filled with a working fluid, and the working fluid transfers heat as it evaporates at the evaporator section and condenses at the condenser section. An HPR has the advantages of compact design, ease of transport, and improved system reliability and stability. It has attracted attention among

various microreactor concepts since the success of the Kilopower Reactor Using Stirling TechnologY (KRUSTY) experiment (Gibson et al., 2018). Since then, space reactors and land-based reactors such as the Los Alamos National Laboratory (LANL)'s Megapower reactor (Mcclure et al., 2015), the Westinghouse' eVinci (Swartz et al., 2021), Oklo's Aurora (OKLO Inc., 2020), and China's NUSTER-100 (Tang et al., 2022) have been studied.

The representative form of an HPR core comprises many heat pipes, and fuel rods, which are contained in a solid structure called the monolith. The heat generated from the nuclear fuel is transferred to the heat pipes through the monolith via conduction, and the heat pipe transfers heat from the core to the power conversion system.

A land-based HPR with several MWe of power requires the integration of many nuclear fuels and heat pipes in the small space of the monolith. This spatial integration increases the temperature gradient within the monolith and may induce high thermal stress. This high thermal stress is one of the critical issues in the core design of existing monolith-based HPRs. Additionally, the thermal expansion of a metal monolith results in reactivity feedback owing to the change in neutron leakage, especially in fast reactors. Neutronics analysis has revealed that most reactivity feedback is due to such thermal expansions (Hu et al., 2019).

To reflect the consideration of these variations in the design and safety analysis of an HPR core, a high-fidelity multiphysics analysis tool is required. Accordingly, the Idaho National Laboratory (INL) conducted a PIRT analysis of the Megapower reactor (Sterbentz, 2017), and developed Direwolf (Lange, 2020), a heat pipe reactor multiphysics analysis tool, using the Multiphysics Object-Oriented Simulation Environment (MOOSE); Direwolf can perform neutronics-thermal-structural analysis. Additionally, steady-state and transient multiphysics analyses have been performed on the EMPIRE core (Matthews et al., 2021).

The Korea Atomic Energy Research Institute (KAERI) developed a heat pipe code called LUHPIS (Tak et al., 2020), and performed a thermal analysis of two conceptual heat pipe cooled reactor cores using LUHPIS and HEPITOS coupled code (Lee et al., 2021). The Argonne National Laboratory (ANL) performed the PROTEUS-FLUENT-ANLHTP coupled analysis in cooperation with the Seoul National University (SNU) (Lee et al., 2019). Additionally, steady-state and transient multiphysics analyses were performed on an HP-MR reactor using the MOOSE platform (Stauff et al., 2021). The Xi'an Jiaotong University performed steady-state and transient multiphysics analyses on the NUSTER-100 core (Huang et al., 2022; Tang et al., 2022) and validation calculations for the KRUSTY experiment (Ge et al., 2022).

Thermal-structural analysis of the monolith in an HPR is necessary in HPR core analysis for confirming whether safety criteria such as the fuel centerline temperature and maximum thermal stress in the monolith are satisfied. For this purpose, OpenFOAM was selected for the thermal-structural analysis of the monoliths in this study. OpenFOAM is an open-source CFD software that has a built-in basic structural analysis solver. Additionally, studies in the nuclear community have been conducted using the OpenFOAM solver (Fiorina et al., 2015; Scolaro et al., 2020). Since OpenFOAM is open-source software, its solver could be modified and improved easily, and could be coupled easily it with other codes. Taking these advantages of OpenFOAM, Tsinghua University performed multiphysics analysis of KRUSTY using the OpenFOAM-RMC code (Guo et al., 2021; Guo et al., 2022).

In this study, a multiphysics simulation was conducted to develop a high-fidelity multiphysics analysis tool for HPRs. The OpenFOAM stress analysis solver was coupled with the Monte Carlo neutron transport code PRAGMA and the heat pipe analysis code ANLHTP. The applicability of the coupled code was tested through an analysis of two types of microreactor cores from existing literature. Subsequently, based on the simulation results, a strategy to reduce the thermal stress in a monolith is proposed. The simulation results showed that the uniformity of the temperature field in the monolith could significantly reduce the thermal stress, which could be achieved by adjusting the heat sink temperature of the heat pipes. This suggested that the heat sink temperature distribution could be an optimization parameter in HPR core design.

This study introduces the verification results of the OpenFOAM stress analysis solver, the coupling methodology for the multiphysics simulation, and the specifications of PRAGMA and ANLHTP. Subsequently, the application of the coupled code to reactor core analyses is presented. Finally, the effect of heat sink temperature adjustment on thermal stress reduction is described.

2 Establishment of OpenFOAM-ANLHTP code coupling system

2.1 OpenFOAM

The OpenFOAM code was selected as a tool in the thermal-structural analysis of an HPR core. OpenFOAM is an open-source-based CFD tool that has a built-in basic thermal-structural analysis solver (The OpenFOAM Foundation Ltd., 2019, Accessed 2023). This solver enables the thermal-structural analysis of small deformation conditions under the assumption of linear elasticity. This assumption does not consider plastic deformation after yielding; however, it is effective and sufficient in determining whether an HPR core reaches the yield strength. The governing equations are expressed as Eqs 1, 2:

Momentum equation

$$\frac{\partial^2(\rho \boldsymbol{u})}{\partial t^2} = \nabla \cdot \left[(2\mu + \lambda)\nabla \boldsymbol{u}\right] + \nabla \cdot \left[\mu(\nabla \boldsymbol{u})^T + \lambda \boldsymbol{I} tr(\nabla \boldsymbol{u}) - (\mu + \lambda)\nabla \boldsymbol{u}\right] - \nabla(3K\alpha T), \quad (1)$$

where ρ: density (kg/ m^3), u: displacement (m), μ: Lame's second coefficient (shear modulus) (Pa), λ: Lame's first coefficient (K), $\boldsymbol{I}$: unit tensor, K: bulk modulus (Pa), α: thermal expansion coefficient (/ K), and T: temperature (K).

Heat conduction equation

$$\rho c \frac{\partial T}{\partial t} = \nabla \cdot \boldsymbol{k} \nabla T + q''', \quad (2)$$

where c: specific heat capacity (J/kgK), k: thermal conductivity (W/mK), and q''': volumetric heat generation rate (W/m^3).

According to the official OpenFOAM user guide, this solver has been verified against simple structural analysis problems; however, no such verification has been reported for thermal stress. Furthermore, the temperature dependencies of the material properties have not been considered by the solver, and multiple-material handling, which is necessary for reactor core analysis, could

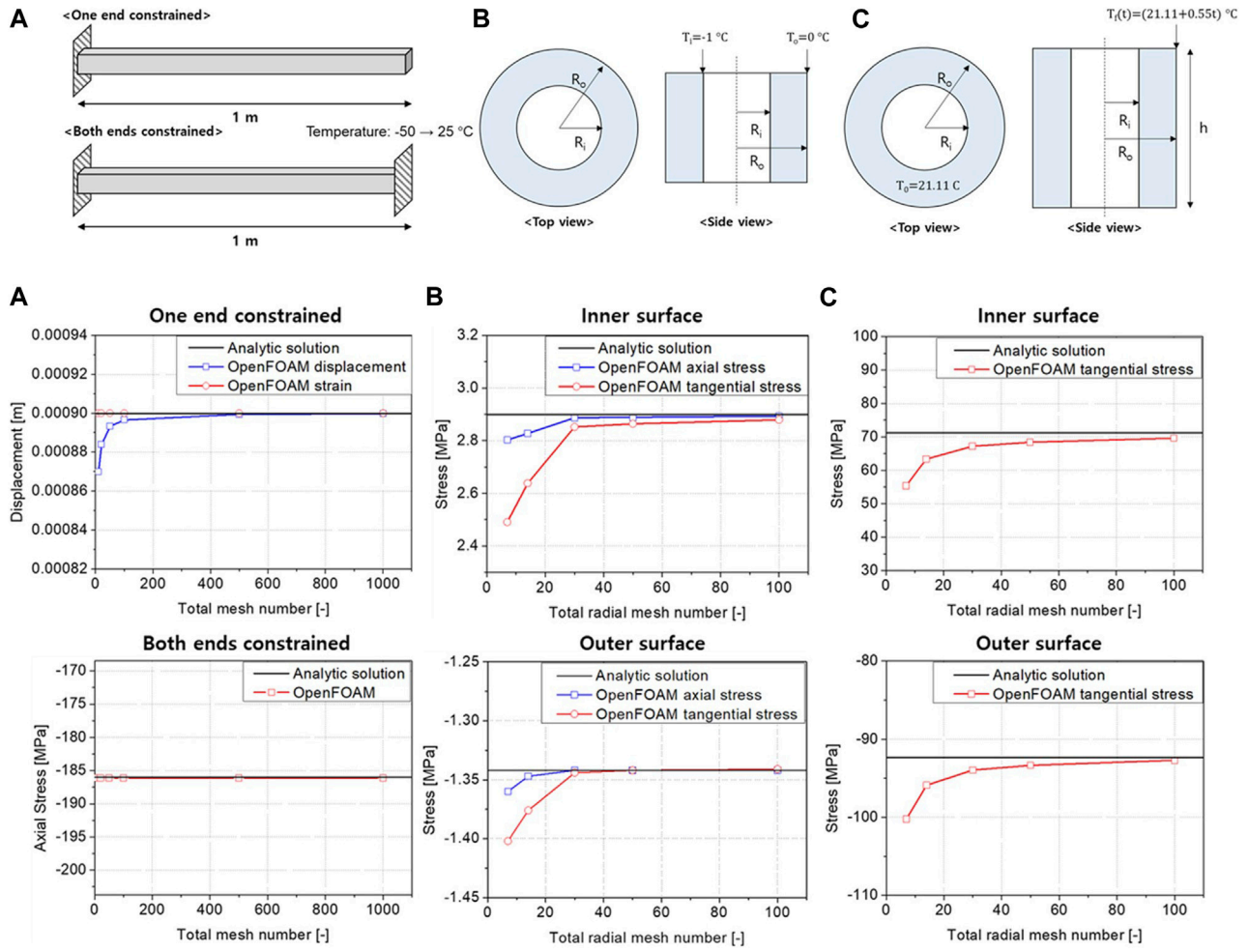

FIGURE 1
Conceptual representations and calculation results **(A)** constrained heated beam, **(B)** cylinder with thermal gradient (steady-state), and **(C)** cylinder with thermal gradient (transient).

not be carried out. Therefore, in this study, various improvements were made to the solver.

First, the thermal-structural analysis was verified. The verification problems were selected from the Autodesk Nastran verification manual (Autodesk Inc., 2015) and the ANSYS Mechanical APDL verification manual (ANSYS Inc., 2013).

The concepts of the verification problems and calculation results are illustrated in Figure 1. The first problem is constrained beam analysis with heating. Two cases were tested under single-end and both-end constraint boundary conditions. In both cases, the body temperature was increased from −50°C to 25°C. The predicted values of the displacement and axial stress were compared with the values in the analytical solution. The second problem is the steady-state calculation of a cylinder, with a linear temperature difference gradient between its inner and outer surfaces. The final problem is the transient calculation of the cylinder, wherein the outer surface temperature increases gradually. In the second and third cases, the stresses on the inner and outer surfaces were compared with the analytical solutions. For three verification problems, as the number of meshes increased, the solutions gradually converged to the analytical solutions. The thermal-structural analysis capability of the solver was confirmed through these simple verifications.

Subsequently, the capabilities of the solvers were extended to consider the temperature dependencies of structural materials and multiple-material handling. Therefore, a new field variable containing the material type was defined for each cell. Additionally, another field variable storing the volumetric heat generation rate was defined, and this value was added to the variable transferable from the external solver, considering the coupling of the code with a neutronics code.

2.2 Heat pipe analysis code, ANLHTP

ANLHTP is a one-dimensional steady-state thermal analysis code for sodium heat pipes (McLennan, 1983). The source code is available in existing literature, and the code used in the study was resurrected based on it (Lee et al., 2019). ANLHTP is a simple and

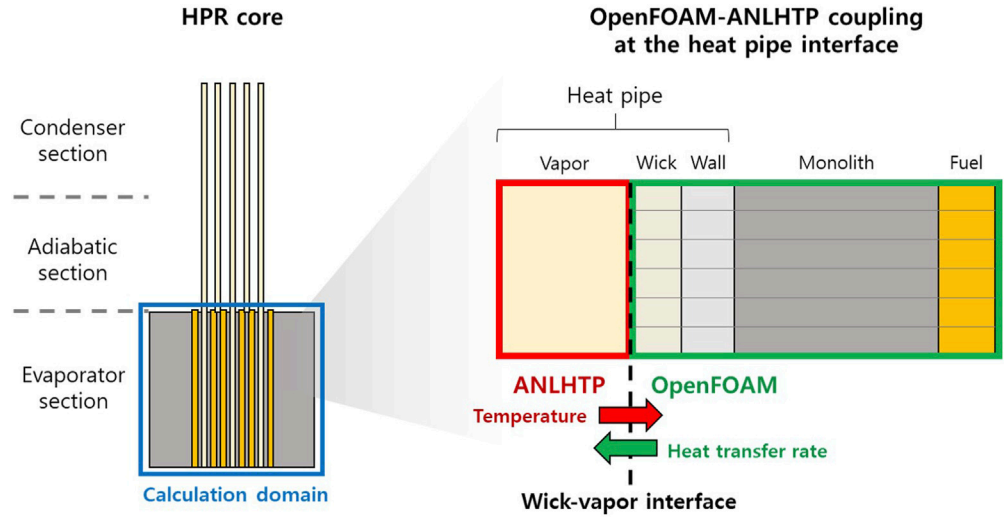

FIGURE 2
OpenFOAM-ANLHTP data exchange at the wick-vapor interface of the heat pipe.

fast lumped parameter code, and using a thermal resistance network, it predicts the heat transfer rate, temperature at each part, and operation limits of the heat pipe. The validation was performed against the ANL HPTF experiment (Holtz et al., 1985) and LASL experiment (Kemme et al., 1978); the heat pipe heat removal performance and operation limits were compared with those under these experiments. The details of the heat pipe specifications and experimental setup are presented in Ref. (Kemme et al., 1978; Holtz et al., 1985). The validation results confirmed that ANLHTP has reasonably predicted the heat pipe performance and operating limits and that the code had been correctly resurrected (Lee et al., 2019).

2.3 OpenFOAM-ANLHTP data exchange

The coupling of OpenFOAM and ANLHTP was established for the thermal-structural analysis of the HPR core. The coupled code used the coupling interface provided by OpenFOAM for external coupling (The OpenFOAM Foundation Ltd., Accessed 2023). Additionally, a Python wrapper code was developed to manipulate the data from the two codes. OpenFOAM sent the heat transfer rate field to the coupling boundary of the wrapper. Averages were then obtained for each part of the heat pipe, such as the evaporator, adiabatic section, and condenser. The averaged values were transferred from the wrapper to ANLHTP. ANLHTP calculates the temperatures of the three parts, returns them to the wrapper, and assigns these values to the meshes in each part; the three-dimensional code and lumped parameter code. This implied that the average heat transfer rate values in the multiple boundary faces of OpenFOAM were used for ANLHTP, and a single temperature value in each part of the heat pipe was used for the multiple boundary faces. This difference in the simulation dimensions can distort practical changes in parameters.

To minimize this distortion, the wick-vapor interface of the heat pipe evaporator was set as the data exchange interface, as shown in Figure 2. The temperature at the wick-vapor interface was assumed to have an insignificant temperature variation along the axis because its temperature was close to the saturation temperature in the vapor core. Using this method, the axially non-uniform heat transfer rate could be considered using the lumped parameter code ANLHTP (Zuo and Faghri, 1998).

2.4 Demonstration: mini-core problem

To demonstrate the capabilities of the OpenFOAM-ANLHTP, a mini-core problem was devised. The objective of the simulation was to verify whether the coupled code worked reasonably well under steady-state conditions. The mini-core problem is a conceptual problem referring to a non-nuclear testbed, such as the MAGNET experimental device (Morton et al., 2020). The mini-core is a 1-m height core containing 55 heat pipes and 84 fuel rods, and the helium gap exists between the fuel rod and monolith. Figure 3 shows the total geometry and computational mesh of the mini-core, and Table 1 shows the specifications and configuration of the mini-core. The arrangement of the heat pipes and fuel rods, including the diameter and pitch between them, followed that of the Megapower reactor (Mcclure et al., 2015). The thermal powers of each fuel rod and the reactor core were 1573 W and 132 kW, respectively. Following the first multiphysics conceptual problem, a uniform power distribution along the axis was assumed for the steady-state analysis. The screen wick of the heat pipe was referred to as the heat pipe of NASA (Reid, 2004), and the size and heat sink temperature of the heat pipe were referred to as the heat pipe of the Megapower reactor.

Regarding the thermal analysis using OpenFOAM, all boundaries except the heat pipe boundaries were set to adiabatic conditions. For the heat pipe boundaries, temperature boundary conditions were imposed; these conditions were obtained from the heat pipe thermal analysis using ANLHTP

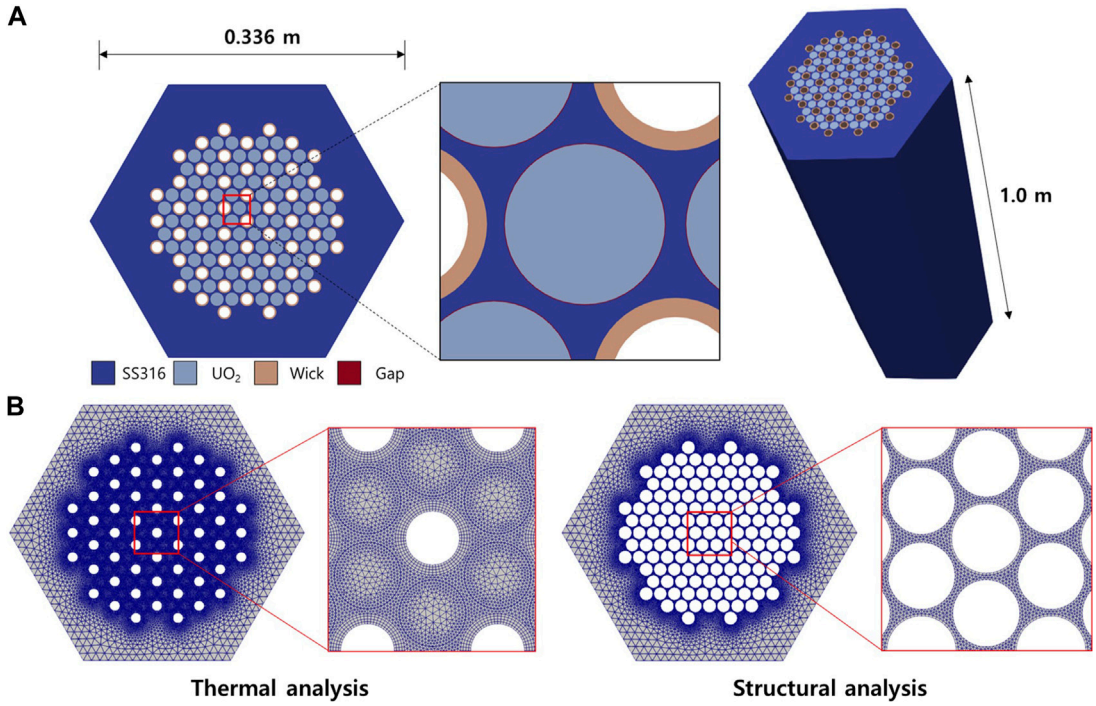

FIGURE 3
(A) Geometry and **(B)** computational mesh of the mini-core problem.

TABLE 1 Specific geometry and configuration of the mini-core.

Specifications of the core			
Fuel form	UO2	Fuel-to-fuel pitch	1.6 cm
U-235 enrichment	19.75 wt%	Fuel-to-HP pitch	1.6 cm
Outer diameter of fuel pellet	1.412 cm	Monolith material	SS316
Helium gap thickness	0.0065 cm	Monolith length	33.6 cm
Specifications of the heat pipe			
Working fluid	Sodium	Container OD	15.75 mm
		Container ID	14.75 mm
Wick structure	Screen wick + artery	Artery diameter	3.18 mm
Material of container and wick	Stainless steel 304	Number of arteries	1
Length (Evaporator—Adiabatic—Condenser)	1.0–1.0–1.0 m	Heat sink temperature	351°C

for each heat pipe. For the given boundary temperatures, the temperature field in the monolith was obtained, and the heat flux was evaluated for the heat pipe boundaries. The heat flux of each heat pipe was considered when conducting ANLHTP analyses on the heat pipes. Following the ANLHTP calculations, the temperature boundary conditions were updated for the next iteration. This procedure was repeated until the temperature field converged, following which the temperature field was transferred to the structural analysis solver. Since the concern of the structural analysis is the thermal stress in the monolith region, the computational domain of the analysis was limited to this region. Regarding the boundary conditions, a normally fixed condition was imposed on the bottom surface.

Thermal-structural analysis using the OpenFOAM-ANLHTP coupled code was performed to check the mesh convergence. The analysis results with three different meshes are presented in Figure 4A; the convergence of the maximum temperature and von Mises stress in the monolith was observed. Based on these results, the simulations were performed using the mesh size in case (c). Meanwhile, the maximum thermal stress was 200.8 MPa, exceeding the yield strength of SS316, which was 100 MPa at 700°C. This was because the problem was conceptually designed

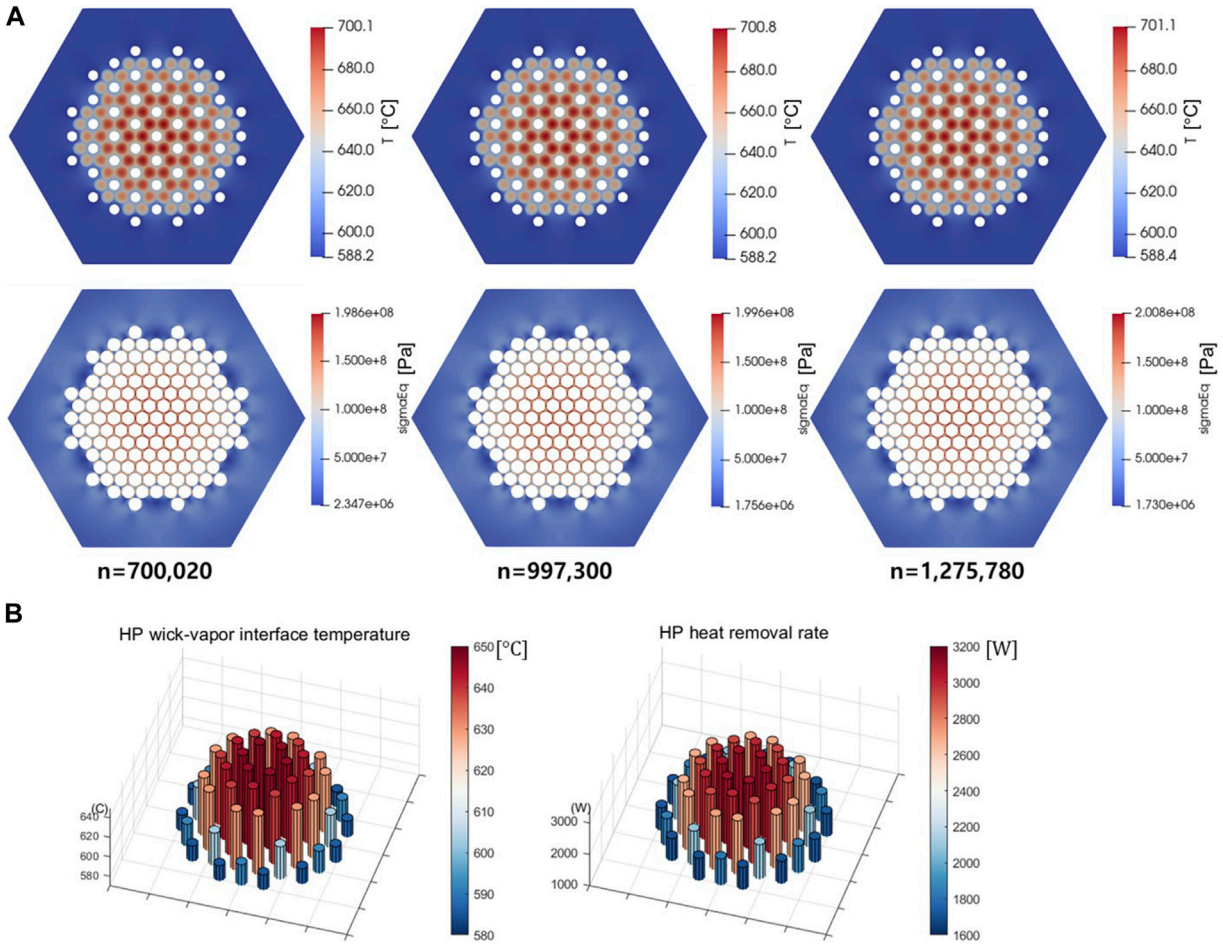

FIGURE 4
(A) Steady-state thermal-structural analysis results **(B)** interface temperature and heat removal rate of heat pipes for the mini-core problem.

for coupled thermal-neutronics analysis; structural integrity aspects such as the thermal stress were not the primary concern. Figure 4B shows the wick-vapor interface temperature and heat removal rate of the heat pipes in the mini-core problem. We observed a high heat removal rate and temperature in the central region and a decreasing trend toward the outside that caused a temperature difference within the monolith.

One of the main causes of high thermal stress was the relatively low temperature in the thick outer monolith region, which acted as a resistance to thermal expansion. To solve this problem, the mini-core geometry was modified to minimize the low-temperature region; the outer area of the reactor core edge was chopped off. Figure 5A presents the modified geometry assuming that the reflector surrounding the reactor core had a sufficient gap to dampen thermal expansion. However, if the outer monolith is too thin, thermal stress can increase at the outer monolith. Therefore, to find the optimal size of the monolith to reduce the maximum thermal stress, a parametric study of the monolith size was performed.

The same thermal-structural analysis was repeated for the chopped monolith geometry with various distances between the heat pipes and the outer periphery of the monolith, and the results are shown in Table 2. If the distance is too short, the stress in the outer area of the monolith becomes higher than that at the center. When the radius of the monolith was 0.133 m, the stress at both locations were similar. If the monolith radius is further increased, the stress at the center is expected to increase and gradually approach that of the original geometry. Also, as shown in Figure 5B, while the temperature distribution was almost the same as that of the original geometry, the maximum thermal stress was reduced from 200.8 to 167.6 MPa at the center. This implied that the outer space of the monolith needed to be considered during the design optimization process. The simulation of this conceptual problem revealed that the coupled code worked properly and that the convergence of the coupled simulation could be achieved stably.

3 OpenFOAM-ANLHTP-PRAGMA coupled code system

The aforementioned simulation was conducted using coupled OpenFOAM and ANLHTP, which imposed a uniform heat

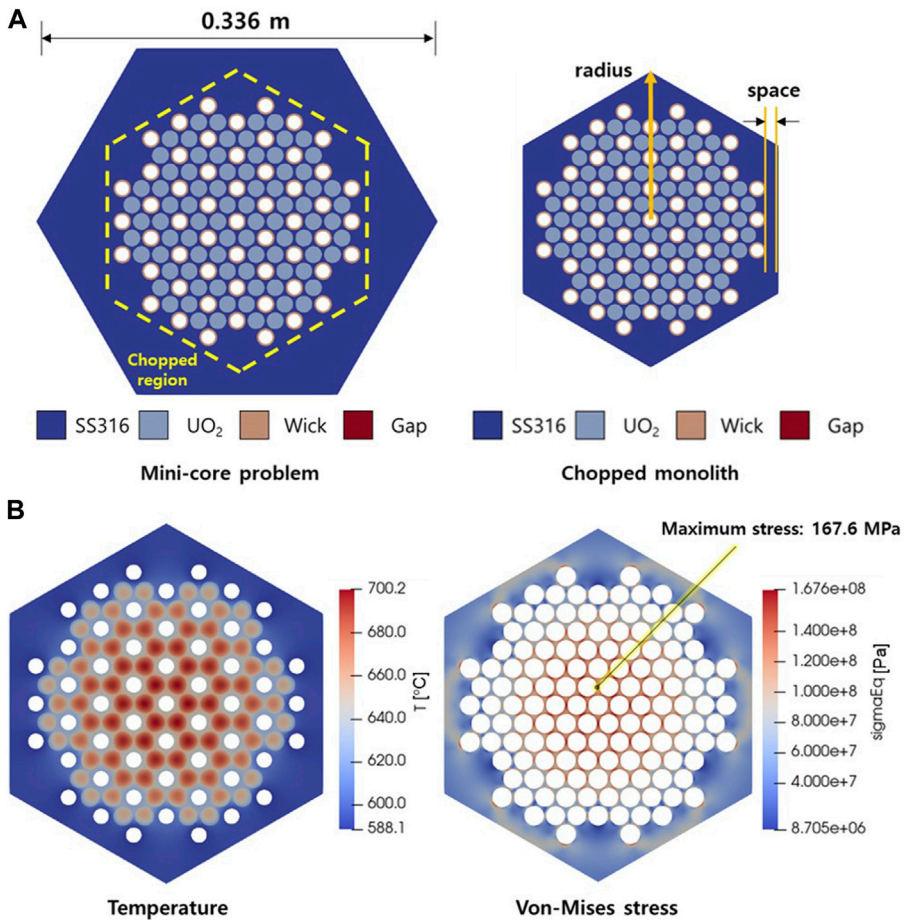

FIGURE 5
(A) Geometry and **(B)** thermal-structural analysis results (radius 0.133 m) of the mini-core with a chopped monolith.

TABLE 2 Parametric study on the size of the monolith.

Monolith radius (m)	Outer monolith space (mm)	Maximum stress at center (MPa)	Maximum stress at outer monolith (MPa)
0.121	1.50	135.5	329.7
0.124	4.01	144.3	219.4
0.127	6.61	151.6	198.2
0.130	9.21	160.0	181.8
0.133	11.81	167.6	163.8

generation rate to the core. For a more realistic simulation of the power distributions in the axial and radial directions, neutronics code coupling was required. In this study, a Monte Carlo neutron transport code, PRAGMA, was coupled with the other codes for the multiphysics simulations.

PRAGMA is a GPU-accelerated continuous energy Monte Carlo neutronics code developed by Seoul National University and was originally designed to perform simulations for power reactors (Choi et al., 2021). To analyze irregular and complex shapes such as the HPR core, PRAGMA exploits a hardware-accelerated ray tracing library to track neutrons in an unstructured mesh geometry (Im et al., 2023). It can conduct many particle simulations on NVIDIA CUDA-enabled GPU cards with a reasonable timescale. For the efficient coupling of the GPU and CPU parallelization schemes, the coupling system was established by employing an MPI dynamic process management mode, wherein manager-worker parallelism was maintained, as shown in Figure 6. Both PRAGMA and OpenFOAM were linked to their respective workers as dynamic libraries, and their workers

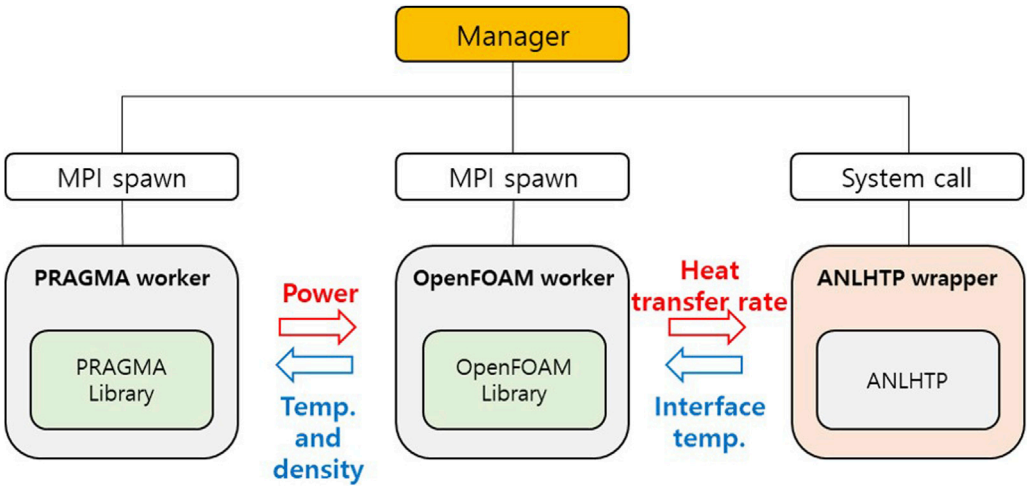

FIGURE 6
Manager-worker system of OpenFOAM-ANLHTP-PRAGMA.

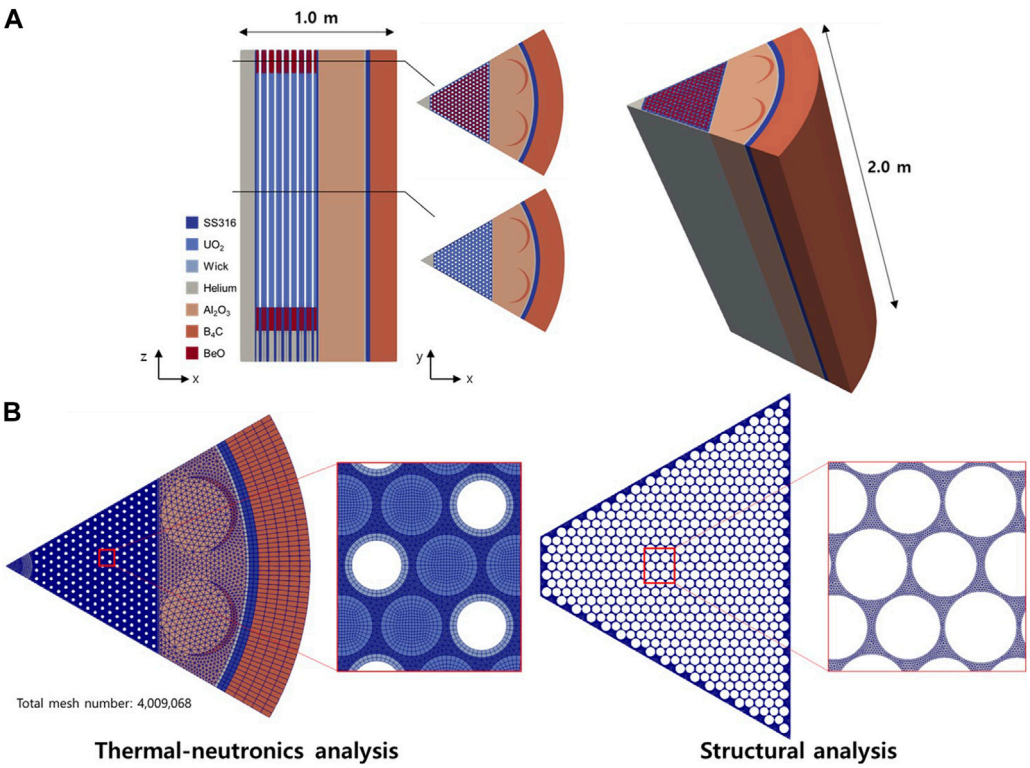

FIGURE 7
(A) Geometry and **(B)** computational mesh of the Megapower reactor.

communicated through the manager. The wrapper script for the OpenFOAM and ANLHTP coupling was executed in the background by the manager. For the reactivity feedback, OpenFOAM provided the temperature and density, and PRAGMA calculated the power from the received temperature and density fields.

The Megapower reactor core was analyzed to demonstrate the capability of the OpenFOAM-ANLHTP-PRAGMA coupled code. For the steady-state analysis, 1/6 section of the reactor core was considered for the computational domain. The Megapower reactor is an HPR design suggested by LANL. The geometry and computational mesh of the sectioned Megapower reactor core are

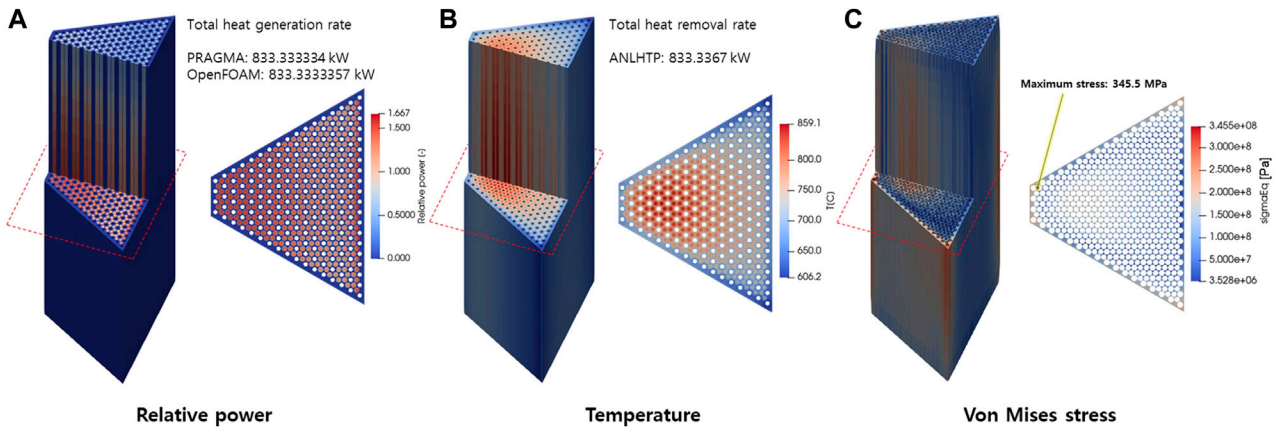

FIGURE 8
Analysis results of the Megapower reactor **(A)** power **(B)** temperature **(C)** stress.

shown in Figure 7. It included 352 fuel rods and 204 heat pipes, and the total power of the 1/6 section core was 833 kW. Sodium was selected as the working fluid of the heat pipe. The geometry and specifications of the heat pipe were the same as those used in the mini-core problem, except that the evaporator length was 1.5 m. Like the mini-core problem, all the boundaries, except for the heat pipe boundary, were set to adiabatic conditions, and the structural analysis was conducted with a normally fixed bottom surface.

The results of the multiphysics analysis are shown in Figure 8. A cosine-shaped power distribution in the axial direction, maximum power in the center, and power increase in the radial direction near the outer reflector were observed. Regarding the uncertainty of power distribution of PRAGMA, RMS averaged mesh-wise power uncertainty was 0.318%. The maximum temperatures of the fuel rod and monolith were 859.1° and 798.3°C, respectively. The total heat generation rate of PRAGMA and OpenFOAM, and heat removal rate of ANLHTP were consistent within a difference of a maximum 3 W, confirming that the variable exchange between the coupled codes is working well. The high temperature of the monolith could decrease the yield strength, resulting in the deterioration of the structural integrity of the monolith. One reason for the high temperature of the monolith was that the working fluid of the heat pipe was sodium, which has a higher working temperature than potassium, the actual working fluid in the Megapower reactor design. Hence, to reduce the temperature, additional optimizations, such as changing the working fluid or modifying the heat pipe design, can be considered. A maximum thermal stress of 345.5 MPa appeared in the corner region of the monolith, exceeding 100 MPa, which was the yield strength of SS316 at that temperature.

4 Parametric study on the heat sink temperature of heat pipes

The reasons for the high thermal stress shown in the mini-core and Megapower reactor core calculations were temperature difference within the monolith and the geometry. Figure 9 shows the temperature and stress distributions at the point where the maximum thermal stress appeared in the mini-core. A large temperature gradient was observed between the fuel rods and heat pipes in a narrow region between the fuel rods. Therefore, it was necessary to reduce the temperature difference or extend the distance between the fuel rods and heat pipes to reduce thermal stress. However, it is difficult to improve the geometry of the core because its small size is a requirement for transportation. Therefore, to flatten the temperature within the monolith, the heat removal rate of the heat pipes was controlled. In this paper, the sink temperatures of the heat pipes were partially adjusted to control the heat removal rate.

4.1 Cases of parametric study

To evaluate the thermal stress due to the temperature difference within the monolith and confirm the effect of adjusting the heat sink temperature, four simulations were conducted depending on the application of a realistic power distribution, heat pipe code coupling, and heat sink temperature adjustment, as listed in Table 3.

Case 1 is the simplest condition for comparison, where a uniform power distribution is applied, and the heat pipe interface temperature is assumed to be constant at all locations. From Case-1 to Case-2, the power distribution obtained from the PRAGMA was applied, which increased the temperature difference within the monolith as more heat was generated locally in some fuel rods; this increased the thermal stress in the monolith. From Case-2 to Case-3, non-uniform heat pipe interface temperatures were applied at every heat pipe as the heat pipe code was coupled. The temperature difference in the monolith was expected to increase as a higher heat pipe interface temperature would be applied at a region where high heat generation rate was applied. This resulted in an increased thermal stress in the monolith. Finally, to reduce the increased thermal stress in Case-2 and Case-3 and flatten the temperature

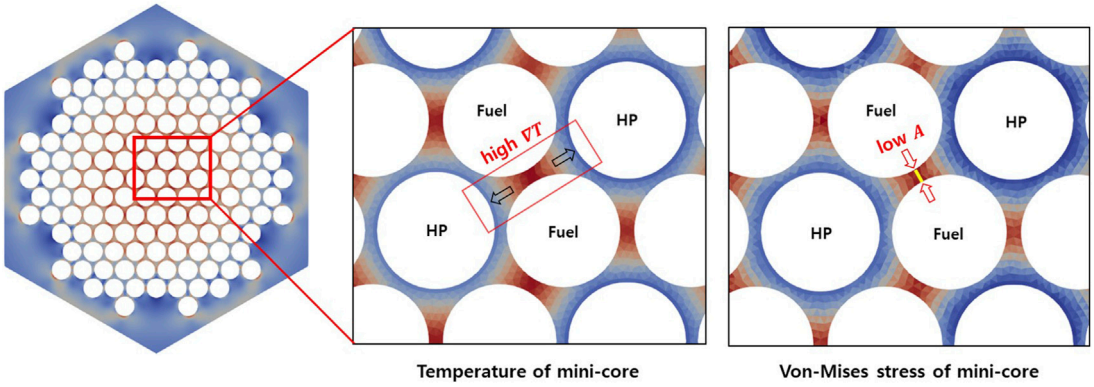

FIGURE 9
Temperature and stress at the maximum thermal stress region of the mini-core.

TABLE 3 Calculation conditions of parametric study.

	Core power distribution	Heat pipe code coupling	Heat pipe sink temperature
Case-1	Uniform	No, uniform temperature	Not available
Case-2	From neutronics code	No, uniform temperature	Not available
Case-3	From neutronics code	Heat pipe code coupling	Uniform heat sink temperature
Case-4	From neutronics code	Heat pipe code coupling	Adjusted heat sink temperature

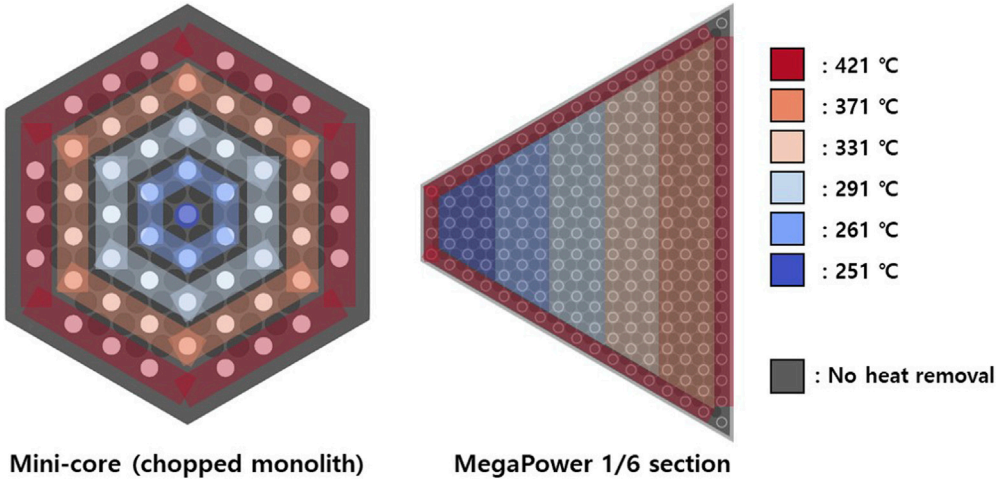

FIGURE 10
Heat pipe grouping for the heat sink temperature adjustment.

field in the monolith, the heat sink temperatures at each heat pipe were adjusted in Case-4. The heat pipes were divided into five or six groups based on their locations, and different heat sink temperatures were imposed depending on the groups. Higher temperature conditions were applied where the monolith temperature was lower, and *vice versa*. It was expected that the temperature difference in the monolith could be reduced with this adjustment because more and less heat could be removed when the monolith temperature was higher and lower, respectively. The heat pipe groupings for the mini-core

TABLE 4 Thermal-structural analysis results of the mini-core and Megapower reactor.

Mini-core (chopped monolith)				
	Case-1	Case-2	Case-3	Case-4
Maximum fuel temperature (°C)	675.3	713.9	753.0	724.3
Maximum monolith temperature (°C)	637.9	649.7	688.0	659.5
Minimum monolith temperature (°C)	619.4	619.4	585.7	602.6
Monolith temp. diff. (max-min) (°C)	18.5	30.3	102.3	56.9
Monolith max. thermal stress (MPa)	41.2	69.3	232.4	127.6
1/6 section of Megapower reactor				
	Case-1	Case-2	Case-3	Case-4
Maximum fuel temperature (°C)	756.9	786.4	859.1	801.7
Maximum monolith temperature (°C)	718.5	727.8	798.5	743.0
Minimum monolith temperature (°C)	699.2	699.2	606.4	663.1
Monolith temp. diff. (max-min) (°C)	19.3	28.6	192.1	79.9
Monolith max. thermal stress (MPa)	43.0	62.3	345.5	163.9

and sectioned core of the Megapower reactor are shown in Figure 10. Regarding the Megapower, adiabatic conditions were used for the two heat pipes at the corner, wherein a high thermal stress appeared owing to relatively low temperatures. The imposed heat sink temperatures are shown in Figure 10.

4.2 Parametric study result

The thermal-structural analysis results for each condition for the mini-core and Megapower reactor are shown in Table 4 and Figure 11 shows the comparison results between Cases-3 and 4 in the two geometries. Compared to Case-1, wherein a uniform power distribution and constant heat pipe interface temperature were used, the temperature difference and maximum thermal stress within the monolith increased when the power distribution obtained using PRAGMA was applied (Case-2), and the heat pipe code was coupled (Case-3). Particularly, the maximum temperature difference in the monolith increased remarkably for both geometries when the heat pipe code was coupled (Case-3). When the heat sink temperatures were adjusted depending on the groups (Case-4), the temperature field was relatively flattened as shown in Figure 11, and the temperature difference was reduced, as shown in Table 4. Consequently, the thermal stress within the monolith decreased. These results implied that the non-uniform heat removal rate of heat pipes, depending on their location and monolith temperature, could reduce the thermal stress in the monolith core. The heat sink design of the heat pipes needs to be considered as one of the optimization parameters because an appropriate design can reduce the thermal stress in the monolith

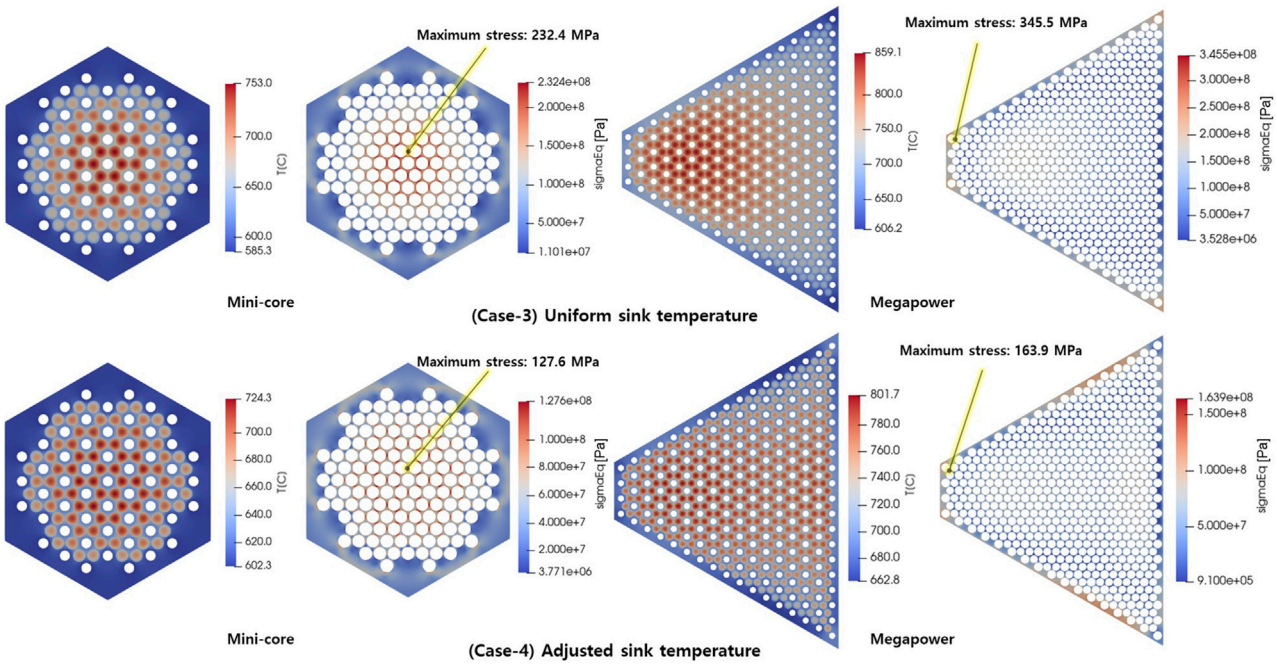

FIGURE 11
Thermal-structural analysis results of the mini-core and Megapower (Case-3 and Case-4).

without modifying the core geometry, and the issue of high thermal stress is one of the challenges in designing a monolith core type microreactor.

5 Conclusion

In this study, a multiphysics analysis tool was developed for an HPR core. First, OpenFOAM and ANLHTP were coupled to establish a thermal-structural analysis system. To demonstrate the thermal-structural analysis capability of the OpenFOAM-ANLHTP coupled code, a steady-state analysis of the mini-core problem was conducted; a high thermal stress was observed in the monolith. To reduce the high thermal stress of the mini-core, a chopped monolith problem was newly defined, and it was confirmed that the thermal stress could be reduced through geometry modification.

Next, coupling with PRAGMA was performed to establish a neutronic-thermal-structural analysis system. To demonstrate the multiphysics analysis capability of the coupled code, a steady-state analysis was performed on the Megapower reactor core, and the coupled code showed physically proper results. However, both the mini-core and the Megapower reactor core exhibited high thermal stress exceeding the yield strength of the monolith. Therefore, to reduce the temperature difference within the monolith, which caused the high thermal stress, a heat pipe sink temperature distribution was applied. With the adjusted heat pipe sink temperature, it was confirmed that thermal stress could be reduced by decreasing the temperature difference within the monolith.

In the future, the coupled code can be used for the design and optimization of HPR cores. Necessary improvements in the coupled codes include transient analysis capability, and mesh deformation for a more realistic neutron leakage evaluation. Particularly, the VandV of each code was separately conducted before the coupling, and the capability of the coupled code has been demonstrated. However, the validation of multi-physics analysis capability of a monolith type HPR core is necessary and will be performed in the future when the required information for the modelling becomes available. Additionally, heat pipe experiments with a monolith are planned for producing validation data.

Data availability statement

The original contributions presented in the study are included in the article/supplementary material, further inquiries can be directed to the corresponding author.

Author contributions

MJ, JI, SL, and HC contributed to conception and design of the study. MJ, JI, and SL carried out the code coupling. MJ and JI carried out the multiphysics analysis using coupled code. MJ, JI, and HC contributed to the interpretation of the simulation results. MJ wrote the first draft of the manuscript. MJ, JI, SL, and HC contributed to manuscript revision, read, and approved the submitted version.

Funding

This work was supported by the National Research Foundation of Korea (NRF) grant funded by the Korea government (Ministry of Science and ICT) (Nos 2020M2D2A1A02066317, 2021M2D6A1048220).

Conflict of interest

The authors declare that the research was conducted in the absence of any commercial or financial relationships that could be construed as a potential conflict of interest.

Publisher's note

References

Ansys Inc (2013). *ANSYS mechanical APDL verification manual*. Canonsburg, Pennsylvania: Ansys Inc.

Autodesk Inc (2015). *Autodesk® Nastran® 2016 verification manual*. San francisco, CA, USA: Autodesk.

Choi, N., Kim, K. M., and Joo, H. G. (2021). Optimization of neutron tracking algorithms for GPU-based continuous energy Monte Carlo calculation. *Ann. Nucl. Energy* 162, 108508. doi:10.1016/j.anucene.2021.108508

Fiorina, C., Clifford, I., Aufiero, M., and Mikityuk, K. (2015). GeN-foam: A novel OpenFOAM®based multiphysics solver for2D/3D transient analysis of nuclear reactors. *Nucl. Eng. Des.* 294, 24–37. doi:10.1016/j.nucengdes.2015.05.035

Ge, L., Li, H., Tian, X., Ouyang, Z., Kang, X., Li, D., et al. (2022). Improvement and validation of the system analysis model and code for heat-pipe-cooled microreactor. *Energies* 15 (7), 2586. doi:10.3390/en15072586

Gibson, M. A., Poston, D., Mcclure, P., Godfroy, T. J., Briggs, M. H., and Sanzi, J. L. (2018). "Kilopower reactor using stirling technology (krusty) nuclear ground test results and lessons learned," in Proceedings of the 2018 International Energy Conversion Engineering Conference, Cincinnati, Ohio, July 2018. doi:10.2514/6.2018-4973

Guo, Y., Li, Z., Huang, S., Liu, M., and Wang, K. (2021). A new neutronics-thermal-mechanics multi-physics coupling method for heat pipe cooled reactor based on RMC and OpenFOAM. *Prog. Nucl. Energy* 139, 103842. doi:10.1016/j.pnucene.2021.103842

Guo, Y., Li, Z., Wang, K., and Su, Z. (2022). A transient multiphysics coupling method based on OpenFOAM for heat pipe cooled reactors. *Sci. China Technol. Sci.* 65, 102–114. doi:10.1007/s11431-021-1874-0

Holtz, R. E., McLennan, G. A., and Koehl, E. R. (1985). *On the experimental operation of a sodium heat pipe*. Lemont, IL, USA: Argonne National Laboratory. doi:10.2172/5100887

Hu, G., Hu, R., Kelly, J. M., and Ortensi, J. (2019). *Multiphysics simulations of heat pipe micro reactor*. Lemont, IL, USA: Argonne National Laboratory. doi:10.2172/1569948

Huang, J., Wang, C., Tian, Z., Guo, K., Su, G. H., Tian, W., et al. (2022). Preliminary conceptual design and analysis of a 100 kW e level Nuclear Silent Thermal-Electrical Reactor (NUSTER -100). *Int. J. Energy Res.* 46 (14), 19653–19666. doi:10.1002/er.8542

Im, J., Jeong, M. J., Kim, K. M., Cho, H. K., and Joo, H. G. (2023). Multiphysics analysis system for heat pipe cooled micro reactors employing PRAGMA-OpenFOAM-ANLHTP. *Nucl. Sci. Eng.* 26. doi:10.1080/00295639.2022.2143209

Kemme, J. E., Keddy, E. S., and Phillips, J. R. (1978). "Performance investigations of liquid-metal heat pipes for space and terrestrial applications," in Proceedings of the 3rd International Heat Pipe Conference, Palo Alto,CA,USA, May 1978.

Lange, T. (2020). *Experience with DireWolf for heat-pipe microreactor analysis to support early demonstration*. Idaho Falls, ID, USA: Idaho national laboratory.

Lee, C. H., Jung, Y. S., and Cho, H. K. (2019). *Micro reactor simulation using the PROTEUS suite in FY19*. Lemont, IL, USA: Argonne National Laboratory. doi:10.2172/1571248

Lee, S. N., Choi, S. H., and Kim, C. S. (2021). "Development of heat transfer analysis code for heat pipe cooled space reactor core," in Proceedings of the Transactions of the Korean Nuclear Society Spring Meeting, Kyeongju, Korea, May 2021.

Matthews, C., Laboure, V., DeHart, M., Hansel, J., Andrs, D., Wang, Y., et al. (2021). Coupled multiphysics simulations of heat pipe microreactors using Direwolf. *Nucl. Technol.* 207 (7), 1142–1162. doi:10.1080/00295450.2021.1906474

Mcclure, P. R., Poston, D. I., Dasari, V. R., and Reid, R. S. (2015). *Design of megawatt power level heat pipe reactors*. Los Alamos, NM, USA: Los Alamos National Lab. doi:10.2172/1226133

McLennan, G. A. (1983). *ANL/HTP: A computer code for the simulation of heat pipe operation*. Lemont, IL, USA: Argonne National Laboratory.

Morton, T. J., O'Brien, J. E., and Hartvigsen, J. L. (2020). *Functional and operating requirements for the microreactor agile non-nuclear experimental test bed (MAGNET)*. Idaho Falls, ID, USA: Idaho National Lab.

Oklo Inc (2020). Part II: Final safety analysis report. https://www.nrc.gov/docs/ML2007/ML20075A003.pdf.

Reid, R. S. (2004). Alkali metal heat pipe life issues. Proceedings of the 2004 International Congress on Advances in Nuclear Power Plants, La Grange Park, IL, USA, June 2004.

Scolaro, A., Clifford, I., Fiorina, C., and Pautz, A. (2020). The OFFBEAT multi-dimensional fuel behavior solver. *Nucl. Eng. Des.* 358, 110416. doi:10.1016/j.nucengdes.2019.110416

Stauff, N., Mo, K., Cao, Y., Thomas, J., Miao, J., Zou, L., et al. (2021). *Detailed analyses of a TRISO-fueled microreactor*. Lemont, IL, USA: Argonne National Laboratory. doi:10.2172/1826285

Sterbentz, J. W., Werner, J. E., McKellar, M. G., Hummel, A. J., Kennedy, J. C., Wright, R. N., et al. (2017). *Special purpose nuclear reactor (5 MW) for reliable power at remote sites assessment report using phenomena identification and ranking tables (PIRTs)*. Idaho Falls, ID, USA: Idaho national laboratory. doi:10.2172/1410224

Swartz, M. M., William, A. B., John, L., and Rory, B., (2021). Westinghouse evinci™ heat pipe micro reactor technology development. Proceedings of the 2021 28th International Conference on Nuclear Engineering. Qingdao, China, August 2021. 85246.

Tak, N. I., Lee, S. N., and Kim, C. S. (2020). *Development of computer code for performance analysis of heat pipe of a space nuclear reactor*. Korea Atomic Energy Research Institute.

Tang, S., Liu, X., Wang, C., Zhang, D., Su, G., Tian, W., et al. (2022). Thermal-electrical coupling characteristic analysis of the heat pipe cooled reactor with static thermoelectric conversion. *Ann. Nucl. Energy* 168, 108870. doi:10.1016/j.anucene.2021.108870

The OpenFOAM Foundation Ltd (2023). C++ source code guide. https://cpp.openfoam.org/v7/classFoam_1_1externalCoupledTemperatureMixedFvPatchScalarField.html (Accessed Mar 02, 2023).

The OpenFOAM Foundation Ltd (2019). *OpenFOAM v7*. https://openfoam.org/version/7/ (Accessed Jan 09, 2023).

Zuo, Z. J., and Faghri, A. (1998). A network thermodynamic analysis of the heat pipe. *Int. J. Heat. Mass Transf.* 41 (11), 1473–1484. doi:10.1016/S0017-9310(97)00220-2

frontiers | Frontiers in Energy Research

TYPE Original Research
PUBLISHED 10 October 2023
DOI 10.3389/fenrg.2023.1284230

OPEN ACCESS

EDITED BY
Yugao Ma,
Nuclear Power Institute of China (NPIC), China

REVIEWED BY
Shanfang Huang,
Tsinghua University, China
Zeyun Wu,
Virginia Commonwealth University, United States
Luteng Zhang,
Chongqing University, China

*CORRESPONDENCE
Tengfei Zhang,
zhangtengfei@sjtu.edu.cn

RECEIVED 28 August 2023
ACCEPTED 15 September 2023
PUBLISHED 10 October 2023

CITATION
Wang D, Xiao W, Du Z and Zhang T (2023), An adaptive time stepping stiffness confinement method for solving reactor dynamics equations.
Front. Energy Res. 11:1284230.
doi: 10.3389/fenrg.2023.1284230

An adaptive time stepping stiffness confinement method for solving reactor dynamics equations

Dan Wang, Wei Xiao, Zhaohui Du and Tengfei Zhang*

School of Mechanical Engineering, Shanghai Jiao Tong University, Shanghai, China

The stiffness confinement method (SCM) is frequently employed to solve the reactor dynamics equations because it confines the stiffness of the problem by frequency transformation. However, the balance between the error and efficiency of the SCM has not been well studied. This paper reports the error analysis of the SCM. The error by SCM is derived mathematically and written as integral error, driven by the integral of the frequency interpolation function. An easy-to-implement adaptive time-stepping (ATS) algorithm is proposed based on the error analysis by controlling the neutron flux amplitude error. First, a fine-step PKE is leveraged to estimate the second-order derivative of the flux amplitude-frequency, which is used to predict the error of the neutron flux amplitude. The low cost of solving the PKE incurs a negligible effect on the algorithm's efficiency. Second, based on the error analysis, an error estimator proposed to determine an optimal time-step size for the neutron temporal-spatial equation. With a pre-set error tolerance, the ATS algorithm is exempted from the empirical selection of the time-step size in transient simulations. Numerical tests with TWIGL and modified 2D LMW benchmark problems show that the optimal time-step size effectively confines the local truncation error of the flux amplitude within the pre-set tolerance. The ATS algorithm yields a higher accuracy at a commensurate computational cost than calculations with fixed time-steps.

KEYWORDS

stiffness confinement method, reactor dynamics equation, error analysis, adaptive time stepping algorithm, nuclear reactor

1 Introduction

Reactor dynamics equations (NDEs), such as the neutron temporal-spatial equation (NTSE) and the point kinetics equation (PKE), are employed to predict the transient behaviors of the neutron flux and precursors in a nuclear reactor. In the NDEs, the generation time of prompt and delayed neutrons involves multiple time scales. As these different time scales bring stiffness in the NDE, the time-step size must be sufficiently small to yield accurate results. The fine time-step causes a significant computational burden to the reactor dynamics calculations. Therefore, the stiffness confinement method (SCM) was proposed. In doing so, the SCM introduces the flux frequency and the precursor frequency to decouple the precursor equation from the NDE, thus confining the stiffness to the prompt neutron equation (Chao and Attard, 1985). Next, an exponential solution assumption decomposes the flux amplitude-frequency into the amplitude and shape frequencies (Park and Joo, 2015). By these means, the problem is transformed into a dynamic eigenvalue problem (EVP) that exhibits a similar equation form as that for the steady-state eigenvalue

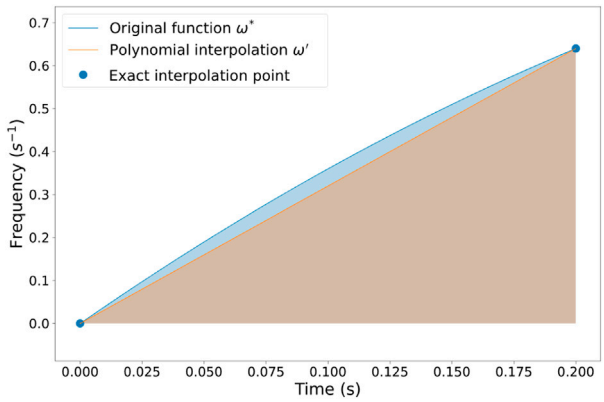

FIGURE 1
Illustration of integral error and zero-point bias with linear approximation.

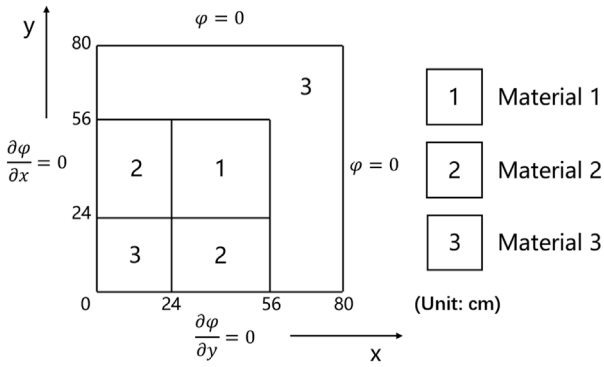

FIGURE 2
Layout of TWIGL benchmark problem.

problem. Therefore, the dynamic EVP can be solved efficiently by power iteration and the non-linear iteration algorithm.

The SCM has already been applied in the PKE and the diffusion and transport NTSEs (Park and Joo, 2015; Tang et al., 2019). It has been demonstrated that the SCM can provide accurate and stable solutions. However, although the SCM enables solving the NTSE with a large time-step size, the computational cost of the NTSE at each time step is still high, especially for transport calculations. The adaptive time-stepping (ATS) algorithm has received much attention for further reducing computational costs. It allows transient solvers to optimally determine the time-step sizes according to the current transient state and the pre-set error tolerance. The algorithm improves the computational efficiency by allocating more time steps in time intervals where necessary. In addition, the ATS algorithm saves the trouble of empirically selecting the time-step size in transient simulations. Hence, ATS algorithms have been applied in solution methods to NTSE, such as the implicit Euler method, the quasi-static method, and the PKE-based SCM (Caron et al., 2017). However, an effective ATS algorithm for the three-dimensional SCM has yet to be developed because of the lack of comprehensive error analysis.

ATS algorithms are generally based on estimating and controlling of the local truncation error. Classically, the local truncation error ε of a numerical method of order q can be expressed as (Tang et al., 2019):

$$\varepsilon(t) = \Theta(t)h^{q+1} + O\left(h^{q+2}\right) \tag{1}$$

where t denotes the time, Θ is the norm of the principal error function, and h is the time-step size. Generally, Θ is estimated with an error bound. The error bound is appropriated via the high-order derivative or even the Jacobian matrix of the solution. For lower complexity, Θ can be assumed as constant between successive time steps and calculated by numerical differentiation. The numerical differentiation is computed using solutions from previous time steps (Caron et al., 2017). This approach does not require extra computation, but the predicted error may deviate significantly from the actual error. The deviation leads to a non-optimal time-step size and affects the efficiency of the ATS algorithm. Another practical ATS algorithm estimates the error by comparing the solution with a reference solution. With gradually reduced time-step size, the solution is rejected until the error between the computed solution and the reference solution reaches the pre-set tolerance. The adaptive time-step size is found by successively comparing solutions with two different time-step sizes and choosing the finer step solution as the reference one (Boffie and Pounders, 2018). Another approach is the embedded pair, which selects the time-step size by embedding low-order methods in the high-order method. For instance, a generalized Runge-Kutta method of fourth-order accuracy embeds a third-order solution to estimate the adaptive time-step size (Zimin and Ninokata, 1998). Although these ATS algorithms are easy to implement, the rejection-acceptance procedure calls for extra computation. Therefore, it is beneficial to develop an ATS algorithm that can efficiently and accurately control the time-step size for the SCM.

In this work, a theoretical error analysis of the SCM is performed. The theoretical analysis produces a mathematical error expression of the SCM. Further, an ATS algorithm is proposed by controlling the error of the neutron flux amplitude. In doing so, a fine-step PKE solver is used to evaluate high order derivatives of the neutron flux amplitude in the error expression. In addition, an error estimator based on the error expression is proposed and examined using benchmark problems.

TABLE 1 Transient cases in TWIGL benchmark problem.

Case	Perturbation
Composite	$\Sigma_{a,2}(\vec{r},t) = \begin{cases} \Sigma_{a,2}(\vec{r},0) \times (1 - 0.2905t) & t \le 0.2s \\ \Sigma_{a,2}(\vec{r},0) \times [1.01167 + 0.05833(t - 0.2)] & 0.4s \ge t > 0.2s \\ \Sigma_{a,2}(\vec{r},0) & 0.5s \ge t > 0.4s \end{cases}$

Note: $\vec{r} \in$ regionofMaterial1.

10.3389/fenrg.2023.1284230

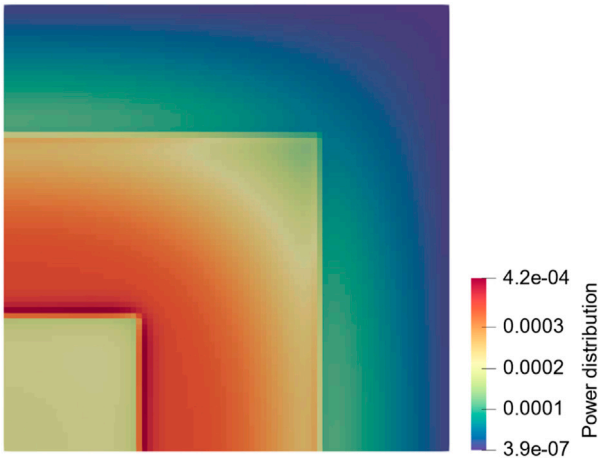

FIGURE 3
Initial power distribution for TWIGL.

It is demonstrated that the ATS algorithm yields a higher accuracy at a commensurate computational cost than calculations with fixed time-steps.

The remainder of the paper proceeds as follows. Section 2 briefly describes the frequency-transformed NTSE and PKE. Solution methods to these equations are introduced in Section 3. In Section 4, the SCM's theoretical error analysis is performed, and an ATS algorithm based on the error analysis is proposed. Section 5 elaborates the coupling between the NTSE solver with the PKE solver. Section 6 illustrates the performance of error estimators and offers comparisons of the efficiency and accuracy between ATS and fixed time-stepping (FTS). Section 7 concludes the paper and points to directions for future research.

2 Frequency-transformation of dynamics models

The derivation of the SCM starts with the definition of the dynamic frequency. The dynamic frequency $\alpha(r,t)$ of a physical quantity $f(r,t)$ is defined as (Chao and Attard, 1985):

$$\alpha(r,t) = \frac{1}{f(r,t)} \frac{\partial f(r,t)}{\partial t} \quad r \in \mathbb{R}^3, t \in \mathbb{R} \tag{2}$$

where r is the spatial variable and t is the time variable. By introducing the dynamic frequency, a composite exponential function is employed to describe $f(r,t)$. Thus, the following exponential form of the solution is obtained:

$$f(r,t) = f(r,t_0) e^{\int_{t_0}^{t} dt' \alpha(r,t')} \tag{3}$$

Transient equations imposed with the dynamic frequency are called frequency-transformed equations. The frequency-transformed equations are solved by discretizing the time variable and searching $\alpha(r,t)$ iteratively.

For simplicity, we investigate the application of the SCM to the NTSE with diffusion approximation. Extending the methodology to neutron transport problems is not arduous (Park and Joo, 2015). Transient multi-group neutron diffusion equations with delayed neutron precursors are given as:

$$\begin{aligned} &\frac{1}{v_g} \frac{d\varphi_g(r,t)}{dt} + \left[-\nabla \cdot D_g(r,t)\nabla + \Sigma_{t,g}(r,t)\right]\varphi_g(r,t) \\ &= \left[\chi_g(r)(1-\beta)Q(r,t) + \sum_{g'=1}^{G} \Sigma_{g'-g}(r,t)\varphi_{g'}(r,t)\right] \\ &\quad + \sum_{i=1}^{I} \chi_{ig}\lambda_i C_i(r,t) \quad g = 1, \cdots, G \end{aligned} \tag{4}$$

$$\frac{dC_i(r,t)}{dt} = \beta_i Q(r,t) - \lambda_i C_i(r,t) \quad i = 1, \cdots, I \tag{5}$$

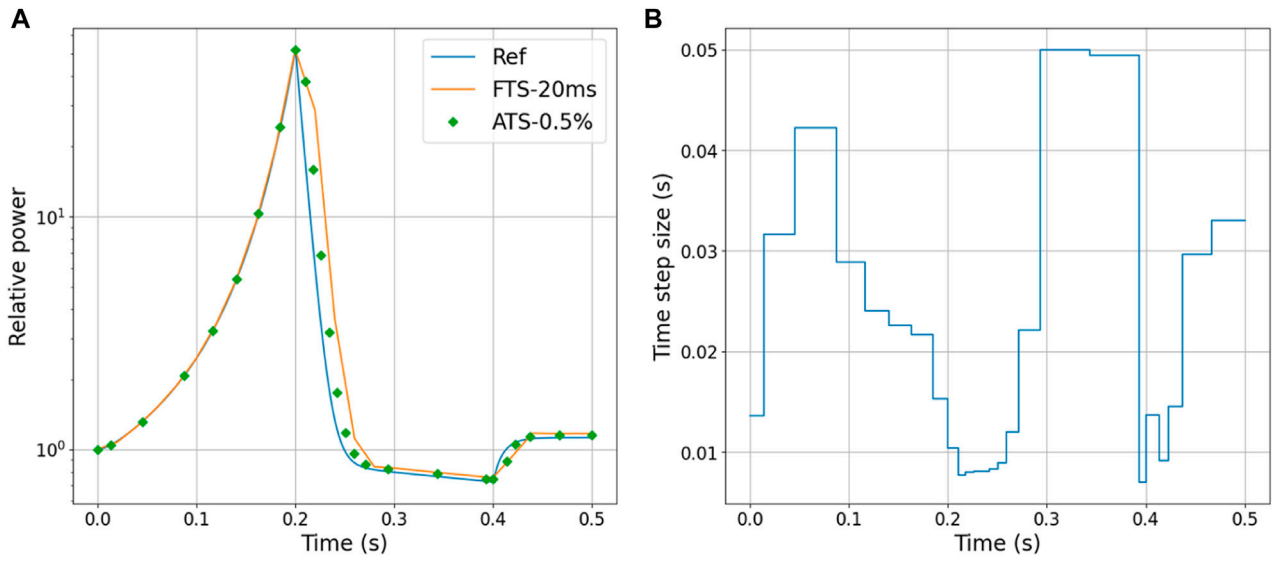

FIGURE 4
Comparison of ATS-0.5% and FTS-20 ms in TWIGL **(A)** Core power **(B)** Time-variant adaptive time-step size.

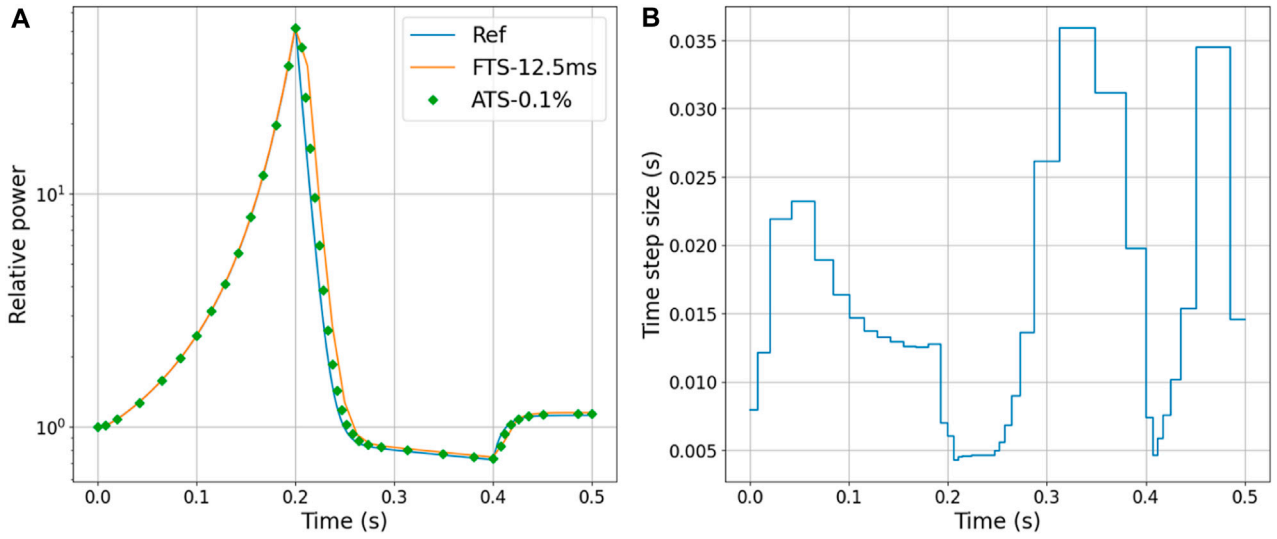

FIGURE 5
Comparison of ATS-0.1% and FTS-12.5 ms in TWIGL **(A)** Core power **(B)** Time-variant adaptive time-step size.

TABLE 2 Comparison of global amplitude error between ATS and FTS in TWIGL.

Time	Reference power	FTS-20 ms error	ATS-0.5% error	FTS-12.5 ms error	ATS-0.1% error
0.2 s	51.222	1.354%	1.504%	0.542%	0.400%
0.4 s	0.725	4.092%	2.514%	2.634%	1.403%
0.5 s	1.123	4.072%	2.412%	2.623%	1.351%
Number of steps	500	25	25	40	41

where $\varphi_g(r,t)$ represents the neutron flux of group g, $C_i(r,t)$ is the delayed neutron precursor concentration of precursor family i, and other notations are conventional. The fission source Q is defined as:

$$Q(r,t) = \sum_{g'=1}^{G} \nu\Sigma_{f,g'}(r,t)\varphi_{g'}(r,t) \tag{6}$$

The neutron flux frequency is introduced to derive the frequency-transformed dynamics model:

$$\omega_g(r,t) \equiv \frac{1}{\varphi_g(r,t)} \frac{\partial}{\partial t}\varphi_g(r,t) \tag{7}$$

where $\omega_g(r,t)$ represents the neutron flux frequency which can be further split as $\omega_g(r,t) = \omega_{S,g}(r,t) + \omega_T(t)$. The flux amplitude-frequency $\omega_T(t)$ represents a global quantity and is dependent only on time; the flux shape-frequency $\omega_{S,g}(r,t)$ is dependent on space, time, and energy. For normalization, a physics-based constraint on the shape-frequency is introduced as (Chao and Attard, 1985):

$$\sum_{g=1}^{G} \int_V dr\kappa\Sigma_{f,g}(r,t)\varphi_g(r,t_0) e^{\int_{t_0}^{t} dt' \omega_{S,g}(r,t')} = P(t_0) \tag{8}$$

where, κ is the heat release per fission reaction, and $P(t_0)$ is the initial total power of the nuclear reactor. The constraint guarantees that the shape-frequency affects only the flux shape, not the total power. The power distribution $q(r,t)$ is defined as:

$$q(r,t) = \sum_{g=1}^{G} \kappa\Sigma_{f,g}(r,t)\varphi_g(r,t_0) \tag{9}$$

The precursor concentration frequency is defined as:

$$\mu_i(r,t) \equiv \frac{1}{C_i(r,t)} \frac{\partial}{\partial t} C_i(r,t) \tag{10}$$

Introducing the frequency-transformation, the transient multi-group neutron diffusion equations and associated delayed neutron precursor equations are rewritten as:

$$\begin{aligned} &\left[-\nabla \cdot D_g(r,t)\nabla + \Sigma_{t,g}(r,t)\right]\varphi_g(r,t) + \frac{\omega_{S,g}(r,t) + \omega_T(t)}{v_g}\varphi_g(r,t) \\ &= \left[\chi_g(r)(1-\beta) + \sum_{i=1}^{I} \frac{\chi_{ig}\beta_i\lambda_i}{\mu_i(r,t) + \lambda_i}\right] Q(r,t) \\ &\quad + \sum_{g'=1}^{G} \Sigma_{g'-g}(r,t)\varphi_{g'}(r,t) \\ &g = 1, \ldots, G \end{aligned} \tag{11}$$

$$\mu_i(r,t)C_i(r,t) = \beta_i Q(r,t) - \lambda_i C_i(r,t) \quad i = 1, \ldots, I \tag{12}$$

Equation 11 is the frequency-transformed temporal-spatial equation. Taking all frequencies in Eq. 11 to be zeros yields the static neutron diffusion equation:

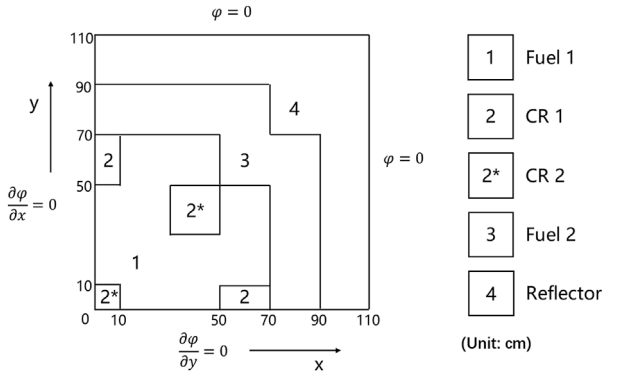

FIGURE 6
Layout of modified LMW-2D benchmark problem.

$$\left[-\nabla\cdot D_g(r,t_0)\nabla+\Sigma_{t,g}(r,t_0)\right]\varphi_g(r,t_0)=\frac{\chi_g(r)}{k_{\text{eff}}}\sum_{g'=1}^{G}\nu\Sigma_{f,g'}(r,t_0)\varphi_{g'}(r,t_0)+\sum_{g'=1}^{G}\Sigma_{g'-g}(r,t_0)\varphi_{g'}(r,t_0)\quad g=1,\cdots,G \tag{13}$$

The adjoint equations corresponding to Eq. 13 are:

$$\left[-\nabla\cdot D_g(r,t_0)\nabla+\Sigma_{t,g}(r,t_0)\right]\varphi_g^{\dagger}(r,t_0)=\frac{\nu\Sigma_{f,g}(r,t_0)}{k_{\text{eff}}}\sum_{g'=1}^{G}\chi_{g'}(r)\varphi_{g'}^{\dagger}(r,t_0)+\sum_{g'=1}^{G}\sum_{g-g'}(r,t_0)\varphi_{g'}^{\dagger}(r,t_0)\quad g=1,\cdots,G \tag{14}$$

The left-hand side of Eq. 14 is the adjoint diffusion-absorption operator, which is self-adjoint, and the right-hand side is the adjoint fission-scattering operator. Eqs 13, 14 are both EVPs, which can be solved by power iteration.

The PKE is a lumped-parameter model used to analyze the dynamic behaviors of the flux amplitude while neglecting the flux shape. As will be shown, this model is beneficial in the error analysis of the SCM. The PKE results by integrating Eqs 4, 5 weighted with the initial adjoint flux. The resulting equations are:

$$\frac{dn(t)}{dt}=\frac{\rho(t)-\beta}{\Lambda}n(t)+\sum_{i=1}^{I}\lambda_i C_i(t) \tag{15}$$

$$\frac{dC_i(t)}{dt}=\frac{\beta_i}{\Lambda}n(t)-\lambda_i C_i(t)\quad i=1,2,...,I \tag{16}$$

in which the notations are conventional thus are neglected for brevity. Readers can find detailed definitions of the dynamic parameters in Appendix-A. Correspondingly, the neutron density frequency for the PKE is be given by:

$$\omega(t)\equiv\frac{1}{n(t)}\frac{dn(t)}{dt} \tag{17}$$

which can also be called the amplitude-frequency. The frequency-transformed point kinetics model is expressed as:

$$\omega(t)=\frac{\rho(t)-\beta}{\Lambda}+\frac{1}{n(t)}\sum_{i=1}^{I}\lambda_i C_i(t) \tag{18}$$

The precursor concentration equations are identical to Eq. 16.

3 Solution method for frequency-transformed equations

Introducing the dynamic eigenvalue k_D in Eq. 11, the equation can be transformed into an EVP:

$$\left[-\nabla\cdot D_g(r,t)\nabla+\Sigma'_{t,g}(r,t)\right]\varphi_g(r,t)=\frac{\chi'_g(r)}{k_D}Q(r,t)+\sum_{g'=1}^{G}\Sigma_{g'-g}(r,t)\varphi_{g'}(r,t)\quad g=1,...,G \tag{19}$$

where, $\Sigma'_{t,g}(r,t)$ is the dynamic total cross-section, and $\chi'_g(r)$ is the dynamic fission spectrum, which are respectively defined as:

$$\sum'_{t,g}(r,t)\equiv\Sigma_{t,g}(r,t)+\frac{\omega_{S,g}(r,t)+\omega_T(t)}{v_g} \tag{20}$$

$$\chi'_g(r)\equiv\chi_g(r)(1-\beta)+\sum_{i=1}^{I}\frac{\chi_{ig}\beta_i\lambda_i}{\mu_i(r,t)+\lambda_i} \tag{21}$$

The dynamic frequencies rendering the maximum eigenvalue k_D equal to 1are the solutions to Eq. 19. It is noted that the dynamic eigenvalue k_D can be expressed as a non-linear function of the flux amplitude-frequency ω_T. Thus, the dynamic frequencies are solved iteratively using power

TABLE 3 Perturbations in modified LMW-2D benchmark problem.

Region	Perturbation
CR 1	$\Sigma_{a,2}(\vec{r}_2,t)=\begin{cases}\Sigma_{a,2}(\vec{r}_2,0)\times(1-10t)+\Sigma_{a,2}(\vec{r}_1,0)\times 10t & t\le 0.1s\\ \Sigma_{a,2}(\vec{r}_1,0) & 0.1s<t\le 0.4s\\ \Sigma_{a,2}(\vec{r}_2,0)\times\left(\frac{5t}{3}-\frac{2}{3}\right)+\Sigma_{a,2}(\vec{r}_1,0)\times\left(\frac{5}{3}-\frac{5}{3}t\right) & 0.4s<t\le 1.0s\end{cases}$
CR 2	$\Sigma_{a,2}(\vec{r}_{2^*},t)=\begin{cases}\Sigma_{a,2}(\vec{r}_{2^*},0)\times(1-10t)+\Sigma_{a,2}(\vec{r}_1,0)\times 10t & t\le 0.1s\\ \Sigma_{a,2}(\vec{r}_1,0) & 0.1s<t\le 0.2s\\ \Sigma_{a,2}(\vec{r}_{2^*},0)\times\left(\frac{5t}{3}-\frac{1}{3}\right)+\Sigma_{a,2}(\vec{r}_1,0)\times\left(\frac{4}{3}-\frac{5}{3}t\right) & 0.2s<t\le 0.8s\\ \Sigma_{a,2}(\vec{r}_{2^*},0) & 0.8s<t\le 1.0s\end{cases}$

Note: $\vec{r}_1\in$ regionofFuel1, $\vec{r}_2\in$ regionofCR1, $\vec{r}_{2^*}\in$ regionofCR2

iteration and the non-linear iteration algorithms. The non-linear iteration algorithm employed in this paper is the $k-\omega$ iteration, as shown in Algorithm 1:

function SpatialSolverSCM(t_N, h, XS)
  $\{tn\} \leftarrow \{0 : h : t_N\}$ Time steps
  $\tilde{\varphi}_g(r,t_0), k_{eff} \leftarrow$ EVPSolver($XS(t_0)$)
  $\tilde{\varphi}_g(r,t_0) \leftarrow \frac{P_0}{\int_V dr\tilde{q}(r,t_0)}\tilde{\varphi}_g(r,t_0)$ Normalize initial flux
  $C_i(r,t_0) \leftarrow \frac{\beta_i}{\lambda_i}Q(r,t_0)$
  $\omega_T(t_0), \omega_{S,g}(r,t_0), \mu_i(r,t_0) \leftarrow 0$
  while $n \le N$ **do**
    $\omega_T^{(0)}(t_n) \leftarrow \omega_T(t_{n-1})$
    $\omega_{S,g}^{(0)}(r,t_n) \leftarrow \omega_{S,g}(r,t_{n-1})$
    $C_i^{(0)}(r,t_n) \leftarrow C_i(r,t_{n-1})$
    KOmegaIteration(⋯)
    $P_n \leftarrow \int_V drq(r,t_n)$
  end while
  return $\{\varphi_g(r,t_n)\}, \{C_i(r,t_n)\}, \{\omega(r,t_n)\}$
end function
function EVPSolver(XS)
  % Any existing neutron transport or diffusion EVP solver
  return $\tilde{\varphi}_g(r), k_{eff}$
end function
function KOmegaIteration( )
  % Input and output variables are omitted
  while $m \le M$ do
    $\tilde{\varphi}_g^{(m)}(r,t_n), k_D^{(m+1)} \leftarrow$ EVPSolver($XS'(t_0)$)
    $\omega_T^{(m+1)}(t_n) \leftarrow$ Update $\omega_T^{(m+1)}(t_n)$ based on Eq. 22
    $\tilde{\varphi}_g^{(m+1)}(r,t_n) \leftarrow \frac{P_{n-1}}{\int_V dr\tilde{q}(r,t_n)}\tilde{\varphi}_g^{(m)}(r,t_n)$
    $\omega_{S,g}(t_n) \leftarrow \frac{1}{h}ln\left(\frac{\varphi_g^{(m+1)}(r,t_n)}{\varphi_g(r,t_{n-1})}\right)^{\frac{\omega_T^{(m+1)}(t_n)+\omega_T(t_{n-1})}{2}}h$
    $\varphi_g(r,t_n) \leftarrow \hat{\varphi}_g^{(m+1)}(r,t_n)e^{\frac{\omega_T^{(m+1)}(t_n)+\omega_T(t_{n-1})}{2}h}$
    $C_i^{(m+1)}(r,t_n) \leftarrow$ Update $C_i^{(m)}(r,t_n)$ based on Eq. 26
    $\mu_i^{(m+1)}(r,t_n) \leftarrow$ Update $\mu_i^{(m)}(r,t_n)$ based on Eq. 28
    if $|k_D^{(m+1)} - 1| < \varepsilon$ **then**
      break
    end if
    $XS'(tn) \leftarrow$ Update dynamics cross-sections based Eqs. 20 and 21
  end while
end function

Algorithm 1. SCM for time-spatial equations.

where XS denotes all coefficients in Eqs 11, 12, including cross-sections and dynamic parameters, h is the time step size, and t_N is the last time point. If not otherwise specified, n and m denote the time step index and iteration index, respectively. In this study, the finite difference method (FDM) is applied to solve the EVP of the neutron diffusion equation, and the solutions are $\tilde{\varphi}_g(r,t)$ and the associated eigenvalue k_{D}. Besides, other spatial discretization algorithms are also applicable, such as the nodal method (Abo et al., 2008) and the finite element method.

The amplitude-frequency is updated using the secant method (Chao and Attard, 1985):

$$\omega_T^{(m+1)}(t_n) = \omega_T^{(m)}(t_n) + \left[\omega_T^{(m-1)}(t_n) - \omega_T^{(m)}(t_n)\right]\frac{1-k_{\mathrm{D}}^{(m)}}{k_{\mathrm{D}}^{(m-1)} - k_{\mathrm{D}}^{(m)}} \quad (22)$$

The iteration continues until the dynamic eigenvalue converges to 1. According to Eq. 8, normalization is necessary to update the shape-frequency with the normalized neutron flux $\hat{\varphi}_g(r,t_n)$:

$$\hat{\varphi}_g(r,t_n) = \frac{P(t_{n-1})}{\sum_{g=1}^{G}\int_V dr\kappa\Sigma_{f,g}(r,t_n)\tilde{\varphi}_g(r,t_n)}\tilde{\varphi}_g(r,t_n) \quad (23)$$

Such a normalization enforces the total power contributed by the normalized flux to equal the power of the previous time step, which ensures that the shape-frequency is independent of the flux amplitude. Thus, the update formula of the shape-frequency is:

$$\bar{\omega}_{S,g}(r,t_n) = \frac{1}{\Delta t_n}\ln\left[\frac{\hat{\varphi}_g(r,t_n)}{\varphi_g(r,t_{n-1})}\right] \quad (24)$$

where $\Delta t_n = t_n - t_{n-1}$, and $\bar{\omega}_{S,g}(r,t_n)$ is the average shape-frequency in $[t_{n-1}, t_n]$. According to Eq. 3, the update formula for the actual neutron flux is:

$$\begin{aligned}\varphi_g(r,t_n) &= \varphi_g(r,t_{n-1})e^{\frac{\omega_T(t_n)+\omega_T(t_{n-1})}{2}\Delta t_n + \bar{\omega}_{S,g}(r,t_n)\Delta t_n} \\ &= \hat{\varphi}_g(r,t_n)e^{\frac{\omega_T(t_n)+\omega_T(t_{n-1})}{2}\Delta t_n}\end{aligned} \quad (25)$$

When the actual neutron flux is solved, the precursor concentration is calculated by:

$$C_i(r,t_n) = C_i(r,t_{n-1})e^{-\lambda_i\Delta t_n} + \beta_i e^{-\lambda_i\Delta t_n}\int_{t_{n-1}}^{t_n}\Delta Q(r,t)e^{\lambda_i t}dt \quad (26)$$

Suppose that the fission source changes linearly within $[t_{n-1}, t_n]$, the expression of the fission source is given by:

$$Q(r,t) = Q(r,t_{n-1}) + \frac{Q(r,t_n) - Q(r,t_{n-1})}{\Delta t_n}(t - t_{n-1}) \quad (27)$$

According to Eq. 12, the precursor frequency is calculated by:

$$\mu_i(r,t) = \begin{cases}\beta_i\dfrac{Q(r,t)}{C_i(r,t)} - \lambda_i & C_i(r,t) \neq 0 \\ 0 & C_i(r,t) = 0\end{cases} \quad (28)$$

The resulting flux and precursor frequencies are then used to update the dynamic cross-section. For the case of the PKE, the non-linear frequency-transformed equations can be solved using Algorithm 2:

function PKESolverSCM(t_N, h, IC, DP)
  $\{t_n\} \leftarrow \{0{:}\ h{:}\ t_N\}$ Time steps
  $n(t_0), C_i(t_0), \omega(t_0) \leftarrow IC$ Initial conditions
  while $n \le N$ **do**
    $\omega^{(0)}(t_n) \leftarrow \omega(t_n - 1)$
    $C_i^{(0)}(t_n) \leftarrow C_i(t_{n-1})$
    while $m \le M$ **do**
      $n^{(m+1)}(t_n) \leftarrow n(t_n)e^{\frac{\omega^{(m)}(tn)+\omega(t_{n-1})}{2}h}$
      $\omega^{(m+1)}(tn) \leftarrow$ Update $\omega^{(m)}(tn)$ based on Eq. 31
      $C(m+1)(tn) \leftarrow$ Update $C_i^{(m)}(t_n)$ based on Eq. 33
      if $|f| < \varepsilon$ then
        break
      end if
    end while
  end while
  return $\{n(tn)\}, \{Ci(tn)\}, \{\omega(tn)\}$
end function

Algorithm 2. SCM for PKE.

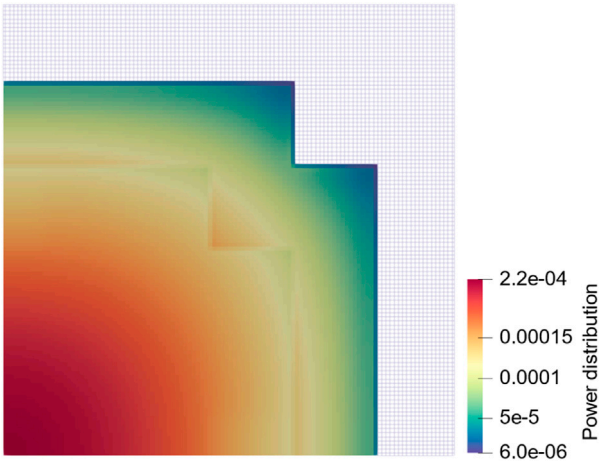

FIGURE 7
Initial power distribution for modified 2D-LMW (Only non-zero power displayed).

where IC represents the initial conditions, and DP is the dynamic parameters in Eqs 16, 18. With a linear approximation of the neutron density frequency, the neutron density can be updated by:

$$n(t_n) = n(t_{n-1})e^{\frac{\omega(t_n)+\omega(t_{n-1})}{2}h} \tag{29}$$

in which ω is solved iteratively. According to Eq. 18, function f is introduced:

$$f(t_n) = -\omega(t_n) + \frac{\rho(t_n)-\beta}{\Lambda} + \frac{1}{n(t_{n-1})e^{\frac{\omega(t_n)+\omega(t_{n-1})}{2}h}} \sum_{i=1}^{I} \lambda_i C_i(t_n) \tag{30}$$

In this case, ω is solved with the secant method until $f(t_n) = 0$:

$$\omega^{(m)}(t_n) = \omega^{(m-1)}(t_n) - \frac{\left[\omega^{(m-1)}(t_n) - \omega^{(m-2)}(t_n)\right]}{\left[f^{(m-1)}(t_n) - f^{(m-2)}(t_n)\right]} f^{(m-1)}(t_n) \tag{31}$$

The precursor concentration $C_i(t_n)$ can be determined using the analytical solution to Eq. 16:

$$C_i(t_n) = C_i(t_{n-1})e^{-\lambda_i \Delta t_n} + \frac{\beta_i}{\Lambda} e^{-\lambda_i \Delta t_n} \int_{t_{n-1}}^{t_n} n(t) e^{\lambda_i t} dt \tag{32}$$

Assuming that the neutron density changes linearly with time, Eq. 32 is transformed into:

$$C_i(t_{n+1}) = C_i(t_n)e^{-\lambda_i \Delta t_n} + \frac{\beta}{\Lambda \lambda_i^2 \Delta t_n} \left\{ \begin{array}{l} [-\Delta t_n \lambda_i n(t_n) - n(t_n) + n(t_{n+1})]e^{-\lambda_i \Delta t_n} \\ +\Delta t_n \lambda_i n(t_{n+1}) + n(t_n) - n(t_{n+1}) \end{array} \right\} \tag{33}$$

4 Error analysis and error estimator

In the SCM, polynomial functions are used to interpolate the exact frequency. The interpolation points are frequencies obtained by solving frequency-transformed equations at different time points. Figure 1 offers a schematic view of errors in the numerical integral. As shown in the figure, when a polynomial interpolation function ω' replaces the original function ω^*, error is introduced when integrating over the time interval. The error can be estimated by the difference in the covered area between the original function and the interpolation function in Figure 1.

With the foregoing considerations, we define the integral error contributing to truncation error in the SCM:

Definition 1. (Integral error): The integral error ε_{int} is defined as the difference between the integral using the original function ω^* and the integral using the polynomial interpolation ω' of ω^*:

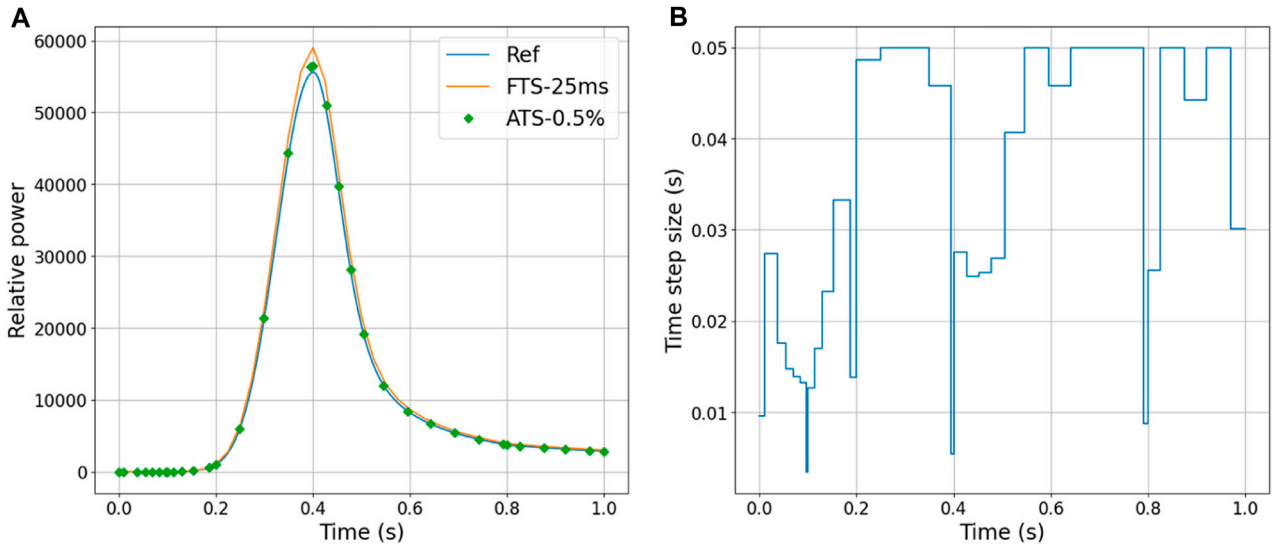

FIGURE 8
Comparison of ATS-0.5% and FTS-25 ms in modified 2D-LMW **(A)** Core power **(B)** Time-variant adaptive time-step size.

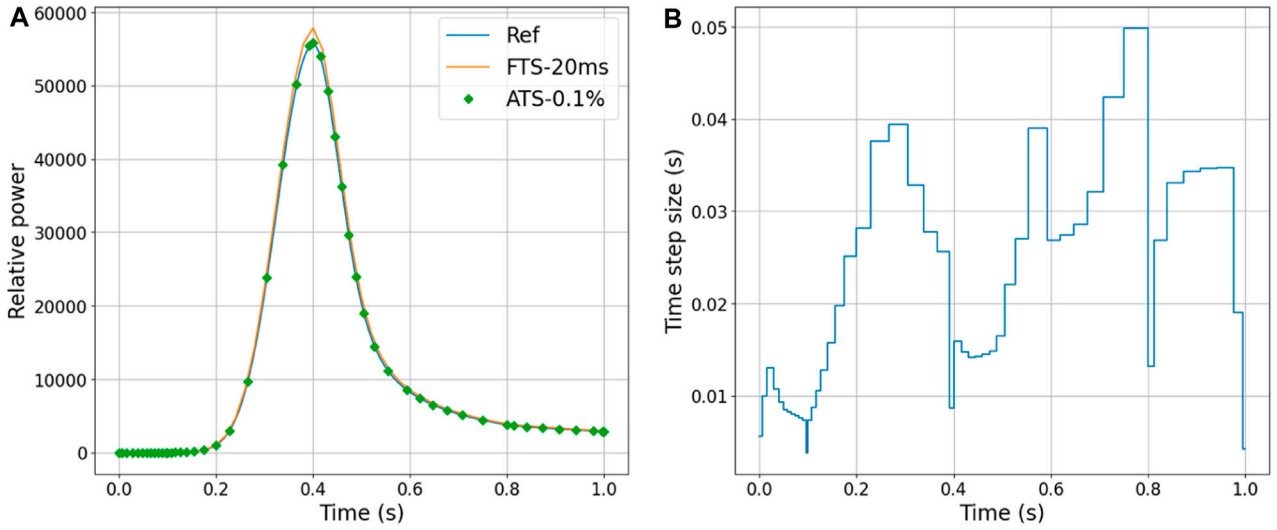

FIGURE 9
Comparison of the ATS-0.1% and FTS-20 ms in modified 2D-LMW **(A)** Core power **(B)** Time-variant adaptive time-step size.

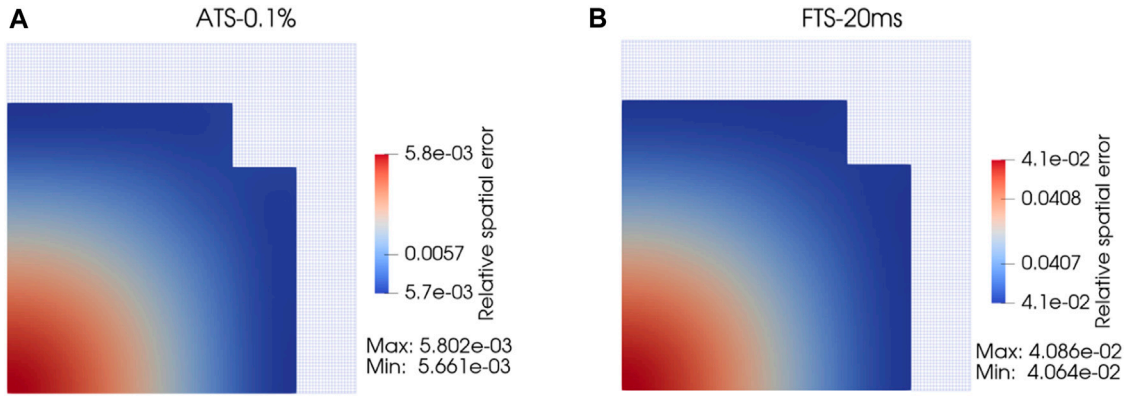

FIGURE 10
Comparison of relative spatial error at 0.4 s between ATS-0.1% and FTS-20 ms. **(A)** ATS-0.1%; **(B)** FTS-20 ms.

$$\varepsilon_{int} \equiv \int_{\Delta t} \omega^{*}(t)dt - \int_{\Delta t} \omega'(t)dt \tag{34}$$

The interpolation error at t is $\omega^{*}(t) - \omega'(t)$, which is the difference between the original function providing the interpolation points and the interpolating polynomial. Assume that $\omega'(t)$ is the (degree n or less) interpolating polynomial fitting the $n+1$ points $\{(t_0, \omega^{*}(t_0)), \cdots, (t_n, \omega^{*}(t_n))\}$. Without loss of generality, it is assumed that the frequency is $(n+1)$-order differentiable due to the smooth variation of reactivity ρ in Eq. 18. The interpolation error is then (Zhang et al., 2017):

$$\omega^{*}(t) - \omega'(t) = \frac{1}{(n+1)!}\omega^{*(n+1)}(\xi_t)\prod_{i=0}^{n}(t - t_i) \tag{35}$$

where ξ_t lies between $[t_0, t_n]$, and $\omega^{*(n+1)}$ is the $(n+1)$-order derivative of the frequency. When the neutron density frequency is interpolated with a linear function within a time step, by applying the mean value theorem of integrals, the integral error in $[t_{n-1}, t_n]$ is obtained as:

$$\varepsilon_{int} = \int_{t_{n-1}}^{t_n} \omega^{*}(t)dt - \int_{t_{n-1}}^{t_n} \omega'(t)dt = -\frac{1}{12}\omega^{*(2)}(\xi)(t_n - t_{n-1})^3 \tag{36}$$
$$\xi \in [t_{n-1}, t_n]$$

Because the exact value of ξ is uncertain, Eq. 36 can be used to provide error bounds to the solutions. Hence, the optimal time step is given using the error estimator:

$$h' = \sqrt[3]{\frac{12\varepsilon_{tol}}{\omega^{(2)}(\xi)}}\, h' \in \mathbb{R}^{+} \tag{37}$$

5 Coupling of the NTSE solver with the PKE predictor

Based on the above discussions, one can select the optimal time steps for the SCM based on Algorithms 3, 4:

TABLE 4 Comparison of global amplitude error between ATS and FTS in modified 2D-LMW.

Time	Reference power	FTS-25 ms error	ATS-0.5% error	FTS-20 ms error	ATS-0.1% error
0.1 s	11.07	3.430%	0.620%	2.182%	0.101%
0.2 s	997.86	5.812%	1.690%	3.651%	0.359%
0.4 s	55591.11	6.017%	1.628%	3.992%	0.570%
0.8 s	3776.35	5.258%	0.402%	3.470%	0.257%
1.0 s	2871.30	5.161%	0.564%	3.295%	0.348%
Number of steps	1,000	40	33	50	50

function SpatialSolverAdaptiveSCM(t_N, h_{max}, h_{min}, ε_{tol}, XS)
  $t_0 \leftarrow 0$
  $\tilde{\varphi_g}(r, t_0), k_{eff} \leftarrow$ EVPSolver($XS(t_0)$)
  $\varphi_g(r, t_0) \leftarrow \frac{P_0}{\int_V dr\tilde{q}(r,t_0)} \tilde{\varphi}_g(r, t_0)$ Normalize initial flux
  $C_i(r, t_0) \leftarrow \frac{\beta_i}{\lambda_i} Q(r, t_0)$
  $\omega_T(t0), \omega_{S,g}(r, t0), \mu i(r, t0) \leftarrow 0$
  for $t_n \le t_N$ **do** n++
    $t'_n \leftarrow t_{n-1} + h_{max}$
    $ICn\text{-}1, DPn\text{-}1 \leftarrow$ Initialized IC and DP
    $h_n \leftarrow$ TimeStepSelection($\varepsilon_{tol}, h_{max}, h_{min}, IC_{n-1}, DP_{n-1}$)
    $tn \leftarrow tn\text{-}1 + hn$
    $\omega_T^{(0)}(t_n) \leftarrow \omega_T(t_{n-1})$
    $\omega_{S,g}^{(0)}(r, t_n) \leftarrow \omega_{S,g}(r, t_{n-1})$
    $C_i^{(0)}(r, t_n) \leftarrow C_i(r, t_{n-1})$
    KOMegaIteration(…)
    $P_n \leftarrow \int_V drq(r, t_n)$
  end for
  return $\{\phi g\ \{r, tn\}, \{Ci(r, tn)\}, \{\omega(r, tn)\}$
end function

Algorithm 3. Adaptive time stepping SCM based on PKE predictor.

function TimeStepSelection(ε_{tol}, h_{max}, h_{min}, IC, DP)
  $h_{sub} \leftarrow \frac{h_{max}}{K}$ Sub − step for PKE
  $\{\omega_k\} \leftarrow$ PKESolverSCM(h_{max}, h_{sub}, IC, DP)
  $\{\omega_k^{[2]}\} \leftarrow \frac{\omega_{k-1} 2\omega_k + \omega_{k+1}}{h_{sub}^2}$
  $\omega^{[2]} \leftarrow max\{|\omega_k^{[2]}|\}$
  $h' \leftarrow$ ErrorControl($\varepsilon_{tol}, \omega^{[2]}$)
  $h \leftarrow \max\{hmin, \min\{h', hmax\}\}$
  return h
end function
function ErrorControl(ε_{tol}, $\omega^{[2]}$)
  $h \sqrt[3]{\frac{12\varepsilon_{tol}}{\omega^{[2]}}}$
  return h'
end function

Algorithm 4. Adaptive time step selection based on PKE.

Algorithm 4 shows the time-step selection subroutine with the error estimator demonstrated in Eq. 37. An optimal time-step size is chosen using the error estimator to control the local error within the pre-set error tolerance in this subroutine. Algorithm 3 is obtained by embedding Algorithm 4 in Algorithm 1.

The key to the ATS algorithm is to solve the PKE in the time interval $[t_{n-1}, t_{n-1} + h_{max}]$ before solving the NTSE. In solving the PKE, dynamic parameters and initial conditions are generated using the solution of the NTSE and the initial adjoint flux. To make appropriate predictions, the following assumptions are used for solving the PKE:

- The flux shape is fixed in the prior interval and the solution $\varphi_g(r, t_{n-1})$ is used to evaluate all necessary parameters and initial conditions;
- All dynamic parameters are constant in the prior interval except the reactivity $\rho(t)$;
- $\rho(t)$ is a linear function in the prior interval, while $\rho(t_{n-1})$ and $\rho(t_{n-1} + h_{max})$ are evaluated based on Supplementary Eq. 4.

The SCM is also applied to solve the PKE because it directly provides the frequency for error estimation.

6 Numerical Results

In this section, the efficiency and accuracy of the ATS algorithm are tested by comparing it with FTS calculation. We examine the time stepping algorithm in the TWIGL problem and the modified LMW-2D problem. The TWIGL problem represents a transient case with step perturbation, and the LMW problem involves smooth reactivity insertions with more complicated geometrical layout that that of the TWIGL problem. The combination of the two problems can be utilized to examine the performance of the ATS algorithm under different transient scenarios.

The cross-sections and dynamic parameters of the two problems are presented in Appendix-B. The reference solutions are obtained by fine time-step size calculations. We apply the ATS algorithm to the problems with specified error tolerance. For comparisons, we also adopt FTS calculations with the same number of time steps as those used to produce the ATS results to evaluate the accuracy improvements of using the ATS algorithm. For ease of description, in these discussions we denote ATS with a tolerance of x% as ATS-x %, and denote FTS with the time step of y ms as FTS-y ms.

6.1 TWIGL

The TWIGL benchmark problem is one quarter of a 2D reactor core consisting of three kinds of fuel materials, as shown in Figure 2 (Kennedy and Riley, 2012).

The TWIGL benchmark problem includes two different reactivity insertion cases: a simple ramp case and a composite case. The composite case is adopted to validate the ATS algorithm, which is shown in Table 1. The transient durations for both cases are 0.5 s. Note that perturbations occur only in Material 1; the other materials remain in their initial conditions. The initial power distribution is shown in Figure 3.

In the TWIGL problem, the pre-set maximum and minimum time-step sizes are chosen as 50 and 1 ms, respectively. Figure 4A compares ATS-0.5% and FTS-20 ms. Figure 4B presents the adaptive time-step size. As shown in Figure 4A, the power curve of ATS agrees well with the reference solution, especially shortly after the step points. Step perturbations are introduced at 0.2 and 0.4 s. Accordingly, the ATS algorithm automatically refines step sizes shortly after step points but otherwise uses a coarse step size. Such a time step adjustment intelligently allocates time steps and spends more computational resources on the interval with rapid changes.

Figure 5A, B compare the results of ATS-0.1% and FTS-12.5 ms. The performance is similar to that in the previous error tolerance setting.

Table 2 summarizes the global core power error at different time step points. The ATS algorithm significantly improves the computational accuracy when the same number of time steps is used, with an error reduction of up to 40~50%. The comparison of ATS-0.5% and FTS-12.5 ms in Table 2 indicates that the ATS algorithm can reduce by 37% the computational time of the FTS calculation with similar numerical accuracy. More significant gains can be expected for large-scale neutron transport problems.

6.2 Modified 2D-LMW

The second 2D benchmark problem is modified from the 3D LMW (Langenbuch, Maurer, Werner) problem without thermal-hydraulic feedback to match the simulation code used in the paper (Kennedy and Riley, 2012). The reactor core is a simplified pressurized water reactor containing two kinds of fuel assemblies and two groups of control rods (CR), as shown in Figure 6.

The modified 2D LMW problem is designed to model a reactivity insertion case, as shown in Table 3. This case is the superposition of ramp perturbations in different regions, by perturbing materials in CR 1 and CR 2. The initial power distribution is illustrated in Figure 7.

For the modified 2D-LMW, Figures 8, 9 present a comparison between the results of the ATS and FTS calculations. In Figure 8A, the error of the power peak, which appears at 0.4 s, is 905.02 and 3344.92 for ATS and FTS, respectively. In Figure 9A, the error of the power peak is 316.87 and 2219.20. The noticeable improvement in the accuracy of the power peak demonstrates the efficacy of the ATS algorithm.

Figure 10 presents the relative spatial error at 0.4s for ATS and FTS. We can observe that the error distribution is fairly uniform in both cases, but the accuracy of ATS is higher than that of FTS.

Table 4 summarizes the global core power error. The results show that the numerical accuracy can be improved significantly. For example, comparing FTS-20 ms and ATS-0.1%, the error reduction can be up to 90%~95%. The core power increases by more than four orders of magnitudes from the initial power, whose variation is much wider than that in the TWIGL problem, but there is no step perturbation. Thus, continuity of frequency enables superior error control.

7 Conclusion

In this work, we perform theoretical and numerical error analyses of the SCM. By expressing the error term using integral error, the mathematical expression of the amplitude error is derived. The integral error is caused by using a polynomial function to represent the exact solution. Based on theoretical analysis, we develop an efficient and easy-to-implement ATS algorithm based on the PKE predictor. A fine-step PKE solver is used to rapidly evaluate high order derivatives of the neutron flux amplitude in the theoretical error expression. The high-order derivatives are used to determine the optimal time-step size for the NTSE. A time step error-estimator for this ATS algorithm is derived, and numerical validation indicates that the ATS is satisfactory in performance and easy to implement.

The accuracy and computational cost of ATS and FTS are examined using benchmark problems. Comparisons show that the ATS algorithm can achieve higher accuracy with the same number of time steps, and significantly improve computational efficiency in the NTSE. It was found that the ATS algorithm significantly improves the computational accuracy when the same number of time steps is used, with error reductions of up to 40%~50% for the TWIGL benchmark and up to 90%~95% for the LMW benchmark. With similar numerical accuracy, the ATS algorithm can reduce by 37% the computational time of the FTS calculation. Future work is to apply the adaptive SCM to 3D neutron transport problems.

Data availability statement

The raw data supporting the conclusion of this article will be made available by the authors, without undue reservation.

Author contributions

DW: Conceptualization, Formal analysis, Methodology, Validation, Writing–original draft. WX: Formal analysis, Methodology, Resources, Writing–review and editing. ZD: Supervision, Writing–review and editing. TZ: Conceptualization, Funding acquisition, Methodology, Writing–review and editing.

Funding

The authors declare that no financial support was received for the research, authorship, and/or publication of this article.

Conflict of interest

The authors declare that the research was conducted in the absence of any commercial or financial relationships that could be construed as a potential conflict of interest.

Publisher's note

All claims expressed in this article are solely those of the authors and do not necessarily represent those of their affiliated organizations, or those of the publisher, the editors and the reviewers. Any product that may be evaluated in this article, or claim that may be made by its manufacturer, is not guaranteed or endorsed by the publisher.

Supplementary material

The Supplementary Material for this article can be found online at: https://www.frontiersin.org/articles/10.3389/fenrg.2023.1284230/full#supplementary-material

References

Aboanber, A. E., and Hamada, Y. M. (2008). Generalized Runge–Kutta method for two-and three-dimensional space–time diffusion equations with a variable time step. *Ann. Nucl. Energy* 35 (6), 1024–1040. doi:10.1016/j.anucene.2007.10.008

Ban, Y., Endo, T., and Yamamoto, A. (2012). A unified approach for numerical calculation of space-dependent kinetic equation. *J. Nucl. Sci. Technol.* 49 (5), 496–515. doi:10.1080/00223131.2012.677126

Boffie, J., and Pounders, J. M. (2018). An adaptive time step control scheme for the transient diffusion equation. *Ann. Nucl. Energy* 116, 280–289. doi:10.1016/j.anucene.2018.02.044

Caron, D., Dulla, S., and Ravetto, P. (2017). Adaptive time step selection in the quasi-static methods of nuclear reactor dynamics. *Ann. Nucl. Energy* 105, 266–281. doi:10.1016/j.anucene.2017.03.009

Chao, Y. A., and Attard, A. (1985). A resolution of the stiffness problem of reactor kinetics. *Nucl. Sci. Eng.* 90 (1), 40–46. doi:10.13182/nse85-a17429

Kennedy, D., and Riley, D. (2012). *Romes Desert Frontiers*. Routledge.

Park, B. W., and Joo, H. G. (2015). Improved stiffness confinement method within the coarse mesh finite difference framework for efficient spatial kinetics calculation. *Ann. Nucl. Energy* 76, 200–208. doi:10.1016/j.anucene.2014.09.029

Tang, C., Bi, G., and Yang, B. (2019). Application of stiffness confinement method in transient neutron transportation calculation. *Atomic Energy Sci. Technol.* 53 (7), 1202. doi:10.7538/yzk.2018.youxian.0836

Wanner, G., and Hairer, E. (1996). *Solving ordinary differential equations II*, 375. New York: Springer Berlin Heidelberg.

Zhang, T., Wang, Y., Lewis, E. E., Smith, M. A., Yang, W. S., and Wu, H. (2017). A three-dimensional variational nodal method for pin-resolved neutron transport analysis of pressurized water reactors. *Nucl. Sci. Eng.* 188 (2), 160–174. doi:10.1080/00295639.2017.1350002

Zimin, V. G., and Ninokata, H. (1998). Nodal neutron kinetics model based on nonlinear iteration procedure for LWR analysis. *Ann. Nucl. Energy* 25 (8), 507–528. doi:10.1016/s0306-4549(97)00078-9

frontiers | Frontiers in Energy Research

TYPE Review
PUBLISHED 04 December 2023
DOI 10.3389/fenrg.2023.1264168

OPEN ACCESS

EDITED BY
Vivek P. Utgikar,
University of Idaho, United States

REVIEWED BY
Xiaodong Sun,
University of Michigan, United States
David Arcilesi,
University of Idaho, United States
Yonghee Kim,
Korea Advanced Institute of Science and Technology (KAIST), Republic of Korea
Shanfang Huang,
Tsinghua University, China

*CORRESPONDENCE
Lei Li,
lileiheu@hrbeu.edu.cn

RECEIVED 20 July 2023
ACCEPTED 23 November 2023
PUBLISHED 04 December 2023

CITATION
Wang E, Ren T and Li L (2023), Review of reactor conceptual design and thermal hydraulic characteristics for heat pipe in nuclear systems.
Front. Energy Res. 11:1264168.
doi: 10.3389/fenrg.2023.1264168

Review of reactor conceptual design and thermal hydraulic characteristics for heat pipe in nuclear systems

Enpei Wang, Tingwei Ren and Lei Li*

Fundamental Science on Nuclear Safety and Simulation Technology Laboratory, Harbin Engineering University, Harbin, China

Heat pipe cooled reactors (HPCRs) have broad application prospects due to their advantages, such as high power density, compact structure, lower cost, and easy modular assembly. Numerous countries have engaged in extensive research and development of HPCR conceptual designs. The heat from the reactor is removed by high temperature heat pipes (HTHPs), which generally employ alkali metals as the working fluid, such as potassium, sodium, and lithium. Understanding the thermal-hydraulic performance of HTHPs is essential for the safe and efficient operation of a reactor. Therefore, the objective of this paper is to provide a comprehensive review of HPCR conceptual designs developed by various countries in recent years. The research progress of HTHPs on flow and heat transfer performance is reviewed, with an emphasis on both transient and steady-state characteristics. Research progress, as well as the issues that need to be focused on in future research, are discussed in detail.

KEYWORDS

heat pipe, alkali metal, heat pipe reactor, heat transfer performance, conceptual design

1 Introduction

The history of the heat pipe (HP) concept can be traced back to 1944, which was developed initially by Gaugler Richard (1944). In 1963, George M. Grover invented a stainless sodium HP and proposed the term "heat pipe" as the prelude of contemporary HP research. A paper on the study for HP was put out by Grover et al. (1964) the next year. Since then, HP has been attracting increasing the interest and attention of worldwide scholars due to its remarkable characteristics such as compact structure, robustness, higher thermal conductivity and longevity (Wang et al., 2020b). HPs offer excellent heat transfer capabilities and a broad operating temperature range, extending from −60°C to over 2,000°C, according to the choice of the working fluid in the pipe. The high temperature heat pipes (HTHPs), which utilize alkali metals such as sodium and potassium as working fluids, can efficiently operate at temperatures ranging from 400°C to 1,200°C (Sun et al., 2022b). The alkali high latent heat of vaporization allows the HP heat transfer power to approach the kilowatt level (Guo et al., 2023). As a result, the heat pipe cooled reactor (HPCR) system design has extensively utilized HTHPs employing alkali metals (Li et al., 2023b).

The thermosyphon (wickless HP) has found widespread use in a variety of industries because of its relatively straightforward manufacturing methods and high heat conductivity. It is believed to have a higher heat transfer limit as a result of its capacity to hold larger quantities of working fluid, even assuring sufficient fluid supply to the evaporator via gravity

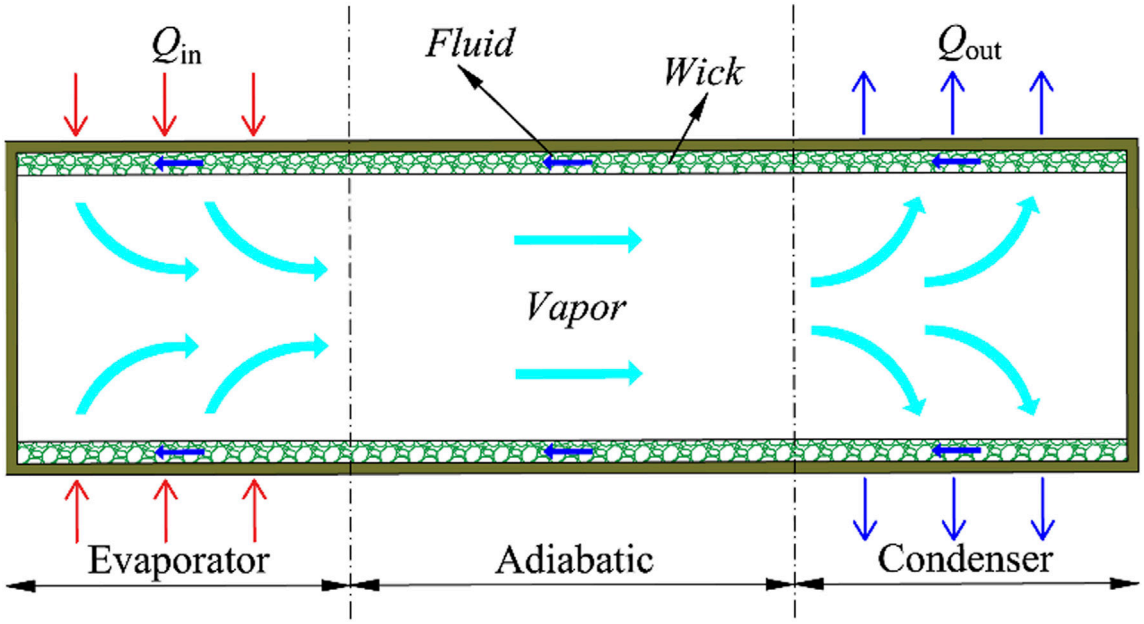

FIGURE 1
The schematic of a conventional wick HP.

(Liu et al., 2022). The conventional wick HP (capillary driven) is most commonly used in nuclear systems, as shown in Figure 1. Typically, the axial length of a HP is commonly divided into three sections: the evaporator section, the adiabatic section, and condenser section. The working fluid absorbs heat from the evaporator section and transforms into a gaseous state through a phase change process. The vapor then travels through the vapor chamber to the condenser section, where it is exposed to a colder environment, leading it to revert to a liquid state. The wick structure, found inside the HP, enables the transportation of the condensed liquid back to the evaporator section. This continuous cycle ensures efficient heat.

In the past two decades, HTHP research has attracted significant attention from various countries in the field of nuclear systems. Based on the published literature, this paper examines the domestic and international research progress and significant outcomes of the HPCR system and the thermal performance of alkali metal HTHP. Additionally, we analyze the shortcomings of previous research and make pertinent recommendations for future research.

2 HPCR conceptual design

In low-power applications, nuclear reactors often require specific characteristics, such as compact size, lightweight design, sustained power output over extended periods, and a focus on safety, reliability, and simplicity of systems. Additionally, it is essential for these reactors to operate autonomously without reliance on human intervention or external agencies in abnormal conditions. Instead, they should rely on inherent safety measures within the core design to self-regulate and restore normal operation or initiate a safe shutdown. Future development efforts will prioritize reactor types that possess high inherent safety, feature simple and compact structures, operate at low pressures, exhibit a high degree of automation, have long core lifetimes, and offer good economic viability. HPCRs offer numerous technical advantages that can contribute to achieving these objectives. In recent years, HP technology has been employed in both domestic and international nuclear reactor conceptual designs and has also been utilized to enhance the reliability of existing safety systems. This chapter will provide an overview of research conducted by various countries on the application of HP technology.

2.1 American HPCR research

The US has been at the forefront of HP research and has contributed significantly to aerospace and energy. American universities and research institutions have been instrumental in promoting and advancing this field of study. Numerous prestigious academic institutions have established state-of-the-art research facilities and programs to advance HP technology. These include MIT, Stanford University, Los Alamos National Laboratory (LANL), and the California Institute of Technology (Caltech). With the help of these well-known institutions and others across the country, the United States has made great strides in HP study and continues to push the boundaries of this useful technology.

The US had pioneered the use of HTHP cooling with alkali metals in nuclear power devices since the 1980s.These advancements are documented in Table 1. One notable development is the Heat pipe Power System (HPS), which was conceptualized and developed at LANL specifically for space applications. The HPS comprises multiple independent models, each possessing promising economic and operational features.

TABLE 1 The main conceptual designs of HPCRs in the United States.

Parameters	Unit	HOMER-15/25	SAFE-400	SP100	SAIRS	MSR	LEGO	HP-STMCs	Megapower	KRUSTY	HPCYHR
Institutions		LANL	LANL	LANL	NMU	MIT	INL	NMU	LANL	NASA	TAMU
References		Poston (2001)	Poston et al. (2002)	Demuth (2003)	El-Genk and Tournier (2004)	Bushman et al. (2004)	Bess (2008)	El-Genk (2008)	McClure et al. (2015)	Poston et al. (2020)	Alawneh et al. (2022)
cooling method		Sodium/ Potassium	Sodium	Lithium	Sodium	Lithium	Sodium	Lithium	Potassium	Sodium	Sodium
Number of heat pipes	Root	19/61	127	290	60	127	43	126	204	8	136
Spectrum		Fast	Fast	Fast	Fast	Fast	Fast	Fast	Fast	Fast	Thermal
Thermal power	kWt	15/93.4	400	2,400	407–487	1,200	20–24	1,600	5,000	5	3,000
Electric power	kWe	3/25	100	100	110	100	5–6	110	2,000	l	1,000
Heat pipe operating temperature	K	<1,100/880	1,200	-	1,100–1,200	1800	-	1,500	950	1,050	1,250
Conversion method		Stirling	Stirling	Thermoelectric conversion	Thermoelectric conversion	Thermal ion conversion	Stirling	Thermocouple conversion	Brayton	Stirling	-
Fuel		UN/UO_2	UN	UN	UN	UN	UO_2	UN	UO_2	U-Mo	UO_2
Enrichment	%	97/93	97	-	83.5	33.1	93	55~85	19.75	93.1	≤10
Core height	cm	54	25	600	42	62	54	66.1	150	25	80
Core diameter	cm	45	48	400	48	90	23.8	56	155.7	11	122
Core mass	kg	385	541.4	4,518 (total)	423.74	2,860	448	745	15,150	32.2	3,989
Application		Space	Space	Space	Space	Space	Space	Space	Space	Space	Terrestrial/ space

10.3389/fenrg.2023.1264168

Originally, the primary objective of the SP100 space nuclear reactor was to serve as an orbital power supply for the United States Strategic Defense Initiative (SDI) during the 1980s (Demuth, 2003). The project was initially sponsored by a consortium consisting of the US Department of Defense, the US Department of Energy, and NASA. However, as the SDI program diminished in importance following the dissolution of the Soviet Union, the focus of the SP100 mission shifted more towards meeting the needs of NASA. In the early 1990s, as NASA ambitious missions faced scrutiny and there was a growing preference for more pragmatic endeavors, the SP100 program was ultimately discontinued. Nonetheless, the preliminary safety analysis conducted for the SP100 nuclear power system, considering scenarios such as unprotected reactivity insertion and unprotected loss of heat sink, demonstrated that the lithium-cooled reactor coupled with the Stirling cycle exhibited satisfactory performance and resilience in the face of accidents (Jin et al., 2022).

In 1997, the initial model of the HPS underwent a successful test, demonstrating favorable conditions. However, it fell short of achieving the originally set heating power target (Houts et al., 1998). Subsequently, a series of experiments were conducted, which yielded highly successful demonstrations (Poston et al., 2000). The Safe Affordable Fission Engine (SAFE) was a HPS reactor specifically designed for generating electricity in space environments (Poston et al., 2002). The SAFE-400 was a 400 kWt reactor that has been specifically designed to be coupled with a 100 kWe Brayton power system. It consisted of 127 identical molybdenum modules. Another derivative design of the HPS, known as the Heat pipe-Operated Mars Exploration Reactor (HOMER), had been adapted for electricity generation during Mars exploration missions (Poston, 2001). The concept of a Martian Surface Reactor for the application of the Martian or Lunar surface power system to promote of human attempts to explore extraterrestrial efforts was initially proposed at MIT (Bushman et al., 2004). The reactor core could produce 1.2 MWt and 0.1 MWe power, operating in a fast spectrum. The reactor was cooled by a lithium HP that was also attached to the power conversion apparatus.

The Scalable AMTEC Integrated Reactor Space (SAIRS) nuclear system utilized a fast neutron spectrum, employing technology developed at the University of New Mexico (UNM). The cooling system for SAIRS involved the use of sodium HPs (El-Genk and Tournier, 2004). The power system of the HPCR with segmented thermoelectric module converters (HP-STMCs) was designed to continue operating even in the event of a unit failure, albeit with a reduction in thermal power output. This system incorporated lithium HPs and was designed with sufficient margins to ensure reliable performance (El-Genk, 2008). The modular HPCR for Lunar Evolutionary Growth-Optimized (LEGO) reactor was developed at the Idaho National Laboratory (INL). This reactor design had the capability to provide a 110 kWe with an efficiency of 6.7% (Bess, 2008). The LEGO reactor design offers improved reliability and safety compared to a single reactor configuration due to its unit design. Each unit in the LEGO system was capable of generating 5 kW of power. This modular approach enhanced the overall system reliability and safety by allowing for redundancy and easier maintenance and replacement of individual units.

The Heat Pipe Encapsulated Nuclear Heat Source (HP-ENHS) reactor was a conceptual design that relied heavily on passive safety features to prevent and mitigate accidents. The reactor incorporated HPs as part of its design to enhance the passive safety mechanisms. These passive safety measures were intended to minimize the reliance on active systems and human intervention during abnormal events, ensuring a high safety level in the reactor operation (Greenspan, 2008). The Special Purpose Reactor (SPR) conceptualized by LANL was an innovative small nuclear reactor (SMR) that offers several advantages. These advantages included significantly improved passive decay heat removal capability, the absence of positive void reactivity coefficient, a smaller and lighter reactor design, and a more robust core for safe transportation. These features made the SPR an appealing option for various applications that require a compact and reliable nuclear power source (Sterbentz et al., 2017). The SPR, designed by LANL, had a nominal core 5 MWt. Utilizing the Brayton thermodynamic cycle, the SPR was capable of producing approximately 2 MWe. This efficient conversion of thermal energy to electrical energy made it suitable for a range of applications that require a compact and high-performance power source (McClure et al., 2015). The expected operational lifespan of the core was designated as 5 years.

MIT had developed a novel reactor concept known as the Fluoride-Salt-Cooled High-Temperature Reactor (FHR) to support human exploration endeavors in extraterrestrial environments (Sun et al., 2016). The proposed design featured a fast spectrum, lithium HPCR utilizing UN fuel, with a thermal output capacity of 1.2 MWt. To generate electrical power, thermionic energy conversion technology was employed, resulting in a DC output of 125 kWe and an AC transmission capability of 100 kWe. The integration of the reactor assembly, power conversion units, and radiators are facilitated through HPs, eliminating the need for a liquid coolant loop in the system. Furthermore, CFD analysis indicated the system exhibits excellent thermal hydraulic characteristics (Wang et al., 2016).

Westinghouse Electric Company was currently engaged in the development of the eVinci microreactor, targeting decentralized generation markets and microgrids. This innovative technology was specifically designed to cater to a variety of applications, including military deployments, remote communities, and remote industrial mines, among others (Maioli et al., 2019). The core design of the eVinci microreactor consisted of a solid monolithic block incorporating three distinct types of channels to accommodate fuel, neutron moderators, and HPs. This versatile design enabled the reactor to support a wide range of electric power levels, ranging from 200 kWe to 25 MWe. The reactor was designed with a lifespan of 5–10 years and incorporates inherent safety features that ensure safe operation even in the absence of active controls or external interventions (Zohuri and McDaniel, 2019). Westinghouse had successfully conducted initial demonstration tests of alkali metal HTHPs utilizing Iron, Chromium, and Aluminum (FeCrAl) alloys. This advancement in HP technology facilitated the implementation of a Low-Enriched Uranium (LEU) micro-reactor core, combined with an open-air Brayton thermodynamic power conversion cycle (Swartz et al., 2021).

(Hernandez et al., 2019) conducted a comprehensive fuel cycle and neutronic analysis of a conceptual design that bore resemblance to the Westinghouse eVinci HPCR. The study they conducted offers

valuable insights into the behavior of the reactor fuel cycle and neutron dynamics. The examined concept incorporates low-enriched urania rods and utilizes potassium HPs for core heat removal. The research findings demonstrated that the HPCR design has the potential to operate continuously for over 10 years without the need for refueling. Moreover, the study suggested that this design was more suitable as a nuclear battery, emphasizing its capacity for decentralized power generation rather than serving as a centralized power source.

The KRUSTY was conceived as a crucial progression in the development of space reactors, aiming for successful deployment in space missions (McClure et al., 2020). KRUSTY served as a prototype for testing a 5 kWt Kilopower space reactor. Kilopower reactor designs make use of HPs to transmit fission energy from a solid fuel block in an effective method. These reactors were developed primarily for basic, low-power (1–10 kWe) space and surface power systems (Poston and Mcclure, 2017). The KRUSTY reactor underwent successful final testing in March 2018.

Texas A&M University (TAMU) recently proposed a micro-reactor design known as the Heat Pipe Cooled Yttrium Hydride Moderated Micro Reactor (HPCYHR). This innovative concept utilized HPs for cooling and employs yttrium hydride as a moderator. The reactor design incorporated low-enriched uranium fuel (Alawneh et al., 2022). For the purpose to investigate the heat transfer characteristics of the HPCYHR, commercial software such as STAR-CCM+ was employed. The power distribution obtained from neutronics calculations was employed in the simulations. The outcomes showcased that the reactor could be operated safely for over 11 years, producing a 3 MWt.

The Aurora power plant developed by Oklo is a liquid metal reactor with a capacity of 1.5 MWe, incorporating HPs to effectively conduct fission heat from the reactor core to generation system. Oklo estimated expenditure for constructing the entire power plant and its infrastructure was approximately $10 million. It was important to note that this cost excluded expenses related to fuel and land, as these would be obtained through separate programs established by the Department of Energy. The requested license and initial fuel load had a duration of 20 years (Adamas, 2020). DeWitte mentioned that Oklo planned to construct reactors that were significantly smaller in scale compared to those being developed by TerraPower (Clifford, 2021).

In April 2019, NuScale made an announcement regarding the development of a “simple and inherently safe compact HPCR” with a power range of 1–10 MWe. This innovative design requires minimal site infrastructure, enables rapid deployment, and features full automation during power operation. Collaborative partners involved in this project include Additech, INL and Oregon State University. It is worth noting that this project emerged following the request for ideas and designs by both the SDI and the Department of Energy (WNA, 2020).

2.2 Chinese HPCR research

Compared to the US, the research and development of HPCR came to a relatively late stage in China. In recent years, various domestic scientific research institutions such as Xi’an Jiaotong University (XJU) and Shanghai Jiao Tong University (SJTU) had actively engaged in numerous conceptual designs for HPCRs. Table 2 shows the main HPCR conceptual design for China in the recent decade.

A concept for a Mars surface HPCR had been proposed, employing lithium HP cooling, multiple Stirling engine conversions, a potassium HP radiator for heat dissipation, and Martian soil shielding (Yao et al., 2016a). The control mechanism is implemented through a rotating control drum. A lithium HPCR was specifically designed to operate at a 2.4 MWt, with a primary focus on achieving an extended lifespan and minimizing noise emissions (Sun et al., 2018a). The Monte Carlo program was employed to evaluate the power distribution and reactivity feedback, of core. The results demonstrated that the designed parameters were satisfactory. (Feng et al., 2022) introduced a megawatt-class HPCR moderated by zirconium hydride. The introduction of a moderator was found to have no substantial impact on the radial and axial power distribution as well as the power peak factor. Additionally, the results indicated that incorporating moderators was advantageous in reducing the thickness and weight of the shielding. To assess feasibility, a preliminary thermal analysis was conducted, revealing that zirconium hydride remains stable within the HPCR. Additionally, the analysis showed that yttrium hydride demonstrated superior thermal stability.

Zhang et al. (2020) developed a HPCR incorporating the use of integrated HP fuel modules. A moderated thermal-neutron spectrum reactor is designed with the 3.2 MWt. The design comprises 234 HP-Fuel elements, where each element consists of a central lithium HP surrounded by highly enriched UN fuel pellets, with cladding on both radial sides. A design idea of 40 kWe nuclear reactor power for Mars surface (NRPMS) was proposed by the China Institute of Atomic Energy (CIAE) (Yao et al., 2016b). The results indicated that the proposed nuclear reactor power scheme is both reasonable and feasible. It demonstrates the capability to meet the safety requirements and achieve the desired operational lifetime. Wang et al. (2020a) presented a preliminary design for a 25 kWe heat pipe cooled reactor power source (HPCRPS). The steady-state and transient performance of the system was analyzed by using a thermal-hydraulic analysis code. The results indicate that all the designed parameters meet the necessary safety requirements. Sun et al. (2018b) developed a design for a 120 kWe lithium heat pipe reactor power source (LHPRPS), intended for various applications. In order to provide shielding, tungsten and water are utilized on both sides of the reactor core. The designed core parameters have been assessed to meet the safety requirements, ensuring the neutronic safety of the reactor.

In the study conducted by Liu et al. (2019), a potassium heat pipe cooled reactor power source system (PHPCRPS) with a power output of 50 kWe was proposed. The HPCR design proposed by the researchers is deemed reasonable and reliable. The residual heat removal system designed for the reactor exhibits a sufficient safety margin to effectively dissipate the decay heat. Furthermore, the study conducted by Chai et al. (2022) introduced a conceptual design for a moderated micro nuclear reactor cooled by heat pipe (MHPR). The MHPR concept was built upon a softened neutron spectrum, which had the potential to enhance the utilization of thermal neutrons and reduce fuel inventory. The reactor had a total

TABLE 2 Main parameters of HPCR in China.

Parameters	Unit	HPCMR	NRPMS	LHPRPS	PHPCRPS	HPCRPS	NUSTER-10	HPCR	NUSTER	MHPR	HPR-CF
Institutions		CIAE	CIAE	XJU	XJU	XJU	XJU	SJTU	XJU	SJTU	CAEP
References		Hu et al. (2013)	Yao et al. (2016b)	Sun et al. (2018b)	Liu et al. (2019)	Wang et al. (2020a)	Tang et al. (2020)	Zhang et al. (2020a)	Liu et al. (2022a)	Chai et al. (2022)	Guo et al. (2023a)
cooling method		Lithium	Lithium	Lithium	Potassium	Potassium	Potassium	Lithium	Sodium	Potassium	Lithium
Number of heat pipes	Root	126	61	37	37	37	19	234	109	780	216
Spectrum		Fast	Fast	Fast	Fast	Fast	Fast	Fast	Fast	softened	Fast
Thermal power	kWt	1,600	210	2,400	500	500	135	3,200	1,000	3,500	3,000
Electric power	kWe	100	40	120	50	25	10	1,000	100	-	1,000
Heat pipe operating temperature	K	1,525–1,529	1,300	1,200	-	850	-	1750	-	948	1,323
Conversion method		Thermoelectric conversion	Stirling	Thermoelectric conversion	Thermoelectric conversion	Thermoelectric conversion	Thermoelectric conversion	Brayton	Thermoelectric conversion	-	Brayton
Fuel		UN	UN	UN	UN	UN	UN	UN	UO_2	UO_2	CERMET
Enrichment	%	42	83.5	70	45	65	-	92	-	16.5	65–85
Core height	cm	60	38	34	34	40	-	40	45	150	<80
Core diameter	cm	34.2	21	43.2	43.5	52	-	46	96	64.7	<85
Core mass	kg	3,200 (total)	433	310	310	310	-	-	-	7,028 (total)	3,100
Application		Space	Space	Space/marine	Space/marine	Terrestrial/marine	Space	Space	marine	Terrestrial	Terrestrial

10.3389/fenrg.2023.1264168

3.5 MWt and its estimated core lifetime was 8.2 years without the need for refueling.

In the study by Ma and Hu (2023), an optimized heat pipe cooled traveling wave reactor (HPTAWR) was developed. This reactor design incorporated a neutron breeding wave to achieve Uranium-Plutonium breeding. The results of the study demonstrated that the HPTWR optimized could attain a power output of 70 MWt and sustain continuous operation for 46 years using lithium HPs. The propagation of the traveling wave in the reactor caused a flattening of the axial power distribution, leading to a gradual decrease in the temperature peak of the HP wall. At the end of the cycle, the temperature peak reached approximately 1784.6 K. This reduction in thermal stress enhanced the safety of the HP wall. Additionally, the study proposed a design for a 65.5 MWt HPTWR (Ma and Hu, 2022). The HPTWR design incorporated an ignition fuel with 14% enrichment and a breeding fuel with 8.5% enrichment. With this configuration, the reactor could operate for 59 years without the need for refueling. This design fulfilled the requirements of utilizing low-enriched fuel while achieving a high power output.

Guo et al. (2023) proposed a compact HPCR design where the ceramic metal composite (CERMET) fuel was used (HPR-CF) from the China Academy of Engineering Physics (CAEP). The CERMET fuel offered several advantages such as high temperature resistance and thermal conductivity. The HPR-CF had excess reactivity that allows it to operate at high temperatures and sustain a thermal power output of 3 MWt for over 3,000 days. In the study by Li et al. (2023a), a design concept for a multi-purpose HPCR was introduced. This micro-reactor employed an enrichment level of 19.75% and had the capability to operate for over 5 years at a 2 MWt without requiring refueling. Monte Carlo simulations were utilized to calculate various parameters, including reactivity, burnup, power distribution, and temperature coefficient, under both normal and accident conditions. The analysis of neutron physics revealed that the preliminary design of the lithium heat pipe cooled modular fast reactor (HPCMR) met the requirements of both economy and safety. This conceptual design held the potential to support future applications in Chinese manned lunar base (Hu et al., 2013). The utilization of HPs in the reactor design allows for a more compact core structure, leading to a reduction in the overall mass of the reactor. This compactness facilitated easier launch and deployment. Additionally, the application of HPs provided redundancy in the system, as damage to certain HPs did not impact the overall energy transfer. This design feature helped to avoid single-point failures and ensured the long-term operation of the reactor without the need for regular maintenance.

XJU had proposed a novel design for the NUclear Silence ThermoElectric Reactor (NUSTER), which utilizes HPs. The study demonstrated that the core components, such as HPs, matrix, and fuel rods, exhibited significant thermal margins during normal operating conditions, indicating their ability to operate with ample safety margins (Huang et al., 2022). The findings indicated that the core design proposed for the Unmanned Portable Reactor in Silence (UPR-S), which operated on the NUSTER power system, successfully fulfilled the criteria of criticality safety and operational longevity (Du et al., 2021). Nonetheless, in the event of a failure of the two adjacent HPs in the 1/8 reactor core, it had been observed that the temperature of the Molybdenum matrix surpasses its temperature threshold, leading to a notable escalation in average thermal stress. These findings underscored the necessity for future design improvements, particularly in terms of optimizing the matrix material (Liu et al., 2022). Furthermore, a novel reactor core design denoted as UPR-SL, had been introduced, utilizing a low-enriched uranium fuel. This design was built upon the foundation of the pre-existing HPCR design, UPR-S (Wu et al., 2023). To reduce the enrichment level of fuel, a high-density UN fuel had been employed as a substitute for the original UO_2 fuel. Additionally, an alternative variant of the NUSTER power system, known as NUSTER-10, had been introduced (Tang et al., 2020; Tang et al., 2021).

2.3 HPCR studies in other countries

The concept of HPCR was initially proposed by Grover's patent in 1965 (Grover George et al., 1967). After 2 years, the European Atomic Energy Community presented a HPCR design based on Grover's original concept (Fiebelmann, 1968). However, in recent years, few studies have been proposed for HPCR designs in Europe from the published literature. In Japan, in addition to government investments, several universities and research institutions had undertaken research in the field of space nuclear reactors. These academic institutions had dedicated manpower and resources to contribute to the advancement and development of space nuclear reactor technology. Moreover, HP technology had been employed to improve the reliability of safety systems in the International Thermonuclear Experimental Reactor (ITER). By implementing HPs, the safety systems of ITER had been enhanced, ensuring efficient heat transfer and overall system reliability (Kovalenko et al., 1995). Additionally, Japan had utilized loop HP (Mochizuki et al., 2014a) technology and conducted thorough system simulation calculations to verify the effectiveness of this design approach. This technology had also been widely adopted in pressurized water reactors in Ukraine, demonstrating its broad applicability and success in practical applications. Furthermore, they proposed a conceptual design for dealing with decay heat removal after reactor shutdown based on the HP with water working fluid (Mochizuki et al., 2014b; Randeep et al., 2014). The designed system, when coupled with HP cooling and initial gravity feed water charge, could effectively reduce the temperature of the nuclear core to below 100°C in less than 6 h. The implementation of a fully passive operational mode had the potential to enhance the safety of nuclear power facilities.

Starting from 2017, Toshiba Energy Systems and Solutions Corporation had been researching and studying a Mobile-Very-small reactor for Local Utility in X-mark (MoveluX) as a viable distributed energy source. The main concept behind MoveluX revolved around utilizing a sodium HP cooling system and a calcium hydride-moderated core. This design approach aimed to streamline the reactor system, enhance inherent safety, and strengthen nuclear security (Kimura and Asano, 2020). This compact reactor design was capable of generating a thermal power output of 10 MWt and an electrical power output ranging from 3 to 4 MWe by utilizing a Helium turbine with a Brayton cycle (Du et al., 2022).

Allaf et al. (2023) investigated the safety aspects of the novel Micro Research Reactor cooled by Heat Pipes (MRR-HP) design.

The unique design feature of the MRR-HP was the incorporation of dual sets of HPs within the monolithic block. The HPs for working fluid water were utilized for normal operation, while fluid potassium HPs were employed during the accident and post-accident scenarios. The implementation of water HPs enables efficient cooling of the reactor, thereby maintaining the fuel temperature below the threshold of 423K.

In Korea, a Hybrid micro modular reactor, which combined the capabilities of renewable energy and energy storage systems, had been designed utilizing potassium HP technology (Choi et al., 2020). The H-MMR offered increased flexibility and efficiency in electricity and thermal generation, capable of producing 10 MWe and 18 MWt through load following strategies. To ensure safety, the RVACS had been specifically designed to effectively remove accident residual heat by cooling the reactor vessel. The Korea Atomic Energy Research Institute had created a conceptual HPCR design that might be used to generate electricity continuously in space and be deployed on a launch vehicle on the lunar surface. This design employed high-assay low-enriched uranium fuel with an enrichment level of 19.5 wt% (Choi et al., 2022). The design objectives for the nuclear reactor core were set to achieve a compact size, with a mass of under 1,200 kg, a height below 5 m, and a diameter less than 2 m. Additionally, the intended operational lifespan of the reactor core was planned to exceed 10 years, while providing a thermal power output of 5 kWt.

3 Heat transfer characteristic of HTHP

Since the application of HTHP, there has been considerable interest in investigating the heat transfer performance of HTHPs in order to optimize their design. However, there are complex flow and heat transfer processes in the HTHP system. In this section, we summarize the impact of several factors on the heat transfer performance of alkali metal HTHPs, which can be mainly divided into transient and steady characteristics. For the research of transient characteristics, the literature on startup and oscillation conditions is reviewed. When all of the working fluid in HP has melted, there is continuous gas flow in the condensing section, and the liquid can keep going back to the evaporation section. The heat transfer capacity of evaporation section and condensing section is the same, and HP will switch to steady-state operation. The thermal performance of HP under steady-state conditions is significantly influenced by several factors, including the presence of non-condensable gas (NCG), different parameters, limitations, and the filling ratio.

3.1 Transient characteristic

3.1.1 Startup characteristic

Startup condition plays an essential role in the performance and reliability of HP system. Ensuring efficient heat transfer and working fluid flow within the HP is essential to achieve stable operation during startup. Various factors, such as the charging amount, types of working fluids, inclination angle, and temperature variations, significantly influence startup. Many researchers have conducted extensive studies investigating these factors and their impact on startups.

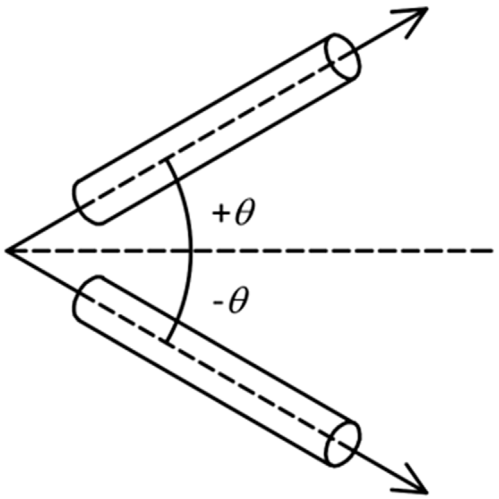

FIGURE 2
The schematic of HP inclination condition.

Some researchers experimentally explored the impact of inclination angles on the startup performance of HP. Ma et al. (2022a) focused on experimentally investigating temperature variations of a sodium HP under near 0° during the frozen startup. The HP position of positive and negative angles was shown in Figure 2 to their research. Their findings highlighted the challenges posed by negative inclination angles, where gravity impeded the flow of liquid from the condenser to the evaporator. This leaded to more pronounced temperature differences and higher startup power requirements compared to horizontal and positive inclination cases. On the other hand, positive inclination angles exhibited periodic temperature oscillations during startup. Guo et al. (2014) found that increasing the inclination angle in the condensing section increased the temperature rise, thereby facilitating the startup of the HP. Wang et al. (2020c) performed research on the effect of heating powers on the frozen startup performance of a potassium HP in addition to the influence of inclination angles. According to their research, a successful frozen startup requires the right matching of inclination angle and heating power. Guo et al. (2018) discovered that the frozen startup time of a Na-K gravity-driven HP increases in proportion to the inclination angle. They further observed that as the inclination angle increases from 0° to 50°, the startup and heat transfer performance of the HP improves, while the temperature difference decreases. A slight decrease was observed when the inclination angle exceeded 60°. However, the experimental results of (Ping et al., 2015) indicated that there was negligible influence on restart characteristic for sodium HP under different angles because the curves for temperature raising almost coincide. Niu et al. (2016) conducted experiments and found that the sodium HTHP can be smoothly started at various angles. Furthermore, they observed that the starting time of the HTHP decreased with an increase in heating power. However, the angle had little effect on the starting time.

In addition, many researchers also have studied the influence of types working fluid on startup. Sun et al. (2020) conducted an analysis on working fluid in the HP and found that the presence of a

liquid pool at the bottom of the HPs leads to a nonlinear temperature reactivity coefficient, indicating the influence of the working fluid on startup dynamics. Another research investigated by Lu et al. (2017) was the charging amount in sodium HPs. Their study revealed that increasing the charging amount from 22.6 g to 26 g resulted in a successful startup, highlighting the significance of the charging ratio in enhancing the startup performance of the HP. Han et al. (2019) conducted a study on the startup performance of potassium HPs with and without a wick structure. Their experiments showed that during startup and heating, wickless HP s operated under intermittent boiling conditions, with decreasing intensity of boiling as the liquid filling decreased. In their study, it was noteworthy that the impact of the inclination angle on the heat transfer performance of the HP was found to be negligible.

For the operation limitations of HTHP, (Chen et al., 2022b) observed the occurrence of the sonic limit during the startup process of frozen cesium HPs. However, they found that this limit disappeared as the heating power was increased. Deng et al. (2023) developed a hardware-in-the-loop test platform capable of dynamically adjusting the heating power of the HP in real-time, taking into account the effect of temperature feedback. During the frozen start-up process of the sodium HP under the temperature feedback heating mode, they identified five distinct stages based on the evolution of power and the state of the sodium vapor. These stages included the transient start-up phase, during which the sonic limit and viscosity limit were observed. Guo et al. (2021) prepared a cesium HP and conducted a study on its heat transfer and start-up performance. Their findings revealed that the cesium HP exhibited a rapid start-up speed and demonstrated good temperature equalization characteristics. Ma et al. (2023) discovered that a significant increase in heat flux could lead to unstable conditions when the heat flux surpassed 40% of the capillary limit critical heat flux.

In conclusion, the frozen startup of HPs presents complex challenges in their operation. The cost is too high to study only through experimental methods. Therefore, many researchers have developed a series of simulation codes for the frozen startup of HPs.

Ma et al. (2022b) employed a numerical approach to simulate the system startup process. They developed a two-dimensional HP model and coupled it with an open-air Brayton cycle model using the Heat Pipe Reactor TRANsient analysis code, HPRTRAN. The model was validated through startup experiments, confirming its accuracy and reliability. Additionally, the startup of the reactor could be controlled by implementing intermittent drum motion, introducing reactivity in a stepwise manner. This control strategy effectively mitigated large power fluctuations and power peaks within the core. Yuan et al. (2016b) had developed a specialized transient analysis code called TAPIRS for simulating the startup process of HPCR from a frozen state. This code had been extensively used to study the system transient performance during the startup process, ranging from zero cold power to full power.

Huaqi et al. (2022) established transient analysis models for HTHPs starting from a frozen state. The results of the study indicated that the predicted trends obtained using the HPCR code were reasonable, and the deviation from experimental data was less than 2%. This finding further supported the applicability and effectiveness of the transient models for HPs. Additionally, the transient performance of sodium HTHP was numerically simulated in the context of a molten salt reactor (Wang et al., 2013). Numerical results obtained using a FORTRAN code demonstrated that sodium HTHP achieved successful startup and were capable of rapidly removing residual heat from the fuel salt during steady-state conditions in the event of an accident.

Zhang et al. (2021c) developed a three-stage frozen startup model to accurately depict the thermal behavior of NaK HPs throughout the startup process. The findings of the study indicated that the temperature rise rate of the condenser in the HP increased as the initial temperature rises. This relationship was beneficial for overcoming the sonic limitation of the HP at a faster rate. Qiu et al. (2022) developed a transient analysis program HEART for NUSTER. A startup scheme based on the analysis of transient thermohydraulic behavior during cold start-up was proposed for a three-stage HPCR with high safety. Hu et al. (2022) developed a network code in Python specifically for ultra-high temperature lithium HPs. The study found that increasing the wall thickness and wick thickness of a HP leaded to an increase in the transition time. Conversely, increasing the length of the condensation section had a beneficial effect in reducing the transition time.

Zhong et al. (2021) investigated the startup characteristics of the MegaPower system using the HPR transient analysis code called HPRTRAN. During the startup process of a HPCR, there might be significant power fluctuations and the occurrence of a “temperature platform,” which could hinder the reactor startup. In comparison, the use of an interval rotating control drum as opposed to a continuous rotating control drum was considered a safer and more feasible scheme for starting the reactor. Zhang et al. (2021b) wrote a HPSTAC program to investigate the startup process of NaK HP. The starting ambient temperature mainly affected the heating rate of the condensing section. The input heat flux had a threshold effect on the starting stages of the HP. As the heating power increases, the outer wall temperature of the HP rose slightly, the start-up time of the condensing section decreased, and the equivalent heat transfer coefficient of the HP and the surface heat transfer coefficients of the evaporation and condensing zones increased linearly with the heating power. Yuan et al. (2016a) wrote the TAPIRS program in FORTRAN language to simulate the transient behavior of a HPCR system based on SAIRS. The model was validated by comparing the full power parameters with the literature, and the maximum relative error was less than 6%.

3.1.2 Oscillation condition

There is potential application for HPCR under marine condition. Therefore, there has been some experimental research for alkali metal HTHP in recent years. Guo et al. (2023) showed that the fuel temperature and the reactor power would change periodically with a similar period as the HP temperature oscillation depending on the simulated results. The buffer layer with a lower thermal diffusion coefficient was found to mitigate the temperature and power oscillations, but it would increase the operating temperature of the reactor, which might compromise the safety of the reactor system. Teng et al. (2020) showed that swinging motion had little effect on the start-up performance of the sodium HP, but it caused small-amplitude periodic temperature fluctuations especially at the evaporator. The frequency of temperature fluctuation was almost the same as the swing.

Additionally, the amplitude of temperature fluctuation increases with the swing amplitude. Sun et al. (2022a) showed that the temperature fluctuation had the same period as the periodic swing. Periodic swing did not significantly affect the heat transfer of HTHP when the condenser length was appropriate, but the thermal resistance increased slightly compared to the steady state. Under periodic swing condition, if the condenser is too long, the HTHP is more likely to fail. Wang and Li (2023) investigated the HTHP for potassium working fluid in the CFD method. They concluded that the influence of the filling ratio is more significant to equivalent thermal resistance than the rolling period. The filling ratio refers to the proportion of the working fluid volume in relation to the HP volume.

3.2 Steady characteristic

3.2.1 NCG influence

The alkali metal inside the HP is activated by the neutron irradiation in the reactor, which produces inert gas constantly. The inert gas, or NCG, hinders the normal condensation of alkali metal working fluid in HTHP at the phase interface and increases the thermal resistance. This phenomenon is disadvantageous to the isothermal property and heat transfer effectiveness. Therefore, it is important to study the effect of NCG on the heat transfer performance of HTHPs.

In terms of previous studies of noncondensing gases, (Shaubach and Gernet, 1992) found that a sodium HP can operate stably under design conditions when the non-condensable gas pressure is below 0.01 bar, and a small amount of non-condensable gas has a negligible effect on the steady-state heat transfer performance of the HP. Matsushita (1975) found that the condensation heat transfer coefficient of the HP decreases significantly with the increase of non-condensable gas content in the tube, and a 5% volume fraction of non-condensable gas can reduce the steam condensation rate by 20% and affect the liquid working fluid reflux. Fukuzawa and Fujiie (1978) found that too much non-condensable gas would build up at the end of the HP's condensing section, leading to a sharp temperature drop there. As the power increased, the drop shifted further into the condensing section, and the gas had less effect. Ponnappan et al. (1990) found that the sodium HTHP could start easily from the frozen state under the NCG loading. Another experiment (Ponnappan and Chang, 1994) investigated the startup performance in vacuum and gas-loaded modes, which the latter took significantly longer. The sodium HTHP in vacuum mode, on the other hand, exhibited rough start-up behavior as seen by high temperature spikes at the evaporator and heater during the frozen start-up process. Zhang et al. (2023) experimentally explored the influence of NCG existence on sodium HTHP. The maximum heat transfer rate under the sonic limit is found to be reduced due to the presence of NCG in the HP. The influence of inner wick structure is negligible to the HTHP sonic limit.

In addition, establishing code modeling is an effective way for analyzing the influence of NCG. Zhang et al. (2022) used the thermal resistance network method to model NCG heat transfer and studied its effect on the steady-state heat transfer of a lithium HTHP. The results indicated that NCG reduced the effective heat transfer length, isothermality and efficiency of the HP. Moreover, as the NCG volume fraction increased, the temperature drop in the NCG region became larger, and the overall temperature of the HP also rose. Another numerical investigation (Zhang et al., 2021) tested the generation of NCG for lithium HTHP under neutron irradiation condition. The amount of helium produced by NCG increased with the development of liquid filling ratio and lithium enrichment. Moreover, The helium production was seldom impacted by the working temperature of the lithium HP. Wang et al. (2022) created a mathematical and physical model for how NCG affected the heat transfer of a lithium HTHP and developed a transient analysis code, HPTAC-NCG. During the steady-state operation, the temperature drop in the NCG region increased with the NCG volume fraction, and the HP average temperature increased, which could cause overheating and drying out at the evaporator bottom. As the evaporator input power increased, the NCG volume fraction for the same mass decreased, but increasing the input power alone was not economical to counteract the negative effects of NCG.

3.2.2 Parameters influence

The HP thermal performance was mainly affected by the parameters of geometry and thermal-hydraulic characteristics. In the experiment, (Dussinger et al., 2005) compared the compatibility of titanium/potassium and titanium/cesium, taking into account the different physical chemistry properties of different alkali metals. This research further confirmed that these HPs could meet the performance requirements for radiator systems. The steady-state performance of sodium HP was investigated by Guillen and Turner (2022). They found the sodium HP with screen-covered grooves was generally superior to that of open grooves in a vertical gravity-assisted orientation. The different wick configuration arrangement is showed in Figure 3. Under the condition of horizontal orientation at 650°C, the performance limit of the annular wick was 15% higher than that of the screen-covered grooved wick. Based on this, it was stated that the annular type has a high-performance limit below 777°C and that the screen-covered grooved wick has a high-performance limit above 777°C, but there were no experimental results conducted above 777°C.

The oscillating HP consists of capillary tubes that are meandering and partially filled with a working fluid. The fluid exhibits oscillatory behavior and propels forward when subjected to thermal loading. For the oscillating HP, (Ji et al., 2020) found that the temperature difference and thermal resistance between the evaporator and condenser first decreased and then increased with the heat input. In their investigation, the NaK HTHP demonstrated the capability to transport 3169 W of heat while achieving a thermal resistance of 0.08°C/W. The heat transfer performance of the HPs improved with an increase in the potassium mass fraction. This enhancement was attributed to the effects of the saturated vapor pressure gradient, viscosity, and wettability (Ji et al., 2022; Wu et al., 2022; Wu et al., 2023) experimentally investigated the heat transfer performance of NaK oscillating HP. Their results showed that the thermal resistance of HP dropped at first, then increased with the filling ratio When the inclination angles were between 30° and 90°. The minimum value was obtained at 48% filling ratio.

Tian et al. (2021) investigated how the heat transfer performance of potassium HP varies with the inclination angle and the filling ratio. They discovered that overheating in the evaporator results from insufficient working fluid and increasing power. Wang et al.

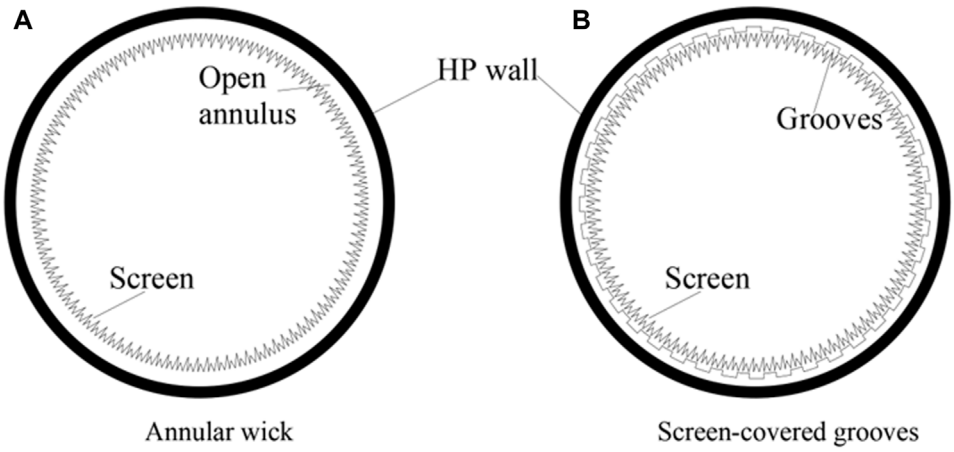

FIGURE 3
The cross section of HP.

(2021) examined how the HP heat transfer performance changes with the heating power and the inclination angle. They observed that overheating occurs when the power surpasses a limit and that increasing the inclination angle improves heat transfer for low filling ratio HP, but has no significant effect for high filling ratio HP. Therefore, they recommended that the heating power should be regulated to avoid overheating in the HP design. Mantelli et al. (2017) showed that the sodium thermosyphon could transport 250 W more heat power on average at an incline position (10°) than at a vertical position, for the same adiabatic section temperature. The thermosyphon could transport 250 W more heat power on average at an incline position (10°) than at a vertical position, for the same adiabatic section temperature.

Yang et al. (2022) investigated how different parameters affect the heat transfer performance of potassium HTHP. The heat transfer performance of HP can be improved by increasing the wicking mesh and the filling charge amount. The latter can also prevent overheating at the evaporation section. Kang et al. (2019) fabricated a sodium HTHP and studied the thermal performance. The HP thermal resistance reached a minimum of 0.11°C/W at a heat load of 790 W and an inclination angle of +90°C, which favored heat transfer.

Guo et al. (2018) studied how the heat transfer performance of a high temperature thermosyphon was affected by charging it with sodium-potassium alloy. The condenser had a higher heat transfer efficiency at high heating temperatures. The temperature difference at the condenser decreased with increasing heating temperature. Below 825°C, the temperature distribution was more uniform with a short condenser length and a large inclination angle. Above 825°C, these factors had no more advantages. The experimental study of (Liu et al., 2020) explored the factors affecting the heat transfer performance of potassium HTHP. The heat transfer performance improved with the increase in heating power. Zhang et al. (2020) studied the isothermal characteristics and start-up performance of cesium HP. The cesium HP could start normally at a furnace temperature of 330 ~ 630°C. The start-up time was shorter at higher furnace temperatures. Wang et al. (2022) conducted experimental and numerical studies on the effect of hydrogen permeation on the heat transfer of sodium HTHP. The model was validated by experimental tests. The experiments showed that the top end of an LMHP dropped to below 400°C after hydrogen inactivation, with the evaporator heating temperature at 950°C. The heat transfer was negatively affected by the gas blanket formed by the hydrogen migration along the condensate in the condenser.

For the numerical method, (Tian et al., 2022a) investigated how the heat transfer of Na and K HP was affected by different parameters using the improved thermal resistance network method. The HP was influenced by different types of wicks, such as main line, channel, wire mesh, and sintering. Zhang et al. (2022) proposed a heat pipe cooled Advanced Reactor Transient analysis code (HEART). HEART could successfully predict the steady-state performance of the NUSTER, which showed that the solid-state core could flatten the temperature well. Ge et al. (2022) developed a code for HPCR analysis called TAPIRSD, which was validated by the experimental data of the KRUSTY prototype of the Kilopower space reactor. The TAPIRSD code results agreed with the experimental data, despite the larger temperature oscillation amplitude. The peak and valley value errors were less than 2%, which showed the accuracy and reliability of the improved model and code.

Sun et al. (2022b) simulated the thermal behavior of potassium HP at high temperature. A liquid pool formed at the bottom of the evaporator in the vertical and inclined cases. This increased the local thermal resistance and the peak temperature at the beginning part, which was 200 K higher than the rest part of the HP. Mao et al. (2022) numerical the heat transfer lithium HP with solid-liquid-gas three-phase coupled model. The tube wall temperature dropped sharply in the steady state operation, while the vapor temperature and pressure were almost constant. This showed that the lithium HP had good isothermal properties. Yu et al. (2022) established the CFD analysis model of sodium HP. Under uniform heating, the velocity of vapor chamber changed linearly in the evaporation section and decreases in the condensing section with increasing pressure. The heating power also affected the vapor flow pressure drop and velocity. The liquid phase flow pressure drop was the main factor

TABLE 3 Representative operation limits correlations of HPs.

Limitation	Description	Phenomenon
Sonic	$Q_{sinic} = A_v \rho_v h_{fg} \sqrt{\frac{\gamma_v R_v T_v}{2(\gamma_v+1)}}$	The vapor flow will be obstructed, and the maximum heat transfer rate will be restricted
Entrainment	$Q_{entra} = A_v h_{fg} \sqrt{\frac{2\pi\sigma\rho_v}{L}}$	Some liquid can be pulled from the wick, which causes pressure drops and lowers the performance of the heat pipe
Boil	$Q_{boil} = \frac{2\pi\sigma l_{eff} k_{eff} T_v}{h_{fg}\rho_v ln\left(\frac{r_n}{r_v}\right)}\left[\frac{1}{r_n} - \frac{1}{r_{eff}}\right]$	The presence of air bubbles inside the wick, resulting in an overheating generation, significantly impacts the liquid backflow
Capillary	$Q_{capil} = \frac{\frac{2\sigma_l}{r_{cap}} - \rho_l g L_{HP} \sin\theta - \rho_l g D_v \cos\theta}{(F_l + F_v) L_{eff}}$	Insufficient liquid withdrawal leads to the drying out of the evaporation section and subsequent impairment of heat transmission
Viscous	$Q_{visic} = \frac{r_v^2 A_v h_{fg} P_v \rho_v}{16 L_{eff} \mu_v}$	The vapor is in a low-density state and exhibits 0 pressure at the condense section. The continuum vapor limit will occur earlier

in the two-phase flow pressure drop for horizontal and inclined HPs. The gas flow velocity dominated the gas-liquid shear effect.

3.2.3 Heat transfer limitations of HP

Internal fluid conditions affect the HP performance. The heat transfer limits for HPs and thermosiphon using the equations are shown in Table 3. The heat transfer performance limits for capillary HPs are viscous, sonic, entrainment, boiling, and capillary limits. When the vapor velocity approaches sonic or supersonic conditions during startup or steady state, a phenomenon known as "vapor choking" takes place. This creates the sonic limit. Only capillary wick HPs are affected by the capillary limit, which occurs when the maximum capillary drive pressure is smaller than the difference in pressure between vapor and liquid (Chi, 1976). The viscosity limit happens when the pressure gradient is lower than the viscous force. The entrainment limit happens when the vapor flow disrupts the countercurrent liquid flow. The boiling limit happens when the radial heat flux is too high and affects the fluid flow by boiling (Nemec et al., 2013).

Ivanovskii et al. (1977) performed the experiments on two sodium heat pipes equipped with distinct composite wicks in order to investigate the impact of wick structure on the sonic limit at 1,500–3,000 W of heating power. Faghri et al. (1991) found the capillary limit for an evaporator tilt angle of 5.7°, which was affected by copper contamination in the working fluid and dry evaporator wicks that caused gases that could not be condensed. Clack (2019) studied the performance limits under different heat fluxes for the sodium HP. This HP started to stay stable when the heat flux reached 84 W/cm^2. The temperature exhibited a consistent upward trend, suggesting the occurrence of HP dry-out. Subsequently, after a duration of 45 s, the HP encountered a failure event. Kemme (1966) researched the heat transfer limits for the potassium and sodium HP. The experimental results showed that a momentum interaction between vapor and returning liquid at lower temperatures could severely limit heat transfer and may even influence HP startup. Significant improvements in heat transfer capability and HP startup behavior could be achieved through the implementation of a two-component wick structure.

According to experiments of (Ma et al., 2023), at the evaporator end, the capillary limit results in a rapid increase in temperature of around 5 K/s, whereas the condenser and adiabatic sections experience a decrease in temperature. To recover from the capillary limit, a HP can increase the positive inclination or decrease the heating power. Walker et al. (2013) investigated at the capability of a sodium HP and a grooved wick HP to function at their capillary limits. At 846 W, 546 W, and 346 W of operational power, the evaporator reached its capillary limit, with further increases of 0.25 cm, 1.52 cm, and 2.54 cm, respectively. The capillary limit was reached for the self-venting sodium HP when the evaporator raised 7.62 cm at 3.4 kW of power and 12.7 cm at 1.4 kW.

Wang et al. (2021) found that the condensation limit only happens when natural air convection and thermal radiation cool the potassium HP condenser section. The viscosity limit is simple to achieve when the HP is in its startup phase at a low-temperature state. This is because both the friction and vapor viscosity forces are considerable for a HP with a high L/D ratio. When it comes to the sonic limit in a high-temperature state, it takes place at the condenser intake because the temperature was lower than the temperature in the surrounding area. After the sonic limit, there was a brief increase in temperature, followed by a steep decline brought on by the force of friction. When the cooling power is increased, the HP will reach its primary heat transfer limit, referred to as the entrainment limit. Chen et al. (2022a) found that the modulated heating mode is better than the constant heating mode, which can prevent the capillary limit, maintain good temperature uniformity, and raise the operating temperature and the effective length of cesium HP.

Tian et al. (2022b) investigated the heat transfer limits for sodium HTHP and the models were evaluated. They found that the model of Chi matched the experiments at 0° with a relative error of 19.0%, and the effective length of the HP affected the model accuracy. However, the model of Chi did not work for the inclined conditions. The research carried out by Zhang et al. (2022) analyzed the amount of heat that could be transferred by a liquid metal sodium HTHP when positioned at a variety of horizontal angles. The startup performance was impacted by its continuous flow limit. Since the transition temperature increased with increasing horizontal angle, the HP was more vulnerable to the continuous flow limit at large angles. Wei et al. (2021) found that the sonic limit was shown to be the most important factor in sodium HP heat transmission between 500°C and 650°C, whereas the carrying limit was determined to be the most important factor in operating temperatures over 650°C.

Zhao et al. (2021) experimentally and numerically studied the start-up process and tested the temperature and heat flux under

steady condition. The experiment results showed that the length-to-diameter ratio, heating heat flow, and operating temperature affected the acoustic velocity limit of HTHP. Guo et al. (2022) proposed an improved model for the HP in simulation, which accounted for the heat conductance in the wall, the vapor flow in the vapor space, and the liquid flow in the wick based on the network method. The model was confirmed by comparing it to data collected from experiments on a copper-water HP. This model was used to examine the sodium HP. The HP was functional at all positive inclination angles. However, its capillary limit was reached at an inclination angle over 30°. Dutra et al. (2023) developed a numerical sodium HP model based on VOF and verified it with experimental data. The experiments confirmed the results and obtained the capillary limits for several cases. These results showed that Sockeye could compute the temperature distribution in HPs and predict the capillary limit.

3.2.4 Geyser boiling

The Geyser Boiling phenomenon, or intermittent boiling, is an instability phenomenon that several researchers observed since 1965 during the thermosyphons' operation. It happens when a vapor bubble forms and releases in the evaporator liquid pool, pushing a lot of liquid at high speed to the condenser's upper regions. The bursting of this bubble can induce significant vibrations in the thermosyphon, with the magnitude depending on the filling ratio. This phenomenon is attributed to the abrupt generation and expansion of vapor resulting from a fall in the hydraulic head, which might potentially induce vibration and cause damage to the pipes (Jafari et al., 2017). Although it does not affect the thermal performance, it should be avoided because it damages the condenser end cap.

Yang et al. (2022) found that HPs containing 50 g of potassium exhibit a severe geyser boiling phenomenon at angles of 45° and 90°, which could pose a risk to safe operation. Manoj et al. (2012) focused on studying the impact of filling ratio on the thermal efficiency of sodium HPs. The results indicated that sodium HPs with a liquid filling rate of 40% exhibited lower heat transfer resistance and better isothermal properties compared to other filling ratios. Mantelli et al. (2017) found that the geyser boiling effect mostly happened in cases with a thermosyphon filling ratio (it is the proportion of working fluid to total evaporator volume in their report) over 100%. In all cases, the effect of geyser boiling occurs mainly at the start of the operation (start-up).

Cisterna et al. (2020) studied the sodium two-phase thermosyphons for different heat transfer on different filling ratios. The researchers suggested the existence of an optimal filling ratio range that can prevent Geyser Boiling and evaporator dry-out in thermosyphons. They proposed an approximate filling ratio of 0.7 as the best value within this range. Thermosyphons with smaller filling ratios were found to have lower start-up temperatures. Moreover, they also proposed a theoretical model that can predict the minimum heat flux for a bubble release, for a given saturation temperature and departure diameter (Cisterna et al., 2021; Zhang et al., 2021) tested the ability to initiate heat transfer and the maximum allowable heating power of a Na-K alloy HP subjected to forced convection cooling. Geyser boiling in the HP improved heat transfer capacity compared to natural convection cooling, especially at lower temperatures and the minimum working temperature. Furthermore, the average temperature of the condensing section improved with the increasing mass flow rate of the Na-K alloy working fluid. In contrast, the average temperature of the evaporating unit changed very slightly with a tiny change in the boiling temperature.

4 Summary and conclusion

In this paper a comprehensive review has been performed on the design and progress of HPCR for different countries. Numerous micro HPCR design concepts are proposed for space power, marine exploration, etc. The design target varies across different HPCR applications. For the application of space, the power density and thermal-electric conversion efficiency are ensured by adopting appropriate working fluid and conversion types. In the context of space exploration, the power density and thermal-electric conversion efficiency are maintained by the selection of suitable working fluids and conversion methods. In addition, maintaining a low mass is important in order to minimize launch costs. For underwater applications, providing a power source that exhibits low noise levels and has a long lifespan is of utmost significance for energy provision. The system's thermal performance and conversion efficiency must account for the additional force caused by ocean conditions during the HPCR design procedure. In the future, it is necessary for the HPCR more compact and smaller, which is consistent with its multipurpose design concept. The energy conversion method must be highly efficient and guarantee a low specific mass. The type of working fluid for alkali metal should be carefully considered based on the operating temperature. In addition, the enrichment of uranium is a major concern. It is effective to use the high enrichment uranium (EU) for lowing the toll mass of HPCR. Despite the fact that the HPCR is not created with commercial usage in mind, the spread of high EU has become a policy issue for many nations. There have been designs for LEU systems with a lower mass in recent years, but it is unlikely that they are substantially lighter than the HEU system. A moderated option typically necessitates substantially higher development costs, time, and risk, in addition to shorter lifetimes and lower dependabilities. As a result, the design of the enrichment process poses a significant difficulty for HPCR.

For the transient characteristic of alkali metal HTHP, the startup process has a significant impact on thermal performance. In terms of inclination research, researchers have realized that temperature variation is influenced by different angles. However, the research results of the effects of inclination on the startup are inconsistent. Developing an analysis code is an effective method to the startup process. In the future, more experimental research for different angles is needed to analyze the mechanism of HTHP. The use of simulation codes not only enhances our understanding of the complex phenomena occurring during frozen startup but also facilitates the design and development of more efficient and reliable HP systems. In order for the developing code to be validated, adequate experimental data are required. The rolling condition in low amplitude is negligible to the heat transfer performance of HTHP. It is essential that relevant research on various kinds of HP and thermal-hydraulic parameters be carried out under ocean conditions.

In static conditions, the thermal performance of HTHP is affected by a variety of parameters, including NCG, inclination, filling ratio, and so on. The existence of NCG inner HP poses a significant impact on heat transfer and the flowing of the working fluid. Nevertheless, it is challenging to investigate the influence of the NCG in experiments for its generation. One of the directions of future research is the design of sufficient experiments and measurements of NCG under different fluids. In addition, the applicability of traditional HP limitation equations is a significant concern. Creating a general equation or modification is an effective strategy. The fluid filling ratio has a major impact on the heat transfer performance. Especially, the geyser boiling, occurring in a high filling ratio, is rarely researched in high temperature range. In the future, it is still necessary to study the geyser boiling for HTHP in experiment and numerical simulation.

In practical application, the HP must possess the ability to endure exceedingly elevated temperatures and tremendous heat flux while concurrently ensuring the preservation of effective heat transfer. Furthermore, the heat pipe is commonly engineered with varying angles and shapes to uphold the necessary specifications, exerting a substantial influence on its reliability. Furthermore, the durability of the HP service is influenced by factors such as corrosion, creep, thermal fatigue, and other related phenomena. In contrast, aside from the experimental test, there are currently no established procedures available for evaluating the service life. The development of a service life evaluation method is of utmost importance and requires immediate attention.

Author contributions

EW: Conceptualization, Funding acquisition, Investigation, Methodology, Supervision, Writing–original draft, Writing–review and editing. TR: Conceptualization, Investigation, Methodology, Resources, Supervision, Writing–original draft, Writing–review and editing. LL: Conceptualization, Investigation, Methodology, Resources, Supervision, Writing–original draft, Writing–review and editing.

Funding

The author(s) declare that no financial support was received for the research, authorship, and/or publication of this article.

Acknowledgments

All authors would like to express thanks to Harbin Engineering University for the funding.

Conflict of interest

The authors declare that the research was conducted in the absence of any commercial or financial relationships that could be construed as a potential conflict of interest.

Publisher's note

References

Adamas, R. (2020). Oklo has filed first combined license application (COLA) with the NRC since 2009. Available at: https://atomicinsights.com/oklo-has-filed-first-combined-license-application-cola-with-the-nrc-since-2009/.

Alawneh, L. M., Vaghetto, R., Hassan, Y., and White, H. G. S. (2022). Conceptual design of a 3 MWth yttrium hydride moderated heat pipe cooled micro reactor. *Nucl. Eng. Des.* 397, 111931. doi:10.1016/j.nucengdes.2022.111931

Allaf, M., Okamoto, K., Suzuki, S., and Erkan, N. (2023). Conceptualization of the micro research reactor cooled by heat pipes (MRR-HP), part-II: safety analyses. *J. Nucl. Sci. Technol.* 60 (08), 881–899. doi:10.1080/00223131.2022.2159560

Bess, J. (2008). "Basic LEGO reactor design for the provision of lunar surface power," in *2008 international conference on advances in nuclear power plants* (United States: Idaho National Lab).

Bushman, A., Carpenter, D. M., Ellis, T., Gallagher, S., Hershcovitch, M. D., Hine, M. C., et al. (2004). *The martian surface reactor: an advanced nuclear power station for manned extraterrestrial exploration*. Massachusetts Institute of Technology. Center for Advanced Nuclear Energy Systems. http://hdl.handle.net/1721.1/67634.

Chai, X., Guan, C., Deng, J., Zhang, T., and Liu, X. (2022). Preliminary conceptual design of a moderated micro nuclear reactor core cooled by heat pipe. *Ann. Nucl. Energy* 179, 109399. doi:10.1016/j.anucene.2022.109399

Chen, H.-X., Guo, Y.-X., Yuan, D.-Z., and Ji, Y. (2022a). Experimental study on frozen startup and heat transfer characteristics of a cesium heat pipe under horizontal state. *Int. J. Heat. Mass Transf.* 183, 122105. doi:10.1016/j.ijheatmasstransfer.2021.122105

Chen, H.-X., Guo, Y.-X., Yuan, D.-Z., and Ji, Y. (2022b). Thermal performance of a medium temperature cesium heat pipe at different inclination angles. *Int. Commun. Heat. Mass Transf.* 138, 106363. doi:10.1016/j.icheatmasstransfer.2022.106363

Chi, S. W. (1976). *Heat pipe theory and practice: a sourcebook*. Hemisphere Pub. Corp. https://www.osti.gov/biblio/5467269.

Choi, S. H., Lee, S. N., Jo, C. K., and Kim, C. S. (2022). Conceptual core design and neutronics analysis for a space heat pipe reactor using a low enriched uranium fuel. *Nucl. Eng. Des.* 387, 111603. doi:10.1016/j.nucengdes.2021.111603

Choi, Y. J., Lee, S., Jang, S., Son, I. W., Kim, Y., Lee, J. I., et al. (2020). Conceptual design of reactor system for hybrid micro modular reactor (H-MMR) using potassium heat pipe. *Nucl. Eng. Des.* 370, 110886. doi:10.1016/j.nucengdes.2020.110886

Cisterna, L. H. R., Cardoso, M. C. K., Fronza, E. L., Milanez, F. H., and Mantelli, M. B. H. (2020). Operation regimes and heat transfer coefficients in sodium two-phase thermosyphons. *Int. J. Heat. Mass Transf.* 152, 119555. doi:10.1016/j.ijheatmasstransfer.2020.119555

Cisterna, L. H. R., Milanez, F. H., and Mantelli, M. B. H. (2021). Prediction of geyser boiling limit for high temperature two-phase thermosyphons. *Int. J. Heat. Mass Transf.* 165, 120656. doi:10.1016/j.ijheatmasstransfer.2020.120656

Clark, A. J. (2019). *Failures and implications of heat pipe systems*. Albuquerque, NM, and Livermore, CA (United States): OSTI. doi:10.2172/1569523

Clifford, C. (2021). Oklo has a plan to make tiny nuclear reactors that run off nuclear waste. Available at: https://www.cnbc.com/2021/06/28/oklo-planning-nuclear-micro-reactors-that-run-off-nuclear-waste.html.

Demuth, S. F. (2003). SP100 space reactor design. *Prog. Nucl. Energy* 42 (3), 323–359. doi:10.1016/S0149-1970(03)90003-5

Deng, J., Wang, T., Liu, X., Zhang, T., He, H., and Chai, X. (2023). Experimental study on transient heat transfer performance of high temperature heat pipe under temperature feedback heating mode for micro nuclear reactor applications. *Appl. Therm. Eng.* 230, 120826. doi:10.1016/j.applthermaleng.2023.120826

Du, S., Li, Y., Sun, T., Jun, W., Liu, X., Su, G., et al. (2022). Research on the development trend of micro nuclear reactor technology. *Nucl. Power Eng.* 43 (04), 1–4. doi:10.13832/j.jnpe.2022.04.0001

Du, X., Tao, Y., Zheng, Y., Wang, C., Wang, Y., Qiu, S., et al. (2021). Reactor core design of UPR-s: a nuclear reactor for silence thermoelectric system NUSTER. *Nucl. Eng. Des.* 383, 111404. doi:10.1016/j.nucengdes.2021.111404

Dussinger, P. M., Anderson, W. G., and Sunada, E. T. (2005). "Design and testing of titanium/cesium and titanium/potassium heat pipes," in *3rd international energy conversion engineering conference* (San Francisco, California: American Institute of Aeronautics and Astronautics).

Dutra, B., Merzari, E., Acierno, J., Kraus, A., Manera, A., Petrov, V., et al. (2023). High-fidelity modeling and experiments to inform safety analysis codes for heat pipe microreactors. *Nucl. Technol.* 2023, 1–25. doi:10.1080/00295450.2023.2181040

El-Genk, M. S. (2008). Space nuclear reactor power system concepts with static and dynamic energy conversion. *Energy Convers. Manag.* 49 (3), 402–411. doi:10.1016/j.enconman.2007.10.014

El-Genk, M. S., and Tournier, J.-M. P. (2004). "SAIRS" — scalable amtec integrated reactor space power system. *Prog. Nucl. Energy* 45 (1), 25–69. doi:10.1016/j.pnucene.2004.08.002

Faghri, A., Buchko, M., and Cao, Y. (1991). A study of high-temperature heat pipes with multiple heat sources and sinks: Part II—analysis of continuum transient and steady-state experimental data with numerical predictions. *J. Heat. Transf.* 113 (4), 1010–1016. doi:10.1115/1.2911194

Feng, K., Wu, Y., Hu, J., Jin, X., Gu, H., and Guo, H. (2022). Preliminary analysis of a zirconium hydride moderated megawatt heat pipe reactor. *Nucl. Eng. Des.* 388, 111622. doi:10.1016/j.nucengdes.2021.111622

Fiebelmann, P. (1968). Nuclear reactor. Available at: https://lens.org/114-677-671-705-043.

Fukuzawa, Y., and Fujiie, Y. (1978). Performance characteristics of potassium heat pipe loaded with argon. *J. Nucl. Sci. Technol.* 15 (2), 109–119. doi:10.1080/18811248.1978.9735497

Gaugler Richard, S. (1944). Heat transfer device. Available at:https://lens.org/039-405-146-456-723.

Ge, L., Li, H., Tian, X., Ouyang, Z., Kang, X., Li, D., et al. (2022). Improvement and validation of the system analysis model and code for heat-pipe-cooled microreactor. *Energies* 15 (7), 2586. doi:10.3390/en15072586

Greenspan, E. (2008). *Solid0Core heat-pipe nuclear batterly type reactor*. United States: Univ. of California. doi:10.2172/940911

Grover, G. M., Cotter, T. P., and Erickson, G. F. (1964). Structures of very high thermal conductance. *J. Appl. Phys.* 35 (6), 1990–1991. doi:10.1063/1.1713792

Grover George, M., Busse Claus, A., and Bohdansky, J. (1967). Nuclear reactor with thermionic converter. Available at: https://lens.org/070-424-404-776-402.

Guillen, D. P., and Turner, C. G. (2022). Assessment of screen-covered grooved sodium heat pipes for microreactor applications. *Nucl. Technol.* 208 (8), 1301–1310. doi:10.1080/00295450.2021.1977085

Guo, H., Guo, Q., Yan, X. K., Ye, F., and Ma, C. F. (2018a). Experimental investigation on heat transfer performance of high-temperature thermosyphon charged with sodium-potassium alloy. *Appl. Therm. Eng.* 139, 402–408. doi:10.1016/j.applthermaleng.2018.04.139

Guo, Q., Guo, H., Yan, X., Ye, F., Wang, X., and Ma, Z. (2014). Experimental study of start-up performance of sodium-potassium heat pipe. *J. Eng. Thermophys.* 35 (12), 2508–2512.

Guo, Q., Guo, H., Yan, X. K., Ye, F., and Ma, C. F. (2018b). Influence of inclination angle on the start-up performance of a sodium-potassium alloy heat pipe. *Heat. Transf. Eng.* 39 (17-18), 1627–1635. doi:10.1080/01457632.2017.1370325

Guo, X., Guo, Y., Guo, S., Wang, G., Li, Z., Li, R., et al. (2023a). Concept design and neutronics analysis of a heat pipe cooled nuclear reactor with CERMET fuel. *Ann. Nucl. Energy* 192, 109974. doi:10.1016/j.anucene.2023.109974

Guo, Y., Chen, H., Yuan, D., Li, L., Wang, L., Wang, Y., et al. (2021). Startup and heat transfer performance of medium temperature cesium heat pipe. *Chem. Industry Eng. Prog.* 40 (11), 5981–5987. doi:10.16085/j.issn.1000-6613.2020-2293

Guo, Y., Su, Z., Li, Z., Wang, K., and Liu, X. (2022). An improved model of the heat pipe based on the network method applied on a heat pipe cooled reactor. *Front. Energy Res.* 10. doi:10.3389/fenrg.2022.848799

Guo, Y., Su, Z., Li, Z., Yu, J., and Wang, K. (2023b). Research on the effect of heat pipe temperature oscillation on heat pipe cooled reactor operation. *Ann. Nucl. Energy* 182, 109587. doi:10.1016/j.anucene.2022.109587

Han, Z., Chai, B., Wei, G., Bi, K., Feng, B., and Long, Y. (2019). Test study for starting performance of high-temperature gravity potassium heat pipes with and without wick. *Atomic Energy Sci. Technol.* 53 (01), 38–44. doi:10.7538/yzk.2018.youxian.0345

Hernandez, R., Todosow, M., and Brown, N. R. (2019). Micro heat pipe nuclear reactor concepts: analysis of fuel cycle performance and environmental impacts. *Ann. Nucl. Energy* 126, 419–426. doi:10.1016/j.anucene.2018.11.050

Houts, M. G., Poston, D. I., and Emrich, W. J., Jr. (1998). Heatpipe power system and heatpipe bimodal system development status. *AIP Conf. Proc.* 420 (1), 1189–1195. doi:10.1063/1.54911

Hu, C., Yu, D., He, M., Li, T., and Yu, J. (2022). Design and heat transfer performance analysis of ultra-high temperature lithium heat pipe. *Nucl. Power Eng.* 43 (03), 21–27. doi:10.13832/j.jnpe.2022.03.0021

Hu, G., Zhao, S., Sun, Z., and Yao, C. (2013). "A heat pipe cooled modular reactor concept for manned lunar base application," in *International conference on nuclear engineering* (Chengdu, China: Nuclear and Emerging Technologies for Space).

Huang, J., Wang, C., Tian, Z., Guo, K., Su, G. H., Tian, W., et al. (2022). Preliminary conceptual design and analysis of a 100 kW _e level Nuclear Silent Thermal-Electrical Reactor (NUSTER -100). *Int. J. Energy Res.* 46 (14), 19653–19666. doi:10.1002/er.8542

Huaqi, L., Zeyu, O., Xiaoyan, T., Li, G., Da, L., Xiaoya, K., et al. (2022). The development of high temperature heat-pipe transient model for system analysis of heat pipe cooled microreactor. *Prog. Nucl. Energy* 146, 104145. doi:10.1016/j.pnucene.2022.104145

Ivanovskii, M. N., Prosvetov, V. V., Sorokin, V. P., Chulkov, B. A., and Yagodkin, I. V. (1977). Investigation of the evaporation process and sonic limits in sodium heat pipes. *J. Eng. Phys.* 33, 1306–1310. doi:10.1007/BF00860904

Jafari, D., Filippeschi, S., Franco, A., and Di Marco, P. (2017). Unsteady experimental and numerical analysis of a two-phase closed thermosyphon at different filling ratios. *Exp. Therm. Fluid Sci.* 81, 164–174. doi:10.1016/j.expthermflusci.2016.10.022

Ji, Y., Wu, M., Feng, Y., Liu, H., Yang, X., Li, Y., et al. (2022). Experimental study on the effects of sodium and potassium proportions on the heat transfer performance of liquid metal high-temperature oscillating heat pipes. *Int. J. Heat. Mass Transf.* 194, 123116. doi:10.1016/j.ijheatmasstransfer.2022.123116

Ji, Y., Wu, M., Feng, Y., Yu, C., Chu, L., Chang, C., et al. (2020). An experimental investigation on the heat transfer performance of a liquid metal high-temperature oscillating heat pipe. *Int. J. Heat. Mass Transf.* 149, 119198. doi:10.1016/j.ijheatmasstransfer.2019.119198

Jin, Z., Wang, C., Liu, X., Dai, Z., Tian, W., Su, G., et al. (2022). Operation and safety analysis of space lithium-cooled fast nuclear reactor. *Ann. Nucl. Energy* 166, 108729. doi:10.1016/j.anucene.2021.108729

Kang, S.-W., Yeh, H.-M., Tsai, M.-C., and Wu, H.-H. (2019). Manufacture and test of a high temperature heat pipe. *J. Appl. Sci. Eng.* 22 (4), 493–499. doi:10.6180/jase.201909_22(3).0010

Kemme, J. E. (1966). *Heat pipe capability experiments*. New Mexico: OSTI. doi:10.2172/4473429

Kimura, R., and Asano, K. (2020). Ensuring criticality safety of vSMR core during transport based on its temperature reactivity. *Nucl. Sci. Eng.* 194 (3), 213–220. doi:10.1080/00295639.2019.1685352

Kovalenko, V., Khripunov, V., Antipenkov, A., and Ulianov, A. (1995). Heat-pipes-based first wall. *Fusion Eng. Des.* 27, 544–549. doi:10.1016/0920-3796(95)90170-1

Li, J., Cai, J., and Li, X. (2023a). Conceptual design and feasibility analysis of a megawatt level low enriched uranium heat pipe cooled reactor core. *Ann. Nucl. Energy* 181, 109576. doi:10.1016/j.anucene.2022.109576

Li, J., Hu, Z., Jiang, H., Guo, Y., Li, Z., Zhuge, W., et al. (2023b). Coupled characteristics and performance of heat pipe cooled reactor with closed Brayton cycle. *Energy* 280, 128166. doi:10.1016/j.energy.2023.128166

Liu, H., Gan, W., Yao, H., Wang, X., Wang, Y., and Zhu, Y. (2022b). Visualization and heat transfer comparative analysis of two phase closed thermosyphon. *Appl. Therm. Eng.* 217, 119172. doi:10.1016/j.applthermaleng.2022.119172

Liu, L., Liu, B., Xiao, Y., Gu, H., and Guo, H. (2022a). Preliminary thermal and mechanical analysis on the reactor core of a new heat pipe cooled reactor applied in the underwater environment. *Prog. Nucl. Energy* 150, 104306. doi:10.1016/j.pnucene.2022.104306

Liu, X., Sun, H., Tang, S., Wang, C., Tian, W., Qiu, S., et al. (2019). Thermal-hydraulic design features of a micronuclear reactor power source applied for multipurpose. *Int. J. Energy Res.* 43 (9), 4170–4183. doi:10.1002/er.4542

Liu, X., Tian, Z., Wang, C., Su, G., Tian, W., and Qiu, S. (2020). Experimental study on heat transfer performance of high temperature potassium heat pipe. *Nucl. Power Eng.* 41 (S1), 106–111. doi:10.13832/j.jnpe.2020.S1.0106

Lu, Q., Han, H., Hu, L., Chen, S., Yu, J., and Ai, B. (2017). Preparation and testing of nickel-based superalloy/sodium heat pipes. *Heat Mass Transf.* 53 (11), 3391–3397. doi:10.1007/s00231-017-2105-5

Ma, K., and Hu, P. (2022). Preliminary conceptual design and neutroncis analysis of a heat pipe cooled traveling wave reactor. *Ann. Nucl. Energy* 168, 108907. doi:10.1016/j.anucene.2021.108907

Ma, K., and Hu, P. (2023). Preliminary neutronics and thermal analysis of a heat pipe cooled traveling wave reactor. *Ann. Nucl. Energy* 190, 109876. doi:10.1016/j.anucene.2023.109876

Ma, Y., Yu, H., Huang, S., Zhang, Y., Liu, Y., Wang, C., et al. (2022a). Effect of inclination angle on the startup of a frozen sodium heat pipe. *Appl. Therm. Eng.* 201, 117625. doi:10.1016/j.applthermaleng.2021.117625

Ma, Y., Yu, H., Wang, X., Zhang, Y., Huang, S., Wang, C., et al. (2023). Experimental study on sodium Screen-Wick heat pipe capillary limit. *Appl. Therm. Eng.* 227, 120397. doi:10.1016/j.applthermaleng.2023.120397

Ma, Y., Zhong, R., Yu, H., Huang, S., Tian, C., He, X., et al. (2022b). Startup analyses of a megawatt heat pipe cooled reactor. *Prog. Nucl. Energy* 153, 104405. doi:10.1016/j.pnucene.2022.104405

Maioli, A., Detar, H., Haessler, R., Friedman, B., Belovesick, C., Cobel, J., et al. (2019). Modernization of technical requirements for licensing of advanced non-light water reactors Westinghouse eVinciTM micro-reactor licensing modernization project demonstration. Avaliable at: https://www.nrc.gov/docs/ML1922/ML19227A322.pdf.

Manoj, R., Kumar, M. C., NarasimhaRao, R., Narasimha, K. R., and Suresh, P. V. S. (2012). PERFORMANCE EVALUATION OF SODIUM HEAT PIPES THROUGH PARAMETRIC STUDIES. *Front. Heat Pipes* 3, 043003. doi:10.5098/fhp.v3.4.3003

Mantelli, M. B., Uhlmann, T., Cisterna, L. H., Marengo, M., and Eskilsson, P. (2017). "Experimental study of a sodium two-phase thermosyphon," in *9th world conference on experimental heat transfer, fluid mechanics and thermodynamics* (Iguazu Falls, Brazil: MECHANICAL POWER ENGINEERING DEPARTMENT).

Mao, S., Zhou, T., Liu, W., Wei, D., and Xue, C. (2022). Numerical simulation of three-phase coupling for high-temperature lithium heat pipe. *Nucl. Power Eng.* 43 (06), 37–42. doi:10.13832/j.jnpe.2022.06.0037

Matsushita, T. (1975). "The effects of noncondensable gas in the heatpipes," in *11th international symposium on space technology and science* (Tokyo, Japan: AGNE Publishing, Inc).

McClure, P. R., Poston, D. I., Dasari, V., and Reid, R. S. (2015). *Design of megawatt power level heat pipe reactors*. USA: Los Alamos National Lab. LANL. doi:10.2172/1226133

McClure, P. R., Poston, D. I., Gibson, M. A., Mason, L. S., and Robinson, R. C. (2020). Kilopower project: the KRUSTY fission power experiment and potential missions. *Nucl. Technol.* 206 (Suppl. 1), S1–S12. doi:10.1080/00295450.2020.1722554

Mochizuki, M., Singh, R., Nguyen, T., and Nguyen, T. (2014a). Heat pipe based passive emergency core cooling system for safe shutdown of nuclear power reactor. *Appl. Therm. Eng.* 73 (1), 699–706. doi:10.1016/j.applthermaleng.2014.07.004

Mochizuki, M., Singh, R., Nguyen, T., and Saito, Y. (2014b). An emergency core cooling system (ECCS) for nuclear power reactor using passive loop heat pipe. *J. Jpn. Inst. Electron. Packag.* 5, 180–184. doi:10.5104/jiep.15.180

Nemec, P., Čaja, A., and Malcho, M. (2013). Mathematical model for heat transfer limitations of heat pipe. *Math. Comput. Model. Dyn. Syst.* 57 (1), 126–136. doi:10.1016/j.mcm.2011.06.047

Niu, T., Zhang, Y., Hou, H., Wang, Y., and He, Z. (2016). Properties of high-temperature heat pipe and its experimental. *Acta Aeronautica Astronautica Sinica* 37 (S1), 59–65. doi:10.7527/S1000-6893.2016.0165

Ping, Y., Hong, Z., Hui, X., and Yan, S. (2015). Restart characteristics of high-temperature sodium heat pipe. *Proc. CSEE* 35 (02), 404–410. doi:10.13334/j.0258-8013.pcsee.2015.02.019

Ponnappan, R., Boehman, L. I., and Mahefkey, E. T. (1990). Diffusion-controlled startup of a gas-loaded liquid-metal heat pipe. *J. Thermophys. Heat. Transf.* 4 (3), 332–340. doi:10.2514/3.185

Ponnappan, R., and Chang, W. S. (1994). Startup performance of a liquid-metal heat pipe in near-vacuum and gas-loaded modes. *J. Thermophys. Heat. Transf.* 8 (1), 164–171. doi:10.2514/3.516

Poston, D. I. (2001). The heatpipe-operated Mars exploration reactor (HOMER). *AIP Conf. Proc.* 552, 797–804. doi:10.1063/1.1358010

Poston, D. I., Gibson, M. A., Godfroy, T., and McClure, P. R. (2020). KRUSTY reactor design. *Nucl. Technol.* 206 (Suppl. 1), S13–S30. doi:10.1080/00295450.2020.1725382

Poston, D. I., Kapernick, R. J., and Guffee, R. M. (2002). Design and analysis of the SAFE-400 space fission reactor. *AIP Conf. Proc.* 608 (1), 578–588. doi:10.1063/1.1449775

Poston, D. I., and Mcclure, P. R. (2017). *White paper – use of LEU for a space reactor*. United States: Idaho National Lab.INL. doi:10.2172/1375148

Poston, D. I., Voit, S. L., Reid, R. S., and Ring, P. J. (2000). The heatpipe power system (HPS) for Mars outpose and manned Mars missions. *AIP Conf. Proc.* 504 (1), 1327–1334. doi:10.1063/1.1290947

Qiu, S., Zhang, Z., Zhang, Z., Wang, C., Guo, K., Tian, W., et al. (2022). Study on thermal-hydraulic characteristics of ocean silent heat pipe cooled reactor. *Atomic Energy Sci. Technol.* 56 (06), 989–1004. doi:10.7538/yzk.2022.youxian.0339

Randeep, S., Masataka, M., Thang, N., and Yuji, S. (2014). "Heat pipe applications in cooling nuclear fuel," in *International heat transfer conference* (Kyoto, Japan: U.S. Department of Energy National Laboratory operated by Battelle Energy Alliance, LLC).

Shaubach, R. M., and Gernet, N. J. (1992). Sodium heat pipe with sintered wick and artery: effects of noncondensible gas on performance. *AIP Conf. Proc.* 246 (1), 1153–1161. doi:10.1063/1.41778

Sterbentz, J. W., Werner, J. E., Hummel, A. J., Kennedy, J. C., O'Brien, R. C., Dion, A. M., et al. (2017). *Preliminary assessment of two alternative core design concepts for the special purpose reactor*. Idaho Falls, ID (United States): Idaho National Lab.INL.

Sun, H., Liu, X., Liao, H., Wang, C., Zhang, J., Tian, W., et al. (2022a). Experiment study on thermal behavior of a horizontal high-temperature heat pipe under motion conditions. *Ann. Nucl. Energy* 165, 108760. doi:10.1016/j.anucene.2021.108760

Sun, H., Pellegrini, M., Wang, C., Suzuki, S., Okamoto, K., Tian, W., et al. (2022b). CFD simulation based on film model of high temperature potassium heat pipe at different positions: horizontal, vertical, and 45° inclined. *Prog. Nucl. Energy* 154, 104442. doi:10.1016/j.pnucene.2022.104442

Sun, H., Wang, C., Liu, X., Tian, W., Qiu, S., and Su, G. (2018a). Reactor core design of micro nuclear power source applied for underwater vehicle. *Atomic Energy Sci. Technol.* 52 (04), 646–651. doi:10.7538/yzk.2017.youxian.0465

Sun, H., Wang, C., Ma, P., Liu, X., Tian, W., Qiu, S., et al. (2018b). Conceptual design and analysis of a multipurpose micro nuclear reactor power source. *Ann. Nucl. Energy* 121, 118–127. doi:10.1016/j.anucene.2018.07.025

Sun, H., Zhang, R., Wang, C., Deng, J., Tian, W., Qiu, S., et al. (2020). Reactivity feedback evaluation during the start-up of the heat pipe cooled nuclear reactors. *Prog. Nucl. Energy* 120, 103217. doi:10.1016/j.pnucene.2019.103217

Sun, K., Hu, L.-W., and Forsberg, C. (2016). Neutronic design features of a transportable fluoride-salt-cooled high-temperature reactor. *J. Nucl. Eng. Radiat. Sci.* 2 (3), 031003. doi:10.1115/1.4032873

Swartz, M. M., Byers, W. A., Lojek, J., and Blunt, R. (2021). "Westinghouse eVinci™ heat pipe micro reactor technology development," in 28th *International conference on nuclear engineering, virtual conference*, ASME. doi:10.1115/ICONE28-67519

Tang, S., Wang, C., Liu, X., Tian, Z., Su, G. H., Tian, W., et al. (2020). Experimental investigations on start-up performance of static nuclear reactor thermal prototype. *Int. J. Energy Res.* 44 (4), 3033–3048. doi:10.1002/er.5134

Tang, S., Wang, C., Zhang, D., Tian, W., Su, G., and Qiu, S. (2021). Thermoelectric performance study on a heat pipe thermoelectric generator for micro nuclear reactor application. *Int. J. Energy Res.* 45 (8), 12301–12316. doi:10.1002/er.6450

Teng, W., Wang, X., and Zhu, Y. (2020). Experimental investigations on start-up and thermal performance of sodium heat pipe under swing conditions. *Int. J. Heat. Mass Transf.* 152, 119505. doi:10.1016/j.ijheatmasstransfer.2020.119505

Tian, Z., Liu, X., Wang, C., Zhang, D., Tian, W., Qiu, S., et al. (2021). Experimental investigation on the heat transfer performance of high-temperature potassium heat pipe for nuclear reactor. *Nucl. Eng. Des.* 378, 111182. doi:10.1016/j.nucengdes.2021.111182

Tian, Z., Wang, C., Guo, K., Zhang, D., Tian, W., Qiu, S., et al. (2022a). Parameters sensitivity analys is and optimization of high-temperature heat pipe for heat pipe reactor. *Nucl. Power Eng.* 43 (06), 85–92. doi:10.13832/j.jnpe.2022.06.0085

Tian, Z., Zhang, J., Wang, C., Guo, K., Liu, Y., Zhang, D., et al. (2022b). Experimental evaluation on heat transfer limits of sodium heat pipe with screen mesh for nuclear reactor system. *Appl. Therm. Eng.* 209, 118296. doi:10.1016/j.applthermaleng.2022.118296

Walker, K. L., Tarau, C., and Anderson, W. G. (2013). "High temperature heat pipes for space fission power," in *11th international energy conversion engineering conference* (San Jose, CA: AIAA).

Wang, C., Liu, X., Liu, M., Tang, S., Tian, Z., Zhang, D., et al. (2021). Experimental study on heat transfer limit of high temperature potassium heat pipe for advanced reactors. *Ann. Nucl. Energy* 151, 107935. doi:10.1016/j.anucene.2020.107935

Wang, C., Sun, H., Tang, S., Tian, W., Qiu, S., and Su, G. (2020a). Thermal-hydraulic analysis of a new conceptual heat pipe cooled small nuclear reactor system. *Nucl. Eng. Technol.* 52 (1), 19–26. doi:10.1016/j.net.2019.06.021

Wang, C., Sun, K., Hu, L.-W., Qiu, S., and Su, G. H. (2016). Thermal-hydraulic analyses of transportable Fluoride salt–cooled high-temperature reactor with CFD modeling. *Nucl. Technol.* 196 (1), 34–52. doi:10.13182/NT15-42

Wang, C., Tang, S., Liu, X., Su, G. H., Tian, W., and Qiu, S. (2020b). Experimental study on heat pipe thermoelectric generator for industrial high temperature waste heat recovery. *Appl. Therm. Eng.* 175, 115299. doi:10.1016/j.applthermaleng.2020.115299

Wang, C., Zhang, D., Qiu, S., Tian, W., Wu, Y., and Su, G. (2013). Study on the characteristics of the sodium heat pipe in passive residual heat removal system of molten salt reactor. *Nucl. Eng. Des.* 265, 691–700. doi:10.1016/j.nucengdes.2013.09.023

Wang, C., Zhang, L., Liu, X., Tang, S., Qiu, S., and Su, G. H. (2020c). Experimental study on startup performance of high temperature potassium heat pipe at different inclination angles and input powers for nuclear reactor application. *Ann. Nucl. Energy* 136, 107051. doi:10.1016/j.anucene.2019.107051

Wang, C., Zhang, Z., Zhang, M., Li, P., Tian, Z., Tian, W., et al. (2022). Numerical evaluation of non-condensable gas influence on the heat transfer characteristics of high-temperature lithium heat pipe during reactor operation. *Ann. Nucl. Energy* 173, 109077. doi:10.1016/j.anucene.2022.109077

Wang, E., and Li, L. (2023). Numerical analysis of high temperature potassium heat pipe under marine condition. *Int. Commun. Heat. Mass Transf.* 147, 106978. doi:10.1016/j.icheatmasstransfer.2023.106978

Wang, X., Shi, Y., Liu, T., Wang, S., Wang, K., Chen, H., et al. (2022c). CFD modeling of liquid-metal heat pipe and hydrogen inactivation simulation. *Int. J. Heat. Mass Transf.* 199, 123490. doi:10.1016/j.ijheatmasstransfer.2022.123490

Wei, G., Chai, B., Han, Z., Zhang, Y., Feng, B., Bi, K., et al. (2021). Experimental study on heat transfer performance of high temperature sodium heat pipe. *Atomic Energy Sci. Technol.* 55 (06), 1039–1046. doi:10.7538/yzk.2021.youxian.0115

WNA (2020). Generation IV nuclear reactors. Available at: https://world-nuclear.org/information-library/nuclear-fuel-cycle/nuclear-power-reactors/generation-iv-nuclear-reactors.aspx.

Wu, M., Ji, Y., Feng, Y., Liu, H., and Yang, X. (2023a). Experimental study on the effects of filling ratios on heat transfer characteristics of liquid metal high-temperature

oscillating heat pipes. *Int. J. Heat. Mass Transf.* 209, 124153. doi:10.1016/j.ijheatmasstransfer.2023.124153

Wu, M., Ji, Y., Feng, Y., Yang, X., Li, Y., and Liu, Q. (2022). "Experimental investigation on the effects of inclination angle on heat transfer performance of a liquid metal high-temperature oscillating heat pipe," in *ASME 2021 heat transfer summer conference. Virtual* (ASME). doi:10.1115/HT2021-63718

Wu, Y., Zheng, Y., Tao, Y., Liu, X., Du, X., and Wang, Y. (2023b). The low-enriched uranium core design of a MW heat pipe cooled reactor. *Nucl. Eng. Des.* 404, 112195. doi:10.1016/j.nucengdes.2023.112195

Yang, H., Wang, C., Zhang, D., Zhang, J., Tian, W., Qiu, S., et al. (2022). Parameter sensitivity study on startup characteristics of high temperature potassium heat pipe. *Nucl. Eng. Des.* 392, 111754. doi:10.1016/j.nucengdes.2022.111754

Yao, C., Hu, G., Zhao, S., Xie, J., Guo, J., and Gao, J. (2016a). Scheme research of Mars surface nuclear reactorpower. *Atomic Energy Sci. Technololgy* 50 (08), 1449–1455. doi:10.7538/yzk.2016.50.08.1449

Yao, C., Zhao, S., Hu, G., Xie, J., Guo, J., and Gao, J. (2016b). "Scheme research of Mars surface nuclear reactor power," in *20th pacific basin nuclear conference* (Beijing, China: Spinger).

Yu, Q., Zhao, P., and Ma, Y. (2022). CFD analysis on characteristics of high temperature heat pipe. *Nucl. Power Eng.* 43 (02), 70–76. doi:10.13832/j.jnpe.2022.02.0070

Yuan, Y., Gou, J., Shan, J., Zhang, B., and Zhang, B. (2016a). Startup characteristics of heat pipe cooled space reactor. *Atomic Energy Sci. Technol.* 50 (06), 1054–1059. doi:10.7538/yzk.2016.50.06.1054

Yuan, Y., Shan, J., Zhang, B., Gou, J., Zhang, B., Lu, T., et al. (2016b). Study on startup characteristics of heat pipe cooled and AMTEC conversion space reactor system. *Prog. Nucl. Energy* 86, 18–30. doi:10.1016/j.pnucene.2015.10.002

Zhang, H., Ye, F., Guo, H., and Yan, X. (2021d). Sodium-potassium alloy heat pipe under Geyser Boiling experimental study: heat transfer analysis. *Energies* 14 (22), 7582. doi:10.3390/en14227582

Zhang, J., Tian, Z., Wang, C., Tian, W., Guo, K., Qiu, S., et al. (2022c). Study on heat transfer limitationof liquid metal high-temperature heat pipe. *Atomic Energy Sci. Technol.* 56 (10), 2024–2031. doi:10.7538/yzk.2021.youxian.0806

Zhang, K., Yue, K., Yan, X., and Tong, W. (2020b). Study on lsothermal characteristics of gravity cesium heat pipe. *ACTA METROL. SIN.* 41 (01), 26–31. doi:10.3969/j.issn.1000-1158.2020.01.06

Zhang, M., Miao, Q., Zhang, S., Ma, Y., Ding, S., Zhang, Z., et al. (2023). Experimental study of non-condensable gas effects on sonic limit of sodium heat pipe. *Appl. Therm. Eng.* 232, 120970. doi:10.1016/j.applthermaleng.2023.120970

Zhang, M., Wang, C., Sun, H., Dai, Z., Zhang, D., Tian, W., et al. (2021a). Non-condensable gas generation behavior in high-temperature lithium heat pipe under irradiation. *Atomic Energy Sci. Technol.* 55 (06), 1024–1030. doi:10.7538/yzk.2020.youxian.0482

Zhang, M., Wang, C., Tian, Z., Guo, K., Tian, W., Su, G., et al. (2022a). Study on influence of non-condensable gas on heat transfer characteristics of high temperature lithium heat pipe. *Atomic Energy Sci. Technol.* 56 (06), 1094–1103. doi:10.7538/yzk.2021.youxian.0901

Zhang, W., Zhang, D., Wang, C., Tian, W., Qiu, S., and Su, G. H. (2020a). Conceptual design and analysis of a megawatt power level heat pipe cooled space reactor power system. *Ann. Nucl. Energy* 144, 107576. doi:10.1016/j.anucene.2020.107576

Zhang, Z., Chai, X., Wang, C., Sun, H., Zhang, D., Tian, W., et al. (2021b). Numerical investigation on startup characteristics of high temperature heat pipe for nuclear reactor. *Nucl. Eng. Des.* 378, 111180. doi:10.1016/j.nucengdes.2021.111180

Zhang, Z., Wang, C., Guo, K., Huang, J., Qiu, S., Su, G. H., et al. (2022b). HEART, a specific code for thermal-electrical analysis of heat pipe cooled nuclear reactor. *Int. J. Therm. Sci.* 179, 107666. doi:10.1016/j.ijthermalsci.2022.107666

Zhang, Z., Wang, C., Sun, H., Zhang, D., Qiu, S., Su, G., et al. (2021c). Analysis of startup characteristics for alkali metal high temperature heat pipe. *Atomic Energy Sci. Technol.* 55 (06), 1015–1023. doi:10.7538/yzk.2020.youxian.0464

Zhao, J., Yuan, D., Tang, D., Cao, K., and Ji, Y. (2021). Analytical and experimental study of the high temperature heat pipe sonic limitation. *J. Eng. Thermophys.* 42 (03), 700–705.

Zhong, R., Ma, Y., Deng, J., Liu, Y., Chai, X., and Wang, J. (2021). Reactor startup characteristics of heat pipe cooled reactor with multiple feedback mechanism. *Nucl. Power Eng.* 42 (S2), 104–108. doi:10.13832/j.jnpe.2021.S2.0104

Zohuri, B., and McDaniel, P. (2019). Design and analysis of core design for small modular reactors. *Adv. Smaller Modul. React.* 2019, 187–217. doi:10.1007/978-3-030-23682-3_9

Nomenclature

CAEP	China Academy of Engineering Physics
Caltech	California Institute of Technology
CIAE	China Institute of Atomic Energy
EU	enrichment uranium
FHR	Fluoride-Salt-Cooled High-Temperature Reactor
HEART	HEat pipe cooled Advanced Reactor Transient analysis code
HOMER	Heat pipe-Operated Mars Exploration Reactor
HP	heat pipe
HPCR	heat pipe cooled reactor
HPCRPS	heat pipe cooled reactor power source
HPCYHR	Heat Pipe Cooled Yttrium Hydride Moderated Micro Reactor
HP-ENHS	Heat Pipe Encapsulated Nuclear Heat Source
HPS	Heat pipe Power System
HP-STMC	Heat Pipes-Segmented Thermoelectric Module Converter
HPTAWR	heat pipe cooled traveling wave reactor
HTHP	high temperature heat pipe
INL	Idaho National Laboratory
ITER	International Thermonuclear Experimental Reactor
LANL	Los Alamos National Laboratory
LEGO	Lunar Evolutionary Growth-Optimized
LEU	Low-Enriched Uranium
LHPRPS	lithium heat pipe reactor power source
MHPR	micro nuclear reactor cooled by heat pipe
MoveluX	Mobile-Very-small reactor for Local Utility in X-mark
MRR-HP	Micro Research Reactor cooled by Heat Pipes
NCG	non-condensable gas
NRPMS	nuclear reactor power for Mars surface
NUSTER	NUclear Silence ThermoElectric Reactor
PHPCRPS	potassium heat pipe cooled reactor power source system
SAFE	Safe Affordable Fission Engine
SAIRS	Scalable AMTEC Integrated Reactor Space
SJTU	Shanghai Jiao Tong University
SMR	small nuclear reactor
SPR	Special Purpose Reactor
TAMU	Texas A&M University
UNM	University of New Mexico
UPR-S	Unmanned Portable Reactor in Silence
XJU	Xi'an Jiaotong University

Frontiers in
Energy Research

Advances and innovation in sustainable, reliable and affordable energy

Explores sustainable and environmental developments in energy. It focuses on technological advances supporting Sustainable Development Goal 7: access to affordable, reliable, sustainable and modern energy for all.

Discover the latest Research Topics

See more →

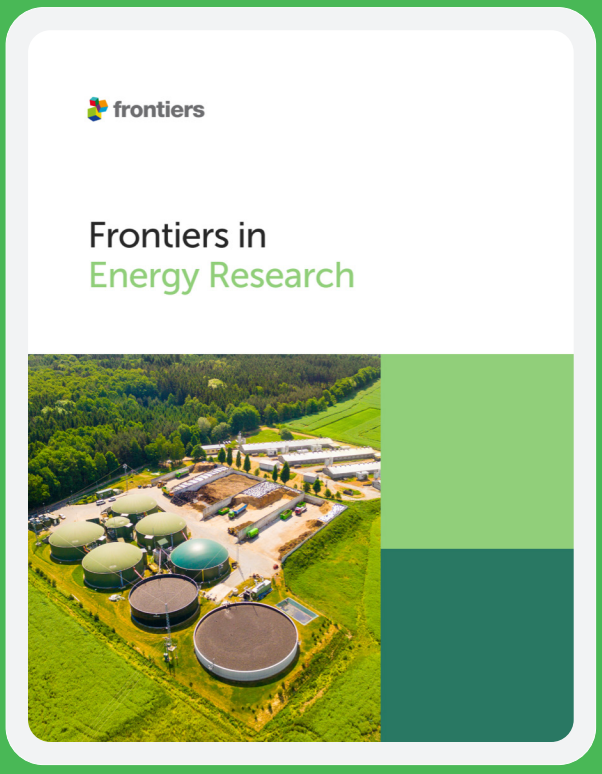

Frontiers

Avenue du Tribunal-Fédéral 34
1005 Lausanne, Switzerland
frontiersin.org

Contact us

+41 (0)21 510 17 00
frontiersin.org/about/contact